Nanostructured Materials and their Application in Thermoelectric Energy Harvesting

Von der Naturwissenschaftlichen Fakultät der
Gottfried Wilhelm Leibniz Universität Hannover

zur Erlangung des Grades

Doktor der Naturwissenschaften
(Dr. rer. nat.)

genehmigte Dissertation

von

Michael Bittner, M. Sc.

[2018]

Referent: apl. Prof. Dr. Armin Feldhoff

Korreferent 1: Prof. Kjell Wiik

Korreferent 2: Prof. Dr. Oliver Oeckler

Tag der Promotion: 30.10.2018

Preface

The represented results of my thesis were achieved from August 2014 to August 2018 during my time as a scientific assistant at the Institute of Physical Chemistry and Electrochemistry at the Gottfried Wilhelm Leibniz University Hannover under the supervision of Prof. Dr. Armin Feldhoff. My work was funded by the Deutsche Forschungsgesellschaft (DFG, German Research Foundation) - FE928/17-1.

Chapter 1 describes the fundamentals of thermoelectricity, synthesis, processing routes and concepts to improve materials, as well as their application in thermoelectric generators. Chapters 2 and 3 consist of six research articles, which are subsequently presented.

The article in section 2.2, *Porous $Ca_3Co_4O_9$ with enhanced thermoelectric properties derived from Sol-Gel synthesis*, was written by myself. The article exhibits the synthesis and growth mechanism of $Ca_3Co_4O_9$ (CCO) particles, which were derived from the sol-gel synthesis. A highly porous CCO ceramic showed a significantly reduced heat conductivity and subsequently enhanced thermoelectric figure-of-merit zT. All oxide powders and ceramics were synthesized and processed by myself. The measurements of electrical conductivity and Seebeck coefficient as well as data evaluation were done by myself. Density, porosity and X-ray diffraction (XRD) measurements as well as investigations of the microstructures by scanning electron microscopy (SEM) were carried out and evaluated by myself. Analyzes of intermediates and calcined CCO powders via transmission electron microscopy (TEM) were done by Lailah Helmich, and data evaluation was carried out by myself. Measurements of heat conductivity and capacity were done by Frederik Nietschke and Marc Krey, respectively, and data evaluation was carried out by myself. All co-authors participated in discussion and improvement of the publication.

The article in section 2.3, *Triple-phase ceramic 2D nanocomposite with enhanced thermoelectric properties*, was written by myself. The article reports a newly developed $Ca_3Co_4O_9$-Na_xCoO_2-$Bi_2Ca_2Co_2O_9$ (CCO-NCO-BCCO) nanocomposite ceramic with increased electrical conductivity σ and thermoelectric power factor $\sigma \cdot \alpha^2$. The three misfit layered thermoelectric oxides CCO, BCCO and NCO grew semi-coherently on each other, forming an all-scale hierarchical architecture. All oxide powders and ceramics were synthesized and processed by myself. The measurements of electrical conductivity and Seebeck coefficient as well as data evaluation were done by myself. Density, porosity and XRD measurements as well as investigations of the microstructures by SEM were carried out and evaluated by myself. Investigations of the nanostructure of the CCO-NCO-BCCO nanocomposite via TEM were done by Frank Steinbach, and data evaluation was carried out by myself. Measurements of heat conductivity were done by myself and Nikola Kanas, and data evaluation

was carried out by myself. Measurements of the heat capacity were done by Marc Krey, and data evaluation was carried out by myself. All co-authors participated in discussion and improvement of the publication.

Chapter 3 is about manufacturing and characterizing new thermoelectric generators, which involve the materials discussed in chapter 2 and others. Thermoelectric generators of different designs were developed, fabricated and power generation was improved.

The article in section 3.2, *Oxide-based thermoelectric generator for high-temperature application using p-type $Ca_3Co_4O_9$ and n-type $In_{1.95}Sn_{0.05}O_3$ legs*, was written by myself. The article reveals the enhancement of electrical power output and power density if an electrically highly conductive indium oxide phase is used as n-type material instead of low conducting ZnO or $CaMnO_3$. All oxide powders and ceramics were synthesized and processed by myself. The measurements of electrical conductivity and Seebeck coefficient as well as data evaluation were done by myself. Density, porosity and XRD measurements as well as investigations of the microstructures by SEM were carried out and evaluated by myself. Mesurements of the thermal expansion coefficient was done and evaluated by myself. Construction and measurement of power characteristics of the thermoelectric generator as well as data evaluation were done by myself. All co-authors participated in discussion and improvement of the publication.

I was participating in improving the simulation tool, as well as in discussion and review of the article in section 3.3, *Experimental characterisation and finite-element simulations of a thermoelectric generator with ceramic p-type $Ca_3Co_4O_9$ and metallic n-type $Cu_{0.57}Ni_{0.42}Mn_{0.01}$ legs*. The article describes a finite-element simulation tool, which is experimentally verified by use of a thermoelectric generator prototype. The tool enables the possibility to predict the performance of a thermoelectric generator from materials properties.

I was involved in discussion and review of the article in section 3.4, *All-oxide thermoelectric module with in-situ formed non-rectifying complex p-p-n junction and transverse thermoelectric effect*. The article presents the first manufactured all-oxide thermoelectric generator made by spark plasma sintering of CCO and $CaMnO_3$. A complex p-p-n junction is in-situ formed at high temperatures and delivers beneficial properties for thermoelectric power generation. I carried out SEM investigations of the CCO, $CaMnO_3$ and $LaAlO_3$ powder samples. Furthermore, I executed Seebeck coefficient measurements of CCO and $CaMnO_3$ and was participating in data evaluation. In addition, I was involved in preparation and measurement of the power characteristics of the all-oxide generator as well as in data evaluation.

The article in section 3.5, *A comprehensive study on improved power materials for high-temperature thermoelectric generators*, was written by myself. The article illustrates an extensive investigation of the development and impact of improved thermoelectric materials on the electrical power output and power density of thermoelectric generators. The used p- and n-type materials were specifically developed to discuss the impact of high-power materials and high-zT materials on the thermoelectric power generation. All oxide powders and ceramics were synthesized and processed

by myself, except spark plasma sintering (SPS) and hot-pressing of powders, which were carried out by Nikola Kanas and Jan Räthel, respectively. The measurements of electrical conductivity and Seebeck coefficient as well as data evaluation were done by myself. Hall-effect measurements were done by Matthias Schrade, and data evaluation was carried out by Matthias Schrade and myself. Density, porosity and XRD measurements as well as investigations of the microstructures by SEM were carried out and evaluated by myself. Measurements of the heat conductivity and capacity were done by Nikola Kanas and Marc Krey, respectively, and data evaluation was carried out by myself. Thermogravimetric measurements were done by Marc Krey, and data evaluation was carried out by myself. Investigations of the nanostructures of the O_2-sintered and the SPS-processed samples via TEM were done by Frank Steinbach, and data evaluation was carried out by myself. Construction and measurement of power characteristics of the thermoelectric generators as well as data evaluation were done by myself. All co-authors participated in discussion and improvement of the publication.

Acknowledgement

Abstract

Keywords: Thermoelectricity; energy harvesting; power generation; oxides

Thermoelectric materials can, reversibly and without any moving parts, convert thermal energy into electrical energy by coupling an entropic and an electrical flux with each other. This ability is becoming increasingly important in concerns of a growing energy demand of the world, sustainability and climate change. The material class of thermoelectric oxides can play an important role in waste heat harvesting from industrial processes and power plants. On the basis of advantageous properties of oxides in the high-temperature range under oxidizing atmosphere, an application in electrical power generation from infinite heat sources seems promising. The thermoelectric research is a highly interdisciplinary field of study, which consists of solid state chemistry and solid state physics, when synthesizing new materials and measuring their properties. In addition, thermoelectric research is also a matter of process and electrical engineering, when p- and n-type materials are assembled to a thermoelectric generator and its power characteristic is estimated.
Material classes like alloys, tellurides, half-Heusler or Zintl phases such as Bi_2Te_3, PbTe-PbS, SiGe, SnSe, FeNbSb and $Yb_{14}MnSb_{11}$, possess significantly improved thermoelectric properties, especially in the low- to mid-temperature range under inert or reducing atmosphere. But these material classes show inferior stability in the high-temperature range under oxidizing conditions, are toxic, or consist of expensive and rare elements. Concerning the thermoelectric figure-of-merit zT, oxides can not compete with other material classes. For this reason, research on oxides should focus on improving the thermoelectric power factor in the high-temperature range in air. Furthermore, the field of application of materials and conditions under which these are applied should be critically discussed. For the scenario of application of a limited heat source and if a maximized conversion efficiency should be obtained, a high-zT material is desirable. However, for the case of an infinite heat source and under the assumption of waste heat recovery at high-temperatures, a stable high-power factor material is superior for power generation. For this reason, on the one hand an unusual approach of manufacturing porous ceramics was carried out to decrease the heat conductivity and therefore, to improve the zT value. On the other hand, co-doping and compositionally alloyed nanostructures were used to develop high-power materials. The applicability of materials for power generation can be evidently estimated in a so-called Ioffe plot, which displays the thermoelectric power factor as a function of the electrical conductivity. The influence and possibility to maximize the electrical power output at high temperatures from infinite heat sources were recently theoretically described. A maximized power factor and a moderate

heat conductivity are the most important parameters to improve power generation under these conditions.

In the present work, different oxides were synthesized and investigated in terms of their thermoelectric properties. Furthermore, synthesis, growing mechanism and structure were investigated using X-ray diffraction (XRD) methods, scanning electron microscopy (SEM) and transmission electron microscopy (TEM). The influence of different processing techniques on micro-, nanostructure and thermoelectric properties were investigated using SEM, TEM, energy dispersive X-ray spectroscopy (EDXS) and thermoelectric property measurements. The stability in air of different materials were analyzed by thermogravimetry, XRD and cycle testing of thermoelectric properties. The behavior of different materials in terms of their coefficient of thermal expansion was investigated using dilatometry.

The primarily investigated phases are p-type $Ca_3Co_4O_9$ (CCO) and n-type In_2O_3 semiconducting oxides. The crystal structure and phase formation of CCO is very complex and subsequent ceramic processing is intricate. However, highly porous CCO ceramics possess significantly reduced values of the heat conductivity and a subsequently enhanced figure-of-merit zT of 0.4, which is the highest reported for pure CCO ceramics. A new thermoelectric triple-phase $Ca_3Co_4O_9$-Na_xCoO_2-$Bi_2Ca_2Co_2O_9$ (CCO-NCO-BCCO) nanocomposite with enhanced thermoelectric properties was developed and characterized. The anisotropic thermoelectric properties were estimated. The highest power factor, electrical conductivity of 6.5 $\mu W \cdot cm^{-1} \cdot K^{-2}$, 116 S·cm^{-1} (Ioffe plot) and figure-of-merit zT of 0.35 for CCO-NCO-BCCO nanocomposites, respectively, were obtained perpendicular to the pressing direction at 1073 K in air. This zT value is the highest obtained for a p-type thermoelectric oxide in a study, which reports anisotropic transport properties perpendicular and parallel to the pressing direction of the ceramic. The thermoelectric properties could be simultaneously enhanced in a co-doped nanocomposite with all-scale hierarchical architecture of three misfit layered oxides, which grew semi-coherently on each other. By interdiffusion and incorporation in a CCO matrix, the thermally less stable phases NCO and BCCO could be stabilized and utilized at high temperatures.

The different synthesized, investigated and developed p- and n-type materials were used and assembled in different designs of thermoelectric generators, which were characterized in terms of proof of principle and maximizing the electrical power output and power density. The first generator was constructed using a conventional chess-board design and showed an enhanced electrical power output and power density at high temperatures, when electrically highly conducting indium oxide phases were used. A finite-element simulation tool was developed to predict power characteristics of thermoelectric generators and to exhibit different fluxes within the devices. In addition, the importance of minimizing contact resistances to improve the electrical power output of a thermoelectric generator was illustrated. By spark plasma sintering of $Ca_3Co_4O_9$ and $CaMnO_3$ powders an all-oxide thermoelectric generator was developed. A complex p-p-n junction formed in-situ at high temperatures, which reduces the contact resistance (ohmic behavior) and boosts the electrical voltage and thereby the electrical power output of the generator by uti-

lizing a transversal thermoelectric effect at the interfaces of the p-p-n junction. This all-oxide generator could be reported for the first time and is comparable in terms of electrical power output and electrical power density to most conventional oxide-based generators. The p-p-n junction at the interface between p- and n-type materials abstain from metallic connectors and is hence applicable to even higher temperatures compared to conventional thermoelectric generators.

The impact of high-power and high-zT materials on the electrical power output and electrical power density of thermoelectric generators was comprehensively studied. A p-type triple-phase CCO-NCO-BCCO nanocomposite was processed using different sintering techniques and the power factor and electrical conductivity (Ioffe plot) were improved to reach 8.2 μW $\cdot$ cm^{-1} $\cdot$ K^{-2} and 143 S$\cdot$cm^{-1}, respectively, at 1073 K in air. The developed p- and n-type materials were used to build three different prototypes of thermoelectric generators. The characterization of the prototypes confirmed the theoretical postulations, a high thermoelectric power factor and a moderate heat conductivity is much more important than a high zT value, to harvest waste heat at high temperatures from infinite heat sources. The best generator provided an electrical power output and electrical power density of 22.7 mW and 113.5 mW$\cdot$cm^{-2}, respectively, when a hot-side temperature of 1073 K and a temperature difference of 251 K were applied. Even though a comparable low temperature difference was applied, the obtained power density is the highest reported from oxide-based generators.

Zusammenfassung

Stichwörter: Thermoelektrizität; Energie ernten; Leistungserzeugung; Oxide

Thermoelektrische Materialien können reversibel und ohne Verwendung beweglicher Teile durch Kopplung eines entropischen und eines elektrischen Flusses thermische Energie in elektrische Energie umwandeln. Diese Fähigkeit wird angesichts des wachsenden Energiebedarfs der Welt, einer geforderten Nachhaltigkeit und des Klimawandels immer wichtiger. Die Materialklasse der thermoelektrischen Oxide kann eine wichtige Rolle bei der Energiegewinnung aus Abwärme aus Industrieprozessen und Kraftwerken spielen. Oxide besitzen, verglichen mit anderen Materialklassen, vorteilhafte Eigenschaften im Hochtemperaturbereich und unter oxidierender Atmosphäre, wenn unendliche Wärmequellen vorliegen. Das Forschungsgebiet der Thermoelektrik ist stark interdisziplinär. Es besteht einerseits aus der Synthese neuer Materialien und Messung ihrer Eigenschaften, die der Festkörperchemie und Festkörperphysik zuzuordnen sind. Und andererseits besteht das Forschungsgebiet der Thermoelektrik auch aus Prozess-und Elektrotechnik, beispeilsweise dem Bau und der Vermessung von elektrischen Bauelementen.
Materialklassen wie Legierungen, Telluride, Halb-Heusler- oder Zintl-Phasen wie beispielsweise Bi_2Te_3, PbTe-PbS, $Yb_{14}MnSb_{11}$, SiGe, SnSe und FeNbSb, besitzen deutlich attraktivere thermoelektrische Eigenschaften, insbesondere im niedrigen bis mittleren Temperaturbereich, solange eine inerte oder reduzierende Atmosphäre vorliegt. Diese Materialklassen zeigen jedoch im Hochtemperaturbereich unter oxidierenden Bedingungen im Vergleich zu Oxiden eine schlechtere Stabilität, sind toxisch oder bestehen aus teuren und seltenen Elementen. Thermoelektrische Oxide können nicht mit den Werten des thermoelektrischen Gütefaktors zT von Materialklassen wie Halb-Heusler-Phasen oder Telluriden konkurrieren. Daher sollte sich die Forschung an Oxiden auf die Verbesserung des Leistungsfaktors im Hochtemperaturbereich unter Luft konzentrieren. Darüber hinaus sollte der Anwendungsbereich von Materialien und Bedingungen, unter denen diese angewendet werden, kritisch diskutiert werden. Für das Szenario der Anwendung einer begrenzten Wärmequelle und wenn eine maximierte Umwandlungseffizienz erhalten werden sollte, ist ein hoch-zT Material wünschenswert. Für den Fall einer unendlichen Wärmequelle und unter der Annahme einer Abwärmerückgewinnung bei hohen Temperaturen ist jedoch ein stabiles Material mit hohem Leistungsfaktor für die elektrische Leistungserzeugung erstrebenswert. Aus diesem Grund wurde zum einen, ein ungewöhnlicher Ansatz, in der Herstellung von porösen Keramiken durchgeführt, um die Wärmeleitfähigkeit zu verringern und somit den Wert von zT zu verbessern. Zum anderen wurde eine Co-Dotierung und kompositionell legierte Nanostrukturen ver-

wendet, um Hochleistungsmaterialien zu entwickeln. Die Anwendbarkeit von Materialien zur Leistungserzeugung kann anschaulich anhand eines sogenannten Ioffe-Diagramms eingeschätzt werden, welches den thermoelektrischen Leistungsfaktor in Abhängigkeit von der elektrischen Leitfähigkeit darstellt. Der Einfluss und die Möglichkeit, die elektrische Leistungserzeugung bei hohen Temperaturen aus unendlichen Wärmequellen zu maximieren, wurden kürzlich theoretisch beschrieben. Ein maximierter Leistungsfaktor und eine moderate Wärmeleitfähigkeit sind die wichtigsten Parameter zur Verbesserung der Leistungserzeugung unter diesen Bedingungen.

In der vorliegenden Arbeit wurden verschiedene Oxide synthetisiert und hinsichtlich ihrer thermoelektrischen Eigenschaften untersucht. Darüber hinaus wurden Synthese, Wachstumsmechanismus und Struktur mittels Röntgenbeugung (XRD), Rasterelektronenmikroskopie (REM) und Transmissionselektronenmikroskopie (TEM) untersucht. Der Einfluss verschiedener Verarbeitungstechniken auf Mikro-, Nanostruktur und thermoelektrische Eigenschaften wurde mittels SEM, TEM, EDXS (energiedispersive Röntgenspektroskopie) und thermoelektrischen Messungen untersucht. Die Stabilität verschiedener Materialien an Luft wurde mittels Thermogravimetrie, XRD und Zyklustests der thermoelektrischen Eigenschaften untersucht. Das Verhalten verschiedener Materialien hinsichtlich ihres thermischen Ausdehnungskoeffizienten wurde mittels Dilatometrie untersucht. Die primär untersuchten Phasen sind halbleitende Oxide wie p-leitendes $Ca_3Co_4O_9$ (CCO) und n-leitendes In_2O_3. Die Kristallstruktur und Phasenbildung von CCO ist sehr komplex und die anschliessende keramische Verarbeitung ist ebenfalls kompliziert. Hochporöse CCO-Keramiken besitzen jedoch deutlich reduzierte Wärmeleitfähigkeiten und eine verbesserte Gütezahl zT von 0,4, gemessen parallel zur Pressrichtung der Keramik. Dieser Wert stellt den höchsten Wert (parallel zur Pressrichtung) für eine reine CCO-Keramik dar. Ein neues, thermoelektrisches drei-phasiges $Ca_3Co_4O_9$-Na_xCoO_2-$Bi_2Ca_2Co_2O_9$ (CCO-NCO-BCCO) Nanokomposit mit verbesserten thermoelektrischen Eigenschaften wurde entwickelt und charakterisiert. Die anisotropen thermoelektrischen Eigenschaften wurden untersucht und zeigten den höchsten Leistungsfaktor von 6,5 μW $\cdot$ cm^{-1} $\cdot$ K^{-2}, elektrische Leitfähigkeit von 116 S$\cdot$cm^{-1} (Ioffe-Diagramm) und zT Wert von 0,35 für ein CCO-NCO-BCCO-Nanokomposit bei 1073 K in Luft, gemessen senkrecht zur Pressrichtung der Keramik. Dieser zT-Wert ist der höchste, der in einer Studie, welche die anisotropen Transporteigenschaften eines thermoelektrischen p-artigen Oxids senkrecht und parallel zur Pressrichtung der Keramik angibt, gemessen wurde. Die thermoelektrischen Eigenschaften konnten gleichzeitig mit Hilfe einer co-dotierten Nanokomposit-Bildung aus drei komplex geschichteten thermoelektrischen Oxiden verbessert werden. Das Komposit besteht aus Strukturen, die Ausdehnungen aller Grössenskalen (mikroskopische, nanoskopische, atomare Skala) aufweisen. Die drei komplex geschichteten thermoelektrischen Oxide wuchsen semi-kohärent aufeinander. Die thermisch weniger stabilen Phasen NCO und BCCO konnten durch Interdiffusion und Einbau in eine CCO-Matrix bei hohen Temperaturen stabilisiert und dadurch an Luft erstmals genutzt werden.

Die verschiedenen synthetisierten, untersuchten und entwickelten p- und n-leitenden

Materialien wurden für thermoelektrische Generatoren unterschiedlicher Bauweisen verwendet. Diese Generatoren wurden im Hinblick auf einen prinzipiellen Nachweis der Machbarkeit und Maximierung der elektrischen Leistung und Leistungsdichte charakterisiert. Der erste Generator wurde mit einem herkömmlichen Schachbrettmuster konstruiert und zeigte eine erhöhte elektrische Leistungsabgabe und Leistungsdichte bei hohen Temperaturen, wenn elektrisch hochleitende Indiumoxidphasen verwendet werden. Ein Finite-Elemente-Simulationstool wurde entwickelt, um die Leistungseigenschaften von thermoelektrischen Generatoren vorherzusagen und die unterschiedlichen Flüsse in den Bauteilen zu zeigen. Darüber hinaus wurde die Wichtigkeit der Minimierung von Übergangswiderständen zur Verbesserung der elektrischen Ausgangsleistung eines thermoelektrischen Generators herausgestellt.

Ein vollständig oxidischer thermoelektrischer Generator wurde entwickelt und charakterisiert, welcher mit Hilfe von Funkenplasmasintern von CCO- und $CaMnO_3$-Pulvern hergestellt wurde. Ein in-situ bei hohen Temperaturen gebildeter, komplexer p-p-n-Übergang verringert den Kontaktwiderstand und erhöht die elektrische Spannung durch Auftreten eines transversalen thermoelektrischen Effekts an den Grenzflächen des p-p-n-Übergangs. Dieser Effekt wiederum erhöht die elektrische Ausgangsleistung des Generators. Dieser vollständig oxidische, thermoelektrische Generator konnte zum ersten Mal gefertigt und ist hinsichtlich der elektrischen Ausgangsleistung und der elektrischen Leistungsdichte vermessen worden. Er ist mit den meisten herkömmlichen, oxid-basierten Generatoren vergleichbar. Der p-p-n-Übergang an der Grenzfläche zwischen p- und n-leitenden Materialien nutzt keine metallischen Leiter und ist daher im Vergleich zu konventionellen Generatoren auch bei noch höheren Temperaturen in Luft verwendbar.

Die Auswirkungen von Hochleistungsmaterialien und hoch-zT Materialien auf die elektrische Ausgangsleistung und Leistungsdichte von thermoelektrischen Generatoren wurden umfassend untersucht. Ein p-leitendes CCO-NCO-BCCO-Nanokomposit wurde unter Verwendung verschiedener Sintertechniken verarbeitet, wodurch der Leistungsfaktor und die elektrische Leitfähigkeit (Ioffe-Diagramm) verbessert wurden und $8{,}2~\mu W \cdot cm^{-1} \cdot K^{-2}$, beziehungsweise $143~S \cdot cm^{-1}$ bei 1073 K in Luft erreichten. Die entwickelten p- und n-leitenden Materialien wurden verwendet, um drei verschiedene Prototypen von thermoelektrischen Generatoren zu bauen. Die Charakterisierung der Prototypen bestätigte die theoretischen Überlegungen, ein hoher thermoelektrischer Leistungsfaktor und eine moderate Wärmeleitfähigkeit seien viel wichtiger als ein hoher Wert von zT, um Energie aus Abwärme bei hohen Temperaturen aus unendlichen Wärmequellen zu gewinnen. Der beste Generator lieferte eine elektrische Ausgangsleistung und eine Leistungsdichte von 22,7 mW bzw. 113,5 $mW \cdot cm^{-2}$, wenn eine Heissseitentemperatur von 1073 K und eine Temperaturdifferenz von 251 K vorliegt. Obwohl eine vergleichweise geringe Temperaturdifferenz verwendet wurde, ist die erhaltene Leistungsdichte die höchste, die für Oxid-basierte Generatoren berichtet wird.

Abbreviations

BCCO $Bi_2Ca_2Co_2O_9$

CCO $Ca_3Co_4O_9$

CCO-30-35-6 CCO-NCO-BCCO nanocomposite (derived from $Ca_{2.35-z}Na_{0.3}Bi_{0.35}Tb_zCo_4O_9$)

CCO-30-35-8 CCO-NCO-BCCO nanocomposite

CCO-30-35-10(-air) CCO-NCO-BCCO nanocomposite
air - pressureless sintered in air

CCO-30-35-10-HP hot-pressed CCO-30-35-10

CCO-30-35-10-SPS spark plasma sintered CCO-30-35-10

CCO-30-35-10-O$_2$ O_2-sintered CCO-30-35-10
O_2 - pressureless sintered in O_2

CMO $CaMnO_3$

DOS electronic Density of states

EDTA Ethylenediaminetetraacetic acid

EDXS Energy dispersive X-ray spectroscopy

EELS Electron energy-loss spectroscopy

E_F Fermi energy

FEM Finite-element simulation method

HRTEM High-resolution transmission electron microscopy

Ge,Mn,Zn:In$_2$O$_3$ Germanium, manganese, zink co-doped indium oxide

ITO Indium tin oxide, $In_{2-x}Sn_xO_3$

NCO Na_xCoO_2

n-type electron conducting semiconductor

PF Thermoelectric power factor

p-type hole conducting semiconductor

rFFT Reduced fast Fourier transformation

SAED Selected area electron diffraction

Sn,Al:In$_2$O$_3$ Tin, aluminum co-doped indium oxide

SEM Scanning electron microscopy

TE Thermoelectric

TEG Thermoelectric generator

TEM Transmission electron microscopy

XRD X-ray diffraction

zT Thermoelectric figure-of-merit of a material

$Z\overline{T}$ Thermoelectric figure-of-merit of a generator

Contents

1 Introduction

1.1 Thermoelectricity

The phenomenon of thermoelectricity can be described by the reversible coupling of entropic I_S and electrical I_q currents in a way that heat is transferred to electrical energy and vice versa. When a thermoelectric solid state material is exposed to a temperature gradient, an electrical potential gradient is coupled and generated due to the thermal diffusion of charge carriers. The phenomenon of coupling entropy I_S and electrical I_q currents (fluxes) with each other (Figure 1) can be well described with a material-specific tensor, shown in Equation 1. This tensor consists of material-specific parameters like the isothermal electrical conductivity σ, the Seebeck coefficient α, the electric open-circuited entropy conductivity Λ and geometrical parameters like area A and length L, which are linked by differences of temperature and electrical potential to the generated entropy and electrical currents [1–3].

$$\begin{pmatrix} I_S \\ I_q \end{pmatrix} = \frac{A_{leg}}{L_{leg}} \cdot \begin{pmatrix} \sigma \cdot \alpha^2 + \Lambda & \sigma \cdot \alpha \\ \sigma \cdot \alpha & \sigma \end{pmatrix} \cdot \begin{pmatrix} \Delta T \\ \Delta \varphi \end{pmatrix} \tag{1}$$

The first entry of the material tensor is the so called thermoelectric power factor $\sigma \cdot \alpha^2$, which describes the charge carrier related entropy conductivity. The electric open-circuited entropy conductivity Λ is added to the thermoelectric power factor. The entry $\sigma \cdot \alpha$ is the coupling parameter. The last entry is the isothermal specific electrical conductivity σ, which results directly from Equation 1 for a disappearing temperature difference in the isothermal description of Ohm's law, as described in section 1.1.2. The entropy conductivity consists of an electronic part and a lattice part. The electronic part is ruled by the thermoelectric power factor $\sigma \cdot \alpha^2$, since charge carrier also carry entropy, as described in section 1.1.3. The lattice part is determined by lattice vibrations and is described by the electric open-circuited entropy conductivity Λ. The material-specific parameters like the Seebeck coefficient α and the isothermal electrical conductivity σ are measured under vanishing electrical ($\Delta \varphi =0$) or thermal differences ($\Delta T =0$), respectively. The entropy conductivity Λ is measured under vanishing electrical ($\Delta \varphi =0$) and thermal differences ($\Delta T =0$). The dependance of the entropy conductivity Λ and heat conductivity λ is shown in Equation 2 and is related by the absolute temperature T [1–3].

$$\lambda = T \cdot \Lambda \tag{2}$$
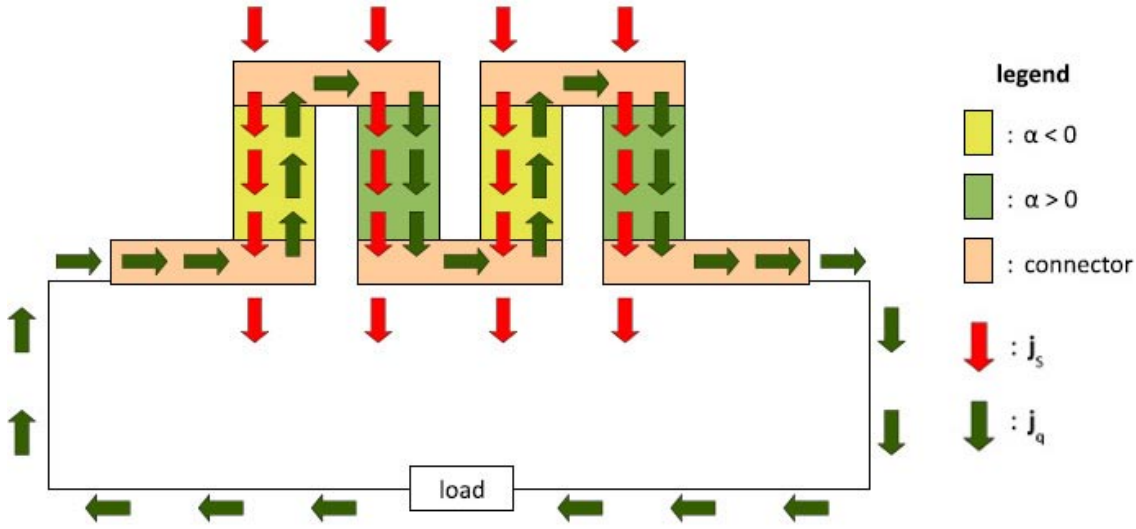
Figure 1: Principle of a thermoelectric generator: Coupling an entropy (j_S) and an electric (j_q) flux with each other, in same direction for a p-type ($\alpha > 0$) and in opposite direction for a n-type ($\alpha < 0$) material. Copyright De Gruyter [3].

The thermoelectric phenomenon of coupling entropy and electrical currents with each other in a thermoelectric generator to convert thermal energy into electrical energy is schematically illustrated in Figure 1. The entropy and electrical currents (fluxes) are coupled with each other in the same and opposite direction for p- and n-type materials.

The thermoelectric effect was first observed by Thomas Johann Seebeck in the 19th century as he noticed the deflection of a compass needle, when he exposed two different metals to a temperature difference [4]. A thermal induction of an electrical current led to a magnetic field, which deflected the needle. But Seebeck came to a false interpretation. In his opinion, thermomagnetism was the reason for his observations. Hans Christian Ørsted was inspired by Seebeck's findings and carried out his own experiments and observed deflections of compass needles in current-carrying electric circuits. He made the correct conclusions of induced electrical currents and reported his results in 1820 in a publication about thermoelectricity [5]. The underlying material-specific quantity has been called later the Seebeck coefficient α or thermopower, shown in Equation 3 and is determined by the entropy S^* per unit transported charge q [1].

$$\alpha = \frac{S^*}{q} \tag{3}$$

In the field of thermoelectric research, the ability of a material to convert heat into electrical energy can be evaluated by the so called figure-of-merit zT, shown in Equation 4, which was first derived by Ioffe [6].

$$zT := \frac{\sigma \cdot \alpha^2}{\Lambda} = \frac{\sigma \cdot \alpha^2}{\lambda} \cdot T \tag{4}$$

In this way a figure-of-merit zT, which solely depends on material-specific parameters can be obtained, which is given in Equation 4. The involved material-specific parameters are the Seebeck coefficient α, the isothermal electrical conductivity σ and the entropy conductivity Λ. Only when the entropy conductivity Λ is not accepted as basic material parameter, the heat conductivity λ and the absolute temperature T according to Equation 2 are used, as shown in Equation 4. The figure-of-merit zT composed of the heat conductivity λ and the absolute temperature is generally more often used in the thermoelectric society. The isothermal electrical conductivity σ and the electric open-circuited heat conductivity λ were explored by Georg Simon Ohm [7] and Jean Baptiste Joseph Fourier, respectively [8]. The ability to convert energy can be improved by an enhancement of σ and α or reduction of Λ.

1.1.1 Seebeck coefficient α

The principle of a Seebeck coefficient α measurement is shown in Figure 2. A thermoelectric material between two contacts will show an electrical voltage U (potential difference $\Delta\varphi$), which is equal to the temperature difference ΔT multiplied with the Seebeck coefficient α, as shown in Equation 5.

$$U = \Delta\varphi_{th} = -\alpha \cdot \Delta T \tag{5}$$

This equation can be easily derived from Equation 1 under the assumption of electrical open-circuited conditions ($I_q = 0$). In this way, the Seebeck coefficient α can be calculated from the measured temperature difference ΔT and the electrical voltage U.
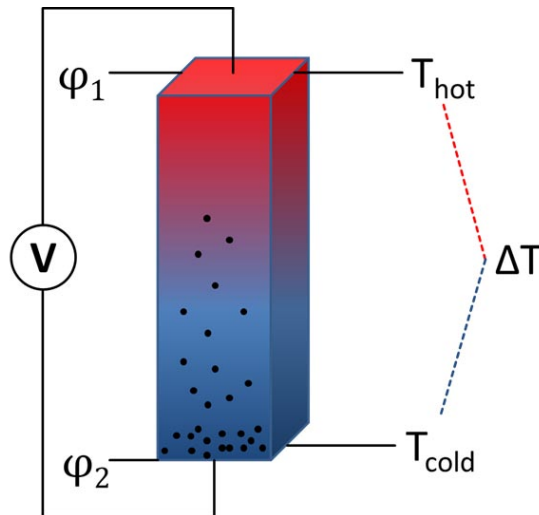
Figure 2: Schematic representation of the appearance of a electrical voltage (potential gradient) when a temperature difference ΔT is applied to p- or n-type conductor. Measurement assume a vanishing Thomson coefficient ($\tau \approx 0$). Black spheres represent major charge carrier, which migrate through the material from hot to cold-side.

If one side of the material is heated, charge carrier will be activated and migrate

from hot to cold-side since hot charge carriers have a higher velocity. As a result, the quantity of charge carriers will be higher at the cold-side of the material than at the hot-side, leading to different electrical potentials at these two sides and finally in a potential gradient across the material, see Figure 2. The Seebeck coefficient α is mostly given in $\mu V/K$ (equal to $\frac{J}{s \cdot C} = \frac{V \cdot A \cdot s}{K \cdot A \cdot s}$, entropy S^* per transported charge carrier q, see section 1.1) and can be positive or negative, depending on the major charge carriers in the material, since generated potential gradients have reverse signs. The Seebeck coefficient is a material-specific value and is defined by the entropy S^* per transported charge carrier q according to Equation 3 in section 1.1. The Seebeck coefficient α is thereby depending on the electronic band structure and electronic density of states (DOS), as shown in Figure 3, of the material. For degenerated ($k_B T \ll E_F$) semiconductors, this correlation can be described by Equation 6 [9, 10].
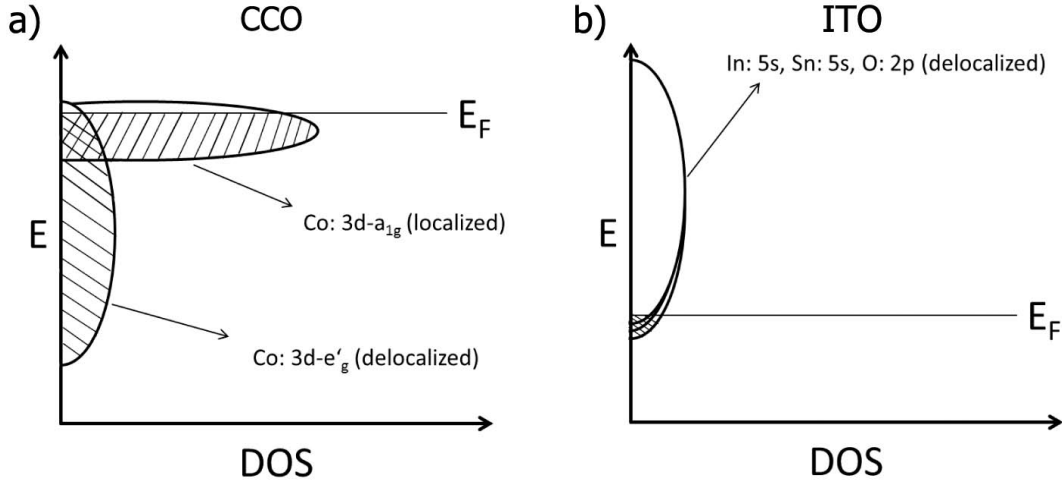
Figure 3: Electronic density of states near the Fermi level E_F of a) $Ca_3Co_4O_9$ (CCO) and b) $In_{1.95}Sn_{0.05}O_3$ (ITO). Areas of occupied states are hatched. Copyright De Gruyter [11].

$$\alpha \sim -(\delta ln A(E)/\delta E)_{E=E_F} \tag{6}$$

$A(E)$ is proportional to the area of the electronic density of states at the Fermi level E_F. The Seebeck coefficient α is also described by Equation 7.

$$\alpha = \frac{2}{3} \left(\frac{\pi}{3}\right)^{\frac{2}{3}} \left(\gamma + \frac{2}{3}\right) \frac{k_B^2 m^*}{e\hbar^2 n^{\frac{2}{3}}} \tag{7}$$

An enhancement of the effective mass m^* or a decrease in the carrier concentration n would have immediate impact on the Seebeck coefficient α. The other parameters are the Boltzmann constant k_B, Planck's quantum $\hbar$, the elementary charge e and a scattering factor γ, which depend on the scattering mechanism (-0.5 for acoustic phonons, 0 for neutral impurities and 1.5 for ionized impurities). These two equations show the possibilities to enhance the Seebeck coefficient α, both correlate to the electronic band structure of the material. A general challenge in thermoelec-

tricity is the interrelation of the effective mass m^* and the carrier concentration n, since changes in one of them also affects the other. For this reason, new approaches to improve the Seebeck coefficient α have been conducted, which are discussed in sections 1.2.2 and 1.2.3.

1.1.2 Isothermal electrical conductivity σ

The electronic band structure of the material, determines not only the Seebeck coefficient α but also the electrical conductivity σ. The most frequently used models to explain the electronic band structure are the tight-binding model and the Bloch theorem (plane wave expansion model) [12, 13]. The first model is assuming a superposition of atomic orbitals of a periodic solid-state matter, which form, by interaction of discrete atomic energy levels, energy bands. The second model treats an electron as a wave which is propagating and interacting with a periodic potential. The interaction of the electron waves with the crystal potential leads to an altered electronic dispersion and the formation of energy bands and band gaps. Both models provide the conception of energy bands, namely conduction and valence bands, in dependence of the electronic wave vectors. For metals, the conduction and valence bands are overlapping and the Fermi energy E_F is located within the conduction band. For intrinsic semiconductors, the conduction and valence bands are separated by a band gap and the Fermi energy E_F is located in the middle of the gap [14]. The band structure of semiconductors can be modified by doping and other approaches, which are discussed in sections 1.2.1, 1.2.2 and 1.2.3. The introduction of lower valent dopants into the semiconductor will introduce holes and shifts the Fermi energy E_F towards the valence band. Higher valent dopants introduce electrons and shift the Fermi energy E_F towards the conduction band. The semiconductor is called p- and n-type, respectively, according to the major charge carrier. The specific isothermal electrical conductivity σ in solid-state matter can thereby be described as the product of carrier concentration n, charge carrier mobility μ and elemental charge e, as shown in Equation 8 [15].

$$\sigma = n \cdot \mu \cdot z \cdot e \tag{8}$$

The charge carrier concentration n is directly connected to the electronic band structure of the material. It is defined by the electronic DOS in the conduction band N_C and in the valence band N_V, the energies of the conduction band edge E_C, valence band edge E_V, the Fermi energy E_F and temperature T, shown in Equations 9 and 10 for p (n_p) and n-type (n_n) semiconductors.

$$n_p = N_V \cdot exp\left(-\frac{E_F - E_V}{k_B \cdot T}\right) \tag{9}$$

$$n_n = N_C \cdot exp\left(-\frac{E_C - E_F}{k_B \cdot T}\right) \tag{10}$$

If the semiconductor is p- or n-type doped, the charge carrier concentration for a

non-degenerated semiconductor can be described by Equations 11 and 12.

$$n_p = 2N_A \cdot exp \left(1 + \sqrt{1 + 4 \cdot \frac{N_A}{N_V} \cdot exp\frac{E_A - E_V}{k_B \cdot T}} \right)^{-1} \tag{11}$$

$$n_n = 2N_C \cdot exp \left(1 + \sqrt{1 + 4 \cdot \frac{N_D}{N_C} \cdot exp\frac{E_C - E_D}{k_B \cdot T}} \right)^{-1} \tag{12}$$

Both Equations (11, 12) describe the charge carrier concentration of a non-degenerated semiconductor at different temperatures T, thereby N_A and N_D are the electronic densities of states (DOS) of the acceptor and donator, respectively, and E_A and E_D are the corresponding energies.

The charge carrier mobility is determined by the curvature of the conduction band, valence band for electrons and holes, respectively, and can be also described, as shown in Equation 13, as a function of the median flight time τ between collisions, the elementary charge e and the effective mass m^* [12, 13].

$$\mu = \frac{e \cdot \tau}{m^*} \tag{13}$$

According to Equation 13, the isothermal electrical conductivity σ can be enhanced by a reduced effective mass m^*, but at the same time, the Seebeck coefficient α will be decreased, as shown by Equation 7. The isothermal electrical conductivity σ, shown in Equation 14, can be easily derived from Equation 1 under vanishing temperature difference ($\Delta T = 0$).

$$\sigma = \frac{-I_q \cdot L}{U \cdot A} \tag{14}$$

The electrical current I_q is linked by the electrical current density J_q and the cross-sectional area A by Equation 15 and follows, under isothermal conditions ($\Delta T = 0$), Ohm's law [7] (derived from Equation 1) according to Equations 14.

$$I_q = \int_0^A J_q \cdot dA \tag{15}$$

1.1.3 Heat conductivity λ

The thermal conductivity of solid-state matter can be described by Fourier's law at electric open-circuit conditions, and evanescent electric current (derived from Equation 1) [8]. The heat conductivity consists of three parameters, the heat capacity C_P the density ρ and the thermal diffusivity D_{th}, and can be calculated according to Equation 16.

$$\lambda = C_P \cdot \rho \cdot D_{th} \tag{16}$$

Besides, the heat conductivity is composed of two terms, as shown in Equation 17. The first term describes the heat conductivity, which is associated to lattice

vibrations λ_{ph} (phonons) and the second correlates to the heat transport by charge carriers λ_{el}, since electrons or holes carry both, charge and entropy, according to Equation 3 [16, 17].

$$\lambda = \lambda_{ph} + \lambda_{el} \tag{17}$$

The density ρ can be obtained by the Archimedes method, measured from dry mass, mass in solvent (buoyancy), mass with incorporated solvent, density of the solvent and temperature after ISO 5018:1983 (the International Organization for Standardization). The heat capacity C_{P} is either measured by the sapphire method [18] or estimated by Dulong-Petit, assuming the molar heat capacity C_{m} is three times the gas constant R. The heat conductivity λ can be influenced by several approaches, which are described in section 1.2.3.

1.2 Energy conversion efficiency

According to Ioffe [6], the energy conversion efficiency η of a thermoelectric generator (TEG) can be calculated by Equation 18 and depends on the Carnot efficiency ($\Delta T / T_{\mathrm{H}}$), that is reduced by a factor, which consists of the figure-of-merit $Z\overline{T}$, the hot T_{H}, cold-side T_{C} and the mean temperature $\overline{T}$.

$$\eta(\%) = 100 \cdot \left(\frac{T_H - T_C}{T_H} \right) \cdot \frac{\sqrt{1 + Z\overline{T}} - 1}{\sqrt{1 + Z\overline{T}} + (T_H/T_C)} \tag{18}$$

Note, for this figure-of-merit $Z\overline{T}$, the mean temperature $\overline{T}$ across the TEG is used, and is calculated according to Equation 4. The enumerator in Equation 4 is called the thermoelectric power factor ($\sigma \cdot \alpha^2$), which defines the amount of electrical power which is converted from heat. Equation 18 is based on the assumption, heat would flow back in direction of the hot-side [6]. However, a heat flow against its own driving force, the thermal gradient ∇T, seems unlikely. Furthermore, Equation 18 is based on the assumption that Z is temperature independent. Most thermoelectric materials have highly temperature dependent properties (σ, α and Λ) and the zT value is thereby, not constant or of linear trend. As a consequence, the efficiency after Equation 4 seems inadequate and is not reliable, when Z is temperature dependent [19]. Altenkirch also discussed the efficiency and figure-of-merit of a thermoelectric material in 1909 [20]. However, he neglected the heat (entropy) conductivity in his calculations. Fuchs [1] postulated another Equation to estimate the second law efficiency of thermoelectric generators, which abstain from temperatures. This Equation is only determined by a single external parameter, the external resistance, and by the parameters of the generator [1]. As a result, this Equation is more suitable to calculate the efficiency of a thermoelectric generator compared to the Equation, which is derived according to Ioffe [6].

A thermoelectric generator, as shown in Figure 1, should consist of materials, which are optimized for the area of application of the TEG. Two scenarios of application

are possible: Energy harvesting from infinite or limited heat sources. For the case of infinite heat sources, thermoelectric materials with maximized power factors should be used in order to enhance the electrical power output of the generator, see Figure 9. When a limited heat source is present, for example in space employments, materials with maximized zT value are beneficial to decrease the heat loss and subsequently enhance the efficiency, see Figure 9. In order to enhance the power conversion efficiency of a thermoelectric material and generator, the figure-of-merit zT must be improved.

Ideally, the thermoelectric power factor is enhanced and at the same time, the heat conductivity λ is reduced. With respect to zT values, thermoelectric oxides can not compete with other materials like alloys [21–23], tellurides [24] or half-Heusler [25], Zintl phases [26]. A generator made of oxides should therefore be used at high temperatures under oxidizing conditions and maximized power factor. Narducci [27] showed that a high zT value is not necessary for a high electrical power generation, if an infinite heat source is present. A moderate heat conductivity λ is necessary for both, introducing enough heat into the system to sustain a temperature difference ΔT, and enough heat to be converted into electrical energy, as shown in Figure 4 [27].
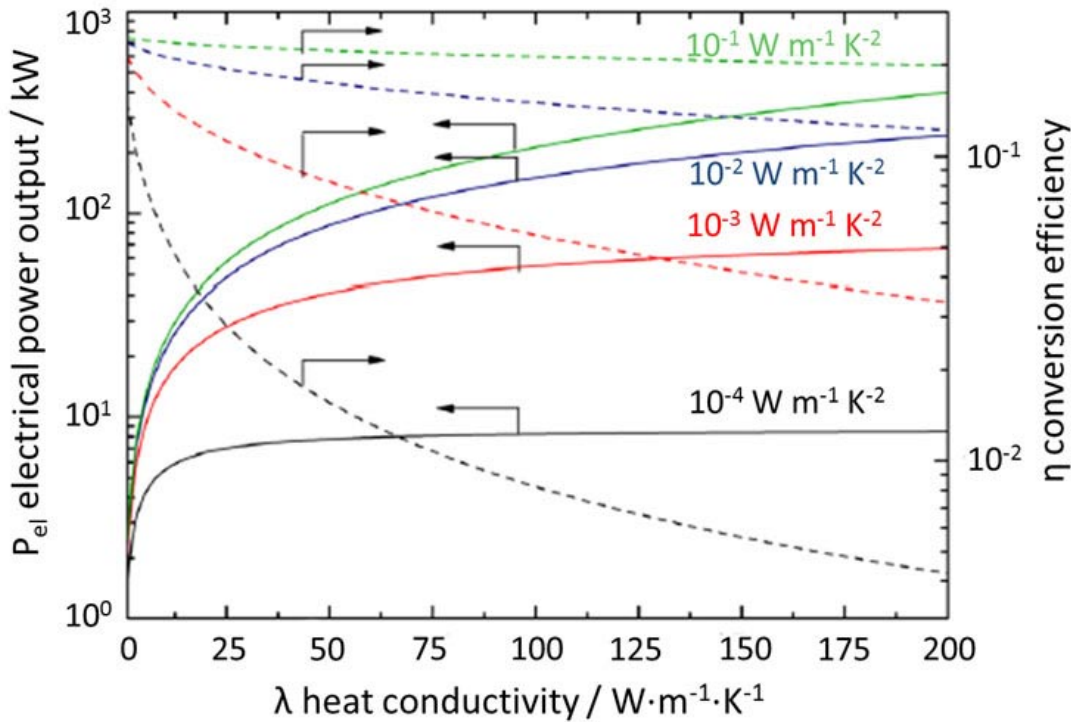
Figure 4: Narducci plot showing the increase of the electric power output P_{el} for different power factors (solid lines) and the conversion efficiency η (dashed lines) as a function of the heat conductivity λ. Copyright American Institute of Physics [27].

When an infinite heat source is assumed, the conversion efficiency η in Equation 18 can be modified to Equation 19. Remember, the Equation 18 according to Ioffe [6]

seems inadequate to calculate the efficiency, when Z is temperature dependent. However, the conclusion of maximized electrical power outputs by maximizing the power factor of applied materials remains.

$$\eta = \frac{1}{2} \cdot \frac{T_H - T_C}{T_H} \cdot \left(1 + \frac{2}{Z \cdot T_H} - \frac{\Delta T}{4 \cdot T_H}\right)^{-1} \tag{19}$$

The maximum electrical power outputs of a thermoelectric material $P_{el,max,mat}$ and generator $P_{el,max,TEG}$ can be calculated according to Equations 20 and 21, respectively [28–30].

$$P_{el,max,mat} = \frac{1}{4} \cdot \frac{A}{L} \cdot \sigma \alpha^2 \cdot (\Delta T)^2 \tag{20}$$

$$P_{el,max,TEG} = \frac{U_{OC}^2}{4 \cdot R_{TEG}} \tag{21}$$

The involved parameters are the open-circuited voltage U_{OC} and the resistance R_{TEG} of the generator. These values only depend on electrical properties like α for generated electrical voltage U ($U = \Delta\varphi_{th} = -\alpha \cdot \Delta T$) and σ ($\sigma = \frac{-I_q \cdot L}{U \cdot A}$) for resistance R_{TEG}. According to Figure 4, the heat conductivity is indirectly connected with the electrical power output. Figure 4 illustrates the correlation between the electrical power output $P_{el,max,TEG}$, energy conversion efficiency η as a function of the heat conductivity λ for different power factors [27]. With increasing the power factor of applied materials, the electrical power output and energy conversion efficiency are subsequently improved. The importance to increase the power factor of p- and n-type materials is also illustrated in Equations 20 and 21. In consequence of a maximized power factor, the electrical power output and electrical power density of a generator are simultaneously increased.

1.2.1 Carrier concentration engineering and synergistic alloying

One approach to improve thermoelectric materials is carrier concentration engineering, shown in Figure 5, which is used to maximize the thermoelectric power factor by balancing σ and α, according to Equations 7 and 8 [24]. Figure 5a shows, introduced dopants can be used in synergistic alloying (co-doping) to decrease the heat conductivity λ. The impact of dopants on the heat conductivity λ can be estimated by the scattering factor Γ, represented in Equation 22. The scattering factor Γ consist of, the doping fraction x, mass difference $\Delta M/M$ and lattice mismatch $a_{disorder}/a_{pure}$ and the adjusting parameter ϵ. The adjusting parameter ϵ is related to the elastic properties.
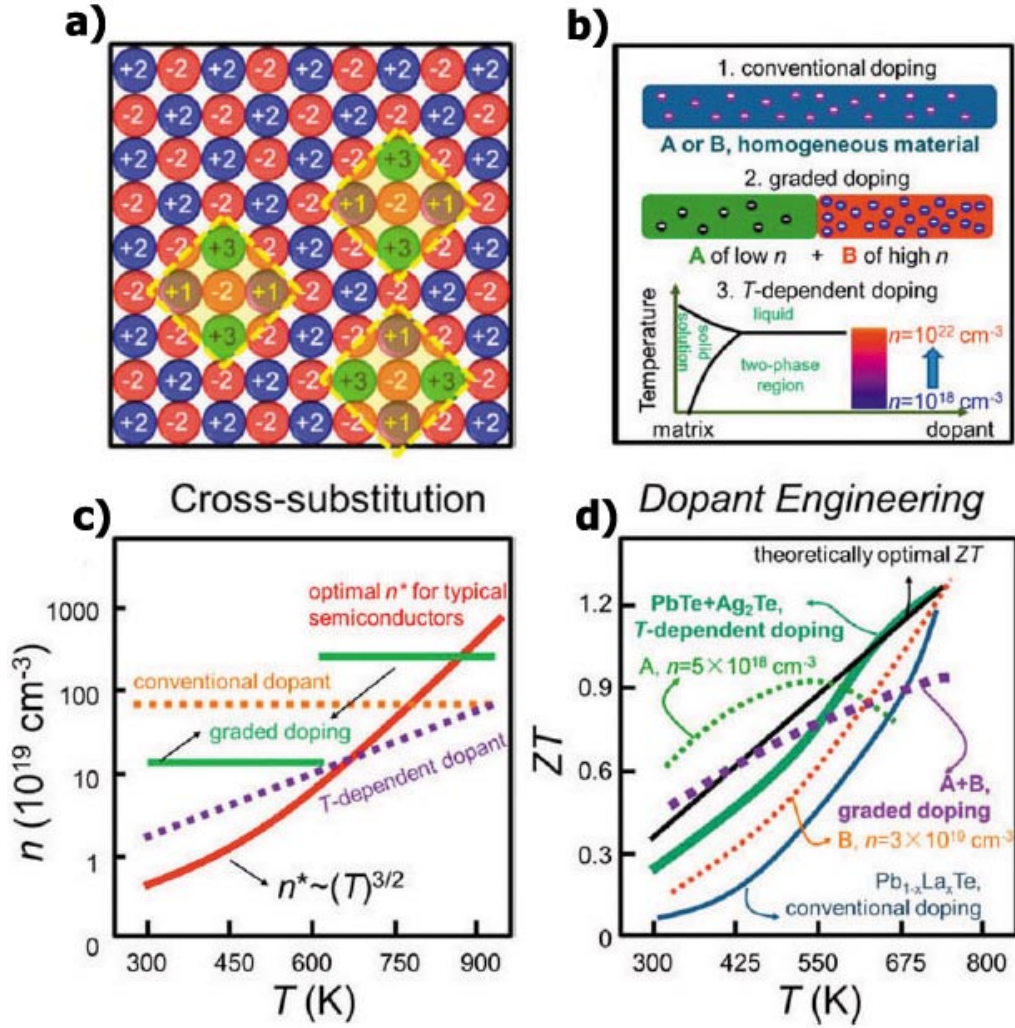
Figure 5: a) Co-doping (cross-substitution) with different valent elements. b) Schematic representation of different doping techniques. c) carrier concentration n as a function of temperature and different doping techniques to tune it. d) Figure of merit zT as a function of temperature and impact of doping techniques. Copyright American Chemical Society [31].

$$\Gamma = x(1-x)\left[\left(\frac{\Delta M}{M}\right)^2 + \epsilon\left(\frac{a_{\text{disorder}} - a_{\text{pure}}}{a_{\text{pure}}}\right)^2\right]\tag{22}$$

Figure 5b shows different doping techniques, which were developed over the years. Depending on desired properties, the material is homogeneously doped or graded doped, when different charge carrier concentrations are favored, for example to decrease contact resistances. The temperature-dependent doping can be used to ensure a constant charge charier concentration across a certain temperature range [32, 33]. Since the carrier concentration in most semiconducting materials increases with temperature in the order of $T^{3/2}$, as illustrated in Figure 5c, the aforementioned temperature-dependent doping is of interest [34]. In the case of an increasing

charge carrier concentration, the Seebeck coefficient α can be decreased and the heat conductivity λ increased, according to Equations 7 and 17. For this reason, carrier concentration engineering showed beneficial effects on various materials [21, 35], verifying its impact on enhancing the thermoelectric properties [31, 36, 37]. As a result of these doping techniques, a decreased heat conductivity λ leads to enhanced values of the figure-of-merit zT, as shown in Figure 5d [38].

1.2.2 Electronic band-structure engineering and resonant impurities

Another important and most promising approach to enhance the thermoelectric power factor in an almost temperature-independent manner is band-structure engineering [39, 40]. The objective of this effort is to distort and increase the electronic DOS in the vicinity of the Fermi level as much as possible, to increase σ and α simultaneously. The introduction of a second electronic band as shown in Figure 6a, is achieved by doping the material. Resonant level or states, as indicated in Figure 6b,e also increase the density of states and introduce additional available energy levels in the conduction or valence band. As a result, these approaches improve the Seebeck coefficient α [39, 40]. The success of electronic band-structure engineering was verified by rare-earth doping, due to the hybridization (Figure 6c) of electronic bands with sp character [41–44] and the introduction of resonant impurities (Figure 6e) [39, 41]. The dilute Kondo approach, shown in Figure 6d, is attributed to a change of the electron spin state when scattering on magnetic impurities and therefore, increasing the electronic DOS. Also compositionally-alloyed nanostructures can increase σ and α at the same time [31, 45].

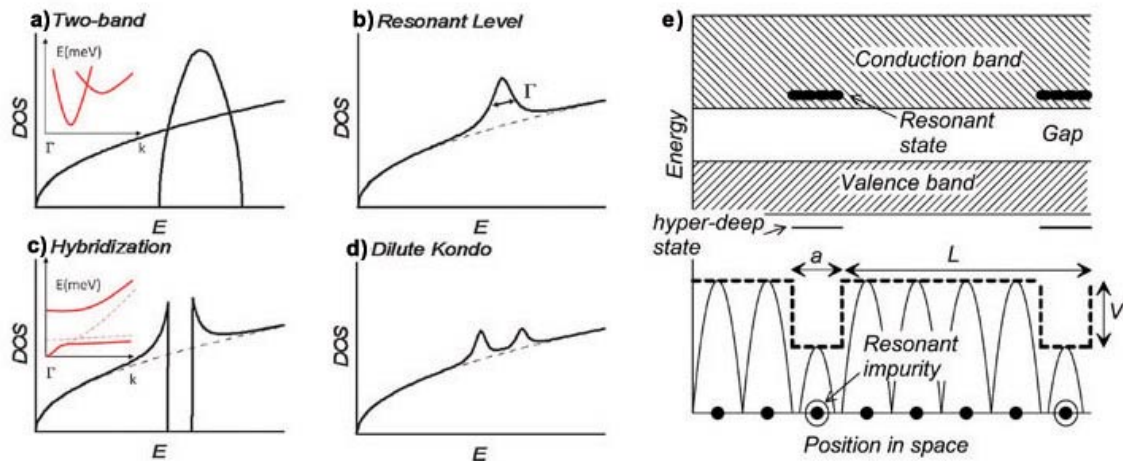**Figure 6:** a-d) Band structure engineering to distort the electronic density of states (DOS) in order to enhance the Seebeck coefficient α. e) Introduction of resonant impurities creating additional available energy levels in the conduction or valence band. Dilute Kondo is attributed to a change of the electron spin state when scattering on magnetic impurities. Copyright Royal Society of Chemistry [41].

1.2.3 Compositionally-alloyed nano-structures and multiscale structuring

A reduction of the heat conductivity λ can be achieved by tuning the micro-, nano- and atomic structure to scatter phonons on all length scales [46, 47]. This approach of an all-scale hierarchical architecture, which is shown in Figure 7a-e, introduces structures in the mesoscale, nanoscale and atomic scale into the material [31, 48]. Hicks and Dresselhaus forecasted nanostructures such as 2-dimensional (2D) quantum wells and 1D quantum wires to be suitable to tune the electronic DOS in the vicinity of the Fermi level [49]. A combination of both techniques, an all-scale hierarchical architecture of compositionally alloyed structures, which possess energy matched electronic bands, could scatter solely phonons on all length scales, and at the same time electronic properties could be improved [31, 50].
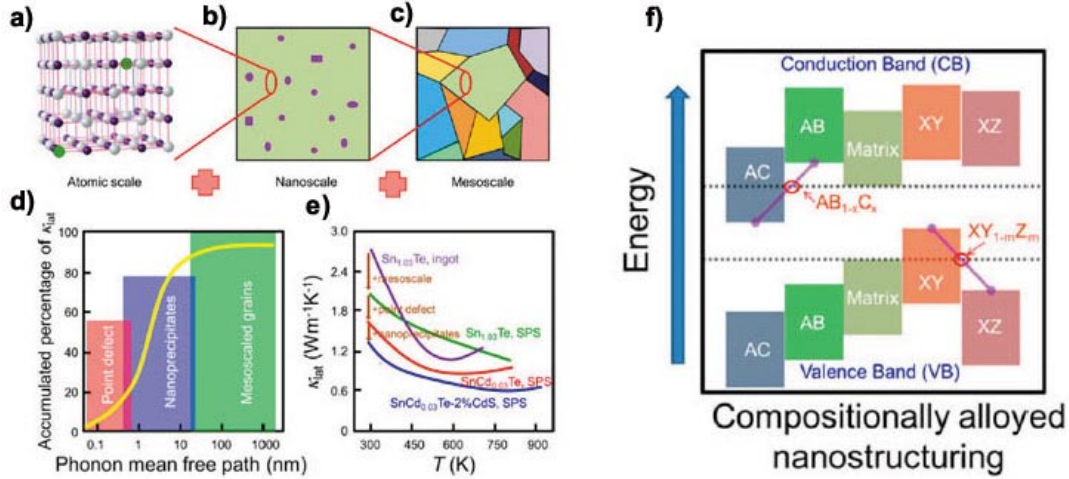
Figure 7: Influence of an all-scale hierarchical architecture via microstructuring (mesoscale), nanostructuring (nanoscale) and introduction of point defects (atomic scale) on the heat conductivity λ. a) Atomic scale, b) nanoscale, c) mesoscale, d) percentage of reduction to λ from different structures and e) reduction of λ in dependence of temperature and structures. f) Alignment of electronic bands by compositionally-alloyed nanostructuring. Copyright American Chemical Society [31].

Introducing porosity into the material represents another appraoch to decrease the heat conductivity. A change of the the degree of porosity leads to increased or decreased thermal contact resistances [51], as given in Equation 23 [52].

$$\lambda = \frac{1 - P}{1 + nP^2} \cdot \lambda_0 \tag{23}$$

Thereby λ is the calculated heat conductivity, in dependency of the porosity, λ_0 is the reference value of a dense ceramic, P is the volume fraction of the pores (or porosity) and n is a constant between 1 and 14. Since the electronic part λ_{el} (Equation 17) also contributes to the total heat conductivity λ, the challenge in thermoelectricity, regarding the interdependency of the three parameters σ, α and

λ, which is illustrated in Figure 9, may become clearer. An increased density may enhance σ but also λ, due to reduced electrical and thermal intergrain contact resistance. Doping could improve either α or σ but at the same time reducing the other and vice versa (sections 1.1 and 1.1.2) [6, 53].

1.3 Thermoelectric materials

1.3.1 Overview of state of the art materials

Several classes of materials like tellurides [24, 54], alloys [21–23, 55], skutterudites [56], Zintl-phases [26], Half-Heusler phases [25] and oxides [30, 57–60] are known and were investigated in the field of thermoelectricity over the years.
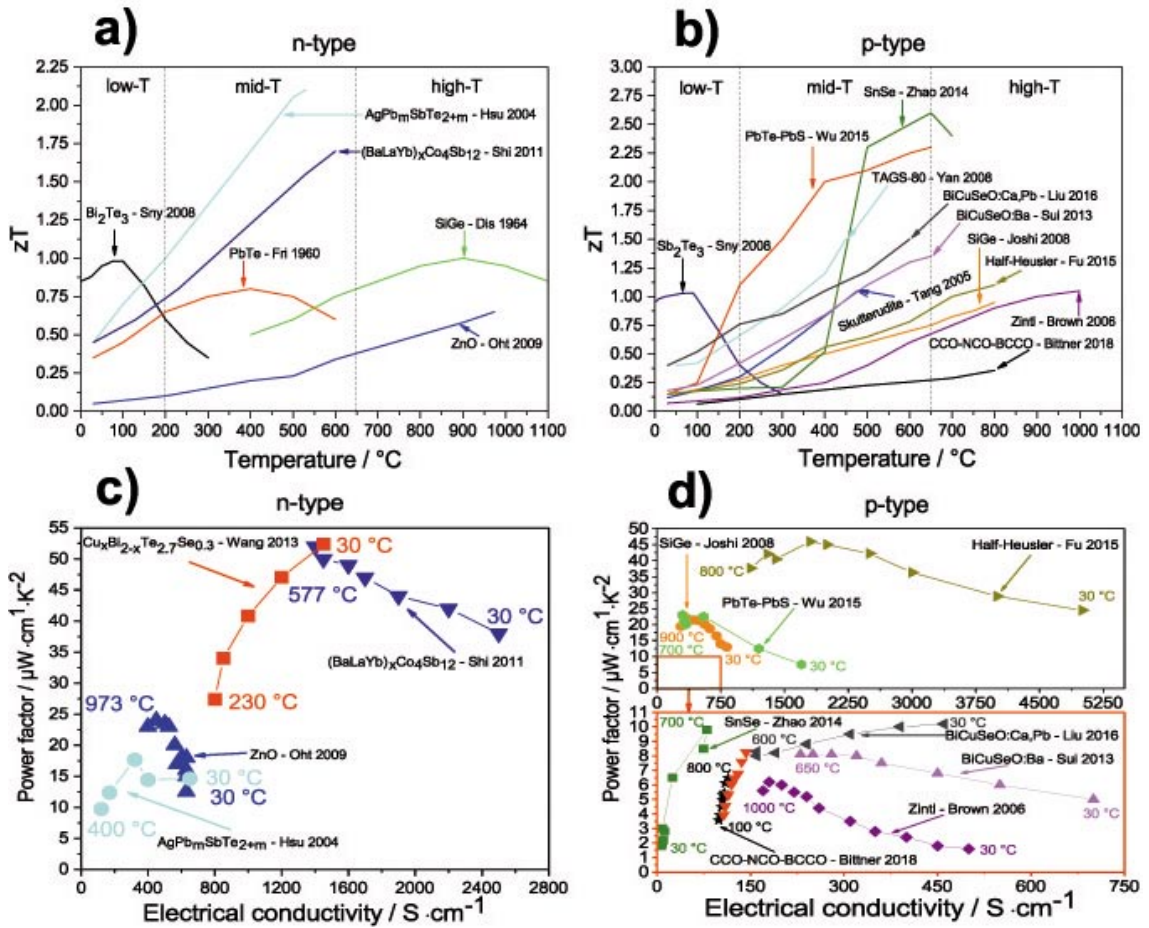
Figure 8: Thermoelectric properties of different n- and p-type material classes like tellurides [24, 54], alloys [21–23, 55], skutterudites [56], Zintl-phases [26], Half-Heusler phases [25] and oxides [30, 57–60]: a,b) figure-of-merit zT as a function of temperature. c,d) Ioffe plots: power factor $\sigma\alpha^2$ as a function of the electrical conductivity σ. Start and endpoints of temperature ranges are indicated.

These materials can be used in different temperature regimes, tellurides like Bi_2Te_3

for example show limited thermal stability. Alloys, Zintl- and Half-Heusler-phases show enhanced thermal stability, but suffer from chemical stability under oxidizing conditions. Oxides possess a good thermal and chemical stability at high temperatures in air and have, therefore, benefits under these conditions, compared to the other material classes. However, compared to the other materials, oxides show poor thermoelectric properties like figure-of-merit zT or power factor. In general a thermoelectric material is evaluated by its figure-of-merit zT, shown in Figure 8a,b for different n- and p-type materials. However, as discussed in section 1.2, the zT value on its own is insufficient to evaluate a thermoelectric material, that is designed to maximize the electrical power output of a thermoelectric generator from infinite heat sources [27]. A so-called Ioffe plot [6, 61] is much more suitable to evaluate the material in terms of maximizing the electrical power output of a generator. Examples are shown in Figure 8c,d, for different n- and p-type materials.

1.3.2 Developed oxide materials

Thermoelectric materials have to be evaluated, as discussed in section 1.2, in consideration of their area of application. Furthermore, the materials should be specifically designed, as shown in Figure 9, for their area of application by reasons of high power factor or zT values.
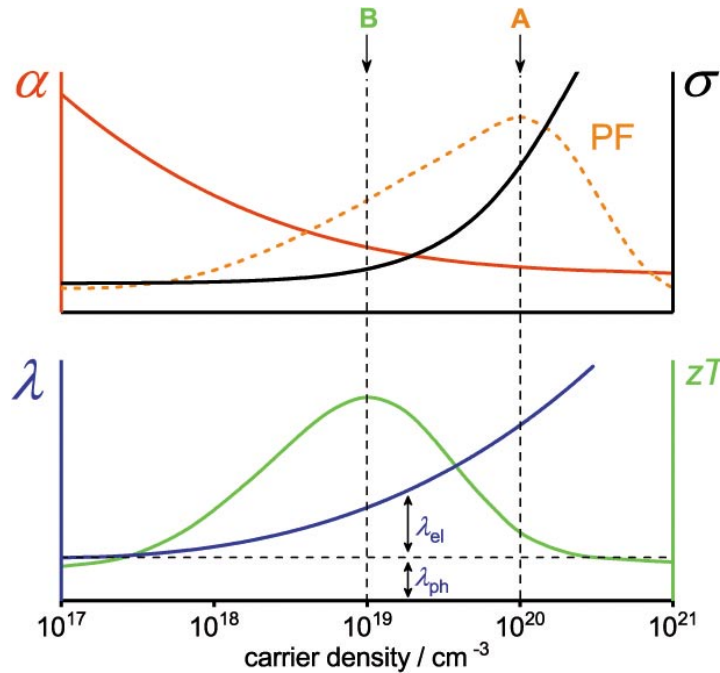
Figure 9: Thermoelectric parameters: Seebeck coefficient α, electrical conductivity σ, phononic and electrical part of the heat conductivity λ_{ph}, λ_{el}, calculated power factor $\sigma \cdot \alpha^2$ (PF) and figure-of-merit zT (according to Equation 4) as a function of charge carrier concentration n. **A** and **B** indicate charge carrier concentrations n of materials, which should be used for high power generation (infinite heat sources), or high energy conversion efficiency (limited heat sources), respectively. Modified from Ioffe [6].

If a limited heat source is present, materials with a high figure-of-merit zT (B in Figure 9) are needed. On the other hand, if an infinite heat source is present, a high electrical conductivity and thermoelectric power factor (A in Figure 9) are needed. The case of SnSe with its record figure-of-merit zT (Figure 8b) and its quite low thermoelectric power factor of SnSe (Figure 8d), confirms this argument. Even though SnSe has a very high zT value, it is a bad material for energy harvesting and power generation, since it shows a limited temperature range and electrical conductivity σ. For this reason, the p-type CCO and n-type In_2O_3 materials have been improved, as shown in Figure 10, by different approaches, as discussed in sections 1.2.1, 1.2.2 and 1.2.3.

Figure 10: Thermoelectric properties of synthesized and characterized p- and n-type oxides of $Ca_3Co_4O_9$ (**CCO**) (rectangle, green), $Ca_{2.25}Na_{0.3}Bi_{0.35}Tb_{0.1}Co_4O_9$ (**CCO-30-35-10-air**) (stars, black), hot-pres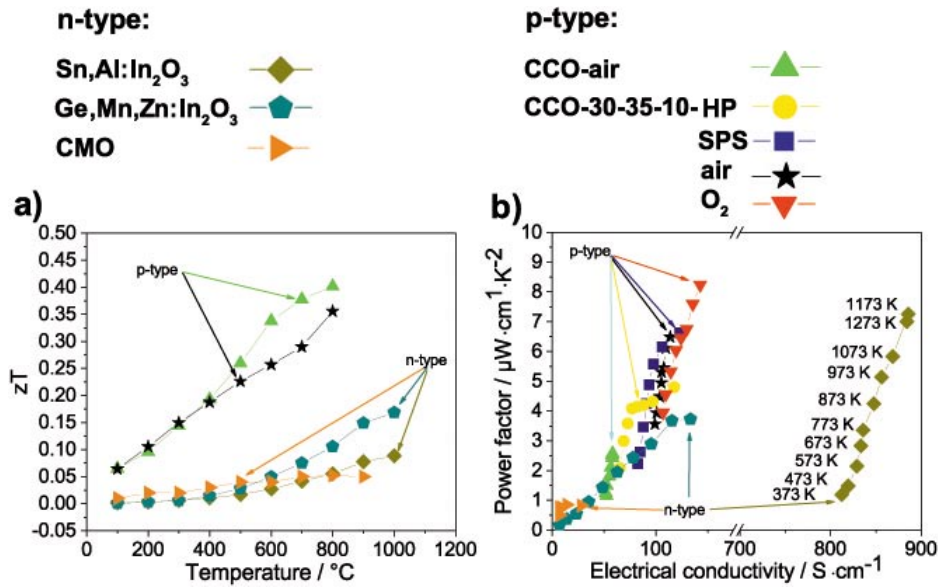sed $Ca_{2.25}Na_{0.3}Bi_{0.35}Tb_{0.1}Co_4O_9$ (**CCO-30-35-10-HP**) (circle, yellow), spark plasma sintered $Ca_{2.25}Na_{0.3}Bi_{0.35}Tb_{0.1}Co_4O_9$ (**CCO-30-35-10-SPS**) (square, dark blue), O_2-sintered $Ca_{2.25}Na_{0.3}Bi_{0.35}Tb_{0.1}Co_4O_9$ (**CCO-30-35-10-O₂**) (reverse rectangle, red), $In_{1.9}Sn_{0.05}Al_{0.05}O_3$ (**Sn,Al:In₂O₃**) (diamond, dark yellow), $In_{1.95}Ge_{0.01}Mn_{0.01}Zn_{0.03}O_3$ (**Ge,Mn,Zn:In₂O₃**) (pentagon, dark green) and $CaMnO_3$ (**CMO**) (rotated rectangles, orange) [30, 60, 62, 63]: a) figure-of-merit zT as a function of temperature. b) Ioffe plot: power factor $\sigma\alpha^2$ as a function of the electrical conductivity σ. Values are increasing with indicated temperature.

The interrelation of σ, α and λ (here in dependence of the carrier concentration n), as shown in Figure 9, is the fundamental challenge in thermoelectric research. The isothermal electrical conductivity σ is increasing with n, according to equation 8, while α is decreasing in accordance to Equation 7, at the same time, λ is also increasing due to the increased electrical part (Equation 17). However, the aforementioned techniques were proved to be suitable to enhance the thermoelectric properties σ, α and λ simultaneously [24, 31, 39, 40, 50]. The degree of porosity (section 1.2.3) in CCO ceramics was changed and a high figure-of-merit zT (B in

Figure 9), as shown in Figure 10a, was obtained. This approach to increase the zT value was also used for co-doped Ge,Mn,Zn:In$_2$O$_3$, as illustrated in Figure 10a. Carrier concentration engineering (section 1.2.1) was carried out to obtain Sn,Al:In$_2$O$_3$, which shows both, high electrical conductivity and thermoelectric power factor (A in Figure 9), as shown in Figure 10b. The three different approaches of carrier concentration engineering, electronic band structure engineering (section 1.2.2) and compositionally alloyed nanostructures (section 1.2.3) were combined to develop the CCO-NCO-BCCO nanocomposite. This material shows a high electrical conductivity and thermoelectric power factor (A in Figure 9), as revealed in Figure 10b. The application of alternative processing techniques improved the nanocomposite. As a consequence, the electrical conductivity and thermoelectric power factor, as shown in Figure 10b, were further increased O$_2$-sintering. The developed high power factor (A in Figure 9) materials are suitable for high temperature power generation from infinite heat sources.

1.3.3 Indium oxide (In$_2$O$_3$)

Indium oxide crystallizes in the calcium fluorite CaF$_2$ structure type of the cubic space group Ia$\bar{3}$ and is an indirect semiconductor with a band gap of 1.16 eV. This structure, and its properties as a semiconductor, are easy to tune by introducing dopants on In positions, as shown in Figure 11, and described in section 1.1.2.
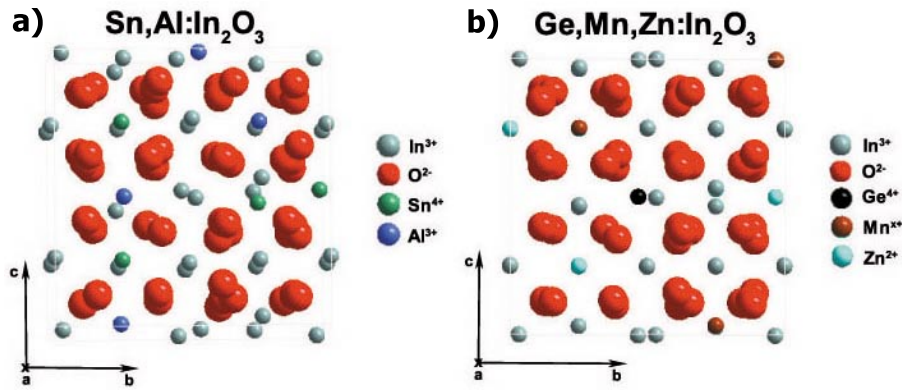
Figure 11: Crystal structure of indium oxide In$_2$O$_3$ (IO) along the a-axis, spacegroup Ia$\bar{3}$ (ICSD-50847). Different compositions of doped indium oxides: a) Sn,Al:In$_2$O$_3$ and b) Ge,Mn,Zn:In$_2$O$_3$ are shown and indicated by spheres of different size and colour. In-olive-green, O-red, Sn-green, Al-blue, Ge-black, Mn-brown and Zn-turquoise. Figure was drafted using Diamond - Crystal and Molecular Structure Visualization software.

In$_2$O$_3$ is a promising thermoelectric n-type oxide for energy harvesting at high temperatures and under oxidizing conditions, due to its good thermal, chemical stability and convenient electronic properties like high electrical conductivity and power factor (Figure 10b). Thereby, the electrical conductivity is mostly enhanced via carrier concentration engineering by doping with higher valent elements like Sn or Ge [64–66]. The introduction of Sn and Ge leads to strong hybridization of 5s (In,

Sn, Ge) and 2p (O) atomic orbitals, which maintains a small band gap [11, 67]. To enhance the thermoelectric properties of indium oxide, several approaches like band gap engineering [68–70], point defect engineering [71, 72] and nanostructuring via spark plasma sintering (SPS) [73, 74], were done. All these studies started with a doped nanograined powder, derived from a wet-chemical bottom-up synthesis like the sol-gel synthesis, followed by a fast and kinetically-controlled spark plasma sintering, to densify the ceramic body and introduce small grains to decrease the thermal conductivity [66, 69, 71–75]. In this way thermoelectric power factors between 9 and 8.5 μ W $\cdot$ cm^{-1} $\cdot$ K^{-2} and zT values of 0.35 and 0.4 at 973, 1273 K, respectively, are possible [66, 69]. Also composites of ZnO and In$_2$O$_3$ layers are feasible to enhance the Seebeck coefficient by introducing different amounts of ZnO layers [76, 77].

1.3.4 Calcium manganese oxide (CaMnO$_3$)

The Calcium manganese oxide (CaMnO$_3$, CMO, $t>1$) is another n-type semiconducting material, which possess a perovskite structure type of a orthorhombic crystal system in the space group Pbnm. The structure consists of corner-sharing MnO$_6$ octahedra and Ca atoms in the cavities. This material is feasible to dope on both, A and B-site, and subsequently the thermoelectric properties can be adjusted. The lattice of the perovskite ABO$_3$ structure can be distorted by implementing differently sized cations.
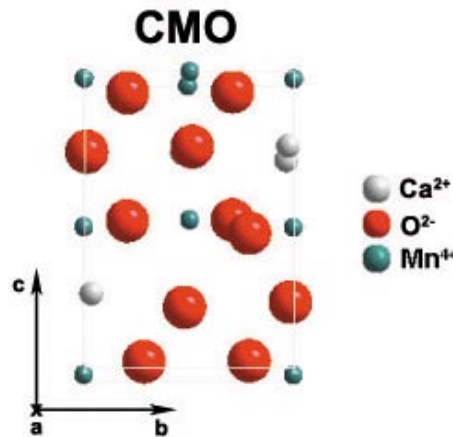
Figure 12: Crystal structure of calcium manganese oxide CaMnO$_3$ (CMO) along the *a*-axis, space group Pbnm (ICSD-92083). Different elements are shown and indicated by spheres of different size and colour. Ca-grey, O-red, Mn-olive-green. Figure was drafted using Diamond - Crystal and Molecular Structure Visualization software.

This distortion can be evaluated by the Goldschmidt's tolerance factor t [78]. As long as the factor shown in Equation 24 is between 0.89 and 1.02, the material remains in the cubic perovskite structure type, which is shown in Figure 12. The involved parameters are the ionic radii of the A-site cation r_A, B-site cation r_B and the anion r_O (in general oxygen).

$$t = \frac{r_A + r_0}{\sqrt{2}(r_B + r_0)} \tag{24}$$

The structure of CMO is also influenced by temperature, leading to different formed phases from orthorhombic (until 1169 K) to tetragonal (from 1169 to 1186 K, $t<1$) and cubic nature (above 1186 K), reported by Taguchi et al. [79]. The conduction mechanism of electrons in CMO is based on a polaron hopping mechanism, in which the mobility of the localized electrons is dependent on their thermal activation energy [80, 81]. The thermoelectric properties of CMO can be modified by doping, but also by control of the lattice distortion of the material. Several publications reported a beneficial influence of adjusting the charge carrier as well as the oxygen vacancy concentration of the material [82, 83]. These approaches also changed the lattice parameters, when dopants are introduced into the structure, which causes distortions and can also improve the thermoelectric properties of CMO [84–86]. Different doping, vacancy concentrations and compositions of CMO led to good zT values of around 0.32 at high temperatures [87–89]. The electrical conductivity can also be increased by introducing Nb dopants, which lead to a strong hybridization of Nb:d-O:p orbitals of Nb-O bonds [90, 91]. The lattice distortions, caused by doping or Ca vacancies, can also reduce the thermal conductivity [92, 93]. The spark plasma sintering technique is suitable to manufacture an all-oxide generator, shown in sections 1.5 and 3.4, since it does not reduce or change the structure of CMO [94].

1.3.5 Sodium cobalt oxide (Na_xCoO_2)

The layer-structured sodium cobalt oxide (Na_xCoO_2, NCO) has already been investigated in some publications and can be used in the moderate-temperature range [95–97]. NCO has a monoclinic crystal structure, as shown in Figure 13, which is formed by layers of CdI_2-type CoO_2 (subsystem 1) with a triangular lattice and of a layered rock-salt type (subsystem 2), formed by a Na.

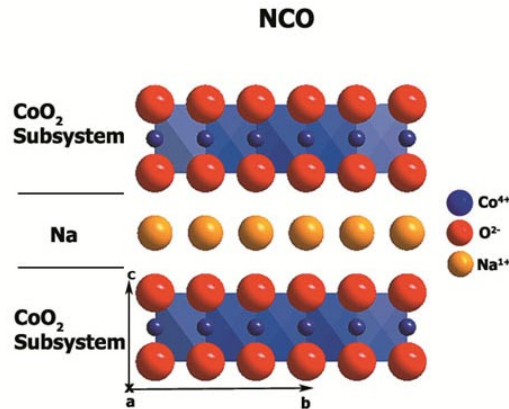**Figure 13:** Crystal structure of sodium cobalt oxide Na_xCoO_2 (NCO) along the a-axis after [95]. Different elements are shown and indicated by spheres of different size and colour. Co-blue, O-red, Na-orange. Figure was drafted using Diamond - Crystal and Molecular Structure Visualization software. Copyright [60]

These layers alternate along the *c*-axis (Figure 13). This structure constitutes the basis for the $Ca_3Co_4O_9$ (CCO) and $Bi_2Ca_2Co_2O_9$ (BCCO) structure, in which the rocksalt layer is exchanged by other building blocks. As a single crystal, but also as polycrystalline ceramics, the NCO phase shows a very high electrical conductivity and provide, therefore, excellent properties [96–98]. The properties of the NCO phase can be further modified by its sodium content, leading to a very high Seebeck coefficient at low temperatures, reported by Lee et al. [99]. However the NCO phase suffer from inferior mechanical, thermal and chemical stability at high temperatures under oxidizing atmospheres [96].

1.3.6 Calcium cobalt oxide ($Ca_3Co_4O_9$)

The layer-structured calcium cobalt oxide ($Ca_3Co_4O_9$, CCO), based on the structure of NCO, see section 1.3.5, has already been investigated in several publications and can be used in the high-temperature range in air [36, 62, 100]. Figure 14 reveals the crystal structure of CCO. CCO has a monoclinic crystal structure built by a misfit-layered structure of a CdI_2-type CoO_2 subsystem with a triangular lattice and a layered rock-salt subsystem of Ca_2CoO_3 units, which are alternating arranged along the *c*-axis. As shown in Figure 14, the *b*-axis parameters within the two subsystems of the monoclinic structure of CCO are different and compose a non-rational ratio. As a consequence, the CCO structure is described as an incommensurate structure [101].
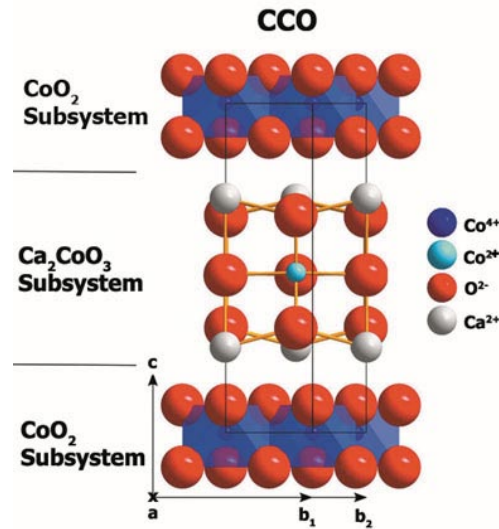
Figure 14: Crystal structure of calcium cobalt oxide $Ca_3Co_4O_9$ (CCO) along the *a*-axis after [101]. Different elements are shown and indicated by spheres of different size and colour. Co-blue (4+), Co-turquoise (2+), O-red, Ca-grey. Figure was drafted using Diamond - Crystal and Molecular Structure Visualization software. Copyright [60]

CCO is the most promising candidate for energy harvesting at high temperatures in air, plenty of research activities has been carried out. Wang et al. [102] investigated the influence of different dopants like Fe, Mn and Cu on the effective mass of holes

in CCO, due to the impact of the effective mass on both Seebeck coefficient and electrical conductivity, see sections 1.1.1 and 1.1.2. Also engineering approaches like different synthesis or processing techniques, which result in different densities or porosities of the obtained CCO ceramics, were done [62, 103, 104]. The CCO structure was also doped with different elements in order to increase either the electrical conductivity or the Seebeck coefficient by adjusting the charge carrier concentration or by the introduction of additional electronic bands, see section 1.2.1 and 1.2.2 [37, 43, 44, 105, 106]. Based on the crystal structure, CCO tends to form plate-like particles during synthesis. These particles are difficult to process in order to obtain a CCO ceramic of high density [62, 103]. The spark plasma sintering technique can solve this problem, since the pressure during compaction can be enhanced as well as the sintering temperature can be adjusted [107, 108]. The thermoelectric properties σ and α of CCO can be improved simultaneously by tuning the charge carrier concentration and introducing additional electronic bands. The processing via spark plasma sintering forms nano-sized grains, which scatter more efficiently phonons [42]. But the processing via spark plasma sintering leads to a concurrent high texture and orientation of grains, which lead to an enhancement of the already existing anisotropy in CCO ceramics [109–112]. This anisotropy of thermoelectric properties in different directions (perpendicular or parallel to the pressing direction) result in the necessity of characterizing a highly textured CCO ceramic in each direction and to determine their power factor or zT value just from values measured from the same direction [30, 60, 62, 111, 112].

1.3.7 Bismuth calcium cobalt oxide ($Bi_2Ca_2Co_2O_9$)

The layer-structured bismuth calcium cobalt oxide ($Bi_2Ca_2Co_2O_9$, BCCO) is also based on the structure of NCO, see section 1.3.5. Its structure, shown in Figure 15, has been investigated by Leligny et al. and Muguerra et al. [113–115].
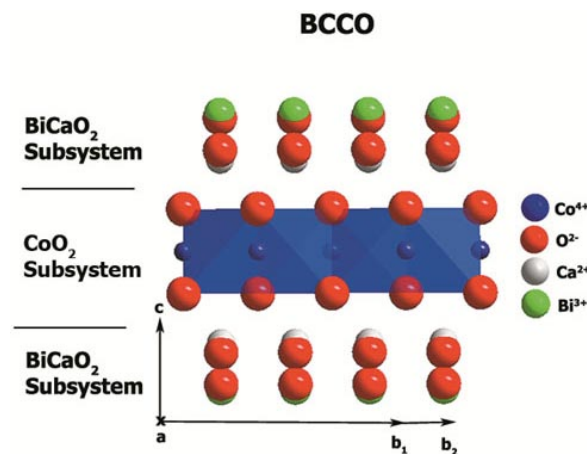
Figure 15: Crystal structure of bismuth calcium cobalt oxide $Bi_2Ca_2Co_2O_9$ (BCCO) along the a-axis after [115]. Different elements are shown and indicated by spheres of different size and colour. Co-blue, O-red, Ca-grey, Bi-green. Figure was drafted using Diamond - Crystal and Molecular Structure Visualization software. Copyright [60]

BCCO has a monoclinic crystal structure built by a misfit-layered structure of a CdI_2-type CoO_2 subsystem with a triangular lattice and a layered rock-salt subsystem of $BiCaO_2$ instead of Na or Ca_2CoO_3 units, which are alternatingly arranged along the c-axis. Within the two subsystems of the monoclinic structure, shown in Figure 14, the b-axis parameters are varying, forming an incommensurate structure. The two $BiCaO_2$ units of the BCCO phase lead to both, a much lower electrical conductivity, but at the same time, the Seebeck coefficient is significantly enhanced, compared to the values of σ, α of NCO or CCO [116, 117]. The BCCO phase can be used in the moderate-temperature range, but it suffers from low mechanical, thermal and chemical stability in the high-temperature range in air [117].

1.3.8 Material synthesis: Sol-gel process

The sol-gel synthesis was used to synthesize all oxide powders. Powders of CCO and CMO for the manufacturing of the all-oxide generator were obtained by spray pyrolysis from CerPoTech AS company. In the sol-gel synthesis, schematically shown in Figure 16, different nitrates of the respective metal cations are stoichiometrically dissolved in water and an ammonia solution is added, which also contains deprotonated citric acid (1.5 M) and EDTA (1.0 M) for complexing the dissolved metal ions in the solution (pH = 9) [62, 118].

Figure 16: Scheme of the sol-gel synthesis, STEM micrographs and EDXS mappings of intermediate and final product powder of $Ca_3Co_4O_9$. Copyright Elsevier [62].

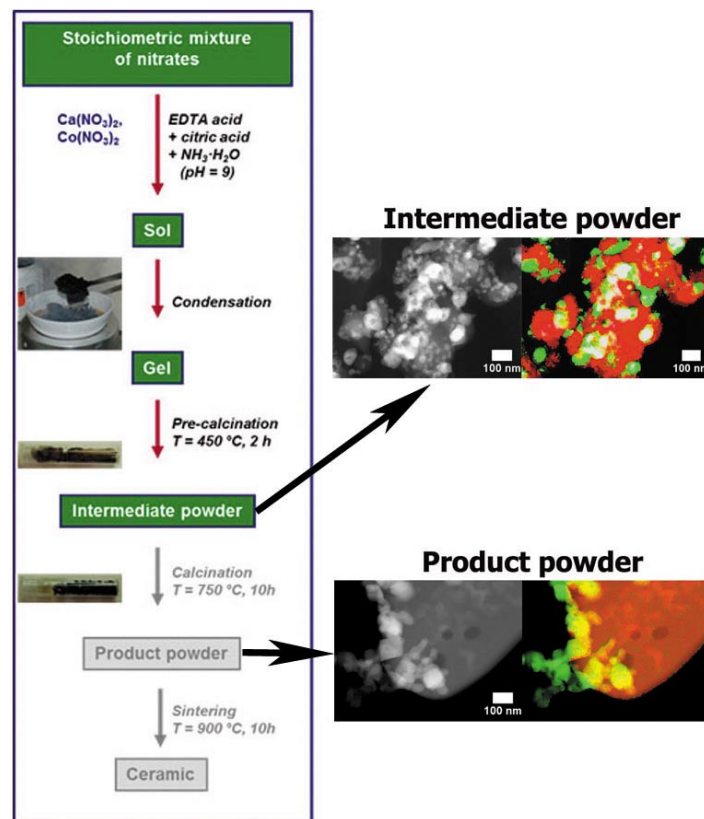This technique provides fine-grained powders of homogeneous composition, see Figure 16, and is, therefore, appropriate to improve thermoelectric properties of various materials by doping and use of different sintering techniques. The water was evaporated and the gel aged over night at approximately 378 K. The aged gel was pre-calcined at around 673-723 K until smouldering was completed. For the synthesis of CCO-based p-type materials, an intermediate powder, which consists of $CaCO_3$ and Co_3O_4 nanoparticles, is obtained after pre-calcination, shown in Figure 16. The obtained intermediate powder was ground and calcined for 10 h at 1023 K with heating and cooling rates of 3 min $\cdot$ K^{-1}. For the calcined powder of CCO, shown in Figure 16, plates of 500 nm width and length but just of a few nm thickness can be obtained. But also after calcination, the formed intermediate Co_3O_4 nanoparticles are present [62]. All steps of the sol-gel route like synthesis, pre-calcination and calcination were conducted under ambient air conditions.

1.4 Sintering techniques

The synthesized powders are further processed to ceramics either by pressureless sintering in air or another atmosphere or by more complex techniques like hot-pressing (HP) and spark plasma sintering (SPS). If pressureless sintering is used, the powders are compressed by uniaxial pressing and a subsequent heat treatment of the ceramic green body [60, 62]. The difference between pressureless and hot-pressing or spark plasma sintering lies in the simultaneous one-step pressing and heating, shown in Figure 17.
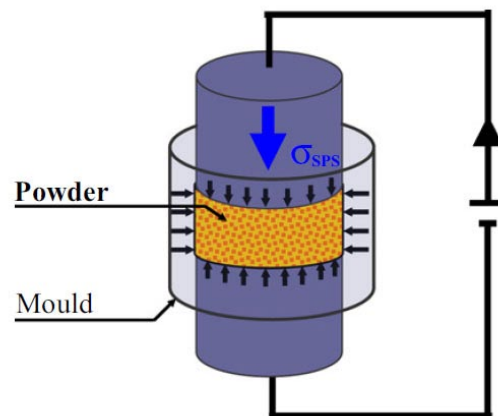
Figure 17: Schematic representation of the spark plasma sintering technique. σ_{SPS} indicate the current, which flows through the powder and leads to a subsequently fast heating rate. Copyright Elsevier [119].

In general, graphite dies and vacuum is used for both hot-pressing and spark plasma sintering, which are thus providing partly reducing conditions [94]. The advantages of the hot-pressing and spark plasma sintering techniques are short processing times,

small grains sizes and high achievable bulk densities. The main disadvantages are partly reducing conditions and thereby limited applicability, especially for oxides. Hence pressureless sintering under different atmospheres like O_2 could be an alternative for oxide-based ceramics [30, 120].

1.5 Thermoelectric generators

1.5.1 Principle of energy conversion

In principle, a thermoelectric generator (TEG) consists of p- and n-type materials (legs), which are electrically connected in series and thermally in parallel. Thermoelectric generators, which are solely made of p- or n-type legs were also prepared in literature [121, 122]. The legs are electrically cross connected (the bottom of leg one to top of leg two) with a metallic connector, which acts as the counterpart. Entropic and electrical fluxes in p- (same direction) and n-type (opposite direction) materials are coupled in a way, that heat is directly converted into electrical energy, as shown in Figure 18 [1–3].
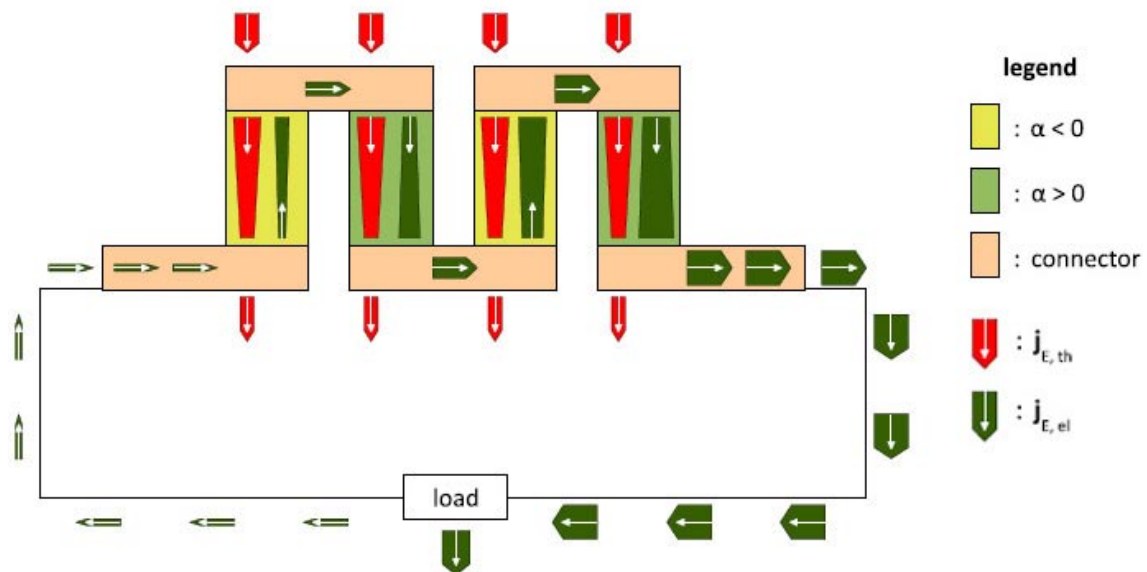
Figure 18: Principle of a thermoelectric generator: Coupling entropy and electric fluxes with each other. Energy conversion in operation, energy is transferred from entropy current to electric current. The width of the arrows indicate the magnitude of the thermal energy flux density ($j_{E,th}$) and of the electric energy flux density ($j_{E,el}$). Copyright De Gruyter [3].

As shown in Figure 18, entropy flows from hot-side to cold-side through the TEG and pumps charge from one side to the other. The phenomenon of pumping is enabled by a difference in thermal energy flux density ($j_{E,th}$), as revealed in Figure 18. As a consequence, energy is transferred from heat to electrical energy and the electric energy flux density $j_{E,el}$ subsequently increases from one side to the other [3].

1.5.2 Characterization of thermoelectric generators

The p- and n-type legs are commonly connected in series using a metallic connector like copper, silver or gold. When the thermoelectric generator is exposed to a temperature gradient ΔT, an electrical voltage U (potential difference $\Delta\varphi$, see sections 1.1 and 1.1.1) within the p- and n-type materials will be build, which can be measured at the contacts of the generator. Figure 19 shows a load-dependent $U - I$ and $P - I$ measurement of a TEG. The electrical voltage U and the electrical current I_q changes in dependence of different applied load resistances. Under electric open-circuit conditions ($I_q = 0$), the measured electrical voltage is called open-circuit voltage U_{OC}. If the setup is under electric short-circuited conditions ($U = 0$), the short-circuit current $I_{\mathrm{q,SC}}$ is obtained.
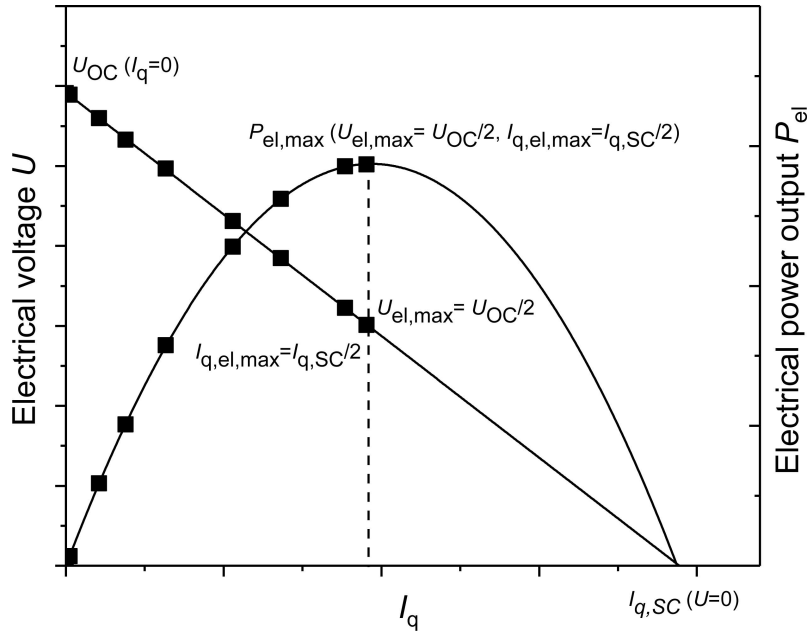
Figure 19: Schematic representation of the load-dependent characterization of a thermoelectric generator. Both, the electrical voltage U and the electrical current I_q were measured in dependence of different applied load resistances. The open-circuit voltage U_{OC} and the short-circuit current $I_{\mathrm{q,SC}}$ were measured under open-circuit or closed-circuit conditions, respectively. The maximum electrical power output is obtained at $R_{\mathrm{load}}{=}R_{\mathrm{TEG}}$, at half of the $U - I$ curve.

The maximum electrical power output (Figure 19) of a thermoelectric generator is defined by the Seebeck coefficient of p- and n-type materials, number of legs, the applied temperature difference ΔT and the resistance (high σ needed) of legs, see Equation 25.

$$P_{el,max} = \frac{(\Sigma\ \alpha_{p-leg} - \Sigma\ \alpha_{n-leg})^2}{4 \cdot (\Sigma\ R_{p-leg} + \Sigma\ R_{n-leg})} \cdot (\Delta T^2)^2 = \frac{U_{OC}^2}{4 \cdot R_{TEG}} \tag{25}$$

The electrical power output will be at the maximum, as shown in Figure 19, if the load resistance is equal to the TEG resistance $R_{\mathrm{load}}{=}R_{\mathrm{TEG}}$ [28]. To increase the

electrical power output of a thermoelectric generator, two approaches are possible. Either improve the specific material properties, like increase the Seebeck coefficient and the electrical conductivity or to build a bigger series connection of p- and n-type legs. The resistance of the generator will subsequently increase according to Equation 26, when contact resistances are neglected.

$$R_{TEG} = R_{leg1} + R_{leg2} + R_{leg3} + R_{leg4} + ... \tag{26}$$

The heat conductivity of p- and n-type materials also play an important role in thermoelectric power generation, since when heat conductivity is too low, not enough thermal energy is transferred into the system to be converted into electrical energy, see sections 1.1 and 1.2. The direct conversion of thermal into electrical energy under electric closed-circuited conditions without any moving mechanical parts, makes a thermoelectric generator autonomous, since maintenance is in principle unnecessary, when it is once mounted and operating. Thermoelectric generators are hence applicable as sensors for space applications or for recovering waste heat in a various number of processes.

1.5.3 Designs of thermoelectric generators

Over the years, different designs for thermoelectric generators were developed, like the conventional with chess-board pattern, the uni-leg, the flexible with different bendable substrates, or the all-oxide without metallic connectors. The conventional design has the advantage of high-temperature application, up to 1173 K and also higher temperatures are possible, depending on used p-, n-type materials and metallic connectors. The conventional design, schematically shown in Figure 20, also possesses good mechanical, thermal and chemical stability at high-temperatures in air, since most generators are assembled on Al_2O_3 plates.
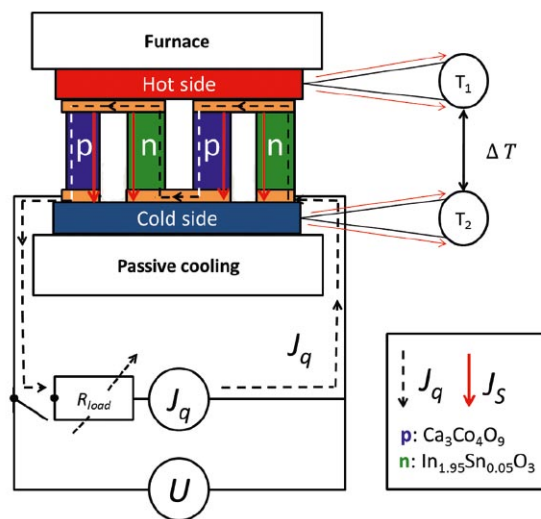

Figure 20: Conventional design and characterization setup of a thermoelectric generator with indicated entropy J_S and electric J_q flux. Copyright De Gruyter [11].

Table 1.1: Characteristics of selected oxide-based thermoelectric generators with conventional design: number of p/n couples, hot-side temperature T_{hot}, temperature difference ΔT, open-circuit voltage U_{OC}, maximum electrical power output $P_{el,max}$, electrical power density ω_{el} and temperature difference dependent electrical power density $\omega_{el}/(\Delta T)^2$. Uni-leg generators are indicated by their missing counter part (-/).

generator p/n	p/n couples	T_{hot} / K	ΔT / K	U_{OC} / mV	$P_{el,max}$ / mW	ω_{el} / mW $\cdot cm^{-3}$	$\omega_{el}/(\Delta T)^2$ / $\mu W \cdot cm^{-2} \cdot K^{-2}$	Ref.
$Ca_{2.75}Gd_{0.25}Co_4O_9$ / $Ca_{0.92}La_{0.08}MnO_3$	8	773	390	988	63.5	44.1	0.29	[123]
$Ca_3Co_4O_9$ / $Ca_{0.95}Sm_{0.05}MnO_3$	2	1000	925	400	31.5	49.2	0.06	[124]
$Ca_3Co_4O_9$ / $CaMnO_3$	8	1273	975	700	170	85	0.09	[121]
-/ $Ca_{0.95}Sm_{0.05}MnO_3$	2	760	360	260	16	21.82	0.17	[125]
$Ca_3Co_4O_9$ / $Ca_{0.95}Sm_{0.05}MnO_3$	2	990	630	400	31.5	49.2	0.12	[126]
$GdCo_{0.95}Ni_{0.05}O_3$ / $CaMn_{0.98}Nb_{0.02}O_3$	4	800	500	340	40	62.5	0.25	[127]
$Ca_3Co_4O_9$ / $Ca_{0.9}Nd_{0.1}MnO_3$	1	1175	727	194	95	93.2	0.18	[128]
$Ca_3Co_{4-x}Ag_xO_9$ / $Ca_{1-y}Sm_yMnO_3$	2	873	523	328	36.8	49.1	0.18	[129]
$Ca_3Co_4O_9$ / $(ZnO)_7In_2O_3$	44	1100	673	1800	423	2.1	0.01	[130]
$Nd_{0.995}Ca_{0.005}CoO_3$ / $LaCo_{0.99}Mn_{0.01}O_3$	10	704	399	1000	44	9.56	0.06	[131]
$Ca_3Co_4O_9$ / $Zn_{0.98}Al_{0.02}O$	8	906	496	700	65.3	45.3	0.18	[132]
$Ca_3Co_4O_9$ / $CaMnO_3$	4	713	346	282	8.42	1.67	0.01	[133]
$Ca_3Co_4O_9$ / $CaMnO_3$	12	473	200	800	1.98	3.3	0.08	[134]
CCO-30-35-10-air/ $Sn,Al:In_2O_3$	10	1173	250	782	25	125	2	[30] section 3.5
CCO-30-35-10-air/ $Ge,Mn,Zn:In_2O_3$	10	1173	280	939.7	22.9	114.5	1.46	[30] section 3.5
CCO-30-35-10-O_2/ $Sn,Al:In_2O_3$	10	1073	258	671.8	22.7	113.5	1.7	[30] section 3.5

The major drawback of thermoelectric generators with conventional design is the enhancement of the fill factor, which is limited by processing issues, because metallic connectors are difficult to mount without introducing electrical shortcuts when the top plate is attached. Characteristics of reported conventional, oxide-based thermoelectric generators of different material combinations [30, 121, 123–134] are shown in Table 1.1.

The different generators are difficult to compare, because the number of p/n couples, leg dimensions, as well as hot-side temperature and temperature difference varies. The calculated electrical power density ω_{el} is suitable to compare the different generators, but hot-side temperature and temperature difference should be in the same range, since ΔT has a major impact on the electrical power output of the generators, see Equation 25 and section 1.2. A more standardized form of the electrical power density ω_{el} by dividing it with the applied temperature difference to the square $\omega_{el}/(\Delta T^2)$ is more suitable. However, values of the highest electrical power output and electrical power density were obtained from generators, operated under high temperature difference or from generators with improved thermoelectric materials [30, 121, 128, 130].

The flexible design exhibits the advantage of a bendable nature and use of lightweight materials. Furthermore, the flexible design is much easier to assemble and to scale up, according to its open layout. In this way, a high fill factor can be obtained and electric short-circuits can be avoided. The flexible thermoelectric generator

can be coiled up and be placed around a pipe or other difficult accessible hot places [122, 135–137]. Figure 21 shows the schematic setup of a flexible thermoelectric generator, made of solid state bulk materials, which are placed on a bendable substrate.
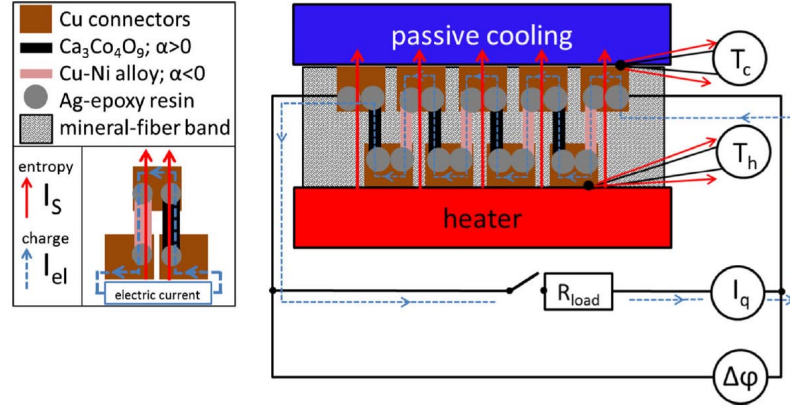

Figure 21: Flexible design and characterization setup of a thermoelectric generator with indicated entropy I_S and electric I_q flux. Copyright De Gruyter [137].

Different material classes like metals [138], alloys [122, 139], polymers [135, 140] and oxides [136, 137] has been used to assemble a p/n or uni-leg generator, see Table 1.2.

Table 1.2: Characteristics of selected flexible thermoelectric generators: number of p/n couples, hot-side temperature T_{hot}, temperature difference ΔT, open-circuit voltage U_{OC}, maximum electrical power output $P_{\text{el,max}}$, electrical power density ω_{el} and temperature difference dependent electrical power density $\omega_{\text{el}}/(\Delta T)^2$. Uni-leg generators are indicated by their missing counter part (/ -). Not available information (n.a.) is also indicated.

generator p/n	p/n couples	T_{hot} / K	ΔT / K	U_{OC} / mV	$P_{\text{el,max}}$ / μW	ω_{el} / μW $\cdot cm^{-3}$	$\omega_{\text{el}}/(\Delta T)^2$ / nW $\cdot cm^{-2} \cdot K^{-2}$	Ref.
Cu/ Ni	12	n.a.	0.12	n.a.	n.a.	0.012	830	[138]
Bi_2Te_3/ Sb_2Te_3	100	n.a.	40	160	n.a.	94.81	60	[122]
Bi_2Te_3-$Bi_{0.5}Sb_{1.5}Te_3$/ Bi_2Se_3	10	330	30	51	0.013	0.118	0.13	[139]
CNT-polystyrene/ -	n.a.	373	70	n.a.	n.a.	5.5	1.12	[135]
$Ca_3Co_4O_9$/ Cu-Ni alloy	4	420	31	16.52	0.082	0.897	0.93	[136]
KOH-PEDOT:PSS/ -	61	n.a.	90	25	0.1	4.098	0.5	[140]
$Ca_3Co_4O_9$:Cu,Ag/ Cu-Ni alloy	10	473	30.8	68.9	59.88	262.05	276	[137]

The major drawbacks are the use of quite expensive or complex thin film, sputtering, printing or growing techniques. These techniques also limit the dimensions of produced p- and n-type legs of the thermoelectric generator in order to keep the device bendable and flexible. Another disadvantage is the small temperature range of materials like polymers, alloys or the used substrates. Application at moderate temperatures often leads to decomposition or loss of flexibility. Therefore, values of achieved electrical power output and power density are in the range of nW to μW and nW to μW $\cdot cm^{-2}$, respectively, see Table 1.2. The use of bulk materials placed

on a flexible substrate can combine the good thermoelectric properties of macroscopic p- and n-type legs with the advantage of flexibility of a bendable substrate, resulting in quite high values of electrical power output and power density [137]. The all-oxide design compared to the conventional design, has the advantage of even higher-temperature application. Metallic connectors can be avoided, the generator is hence just limited by the thermal stability of the p- and n-type materials and the characteristics of the p-n junction. Furthermore, the absence of metallic connectors could lower the contact resistances between the p- and n-type materials. For the manufacturing of a thermoelectric generator with an all-oxide design, schematically shown in Figure 22, the choice of materials is very important. The coefficient of thermal expansion should be in the same range for p-, n-type and used insulator, since difference in thermal expansion during sintering or application at high temperatures could lead to cracks and malfunction of the generator [63].
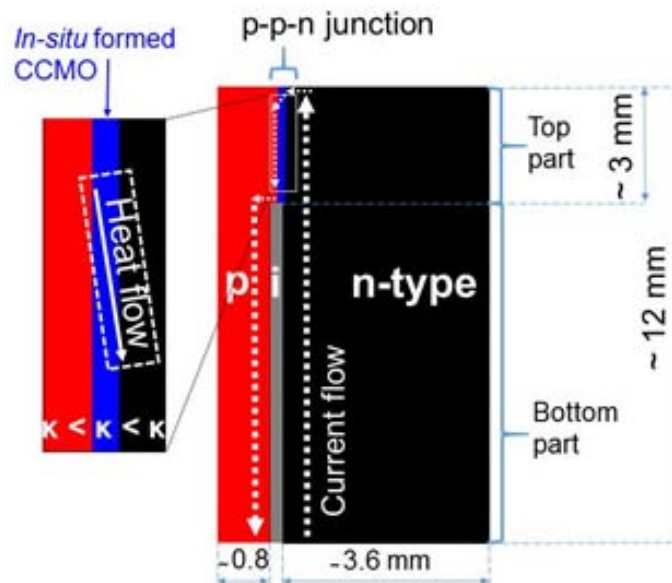
Figure 22: All-oxide design of a thermoelectric generator with indicated thermal and electric flux. Copyright American Society of Chemistry [63].

The used materials should also possess energy-matched electronic bands in order to avoid Schottky contacts and enable ohmic contact behaviour to minimize contact resistances. The p- and n-type materials commonly show no matched electronic bands, an thermoelectrically active interlayer can play an important role to decrease contact resistances, see section 1.2.2. The interlayer also add additional interfaces, which can introduce a transversal thermoelectric effect, which can further improve the electrical power output [63, 141, 142]. The transversal thermoelectric effect takes place if different interfaces of thermoelectric materials are in contact to each other, as shown in Figure 22, and heat is flowing through them. In this case, these interfaces behave like additional p- and n-type materials and participate, depending on the applied temperature difference, to the electrical power output of the thermoelectric generator by boosting the supplied electrical voltage.

Table 1.3: Characteristics of selected all-oxide thermoelectric generators: number of p/n couples, hot-side temperature T_{hot}, temperature difference ΔT, open-circuit voltage U_{OC}, maximum electrical power output $P_{\text{el,max}}$, electrical power density ω_{el} and temperature difference dependent electrical power density $\omega_{\text{el}}/(\Delta T)^2$.

generator p/n	p/n couples	T_{hot} / K	ΔT / K	U_{OC} / mV	$P_{\text{el,max}}$ / mW	ω_{el} / mW $\cdot cm^{-3}$	$\omega_{\text{el}}/(\Delta T)^2$ / μW $\cdot cm^{-2} \cdot K^{-2}$	Ref.
NiO:Li/ $Ba_{0.2}Sr_{0.8}PbO_3$	4	1164	552	380	34.4	71.66	0.24	[143]
Si:B/ Si:P	4	873	573	100	11	22.92	0.07	[144]
$Ca_3Co_4O_9$/ $CaMnO_3$	1	1173	160	213	5.72	22.8	0.89	[63] section 3.4

The manufacturing and up-scaling of an all-oxide thermoelectric generator remains difficult, since thermal expansion and subsequent crack formation is a critical point, but also ceramic up-scaling at all is a difficult topic. Some studies of all-oxide thermoelectric generators are shown in Table 1.3. The obtained values of electrical power output and electrical power density are already in the range of generators following the conventional design.

1.6 List of Figures

Bibliography

[1] H. U. Fuchs. A direct entropic approach to uniform and spatially continuous dynamical models of thermoelectric devices. *EHS*, 1(3-4):253–265, 2014.

[2] H. U. Fuchs. *The Dynamics of Heat – A Unified Aproach to Thermodynamics and Heat Transfer*. Graduate Texts in Physics. Springer, New York, second edition, 2010.

[3] A. Feldhoff. Thermoelectric material tensor derived from the Onsager - de Groot - Callen model. *EHS*, 2 (1):5–13, 2015.

[4] T. J. Seebeck. Ueber die magnetische Polarisation der Metalle und Erze durch Temperaturdifferenz. *Annal. d. Physik. B.*, 82:253–286, 1826.

[5] E. Velmre. Thomas Johann Seebeck (1770-1831). *Proc. Estonian Acad. Sci. Eng.*, 13:276–282, 2007.

[6] A. F. Ioffe. *Semiconductor Thermoelements and Thermoelectric Cooling*. Infosearch Ltd. London, first edition, 1957.

[7] G. S. Ohm. Die Galvanische Kette mathematisch bearbeitet. *T. H. Riemann*, 1:1–245, 1827.

[8] T. N. Narasimhan. Fourier's heat equation: History, influence, and connections. *Rev. Geophys.*, 37:151–172, 1999.

[9] D. J. Singh. Electronic structure of $NaCo_2O_4$. *Phys. Rev. B*, 61:13397–13402, 2000.

[10] K. Seeger. *Semiconductor Physics*. Springer, Berlin, 1991.

[11] M. Bittner, B. Geppert, N. Kanas, S. P. Singh, K. Wiik, and A. Feldhoff. Oxide-based thermoelectric generator for high-temperature application using p-type $Ca_3Co_4O_9$ and n-type $Ca_{1.95}Sn_{0.05}O_3$ legs. *EHS*, 3(3):213–222, 2016.

[12] H. Ibach, H. Lüth. *Festkörperphysik - Einführung in die Grundlagen*. Springer, Jülich, 3rd edition, 1989.

[13] C. Kittel. *Einführung in die Festkörperphysik*. R. Oldenbourg Verlag München Wien, Dresden, 12th edition, 1999.

[14] B. Nag. *Electron Transport in Compound Semiconductors.* Springer-Verlag Berlin Heidelberg New York, Dresden, 11. Series in Solid-State Sciences edition, 1980.

[15] M. Cutler and N. F. Mott. Observation of Anderson localization in an electron gas. *Phys. Rev.*, 181:1336–1340, 1969.

[16] S. Stackhouse and L. Stixrude. Theoretical methods for calculating the lattice thermal conductivity of minerals. *Rev. Mineral. Geochem.*, 71:253–269, 2010.

[17] T. M. Tritt. *Thermoelectric materials: principles, structure, properties, and applications.* Elsevier, Encyclopedia of Materials: Science and Technology, Amsterdam, 2002.

[18] O. Jankovsky, D. Sedmidubsky, Z. Sofer, and J. Hejtmanek. Thermodynamic behavior of $Ca_3Co_4O_{9+\delta}$ ceramics. *Ceram-Silikaty*, 56(2):139–144, 2012.

[19] H. S. Kim, W. Liu, G. Chen, C.-W. Chu, and Z. Ren. Relationship between thermoelectric figure of merit and energy conversion efficiency. *Proc. Natl. Acad. Sci. USA*, 112(27):8205–8210, 2015.

[20] E. Altenkirch. Über den Nutzeffekt der Thermosäule. *Z. Phys. Chem.*, 16:560–568, 1909.

[21] D. Wu, L.-D. Zhao, X. Tong, W. Li, L. Wu, Q. Tan, Y. Pei, L. Huang, J.-F. Li, Y. Zhu, M. G. Kanatzidis, and J. He. Superior thermoelectric performance in PbTe-PbS pseudo-binary: extremely low thermal conductivity and modulated carrier concentration. *Energ. Environ. Sci.*, 8:2056–2068, 2015.

[22] G. Joshi, H. Lee, Y. Lan, X. Wang, G. Zhu, D. Wang, R. Gould, D. C. Cuff, M. Y. Tang, M. S. Dresselhaus, G. Chen, and Z. Ren. Enhanced thermoelectric figure-of-merit in nanostructured p-type silicon germanium bulk alloys. *Nano. Lett.*, 8:4670–4674, 2008.

[23] L.-D. Zhao, S.-H. Lo, Y. Zhang, H. Sun, G. Tan, C. Uher, C. Wolverton, V. P. Dravid, and M. G. Kanatzidis. Ultralow thermal conductivity and high thermoelectric figure of merit in SnSe crystals. *Nature*, 508:373–377, 2014.

[24] G. J. Snyder and E. S. Toberer. Complex thermoelectric materials. *Nat. Mater.*, 7:105–114, 2008.

[25] C. Fu, T. Zhu, Y. Liu, H. Xie, and X. Zhao. Band engineering of high performance p-type FeNbSb based half-Heusler thermoelectric materials for figure of merit zT > 1. *Energ. Environ. Sci.*, 8:216–220, 2015.

[26] S. R. Brown, S. M. Kauzlarich, F. Gascoin, and G. J. Snyder. $Yb_{14}MnSb_{11}$: New high efficiency thermoelectric material for power generation. *Chem. Mater.*, 18:1873–1877, 2006.

[27] D. Narducci. Do we really need high thermoelectric figure of merit? A critical appraisal to the power conversion efficiency of thermoelectric materials. *Appl. Phys. Lett.*, 99:102104–1–102104–3, 2011.

[28] A. Möschwitzer and K. Lunze. *Lehrbuch Halbleiterelektronik.* Dr. Alfred Hüthig Verlag, Heidelberg, 8th edition, 1998.

[29] A. Feldhoff. Direct entropic approach to power conversion and its efficiency in thermoelectric materials. *In preparation*, 2018.

[30] M. Bittner, N. Kanas, R. Hinterding, F. Steinbach, M. Schrade, J. Räthel, K. Wiik, M.-A. Einarsrud, and A. Feldhoff. A comprehensive study on improved power materials for high-temperature thermoelectric generators. *submitted to J. Power Sources*, 2018.

[31] G. Tan, L.-D. Zhao, and M. Kanatzidis. Rationally designing high-performance bulk thermoelectric materials. *Chem. Rev.*, 116:12123–12149, 2016.

[32] Y. Pei, A. F. May, G. J. Snyder, and G. J. Self. Tuning the carrier concentration of $PbTe/Ag_2Te$ composites with excess Ag for high thermoelectric performance. *Adv. Energy Mater.*, 1:291–296, 2011.

[33] A. S. Yamini, T. Ikeda, A. Lalonde, Y. Pei, S. X. Dou, and G. J. Snyder. Rational design of p-type thermoelectric PbTe: Temperature dependent sodium solubility. *J. Mater. Chem. A*, 1:8725–8730, 2013.

[34] E. S. Toberer, A. F. May, and G. J. Snyder. Zintl chemistry for designing high efficiency thermoelectric materials. *Chem. Mater.*, 22:624–634, 2010.

[35] Z. Li, C. Xiao, S. Fan, Y. Deng, W. Zhang, B. Ye, and Y. Xie. Dual vacancies: An effective strategy realizing synergistic optimization of thermoelectric property in BiCuSeO. *J. Am. Chem. Soc.*, 137:6587–6593, 2015.

[36] G. Xu, R. Funahashi, M. Shikano, I. Matsubara, and Y. Zhou. Thermoelectric properties of the Bi- Na-substituted $Ca_3Co_4O_9$ system. *Appl. Phys. Lett.*, 80:3760–3762, 2002.

[37] Y. Masuda, D. Nagahama, H. Itahara, T. Tani, W. S. Seo, and K. Koumoto. Thermoelectric performance of Bi- and Na-substituted $Ca_3Co_4O_9$ improved through ceramic texturing. *J. Mater. Chem.*, 13:1094–1099, 2003.

[38] B. Abeles. Lattice thermal conductivity of disordered semiconductor alloys at high temperatures. *Phys. Rev.*, 131:1906–1911, 1963.

[39] Y. Pei, X. Shi, A. Lalonde, H. Wang, L. Chen, and G. J. Snyder. Convergence of electronic bands for high performance bulk thermoelectrics. *Nature*, 473:66–69, 2011.

[40] J. P. Heremans, V. Jovovic, E. S. Toberer, A. Saramat, K. Kurosaki, A. Charoenphakdee, S. Yamanaka, and G. J. Snyder. Enhancement of thermoelectric efficiency in PbTe by distortion of the electronic density of states. *Science*, 321:554–557, 2008.

[41] J. P. Heremans, B. Wiendlocha, and A. M. Chamoire. Resonant levels in bulk thermoelectric semiconductors. *Energ. Environ. Sci.*, 5:5510–5530, 2012.

[42] N. V. Nong, N. Pryds, S. Linderoth, and M. Ohtaki. Enhancement of the thermoelectric performance of p-type layered oxide $Ca_3Co_4O_{9+\delta}$ through heavy doping and metallic nanoinclusions. *Adv. Mater.*, 23:2484–2490, 2011.

[43] A. I. Klyndyuk and I. V. Matsukevich. Synthesis and properties of $Ca_{2.8}Ln_{0.2}Co_4O_{9+\delta}$ (Ln = La, Nd, Sm, Tb-Er) solid solutions. *Inorg. Mater+.*, 48:1052–1057, 2012.

[44] S. Saini, H. S. Yaddanapudi, K. Tian, Y. Yin, D. Magginetti, and A. Tiwari. Terbium ion doping in $Ca_3Co_4O_9$: A step towards high-performance thermoelectric materials. *Sci. Rep-UK.*, 7:44621, 2017.

[45] M. S. Dresselhaus, G. Chen, M. Y. Tang, R. Yang, H. Lee, D. Wang, Z. Ren, J. P. Fleurial, and P. Gogna. New directions for low-dimensional thermoelectric materials. *Adv. Mater.*, 19:1043–1053, 2007.

[46] M. G. Kanatzidis. Nanostructured thermoelectrics: The new paradigm? *Chem. Mater.*, 22:648–659, 2010.

[47] M. Martín-González, O. Caballero-Calero, and P. Díaz-Chao. Nanoengineering thermoelectrics for 21st century: Energy harvesting and other trends in the field. *Renew. Sust. Energ. Rev.*, 24:288–305, 2013.

[48] J. Yang, H.-L. Yip, and A. K.-Y. Jen. Rational design of advanced thermoelectric materials. *Adv. Energy Mater.*, 3:549, 2013.

[49] L. D. Hicks and M. S. Dresselhaus. Thermoelectric figure of merit of a one-dimensional conductor. *Phys. Rev. B*, 47:16631–16634, 1993.

[50] L. D. Zhao, S. Hao, S.-H. Lo, C.-I. Wu, X. Zhou, Y. Lee, H. Li, K. Biswas, T. P. Hogan, C. Uher, C. Wolverton, V. P. Dravid, and M. G. Kanatzidis. High thermoelectric performance via hierarchical compositionally alloyed nanostructures. *J. Am. Ceram. Soc.*, 135:7364–7370, 2013.

[51] S. Heimann, S. Schulz, J. Schaumann, A. Mudring, J. Stotzel, F. Maculewicz, and G. Schierning. Record figure of merit values of highly stoichiometric Sb_2Te_3 porous bulk synthesized from tailor-made molecular precursors in ionic liquids. *J. Mater. Chem. C*, 3:10375, 2015.

[52] S. K. Rhee. Porosity-thermal conductivity correlations for ceramic materials. *Mater. Sci. Eng.*, 20:89–93, 1975.

[53] D. Paul. *ICT - Energy towards zero - Power Information and Communication technology, Chapter 4: Thermoelectric Energy Harvesting.* InTech, 2014.

[54] S. Wang, H. Li, R. Lu, G. Zheng, and X. Tang. Metal nanoparticle decorated n-type Bi_2Te_3-based materials with enhanced thermoelectric performances. *Nanotechnology*, 24:285702, 2013.

[55] K. F. Hsu, S. Loo, F. Guo, W. Chen, J. S. Dyck, C. Uher, T. Hogan, E. K. Polychroniadis, and M. G. Kanatzidis. Cubic $AgPb_mSbTe_{2+m}$: Bulk thermoelectric materials with high figure of merit. *Science*, 303:818–821, 2004.

[56] X. Shi, J. Yang, J. R. Salvador, M. Chi, J. Y. Cho, H. Wang, S. Bai, J. Yang, W. Zhang, and L. Chen. Multiple-filled skutterudites: High thermoelectric figure of merit through separately optimizing electrical and thermal transports. *J. Am. Chem. Soc.*, 133:7837–7846, 2011.

[57] M. Ohtaki, K. Araki, and K. Yamamoto. High thermoelectric performance of dually doped ZnO ceramics. *J. Electron. Mater.*, 38:1234–1238, 2009.

[58] J. Sui, J. Li, J. He, Y.-L. Pei, D. Berardan, H. Wu, N. Dragoe, W. Cai, and L.-D. Zhao. Texturation boosts the thermoelectric performance of BiCuSeO oxyselenides. *Energ. Environ. Sci.*, 6:2916–2920, 2013.

[59] Y. Liu, L.-D. Zhao, Y. Zhu, Y. Liu, F. Li, M. Yu, D.-B. Liu, W. Xu, Y.-H. Lin, and C.-W. Nan. Synergistically optimizing electrical and thermal transport properties of BiCuSeO via a dual-doping approach. *Adv. Energy Mater.*, 6:1502423, 2016.

[60] M. Bittner, N. Kanas, R. Hinterding, F. Steinbach, D. Groeneveld, P. Wemhoff, K. Wiik, M.-A. Einarsrud, and A. Feldhoff. Triple-phase ceramic 2D nanocomposite with enhanced thermoelectric properties. *submitted to J. Eur. Ceram. Soc.*, 2018.

[61] Q. Zhu, E. M. Hopper, B. J. Ingram, and T. O. Mason. Combined Jonker and Ioffe analysis of oxide conductors and semiconductors. *J. Am. Ceram. Soc.*, 94:187–193, 2011.

[62] M. Bittner, L. Helmich, F. Nietschke, B. Geppert, O. Oeckler, and A. Feldhoff. Porous $Ca_3Co_4O_9$ with enhanced thermoelectric properties derived from sol-gel synthesis. *J. Eur. Ceram. Soc.*, 37:3909–3915, 2017.

[63] N. Kanas, M. Bittner, T. D. Desissa, S. P. Singh, T. Norby, A. Feldhoff, T. Grande, K. Wiik, and M.-A. Einarsrud. All-oxide thermoelectric module with in-situ formed non-rectifying complex p-p-n junction and transverse thermoelectric effect. *submitted to ACS Omega*, 2018.

[64] D. Bérardan, E. Guilmeau, A. Maignan, and B. Raveau. Enhancement of the thermoelectric performances of In_2O_3 by the coupled substitution of M^{2+}/Sn^{4+} for In^{3+}. *J. Appl. Phys.*, 104:064918–1–064918–5, 2008.

[65] E. Guilmeau, D. Bérardan, C. Simon, A. Maignan, B. Raveau, D. Ovono Ovono, and F. Delorme. Tuning the transport and thermoelectric properties of In_2O_3 bulk ceramics through doping at In-site. *J. Appl. Phys.*, 106:053715–1–053715–7, 2009.

[66] D. Bérardan, E. Guilmeau, A. Maignan, and B. Raveau. $In_{2-x}Ge_xO_3$:Ge a promising n-type thermoelectric oxide composite. *Solid State Commun.*, 146:97–101, 2008.

[67] Y. L. Yan and Y. X. Wang. Electronic structure and low temperature thermoelectric properties of $In_{24}M_8O_{48}$ (M = $Ge^{4+}, Sn^{4+}, Ti^{4+}$, and Zr^{4+}). *J. Comput. Chem.*, 33:88–92, 2012.

[68] M. Ohtaki, D. Ogura, K. Eguchi, and H. Arai. High-temperature thermoelectric properties of In_2O_3-based mixed oxides and their applicability to thermoelectric power generation. *J. Mater. Chem.*, 4(5):653–656, 1994.

[69] Y. Liu, W. Xu, D.-B. Liu, M. Yu, Y.-H. Lin, and C.-W. Nan. Enhanced thermoelectric properties of Ga-doped In_2O_3 ceramics via synergistic band gap engineering and phonon suppression. *Phys. Chem. Chem. Phys.*, 17:11229–11233, 2015.

[70] B. Zhu, R. Tian, T. Zhang, R. Donelson, T. T. Tan, Y. Wang, and S. Li. Tunable thermopower and thermal conductivity in Lu doped In_2O_3. *RSC Adv.*, 4:31926–31931, 2014.

[71] B. Cheng, H. Fang, J. Lan, Y. Liu, Y.-H. Lin, and C.-W. Nan. Thermoelectric performance of Zn and Ge co-doped In_2O_3 fine-grained ceramics by spark plasma sintering. *J. Am. Ceram. Soc.*, 94:2279–2281, 2011.

[72] J.-L. Lan, Y. Liu, Y.-H. Lin, C.-W. Nan, and X. Yang. Enhanced thermoelectric performance of In_2O_3-based ceramics via nanostructuring and point defect engineering. *Sci. Rep.*, 5:7783, 2014.

[73] E. Combe, S. D. Bhame, E. Guilmeau, F. Boschini, and R. Cloots. Synthesis of $In_{2-x}Ge_xO_3$ nanopowders for thermoelectric applications. *J. Mater. Res.*, 27:500–505, 2012.

[74] J. Lan, Y.-H. Lin, Y. Liu, S. Xu, and C.-W. Nan. High thermoelectric performance of nanostructured In_2O_3-based ceramics. *J. Am. Ceram. Soc.*, 95:2465–2469, 2012.

[75] E. Combe, C. Chubilleau, D. Berardan, E. Guilmeau, A. Maignan, and B. Raveau. Citrate gel process and thermoelectric properties of Ge-doped In_2O_3 bulk ceramics. *Powder Technol.*, 208:503–508, 2011.

[76] M. Amani, I. M. Tougas, O. J. Gregory, and G. C. Fralick. High-temperature thermoelectric properties of compounds in the system $Zn_xIn_yO_{x+1.5y}$. *J. Electron. Mater.*, 42:114–119, 2013.

[77] L. M. Wang, C.-Y. Chang, S.-T. Yeh, S. W. Chen, Z. A. Peng, S. C. Bair, D. S. Lee, F. C. Liao, and Y. K. Kuo. Synthesis and post-annealing effects on the transport properties of thermoelectric oxide $(ZnO)_m In_2O_3$ ceramics. *Ceram. Int.*, 42:114–119, 2012.

[78] V. M. Goldschmidt. *Naturwissenschaften.* Springer-Verlag, https://doi.org/10.1007/BF01507527, 14th edition, 1926.

[79] H. Taguchi, M. Nagao, T. Sato, and M. Shimada. High-temperature phase transition of $CaMnO_{3-\delta}$. *J. Solid State Chem.*, 78:313–315, 1989.

[80] M. Ohtaki, H. Koga, T. Tokunaga, K. Eguchi, and H. Arai. Electrical transport properties and high-temperature thermoelectric performance of $(Ca_{0.9}M_{0.1)}MnO_3$ (M = Y, La, Ce, Sm, In, Sn, Sb, Pb, Bi). *J. Solid State Chem.*, 120:105–111, 1995.

[81] M. Schrade, R. Kabir, S. Li, T. Norby, and T. G. Finstad. High temperature transport properties of thermoelectric $CaMnO_{3-\delta}$ - indication of strongly interacting small polarons. *J. Appl. Phys.*, 115:103705–1–103705–7, 2014.

[82] J. Briático, B. Alascio, R. Allub, A. Butera, A. Caneiro, M. T. Causa, and M. Tovar. Double-exchange interaction in electron-doped $CaMnO_{3-\delta}$ perovskites. *Phys. Rev. B*, 53:14020–14023, 1996.

[83] M. Molinari, D. A. Tompsett, S. C. Parker, F. Azough, and R. Freer. Structural, electronic and thermoelectric behaviour of $CaMnO_3$ and $CaMnO_{(3-\delta)}$. *J. Mater. Chem. A*, 2:14109–14117, 2014.

[84] Y. Wang, Y. Sui, H. Fan, X. Wang, Y. Su, W. Su, and X. Liu. High temperature thermoelectric response of electron-doped $CaMnO_3$. *Chem. Mater.*, 21:4653–4660, 2009.

[85] J. W. Park, D. H. Kwak, S. H. Yoon, and S. C. Choi. Thermoelectric properties of Bi, Nb co-substituted $CaMnO_3$ at high temperature. *J. Alloys Compd.*, 487:550–555, 2009.

[86] S.-M. Choi, C.-H. Lim, and W.-S. Seo. Thermoelectric properties of the $Ca_{1-x}R_xMnO_3$ perovskite system (R: Pr, Nd, Sm) for high-temperature applications. *J. Electron. Mater.*, 40:551–556, 2010.

[87] L. Bocher, M. H. Aguirre, D. Logvinovich, A. Shkabko, R. Robert, M. Trottmann, and A. Weidenkaff. $CaMn_{1-x}Nb_xO_3$ ($x \leq 0.08$) perovskite-type phases as promising new high-temperature n-type thermoelectric materials. *Inorg. Chem.*, 47:8077–8085, 2008.

[88] L. Bocher, M. H. Aguirre, R. Robert, D. Logvinovich, S. Bakardjieva, J. Hejtmanek, and A. Weidenkaff. High-temperature stability, structure and thermoelectric properties of $CaMn_{1-x}Nb_xO_3$ phases. *Acta Mater.*, 57:5667–5680, 2009.

[89] Y.-H. Zhu, W.-B. Su, J. Liu, Y.-C. Zhou, J. Li, X. Zhang, Y. Du, and C.-L. Wang. Effects of Dy and Yb co-doping on thermoelectric properties of $CaMnO_3$ ceramics. *Ceram. Int.*, 41:1535–1539, 2015.

[90] G. Xu, R. Funahashi, Q. Pu, B. Liu, R. Tao, G. Wang, and Z. Ding. High-temperature transport properties of Nb and Ta substituted $CaMnO_3$ system. *Solid State Ionics*, 171:147–151, 2004.

[91] P. Thiel, S. Populoh, S. Yoon, G. Saucke, K. Rubenis, and A. Weidenkaff. Charge-carrier hopping in highly conductive $CaMn_{1-x}M_xO_{3-\delta}$ thermoelectrics. *J. Phys. Chem. C*, 119:21860–21867, 2015.

[92] R. Kabir, T. Zhang, D. Wang, R. Donelson, R. Tian, T. T. Tan, and S. Li. Improvement in the thermoelectric properties of $CaMnO_3$ perovskites by W doping. *J. Mater. Sci.*, 49:7522–7528, 2014.

[93] H. Kawikami, M. Saito, H. Takemoto, H. Yamamura, Y. Isoda, and Y. Shinohara. Thermoelectric properties of perovskite-type oxide Ca-Mn-O system in relation to A-site vacancies. *Mater. Trans.*, 54:1818–1822, 2013.

[94] J. G. Noudem, S. Quetel-Weben, R. Retoux, G. Chevallier, and C. Estournès. Thermoelectric properties of $Ca_{0.9}Yb_{0.1}MnO_{3-x}$ prepared by spark plasma sintering in air atmosphere. *Scripta Mater.*, 68:949–952, 2013.

[95] L. Viciu, J. W. G. Bos, H. W. Zandbergen, Q. Huang, M. L. Foo, S. Ishiwata, A. P. Ramirez, M. Lee, N. P. Ong, and R. J. Cava. Crystal structure and elementary properties of Na_xCoO_2 (x = 0.32, 0.51, 0.6, 0.75, and 0.92) in the three-layer $NaCoO_2$ family. *Phys. Rev. B*, 73:174104–1–174104–10, 2006.

[96] K. Fujita, T. Mochida, and K. Nakamura. High-temperature thermoelectric properties of $Na_xCoO_{2-\delta}$ single crystals. *Jpn. J. Appl. Phys.*, 40:4644–4647, 2001.

[97] J.-Y. Tak, K. H. Lee, J.-Y. Kim, C.-H. Lim, W.-S. Seo, Y. S. Lim, H. K. Cho, and S.-M. Choi. Optimization of synthesis conditions of $Na_{0.75}CoO_2$ for high thermoelectric performance. *J. Electron. Mater.*, 44:1408–1412, 2014.

[98] M. Mikami, M. Yoshimura, Y. Mori, T. Sasaki, R. Funahashi, and M. Shikano. Thermoelectric properties of two Na_xCoO_2 crystallographic phases. *Jpn. J. Appl. Phys.*, 42:7383–7386, 2003.

[99] M. Lee, L. Viciu, Y. Wang, M. L. Foo, S. Watauchi, R. A. Pascal JR, R. J. Cava, and N. P. Ong. Large enhancement of the thermopower in Na_xCoO_2 at high Na doping. *Nat. Mater.*, 5:537–540, 2006.

[100] Y. Miyazaki. Crystal structure and thermoelectric properties of the misfit-layered cobalt oxides. *Solid State Ionics*, 172:463–467, 2004.

[101] Y. Miyazaki, M. Onoda, T. Oku, M. Kikuchi, Y. Ishii, Y. Ono, Y. Morii, and T. Kajitani. Modulated structure of thermoelectric compound $[Ca_2CoO_3]$ CoO_2. *J. Phys. Soc. Jpn.*, 71:491–497, 2002.

[102] Y. Wang, Y. Sui, P. Ren, L. Wang, X. Wang, W. Su, and H. Fan. Strongly correlated properties and enhanced thermoelectric response in $Ca_3Co_{4-x}M_xO_9$ (M = Fe, Mn, and Cu). *Chem. Mater.*, 22:1155–1163, 2010.

[103] N. Kanas, S. P. Singh, M. Rotan, M. Saleemi, M. Bittner, A. Feldhoff, T. Norby, K. Wiik, T. Grande, and M.-A. Einarsrud. Influence of processing on stability, microstructure and thermoelectric properties of $Ca_3Co_{4-x}O_{9+\delta}$. *J. Eur. Ceram. Soc.*, 38:1592–1599, 2018.

[104] C. S. Huang, F. P. Zhang, X. Zhang, Q. M. Lu, J. X. Zhang, and Z. Y. Liu. Enhanced thermoelectric figure of merit through electrical and thermal transport modulation by dual-doping and texture modulating for $Ca_3Co_4O_{9+\delta}$ oxide materials. *J. Alloy. Compd.*, 687:87–94, 2016.

[105] I. V. Matsukevich, A. I. Klyndyuk, E. A. Tugova, A. N. Kovalenko, A. A. Marova, and N. S. Krasutskaya. Thermoelectric properties of $Ca_{3-x}Bi_xCo_4O_{9+delta}$ ($0.0 \leq x \leq 1.5$) ceramics. *Inorg. Mater+.*, 52:644–650, 2016.

[106] F. Delorme, P. Diaz-Chao, E. Guilmeau, and F. Giovannelli. Thermoelectric properties of $Ca_3Co_4O_9$-Co_3O_4 composites. *Ceram. Int.*, 41:10038–10043, 2015.

[107] Y. Liu, Y. Lin, Z. Shi, and C. W. Nan. Preparation of $Ca_3Co_4O_9$ and improvement of its thermoelectric properties by spark plasma sintering. *J. Am. Ceram. Soc.*, 88:1337–1340, 2005.

[108] D. Kenfaui, G. Bonnefont, D. Chateigner, G. Fantozzi, M. Gomina, and J. G. Noudem. $Ca_3Co_4O_9$ ceramics consolidated by SPS process: Optimisation of mechanical and thermoelectric properties. *Mater. Res. Bull.*, 45:1240–1249, 2010.

[109] J.-W. Moon, D. Nagahama, Y. Masuda, W.-S. Seo, and K. Koumoto. Anisotropic thermoelectric properties of crystal-axis oriented ceramics of layer-structured oxide in the Ca-Co-O system. *J. Ceram. Soc. Jpn.*, 109:647–650, 2001.

[110] D. Kenfaui, B. Lenoir, D. Chateigner, B. Ouladdiaf, M. Gomina, and J. G. Noudem. Development of multilayer textured $Ca_3Co_4O_9$ materials for thermoelectric generators: Influence of the anisotropy on the transport properties. *J. Eur. Ceram. Soc.*, 32:2405–2414, 2012.

[111] D. Kenfaui, D. Chateigner, M. Gomina, J. G. Noudem, B. Ouladdiaf, A. Dauschner, and B. Lenoir. Volume texture and anisotropic thermoelectric properties in $Ca_3Co_4O_9$ bulk materials. *Mater. Today.*, 2:637–646, 2015.

[112] C.-H. Lim, H.-H. Park, S.-M. Choi, K.-H. Lee, and K. Park. Anisotropy of the thermoelectric figure of merit (ZT) in textured $Ca_3Co_4O_9$ ceramics prepared by using a spark plasma sintering process. *J. Korean. Phys. Soc.*, 66:794–799, 2015.

[113] H. Leligny, D. Grebille, O. Pérez, A. C. Masset, M. Hervieu, and B. Raveau. A five-dimensional structural investigation of the misfit layer compound $[Bi_{0.87}SrO_2]_2[CoO_2]_{1.82}$. *Acta Cryst. B*, B56:173–182, 2000.

[114] D. Grebille, H. Muguerra, O. Pérez, E. Guilmeau, H. Rousselière, and R. Funahashi. Superspace crystal symmetry of thermoelectric misfit cobalt oxides and predicted structural models. *Acta Cryst.*, B63:373–383, 2007.

[115] H. Muguerra, D. Grebille, E. Guilmeau, and R. Cloots. Modulated misfit structure of the thermoelectric $[Bi_{0.84}CoO_2][CoO_2]_{1.69}$ cobalt oxide. *Inorg. Chem.*, 47:2464–2471, 2008.

[116] E. Guilmeau, M. Pollet, D. Grebille, M. Hervieu, M. Muguerra, R. Cloots, M. Mikami, and R. Funahashi. Nanoblock coupling effect in iodine intercalated $[Bi_{0.82}CaO_2]_2[CoO_2]_{1.69}$ layered cobaltite. *Inorg. Chem.*, 46:2124–2131, 2007.

[117] A. Sotelo, E. Guilmeau, S. Rasekh, M. A. Madre, S. Marinel, and J. C. Diez. Enhancement of the thermoelectric properties of directionally grown Bi-Ca-Co-O through Pb for Bi substitution. *J. Eur. Ceram. Soc.*, 30:1815–1820, 2010.

[118] A. Feldhoff, M. Arnold, J. Martynczuk, Th. M. Gesing, and H. Wang. The sol-gel synthesis of perovskites by EDTA/citrite complexing method involves nanoscale solid state reactions. *Solid State Sci.*, 10:689–701, 2008.

[119] J. G. Noudem, D. Kenfaui, D. Chateigner, and M. Gomina. Toward the enhancement of thermoelectric properties of lamellar $Ca_3Co_4O_9$ by edge-free spark plasma texturing. *Scripta Mater.*, 66:258–260, 2012.

[120] Y. Wang, Y. Sui, X. Wang, W. Su, and X. Liu. Enhanced high temperature thermoelectric characteristics of transition metals doped $Ca_3Co_4O_{9+\delta}$ by cold high-pressure fabrication. *J. Appl. Phys.*, 107:033708, 2010.

[121] S. Urata, R. Funahashi, T. Mihara, A. Kosuga, S. Sodeoka, and T. Tanaka. Power generation of a p-type $Ca_3Co_4O_9$/n-type $CaMnO_3$ module. *Int. J. Appl. Ceram. Technol.*, 4:535–540, 2007.

[122] L. Francioso, C. De Pascali, I. Farella, C. Martucci, P. Cretì, P. Siciliano, and A. Perrone. Flexible thermoelectric generator for ambient assisted living wearable biometric sensors. *J. Power Sources*, 196:3239–3243, 2011.

[123] I. Matsubara, R. Funahashi, T. Takeuchi, S. Sodeoka, T. Shimizu, and K. Ueno. Fabrication of an all-oxide thermoelectric power generator. *Appl. Phys. Lett.*, 78:3627–3629, 2001.

[124] E. S. Reddy, J. G. Noudem, S. Hebert, and C. Goupil. Fabrication and properties of four-leg oxide thermoelectric modules. *J. Phys. D: Appl. Phys.*, 38:3751–3755, 2005.

[125] S. Lemonnier, C. Goupil, J. Noudem, and E. Guilmeau. Four-leg $Ca_{0.95}Sm_{0.05}MnO_3$ unileg thermoelectric device. *J. Appl. Phys.*, 104:014505–1–014505–4, 2008.

[126] J. G. Noudem, S. Lemonnier, M. Prevel, E. S. Reddy, E. Guilmeau, and C. Goupil. Thermoelectric ceramics for generators. *J. Eur. Ceram. Soc.*, 28:41–48, 2008.

[127] P. Tomeš, R. Robert, M. Trottmann, L. Bocher, M. H. Aguirre, A. Bitschi, J. Hejtmánek, and A. Weidenkaff. Synthesis and characterization of new ceramic thermoelectrics implemented in a thermoelectric oxide module. *J. Electron. Mater.*, 99:1696–1703, 2010.

[128] C.-G. Lim, S.-M. Choi, W.-S. Seo, and H.-H. Park. A power-generation test for oxide-based thermoelectric modules using p-type $Ca_3Co_4O_9$ and n-type $Ca_{0.9}Nd_{0.1}MnO_3$ legs. *J. Electron. Mater.*, 41:1247–1255, 2011.

[129] L. Han, Y. Jiang, S. Li, H. Su, X. Lan, K. Qin, T. Han, H. Zhong, L. Chen, and D. Yu. High temperature thermoelectric properties and energy transfer devices of $Ca_3Co_{4-x}Ag_xO_9$ and $Ca_{1-y}Sm_yMnO_3$. *J. Alloys Compd.*, 509:8970–8977, 2011.

[130] S. M. Choi, K. H. Lee, C. H. Lim, and W. S. Seo. Oxide-based thermoelectric power generation module using p-type $Ca_3Co_4O_9$ and n-type $(ZnO)_7In_2O_3$ legs. *Energ. Convers. Manage.*, 52:335–339, 2011.

[131] A. Inagoya, D. Sawaki, Y. Horiuchi, S. Urata, R. Funahashi, and I. Terasaki. Thermoelectric module made of perovskite cobalt oxides with large thermopower. *J. Appl. Phys.*, 110:123712–1–123712–4, 2011.

[132] N. V. Van and N. Pryds. Nanostructured oxide materials and modules for high-temperature power generation from waste heat. *Adv. Nat. Sci. : Nanosci. Nanotechnol.*, 4:023002, 2013.

[133] K. Park and G. W. Lee. Fabrication and thermoelectric power of Π-shaped $Ca_3Co_4O_9/CaMnO_3$ modules for renewable energy conversion. *Energy*, 60:87–93, 2013.

[134] T. Seetawan, K. Singsoog, S. Srichai, C. Thanachayanont, V. Amornkitbamrung, and P. Chindaprasirt. Thermoelectric energy conversion of p-$Ca_3Co_4O_9$/n-$CaMnO_3$ module. *Energy Procedia*, 61:1067–1070, 2014.

[135] K. Suemori, S. Hoshino, and T. Kamata. Flexible and lightweight thermoelectric generators composed of carbon nanotube-polystyrene composites printed on film substrate. *Appl. Phys. Lett.*, 103:153902–1–153902–4, 2013.

[136] B. Geppert and A. Feldhoff. An approach to a flexible thermoelectric generator farbicated using bulk materials. *EHS*, 3(2):161–171, 2016.

[137] B. Geppert, A. Brittner, L. Helmich, M. Bittner, and A. Feldhoff. Enhanced flexible thermoelectric generators based on oxide-metal composite materials. *J. Electron. Mater.*, 46:2356–2365, 2017.

[138] W. Glatz, S. Muntwyler, and C. Hierold. Optimization and fabrication of thick flexible polymer based micro thermoelectric generator. *Sens. Actuators, A*, 132:337–345, 2006.

[139] M. Feinaeugle, C. L. Sones, E. Koukharenko, and R. W. Eason. Fabrication of a thermoelectric generator on a polymer-coated substrate via laser-induced forward transfer of chalcogenide thin films. *Smart Mater. Struct.*, 22:115023, 2013.

[140] L. Stepien, A. Roch, S. Schlaier, I. Dani, A. Kiriy, F. Simon, M. v. Lukowicz, and C. Leyens. Investigation of the thermoelectric power factor of KOH-treated PEDOT:PSS dispersions for printing applications. *EHS*, 3(1):101–111, 2016.

[141] K. Takahashi, A. Sakai, T. Kanno, and H. Adachi. Tailoring of inclined crystal orientation in layered cobaltite thin films for the development of off-diagonal thermoelectric effect. *Appl. Phys. Lett.*, 95:051913, 2009.

[142] H. J. Goldsmid. Application of the transverse thermoelectric effects. *J. Electron. Mater.*, 40:1254–1259, 2010.

[143] W. Shin, N. Murayama, K. Ikeda, and S. Sago. Thermoelectric power generation using Li-doped NiO and $(Ba,Sr)PbO_3$ module. *J. Power Sources*, 103:80–85, 2001.

[144] R. Chavez, S. Angst, J. Hall, F. Maculewicz, J. Stoetzel, H. Wiggers, L. T. Hung, N. V. Nong, N. Pryds, G. Span, D. E. Wolf, R. Schmechel, and G. Schierning. Efficient p-n junction-based thermoelectric generator that can operate at extreme temperature conditions. *J. Phys. D: Appl. Phys.*, 51:014005, 2018.

2 Thermoelectric materials

2.1 Summary

Material research of high-power and high-zT p-type thermoelectric (TE) oxides is presented. The most promising p-type TE oxide $Ca_3Co_4O_9$ (CCO) for energy harvesting from infinite heat sources at high-temperatures in air is investigated in detail. The synthesis, processing and TE properties of pure CCO and triple-phase $Ca_3Co_4O_9$-Na_xCoO_2-$Bi_2Ca_2Co_2O_9$ (CCO-NCO-BCCO) nanocomposite powders and ceramics are explored and presented. Once the pure CCO was characterized, a co-doping approach was used to tune the charge carrier concentration and to introduce compositionally alloyed nano-structures in order to improve the thermoelectric properties of CCO via exceeding the solubility limit of dopants on the A-site of the CCO structure.

In section 2.2, sol-gel synthesis, growth mechanism and consequential TE transport properties of misfit-layered CCO are presented. Nano-sized intermediates during sol-gel synthesis of CCO were identified as a monoclinic $Ca_{1+x}Co_{1+y}O_{4-\delta}$ and an orthorhombic $CaCO_3$ phase. The sol-gel route formed nano-sized particles in the calcined CCO product powder. A subsequent processing of these nano-sized particles facilitated a ceramic of designed properties. The influence of porosity on the anisotropic TE properties of CCO was evaluated. A high porosity of CCO ceramics led to a low degree of grain orientation and thereby a subsequently low anisotropy. Moreover, the heat conductivity was significantly reduced due to the high porosity, which led to a high figure-of-merit zT.

In section 2.3, a triple-phase p-type CCO-NCO-BCCO nanocomposite was developed that exhibited a high TE power factor and figure-of-merit zT in the high-temperature range in air. The anisotropy (parallel and perpendicular to the pressing direction of the ceramic) of the TE properties was investigated. The nanocomposite ceramics were comprised of an all-scale hierarchical architecture of three misfit layered TE oxides, which were grown semi-coherently on each other. These nanocomposite ceramics had simultaneously enhanced values of the electrical conductivity and Seebeck coefficient. Furthermore, the thermally less stable TE phases NCO and BCCO could be stabilized at high temperatures in air. The synergistic influence of these phases was thereby utilized to increase the TE power factor of the nanocomposites at high temperatures in air. The high electrical conductivity and TE power factor (Ioffe plot) enabled an application for power generation at high temperature from infinite heat sources in air.

2.2 Porous Ca$_3$Co$_4$O$_9$ with enhanced thermoelectric properties derived from Sol-Gel synthesis

Michael Bittner, Lailah Helmich, Frederik Nietschke, Benjamin

Geppert, Oliver Oeckler, Armin Feldhoff

Porous Ca$_3$Co$_4$O$_9$ with enhanced thermoelectric properties derived from Sol–Gel synthesis[☆]

Michael Bittner[a,*], Lailah Helmich[a], Frederik Nietschke[b], Benjamin Geppert[a], Oliver Oeckler[b], Armin Feldhoff[a]

[a] *Institute of Physical Chemistry and Electrochemistry, Leibniz University Hannover, Germany*
[b] *Institute for Mineralogy, Crystallography and Materials Science, Leipzig University, Germany*

ARTICLE INFO

ABSTRACT

Highly porous Ca$_3$Co$_4$O$_9$ thermoelectric oxide ceramics for high-temperature application were fabricated by sol–gel synthesis and subsequent conventional sintering. Growth mechanism of misfit-layered Ca$_3$Co$_4$O$_9$ phase, from sol–gel synthesis educts and upcoming intermediates, was characterized by in-situ X-ray diffraction, scanning electron microscopy and transmission electron microscopy investigations. The Ca$_3$Co$_4$O$_9$ ceramic exhibits a relative density of 67.7%. Thermoelectric properties were measured from 373 K to 1073 K. At 1073 K a power factor of 2.46 µW cm^{-1} K^{-2}, a very low heat conductivity of 0.63 W m^{-1} K^{-1} and entropy conductivity of 0.61 mW m^{-1} K^{-2} were achieved. The maintained figure of merit ZT of 0.4 from sol–gel synthesized Ca$_3$Co$_4$O$_9$ is the highest obtained from conventional, non-doped Ca$_3$Co$_4$O$_9$. The high porosity and consequently reduced thermal conductivity leads to a high ZT value.

© 2017 Elsevier Ltd. All rights reserved.

1. Introduction

The ability to directly convert heat into electrical energy is an interesting field, from which thermoelectric materials got more and more attention. Thermoelectric power generation is a promising technology to exploit waste heat from power plants, industrial processes and combustion engines in automotive applications and thus to manage the challenge of climate change, sustained yield and reducing power consumption. To enhance the efficiency in power generation of a thermoelectric generator (TEG), thermoelectric research has focused on increasing the figure of merit ZT of the materials, which was originally derived in [1] and is shown in Eq. (1).

$$ZT := \frac{\sigma \cdot \alpha^2}{\Lambda} \qquad (1)$$

The relevant material specific parameters are the isothermal electrical conductivity σ, the Seebeck coefficient α and the electric open-circuit entropy conductivity Λ. The thermal energy ("heat") conductivity λ is related to the entropy conductivity Λ by Eq. (2); see [2,3]:

$$\lambda = T \cdot \Lambda \qquad (2)$$

Common materials used for thermoelectric purpose are alloys or intermetallic phases such as Bi$_2$Te$_3$, PbTe and SiGe [4–6]. These possess an iniquitous stability at high temperature (above 900 K), are toxic, consist of rare or expensive elements. To overcome these problems, thermoelectric oxides are supposed to be promising materials, due to their advantages, such as non-toxicity, thermal and mechanical stability at high temperature and moreover high chemical stability under oxidizing conditions [7]. Several publications focus on the layer-structured cobalt oxide Ca$_3$Co$_4$O$_9$ due to its high power factor $\sigma \cdot \alpha^2$ and thus the efficiency of TEGs made of it [8,9]. Ca$_3$Co$_4$O$_9$ is composed of a misfit-layered structure which crystallizes in the monoclinic system. It can be described as a CdI$_2$-type CoO$_2$ subsystem 1 with a triangular lattice and a layered rock-salt type section of three Ca$_2$CoO$_3$ units in the subsystem 2, which are stacked alternatingly along [001]. The two subsystems exhibit a different lattice parameter b [10]. The majority of publications dealing with synthesis and characterization of pure and doped Ca$_3$Co$_4$O$_9$ utilize the solid state reaction as a "top down" technique [11–14]. The synthesis of Ca$_3$Co$_4$O$_9$ via the solid state reaction has several disadvantages as complex proceedings, introduction of impurities due to incorporation of material from the ball mill during the milling process [15]. In this work, the sol–gel synthesis as a "bottom up" technique is investigated to synthesize porous p-type Ca$_3$Co$_4$O$_9$ for use in thermoelectric generators to overcome these challenges. The sol–gel synthesis thereby provides the possibility to intersperse the utilized cations on a molecular level as well

---

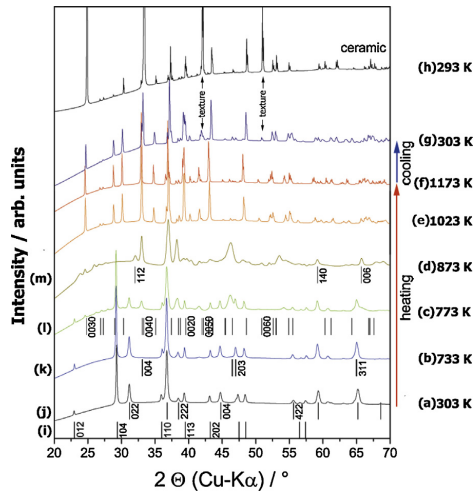[☆] Electronic Supplementary Information (ESI) available.
[*] Corresponding author.

Fig. 1. Rietveld refined structure data†: in-situ X-ray diffraction patterns of a $Ca_3Co_4O_9$ pre-calcined powder (a)–(g) measured during stepwise heating from 303 to 1173 and after cooling to 303 K; measurements at (a) 303 K, (b) 733 K, (c) 773 K, (d) 873 K, (e) 1023 K, (f) 1173 K and (g) 303 K. A sintered ceramic sample was measured at (h) 293 K, texture is visible and indicated (reflections 0050 and 0060). For clarity diffractograms are vertically shifted. The progress of in-situ XRD investigation is displayed with arrows for heating (red) and cooling (blue). Reflection positions and corresponding lattice planes of obtained phases (i)–(m) during in-situ measurement are shown: (i) $CaCO_3$ (trigonal structure); (j) Co_3O_4 (spinel structure); (k) $Ca_{1+x}Co_{1+y}O_{4-\delta}$ (monoclinic structure); (l) $Ca_3Co_4O_9$ (monoclinic structure); (m) $CaCO_3$ (orthorhombic structure); Reflections of $Ca_3Co_4O_9$ (l) correspond to superspace group Cm (0 1 - p 0), equivalent to Bm (0 0 γ), no. 8.3; [31]. Results of the quantitative analysis of different phases are shown in Table 1. (For interpretation of the references to color in this figure legend, the reader is referred to the web version of this article.)

as to introduce dopants into this composition [16]. Modifying the doping level enables various options to improve properties of thermoelectric materials [17]. Former work focused on dense $Ca_3Co_4O_9$ ceramics derived by the sol–gel synthesis and subsequent Spark Plasma Sintering (SPS) treatment [18,19]. More cost-efficient procedures are post-calcination or pressure-less sintering methods, in which $Ca_3Co_4O_9$ is heated above it's decomposition temperature followed by a re-oxidizing step (at 1173 K) [20,21]. Engineering the nano- and microstructure of a thermoelectric material by introduction of nanoparticles or by formation of a hierarchical architectures, can substantially improve the thermoelectric properties [22–24]. The implementation of scattering centers by nanoscale precipitates, interfaces or pores to decrease the fraction of lattice phonons to the heat conductivity λ, can contribute to enhance the figure of merit ZT of thermoelectric materials by significantly lowering the heat conductivity λ [25–27].

2. Materials and methods

$Ca_3Co_4O_9$ was synthesized via a sol–gel route, which allows obtaining fine-grained powders of homogeneous composition as previously described for perovskites [28]. The nitrates of according metal cations were stoichiometrically solved and added to an aqueous ammonia solution of pH 9 which also contained citric acid and EDTA for complexing the metal ions in the solution. Calcium(II) nitrate tetrahydrate 99.98% from Alfa Aesar and cobalt(II) nitrate hexahydrate ACS 98-102.00% from Alfa Aesar were used as sources. The gel was aged over night at 378 K. The aged gel was pre-calcined at 673 K until it stopped glowing combustion. To produce

a $Ca_3Co_4O_9$ ceramic, the obtained powder was ground and calcined for 10 h at 1023 K with a heating and cooling rate of 3 min K^{-1}, respectively. The calcined powder samples were ground again, cold pressed and sintered for 10 h at 1173 K with the same heating and cooling parameters. For in-situ X-ray diffraction (XRD) experiment, a pre-calcined sample was selected. All steps, i.e. synthesis, calcination and sintering, were performed under ambient air conditions.

The phase compositions of synthesized powders and sintered ceramics were characterized by XRD using a Bruker D8 Advance with Cu-K_α radiation. A time per step of 1.1 s, a step size of 0.003942° (2Θ), a voltage of 40 kV and a current of 40 mA were applied for XRD measurement. A XRD measurement of a pre-calcined powder sample was performed by an in-situ XRD setup for analysis of the calcination process and investigation of the growth mechanism of $Ca_3Co_4O_9$ from sol–gel synthesis. The in-situ setup consisted of a Anton Paar HTK 1200 N in-situ cell with an applied temperature range from 303 K to 1173 K, using synthetic air 100 ml min^{-1}, a time per step of 1.8 s, a step size of 0.009199° (2Θ), a voltage of 40 kV and a current of 40 mA. Rietveld refinements of the in-situ XRD investigations utilizing Topas 4.2 software were performed. Nano- and microstructural characterization was carried out by field-emission scanning electron microscope (FE-SEM) of the type JEOL JSM-6700F and by field-emission transmission electron microscope (FE-TEM) of the type JEOL JEM-2100F-UHR, which were equipped with an energy-dispersive X-ray spectrometer (EDXS) of the type Oxford Instruments INCA 300 for elemental analysis. For SEM investigations of the thermoelectric materials, the powders were dispersed on a carbon glue mount, the sintered ceramic was treated with a multistep polishing program followed by vibration polishing with a 50 nm Al_2O_3 polishing suspension. For TEM investigations, powders were dispersed on TEM-grids. Experimental data was used to sustain simulated Debye-Scherrer rings (rotational average) via Digital Micrograph software from Gatan. Density measurements were performed by an Archimedes setup using ISO 5018:1983 (the International Organization for Standardization) in which the dry mass, mass in solvent and wet mass of the sample, were estimated. The heat capacity C_p was measured by Differential Scanning Calorimetry (DSC) with a Netzsch STA 409 PC/PG in synthetic air atmosphere with 30 ml min^{-1} and 5 K min^{-1} heating rate within the range of 313 K to 1173 K. The system was calibrated with pure metal standards, and the sensitivity as a function of temperature of the apparatus was obtained by measuring sapphire standard from Netzsch under the same experimental conditions as for $Ca_3Co_4O_9$ sample. A ceramic DSC sample was cut out by an ultrasound cutter with a diameter of 5.2 mm for standard Al_2O_3 crucibles. The sensitivity ϵ and heat capacity C_p were estimated, using DSC measurements [29].

To determine the thermoelectric properties of the chosen materials, bar samples were cut from pellets regarding uniaxial pressing direction (parallel and perpendicular to pressing direction) using a precision vertical diamond wire saw from O'Well model 3242. Measurements of isothermal electrical conductivity σ, Seebeck coefficient α (on bar samples) and entropy conductivity Λ (on pellet samples) were carried out as a function of temperature. Thereby the power factor $\sigma \cdot \alpha^2$ and figure of merit ZT were estimated, respectively. The isothermal electrical conductivity σ was measured in a horizontal three-heating-zone tube furnace from Carbolite Gero EVZ 12/450B using a home-made measurement cell. The Seebeck coefficient α was measured with a ProboStat A setup from NorECs, the used furnace was an ELITE thermal system. The electronic parameters were logged by KEITHLEY 2100 $6\frac{1}{2}$ Digit Multimeters. Measurement data were acquired and converted using LAB VIEW software. The heat conductivity λ and entropy conductivity Λ were calculated from thermal diffusivity, obtained by a Linseis LFA 1000 setup equipped with an InSb detector and carbon-coated samples under helium atmosphere, heat capacity C_p and density, measure-

ments. Simultaneous heat loss and finite pulse corrections were corrected using Dusza's model [30]. Values were averaged from five measurement points at each temperature.

3. Results and discussion

To verify the crystal structure and phase purity of powders and ceramics, XRD analysis were carried out. The $Ca_3Co_4O_9$ powder obtained after pre-calcination from glowing combustion at 673 K consists of a mixture of calcite $CaCO_3$ and Co_3O_4, shown in Fig. 1a (black pattern). An in-situ XRD measurement was carried out beginning with the pre-calcined powder at 303 K. Table 1 shows the compositions obtained from Rietveld refinements[†] of the powder at different temperatures within the applied temperature range from 303 K (Fig. 1a) to 1173 K (Fig. 1f). The percentage of $Ca_3Co_4O_9$ phase in the obtained powder increased in the range from 773 K (Fig. 1c) to 1173 K (Fig. 1f). A monoclinic $Ca_{1+x}Co_{1+y}O_{4-\delta}$ phase starts to form at about 733 K (Fig. 1b, blue pattern). The $Ca_3Co_4O_9$ phase principally starts to form between 733 (Fig. 1b) and 773 K (Fig. 1c) due to the decomposition of $CaCO_3$ and its coalescence with Co_3O_4 forming the monoclinic $Ca_{1+x}Co_{1+y}O_{4-\delta}$ phase and $Ca_3Co_4O_9$ sheets, shown in Fig. 2 (blue and green pattern). In the temperature range from 733 K (Fig. 1b) to 873 K (Fig. 1d) there is an intermediate phase composition consisting of $Ca_{1+x}Co_{1+y}O_{4-\delta}$, Co_3O_4, calcite (trigonal) $CaCO_3$, vaterite (orthorhombic) $CaCO_3$ and $Ca_3Co_4O_9$ present, shown in Fig. 1d (dark yellow pattern). During heating from 303 K (Fig. 1a) to 873 K (Fig. 1d), the calcite $CaCO_3$ phase is incorporated and partly transformed to the less dense vaterite $CaCO_3$ phase until it is completely embedded at 1023 K (Fig. 1e). From 1023 K (Fig. 1e) on, the intermediates decompose and coalesce with Co_3O_4 until an almost phase pure $Ca_3Co_4O_9$ sample is preserved for the 303 K (Fig. 1g, dark blue pattern) measurement after conducted in-situ investigation. After cold pressing and sintering at 1173 K for 10 h, a nearly pure $Ca_3Co_4O_9$ ceramic is obtained which however shows texture. Texture is visible by changes in relative intensities of reflections 0050 and 0060 in Fig. 1h (black pattern, ceramic).

Based on [10], a Rietveld refinement was performed to analyze the $Ca_3Co_4O_9$ ceramic. The best results were accomplished for superspace group Cm (0 1 - p 0), equivalent to Bm (0 0 γ) [31], the metrics is monoclinic base-centered with a = 4.84 Å, c = 10.84 Å, β = 96.11°. The lattice parameter was refined to be b_1 = 2.82 Å for the CoO_2 subsystem and b_2 = 4.55 Å for the Ca_2CoO_3 subsystem [10].

The SEM investigations shown in Fig. 2a and b of the $Ca_3Co_4O_9$ powder samples reveal the growth mechanism of synthesized powders by sol–gel synthesis. An adsorption mechanism and incorporation of small spherical particles into already existing $Ca_3Co_4O_9$ sheets is observed. The small Co_3O_4 particles are attached to the sheet. The SEM investigations of the $Ca_3Co_4O_9$ polished sample shown in Fig. 2c–e exhibit no visible grain distribution of the p-type material. The sintered $Ca_3Co_4O_9$ ceramic shows a high porosity with a connected pore network. The network consists of two alternating areas, the first region shown in Fig. 2c of coalesced $Ca_3Co_4O_9$ sheets and of the second region, consisting of separated $Ca_3Co_4O_9$ sheets which are disconnected by Co_3O_4 grains, shown in Fig. 2d and e. Fig. 2f shows an EDXS element distribution mapping of the $Ca_3Co_4O_9$ sheets (red and green) and the Co_3O_4 grains (green), compare with Fig. 2e.

TEM investigations were conducted to examine growth mechanism of $Ca_3Co_4O_9$ from sol–gel synthesis as well as composition of grown phases after pre-calcination at 673 K and after calcination at 1023 K for 10 h, shown in Fig. 3a–i. SEM analysis suggest the presence of a Co-rich phase, but XRD measurements could not certainly verify the composition of this phase, due to the overlap of reflections of cobalt oxides and $Ca_3Co_4O_9$. For this reason, TEM analysis

was necessary to confirm phase composition of pre- and calcined powders. Fig. 3a and b shows a STEM image and EDXS element distribution of Ca (red) and Co (green) of a pre-calcined powder sample, compare also with Fig. 2a. A selected area electron diffraction (SAED) measurement of the area shown in Fig. 3a is revealed in Fig. 3c and d. A corresponding radial intensity distribution is indicated in Fig. 3e with marked indices and lattice spacings. The pre-calcined powder consists of as identified nano-grained $CaCO_3$ and Co_3O_4, see Fig. 3a and b, thereby the Co_3O_4 crystallites are bigger than the $CaCO_3$ particles. The $CaCO_3$ particles thereby possess no distinct shape. Electron diffraction measurements in Fig. 3c and d confirm the results from in-situ XRD investigations in Fig. 1a, the pre-calcined $Ca_3Co_4O_9$ powder consists of nanocrystalline $CaCO_3$ and Co_3O_4.

Fig. 3f and g show a STEM image and EDXS element distribution of Ca (red) and Co (green) of a calcined powder sample, 10 h at 1023 K; cobalt-rich and calcium-rich regions are visible, maybe this can be attributed to an island growth mechanism, compare with Fig. 2b. Position 1 (green) and 2 (red) indicate a cobalt-rich region and a grown $Ca_3Co_4O_9$ sheet, electron energy-loss spectroscopy (EELS) measurements were carried out for these positions, shown in Fig. 3h and i. To verify the composition of the cobalt-rich material, EELS measurements of the oxygen and cobalt fine structure at position 1 and possible cobalt oxides, as references, were conducted, indicated in Fig. 3i. The oxygen fine structures of region 1 and Co_3O_4 (ref.) match, illustrating there is still Co_3O_4 present after calcination, this can be also confirmed by XRD investigations, see Fig. 1 and Table 1. Full range EELS measurements are shown in Fig. 3h and exhibit the Ca-L edge (348 eV), O-K edge (532 eV) and Co-L edge (787 eV) of $Ca_3Co_4O_9$ at position 2 (red) and O-K edge, Co-L edge but no Ca-peak at position 1 (green). In comparison to $CaCO_3$, relatively large Co_3O_4 particles derail the growth of $Ca_3Co_4O_9$ sheets, due to a slow inter diffusion, Co_3O_4 crystals are accumulated at the end of the sheet, compare Fig. 3a and f.

The calcined powder, shown in Fig. 2b and Fig. 3f, was pressed into pellets and subsequently sintered. The sintered $Ca_3Co_4O_9$ sample achieved a relative density (compared to theoretical density) of 67.7%. Table 2 shows the estimated values for the density of the bulk ceramic as well as calculated values for open porosity, true porosity and closed porosity for a $Ca_3Co_4O_9$ ceramic.

These investigations confirm the SEM analysis. $Ca_3Co_4O_9$ possesses a low theoretical density, a high open porosity and almost no closed porosity. This reveals that there is a connected network existing between the pores.

Fig. 4c illustrates the measured heat capacities as a function of temperature in the range from 313 K to 1173 K. The heat capacity reaches 0.863 J g^{-1} K^{-1} at 1073 K. The trend and values of the heat capacity as a function of temperature is similar to the values reported in [29] and is corresponding to Debye-Einstein behavior.

Fig. 4a shows the measured values for σ and α of a $Ca_3Co_4O_9$ ceramic as a function of temperature and direction, parallel to pressing direction open symbols and perpendicular closed symbols, due to an obtained texture, see Figs. 1 and 2. The isothermal electrical conductivity σ of a $Ca_3Co_4O_9$ ceramic is almost constant over the whole temperature range and reaches 48.4 (open square) and 58.3 (closed square) S cm^{-1} at 1073 K. The Seebeck coefficient α of a $Ca_3Co_4O_9$ ceramic increases from 373 to 1073 K and reaches 225.3 (open circle) and 210.1 (closed circle) μV K^{-1} at the highest temperature. The isothermal electrical conductivity σ of $Ca_3Co_4O_9$ deviates in absolute values, due to a lower density of the ceramic, compared to other articles [32,33]. The trend of the Seebeck coefficient α proceeds similarly and ends also at comparable values [34,32]. The values for the power factor of a $Ca_3Co_4O_9$ ceramic, calculated from σ and α are shown in Fig. 4d. The course of σ and α on the basis of direction and texture (parallel and perpendicular to pressing direction) is similar but shifted to lower and higher values,

Table 1
XRD investigations of a powder (in-situ) and ceramic (ex-situ) sample: calculated fractions of existing phases, obtained by quantitative analysis from Rietveld refinements[†], see Fig. 1. ICSD: Co_3O_4 – 69374, calcite $CaCO_3$ – 16710, $Ca_{1+x}Co_{1+y}O_{4-\delta}$ – 55459, vaterite $CaCO_3$ – 157302, $Ca_3Co_4O_9$ – [10].

	Temperature/K	Co_3O_4/wt%	calcite $CaCO_3$/wt%	$Ca_{1+x}Co_{1+y}O_{4-\delta}$/wt%	vaterite $CaCO_3$/wt%	$Ca_3Co_4O_9$/wt%
in-situ XRD of powder	303	53.0	46.9	/	/	/
	733	55.2	43.1	1.6	/	/
	773	31.8	34.8	13.5	/	19.8
	873	13.0	/	21.1	4.6	61.2
	1023	5.35	/	/	/	94.6
	1173	5.4	/	/	/	94.5
	303	4.0	/	/	/	95.9
Ceramic	293	3.5	/	/	/	96.5

pre-calcined powder   calcined powder
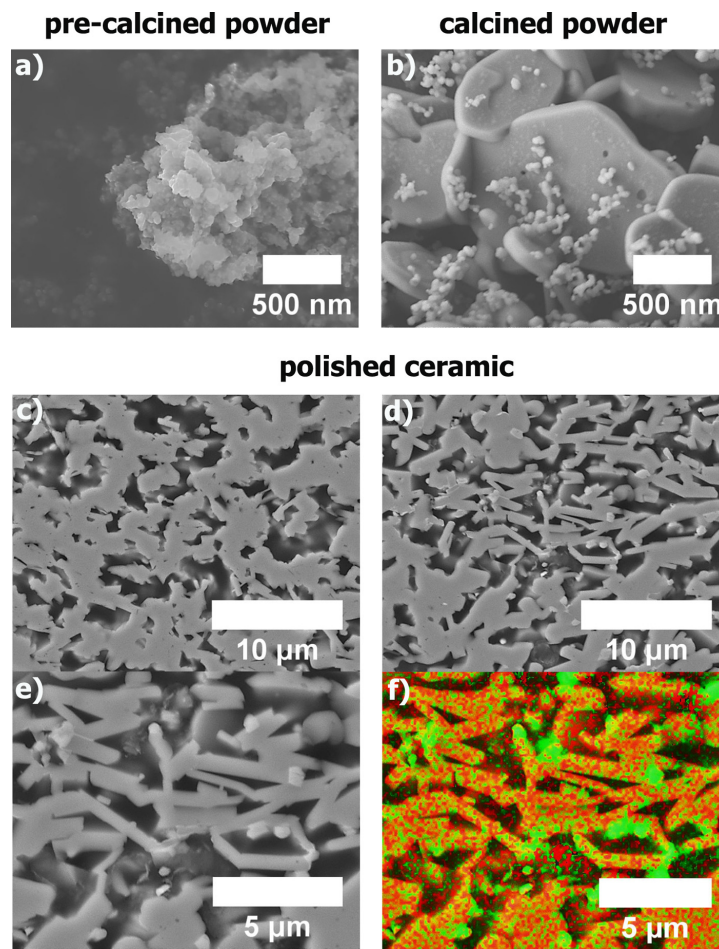
polished ceramic

Fig. 2. SEM micrographs of $Ca_3Co_4O_9$ powder and ceramic samples: (a) pre-calcined powder. (b) calcined powder, 10 h at 1023 K. (c–f) different areas of a polished ceramic, 10 h at 1173 K and EDXS element distribution mapping of the shown scope (Ca-red and Co-green). (For interpretation of the references to color in this figure legend, the reader is referred to the web version of this article.)

Table 2
Measured values of density $Ca_3Co_4O_9$ ceramic (10 h at 1173 K), using ISO 5018:1983 (the International Organization for Standardization). Uncertainties are indicated.

Material	Bulk density/g cm^{-3}	Theoretical density/g cm^{-3}	Open porosity/%	Closed porosity/%	True porosity/%
$Ca_3Co_4O_9$	3.17 ± 0.05	4.68	33.3 ± 0.36	0.2 ± 1.07	33.5 ± 0.7
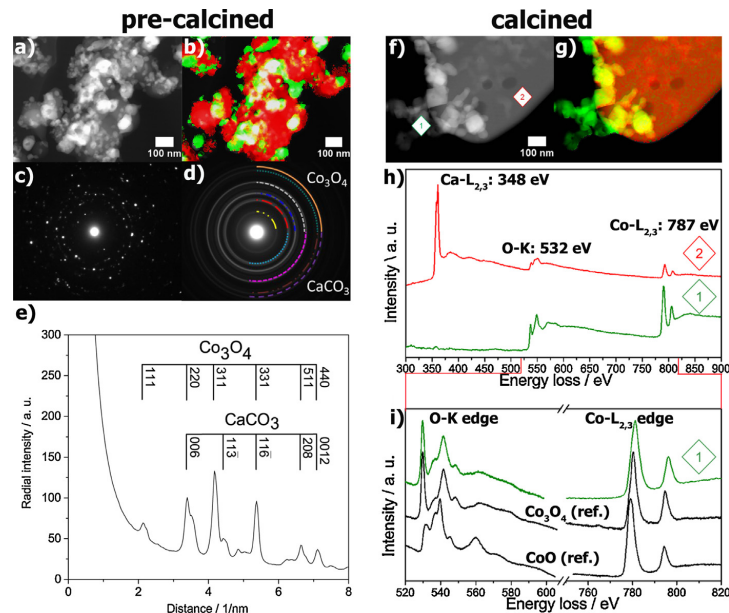
Fig. 3. TEM analysis of $Ca_3Co_4O_9$ growth mechanism: (a and b) STEM dark-field micrograph and EDXS elemental distribution of Ca (red) and Co (green) of the shown scope of a pre-calcined powder. (c and d) selected area electron diffraction (SAED) with a diameter of selected area of 550 nm, experimental and simulated Debye-Scherrer rings. (e) Radial intensity distribution with indicated Laue indices of calcite $CaCO_3$ and Co_3O_4 of the pre-calcined powder. (f and g) STEM micrograph, EDXS elemental distribution of Ca (red) and Co (green) of the shown scope of a calcined powder, position 1 indicates a cobalt-rich region and position 2 a $Ca_3Co_4O_9$ sheet. (h and i) EELS spectra of indicated regions 1 (green), 2 (red) of a calcined powder sample and reference samples of Co_3O_4 and CoO (black). Diagram (h) reveals the full range spectra at position 1 and 2, diagram (i) the oxygen and cobalt fine structures of region 1 and reference samples. (For interpretation of the references to color in this figure legend, the reader is referred to the web version of this article.)

respectively. The trend of the power factors $\sigma \cdot \alpha^2$ is thereby also similar and achieved 2.46 (open symbols) and 2.57 (closed symbols) $\mu W\,cm^{-1}\,K^{-2}$, respectively. The figure of merit ZT of a $Ca_3Co_4O_9$ ceramic was determined from the calculated power factors $\sigma \cdot \alpha^2$ of 2.46 (open diamond) $\mu W\,cm^{-1}\,K^{-2}$ and the entropy conductivity Λ of 0.61 $mW\,m^{-1}\,K^{-2}$ at 1073 K, which was measured via a laser flash setup.

Fig. 4b shows the entropy conductivity Λ of a $Ca_3Co_4O_9$ ceramic as a function of temperature. Fig. 4d shows the calculated figure of merit of a $Ca_3Co_4O_9$ ceramic after Eq. (1) as a function of temperature. The figure of merit of a $Ca_3Co_4O_9$ ceramic achieves 0.4 at 1073 K. The course of the heat conductivity λ and the measured values of 0.63 $W\,m^{-1}\,K^{-1}$ at 1073 K for a porous $Ca_3Co_4O_9$ ceramic also vary compared to the trend and value of 1.7 $W\,m^{-1}\,K^{-1}$ at 1073 K for a dense sample [14]. This can be attributed to a lower absolute density and high open porosity of the measured $Ca_3Co_4O_9$ ceramic sample, which was obtained by the sol–gel synthesis and pursuant production [35].

The heat conductivity as a function of porosity of a ceramic material is described by Eq. (3) [36]:

$$\lambda = \frac{1-P}{1+nP^2} \cdot \lambda_0 \tag{3}$$

Thereby λ and λ_0 are the measured heat conductivities for the porous (this work) and a dense sample (taken from [37]), P is the volume fraction of the pores and n is a constant between 1 and 14.

Fig. 5a displays the heat conductivity λ of a dense $Ca_3Co_4O_9$ sample as a function of the fractional porosity, calculated after Eq. (3). From top down, different values for the heat conductivity λ of a dense sample are shown as a function of fractional porosity and temperature (373 K black and 1073 K blue function). The values of

the heat conductivity λ of the measured porous $Ca_3Co_4O_9$ sample with a fractional porosity of 0.335 are also plotted in Fig. 5a and match with the values, calculated from a dense sample. The heat conductivity λ of a sample with a certain porosity can be extracted at vertical lines as a function of temperature, shown in red ellipse and red rectangle in Fig. 5a and b for reference values. An increasing fractional porosity leads to a very low and narrow distribution of the heat conductivity as a function of temperature. Eq. (3) is satisfactory for samples up to 74% porosity and 773 K [36]. But for the measured porous $Ca_3Co_4O_9$ sample, the course of the two functions match also for temperatures up to 1073 K, if a n-value of 7 is applied for the calculation, see Fig. 5b. Sole exception of the good conformity of calculated and measured values for a porous $Ca_3Co_4O_9$ sample is at 373 K.

A dense $Ca_3Co_4O_9$ ceramic sample possesses a higher isothermal electrical conductivity σ and thereby also a higher power factor $\sigma \cdot \alpha^2$ of about 3.5–3.6 $\mu W\,cm^{-1}\,K^{-2}$, but also a higher heat conductivity λ of 1.8–2.1 $W\,m^{-1}\,K^{-1}$ and thereby a lower ZT value [37,18]. The achieved Seebeck coefficient α of porous $Ca_3Co_4O_9$ remains almost constant with porosity but differs with direction due to obtained texture during compression. A highly porous $Ca_3Co_4O_9$ ceramic, synthesized by sol–gel technique, possess a sufficient power factor $\sigma \cdot \alpha^2$ and simultaneously a significantly reduced entropy conductivity Λ. This behavior can be referred to the microstructure shown in Figs. 2 and 3. As p-type material in a thermoelectric generator, porous $Ca_3Co_4O_9$ has to be investigated in matters of a higher contact resistance. The porosity could enhance the contact resistance but the achieved temperature difference could also be increased, due to the decreased thermal conductivity λ, and therefore maintain a higher voltage.
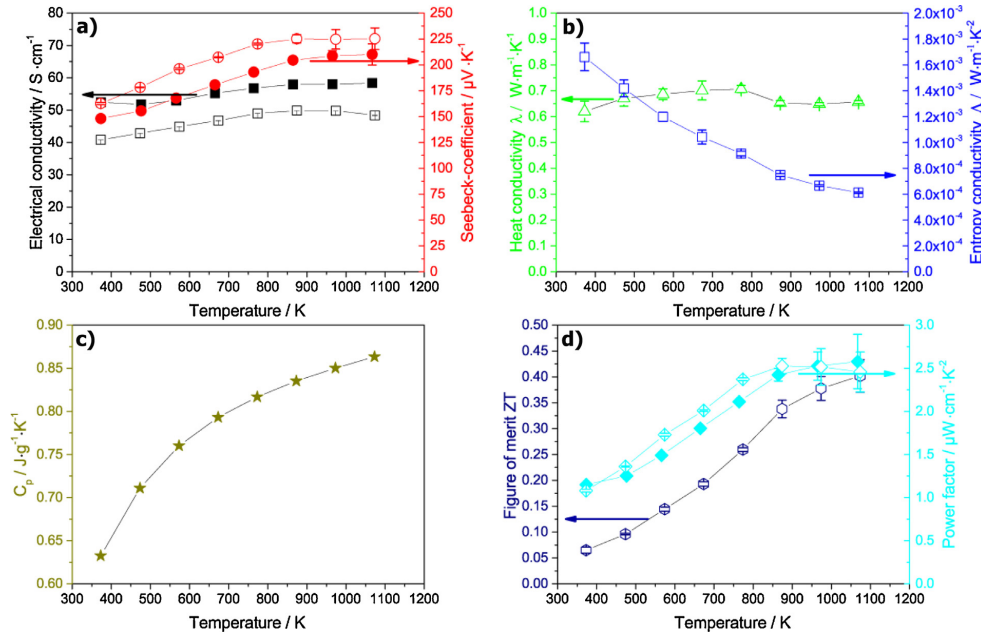
Fig. 4. Thermoelectric parameters as a function of temperature and uniaxial pressing direction, sample cut parallel to pressing direction (open symbols) and perpendicular (closed symbols), from 373 K to bottom (1073 K) of a $Ca_3Co_4O_9$ ceramic: (a) isothermal electrical conductivity σ (square) and Seebeck coefficient α (circle). (b) Heat conductivity λ (triangle) and entropy conductivity Λ (square) (Eq. (2)). (c) Heat capacity C_p (star). (d) Power factor $\sigma \cdot \alpha^2$ (diamond) and figure of merit ZT (hexagon), calculated according to Eq. (1). Uncertainties are indicated.
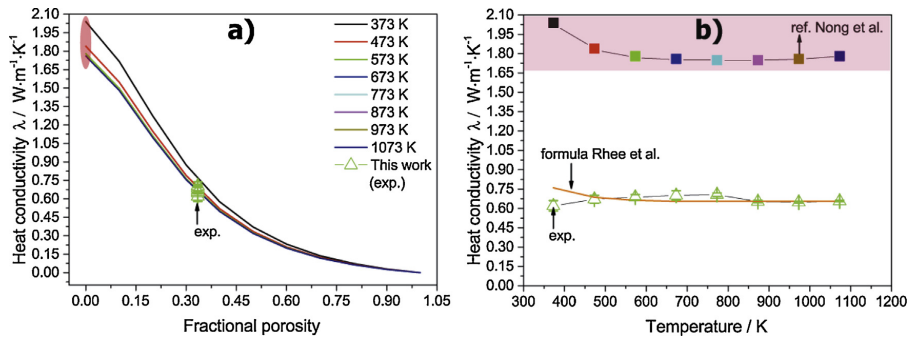

Fig. 5. Heat conductivity λ: (a) as a function of the fractional porosity of a ceramic $Ca_3Co_4O_9$ sample after Eq. (3), different temperatures are indicated with colors, from top (373 K, black) to bottom (1073 K, blue). Measured porous $Ca_3Co_4O_9$ ceramic sample (this work) with a fractional porosity of 0.335 is marked (green, triangle). Heat conductivity λ as a function of temperature can be extracted at vertical lines (red ellipse). (b) as a function of temperature for a dense, taken from [37] (corresponding colors to (a)), porous (green, triangle) $Ca_3Co_4O_9$ ceramic sample and calculated values (orange), after Eq. (3) [36]. Reference values are indicated with a red rectangle, compare with red ellipse in (a). Uncertainties are indicated. (For interpretation of the references to color in this figure legend, the reader is referred to the web version of this article.)

4. Conclusions

The sol–gel technique is more suitable than the most commonly used solid state reaction to obtain $Ca_3Co_4O_9$ ceramics for thermoelectric application. The sol–gel synthesis, as a "bottom up" technique, is much faster, simpler and avoids inadvertent contamination. We examined the growth mechanisms of $Ca_3Co_4O_9$ via intermediate stages of a layered $Ca_{1+x}Co_{1+y}O_{4-\delta}$ and $CaCO_3$. Two areas with different porosity and composition (incorporated nano-scaled particles) could be identified within the microstructure of the obtained ceramic. The isothermal electrical conductivity

σ and the Seebeck coefficient α were measured regarding pressing direction and texture. They differ in absolute values due to direction but differences are almost compensated concerning the power factor. Thereby the power factor $\sigma \cdot \alpha^2$ of a porous $Ca_3Co_4O_9$ ceramic remains similar and beneficial by reason of the obtained microstructure. The heat conductivity λ is reduced due to the high porosity and hence the ZT value of 0.4, which results from this low merit, is the highest value for conventional, non-doped $Ca_3Co_4O_9$. An accurate consideration between a high power factor $\sigma \cdot \alpha^2$ (dense sample) and a low heat conductivity λ (porous sample) can be advantageous, to discover an ideal proportion. The proper-

ties of the thermoelectric materials can be designed by adjusting the porosity of the materials. Porous materials and for this reason materials with a low heat conductivity λ can also enhance the temperature difference for application in a thermoelectric generator and thereby the absolute voltage provided by the generator.

Appendix A. Supplementary data

Supplementary data associated with this article can be found, in the online version, at http://dx.doi.org/10.1016/j.jeurceramsoc.2017.04.059.

References

[1] A.F. Ioffe, Semiconductor Thermoelements and Thermoelectric Cooling, 1st Ed., Info-search Ltd., London, 1957.

[2] H.U. Fuchs, The Dynamics of Heat – A Unified Approach to Thermodynamics and Heat Transfer, 2nd Ed., Graduate Texts in Physics, Springer, New York, 2010.

[3] A. Feldhoff, Thermoelectric material tensor derived from the Onsager – de Groot – Callen model, EHS 2 (1) (2015) 5–13.

[4] G.J. Snyder, E.S. Toberer, Complex thermoelectric materials, Nat. Mater. 7 (2008) 105–114.

[5] S.H. Yang, T.J. Zhu, T. Sun, J. He, S.N. Zhang, X.B. Zhao, Nanostructures in high-performance $(GeTe)_x(AgSbTe_2)_{100−x}$ thermoelectric materials, Nanotechnology 19 (2008) 1–5.

[6] M.S. Dresselhaus, G. Chen, M.Y. Tang, R. Yang, H. Lee, D. Wang, Z. Ren, J.P. Fleurial, P. Gogna, New directions for low-dimensional thermoelectric materials, Adv. Mater. 19 (2007) 1043–1053.

[7] D.M. Rowe, CRC Handbook of Thermoelectrics, 89th Ed., CRC Press, Boca Raton, FL, 1995.

[8] G. Xu, R. Funahashi, M. Shikano, I. Matsubara, Y. Zhou, Thermoelectric properties of the Bi-Na-substituted $Ca_3Co_4O_9$ system, Appl. Phys. Lett. 80 (2002) 3760–3762.

[9] Y. Miyazaki, Crystal structure and thermoelectric properties of the misfit-layered cobalt oxides, Solid State Ionics 172 (2004) 463–467.

[10] Y. Miyazaki, M. Onoda, T. Oku, M. Kikuchi, Y. Ishii, Y. Ono, Y. Morii, T. Kajitani, Modulated structure of thermoelectric compound $[Ca_2CoO_3]\,CoO_2$, J. Phys. Soc. Jpn. 71 (2002) 491–497.

[11] D. Nagahama, T. Tani, Y. Masuda, H. Itahara, T. Yonezawa, K. Koumoto, Thermoelectric properties of $Ca_3Co_{4−x}Ga_xO_9$-based ceramics textured by templated grain growth method, Int. Conf. Thermoelectr. 21 (2002) 211–214.

[12] Y. Masuda, D. Nagahama, H. Itahara, T. Tani, W.S. Seo, K. Koumoto, Thermoelectric performance of Bi- and Na-substituted $Ca_3Co_4O_9$ improved through ceramic texturing, J. Mater. Chem. 13 (2003) 1094–1099.

[13] Y. Wang, Y. Sui, J. Cheng, X. Wang, J. Miao, Z. Liu, Z. Qian, W. Su, High temperature transport and thermoelectric properties of Ag-substituted $Ca_3Co_4O_9$ system, J. Alloy. Compd. 448 (2008) 1–5.

[14] N.V. Nong, C.-J. Liu, M. Ohtaki, Improvement on the high temperature thermoelectric performance of Ga-doped misfit-layered $Ca_3Co_{4−x}Ga_xO_{9+δ}$ ($x = 0$, 0.05, 0.1, and 0.2), J. Alloy. Compd. 491 (2010) 53–56.

[15] O. Ravkina, J. Räthel, A. Feldhoff, Influence of different sintering techniques on microstructure and phase composition of oxygen-transporting ceramic, J. Eur. Ceram. Soc. 35 (2015) 2833–2843.

[16] J. Xu, C. Wei, K. Jia, Thermoelectric performance of textured $Ca_{3−x}Yb_xCo_4O_{9−δ}$ ceramics, J. Alloy. Compd. 500 (2010) 227–230.

[17] M. Lee, L. Viciu, Y. Wang, M.L. Foo, S. Watauchi, R.A. Pascal Jr, R.J. Cava, N.P. Ong, Large enhancement of the thermopower in Na_xCoO_2 at high Na doping, Nat. Mater. 5 (2006) 537–540.

[18] C.S. Huang, F.P. Zhang, X. Zhang, Q.M. Lu, J.X. Zhang, Z.Y. Liu, Enhanced thermoelectric figure of merit through electrical and thermal transport modulation by dual-doping and texture modulating for $Ca_3Co_4O_{9+δ}$ oxide materials, J. Alloy. Compd. 687 (2016) 87–94.

[19] Y. Song, C.-W. Nan, Preparation of $Ca_3Co_4O_9$ by polyacrylamide gel processing and its thermoelectric properties, J. Sol–Gel Sci. Technol. 44 (2007) 139–144.

[20] M.-G. Kang, K.-H. Cho, J.-S. Kim, S. Nahm, S.-J. Yoon, C.-Y. Kang, Post-calcination, a novel method to synthesize cobalt oxide-based thermoelectric materials, Acta Mater. 73 (2014) 251–258.

[21] T. Schulz, J. Töpfer, Thermoelectric properties of $Ca_3Co_4O_9$ ceramics prepared by an alternative pressure-less sintering/annealing method, J. Alloy. Compd. 659 (2016) 122–126.

[22] J.P. Heremans, M.S. Dresselhaus, L.E. Bell, D.T. Morelli, When thermoelectrics reached the nanoscale, Nat. Nanotechnol. 8 (2013) 471.

[23] J. Yang, H.-L. Yip, A.K.-Y. Jen, Rational design of advanced thermoelectric materials, Adv. Energy Mater. 3 (2013) 549.

[24] K. Biswas, J. He, I.D. Blum, C.-I. Wu, T.P. Hogan, D.N. Seidman, V.P. Dravid, M.G. Kanatzidis, High-performance bulk thermoelectrics with all-scale hierarchical architectures, Nature 489 (2012) 414–418.

[25] N. Mingo, D. Hauser, N.P. Kobayashi, M. Plissonier, A. Shakouri, "Nanoparticle-in-Alloy" approach to efficient thermoelectrics: Silicides in SiGe, Nano Lett. 9 (2009) 711.

[26] B. Poudel, Q. Hao, Y. Ma, Y. Lan, A. Minnich, B. Yu, X. Yan, D. Wang, A. Muto, D. Vashaee, X. Chen, J. Liu, M.S. Dresselhaus, G. Chen, Z. Ren, High-thermoelectric performance of nanostructured bismuth antimony telluride bulk alloys, Science 320 (2008) 634–638.

[27] S. Heimann, S. Schulz, J. Schaumann, A. Mudring, J. Stotzel, F. Maculewicz, G. Schierning, Record figure of merit values of highly stoichiometric Sb_2Te_3 porous bulk synthesized from tailor-made molecular precursors in ionic liquids, J. Mater. Chem. C 3 (2015) 10375.

[28] A. Feldhoff, M. Arnold, J. Martynczuk, T.M. Gesing, H. Wang, The sol–gel synthesis of perovskites by EDTA/citrite complexing method involves nanoscale solid state reactions, Solid State Sci. 10 (2008) 689–701.

[29] O. Jankovsky, D. Sedmidubsky, Z. Sofer, J. Hejtmanek, Thermodynamic behavior of $Ca_3Co_4O_{9+δ}$ ceramics, Ceram-Silikaty 56 (2) (2012) 139–144.

[30] L. Dusza, Combined solution of the simultaneous heat loss and finite pulse corrections with the laser flash method, High Temp.-High Press. 27/28 (1995/1996) 467–473.

[31] T. Janssen, A. Janner, A. Looijenga-Vos, P.M. De Wolff, International Tables for Crystallography: 9.8 Incommensurate and commensurate Modulated Structures, volume c Edition, Kluwer Academic Publishers, Dordrecht/Boston/London, 2004.

[32] S. Rasekh, M.A. Torres, G. Constantinescu, M.A. Madre, J.C. Diez, A. Sotelo, Effect of Cu by Co substitution on $Ca_3Co_4O_9$ thermoelectric ceramics, J. Mater. Sci.: Mater. Electron 24 (2013) 2309–2314.

[33] L. Xu, F. Li, Y. Wang, High-temperature transport and thermoelectric properties of $Ca_3Co_{4−x}Ti_xO_9$, J. Alloy. Compd. 501 (2010) 115–119.

[34] Y. Wang, Y. Sui, X. Wang, W. Su, Y. Liu, Enhanced high temperature thermoelectric characteristics of transition metals doped $Ca_3Co_4O_{9+δ}$ by cold high-pressure fabrication, J. Appl. Phys. 107 (2010), 033708-1–033705-9.

[35] A.I. Klyndyuk, I.V. Matsukevich, Synthesis and properties of $Ca_{2.8}Ln_{0.2}Co_4O_{9+δ}$ (Ln = La, Nd, Sm, Tb-Er) solid solutions, Inorg. Mater+. 48 (2012) 1052–1057.

[36] S.K. Rhee, Porosity-thermal conductivity correlations for ceramic materials, Mater. Sci. Eng. 20 (1975) 89–93.

[37] N.V. Nong, N. Pryds, S. Linderoth, M. Ohtaki, Enhancement of the thermoelectric performance of p-type layered oxide $Ca_3Co_4O_{9+δ}$ through heavy doping and metallic nanoinclusions, Adv. Mater. 23 (2011) 2484–2490.

Supporting Information

Porous $Ca_3Co_4O_9$ with Enhanced Thermoelectric Properties Derived from Sol-Gel Synthesis

Michael Bittner[1] , Lailah Helmich[1] , Frederik Nietschke[2] , Benjamin Geppert[1] , Oliver Oeckler[2] , Armin Feldhoff[1]

Schemes, diagrams and SEM- TEM micrographs were created by Microsoft Powerpoint 2010,

OriginPro 9.1G and ImageJ. Figures were arranged, merged and saved by Photoshop CS5.

Supporting information referred to Figure 2: X-ray diffraction patterns, Rietveld refined

structure data and difference curves, shown in Figure 1-8.

Figure 1: a) X-ray diffraction pattern, b) Rietveld refined structure data and c) difference

curve of a pre-calcined powder sample at 303 K.
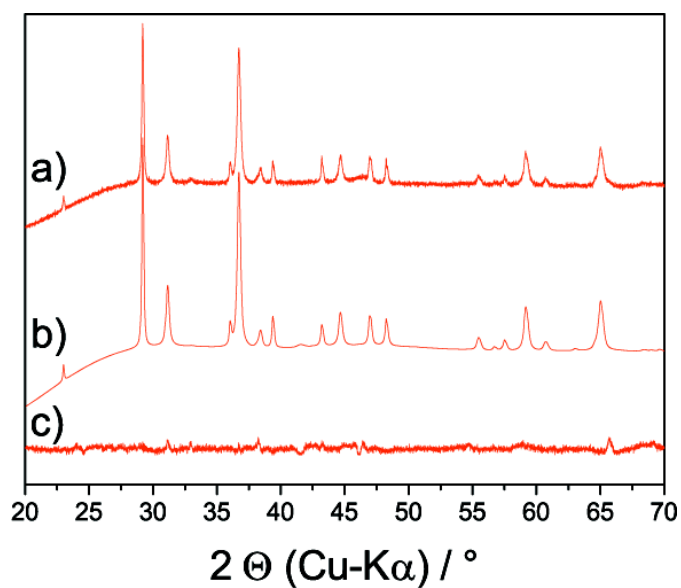
Figure 2: a) X-ray diffraction pattern, b) Rietveld refined structure data and c) difference

curve of a powder sample at 733 K.
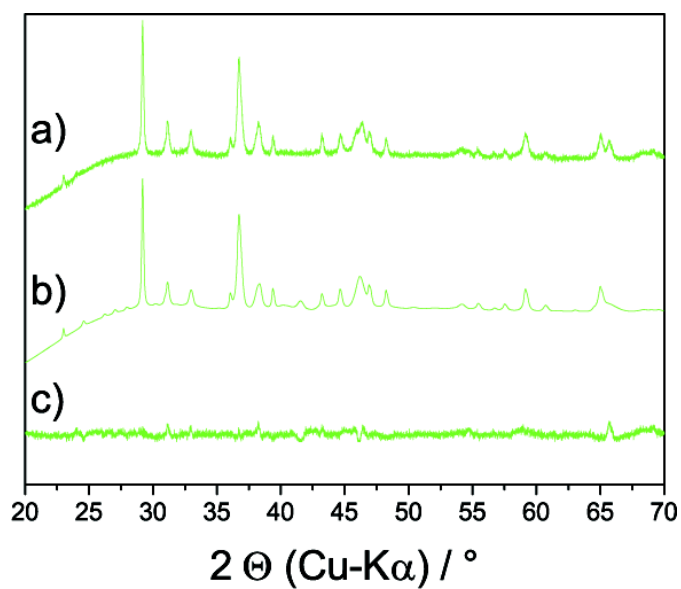
Figure 3: a) X-ray diffraction pattern, b) Rietveld refined structure data and c) difference

curve of a powder sample at 773 K.
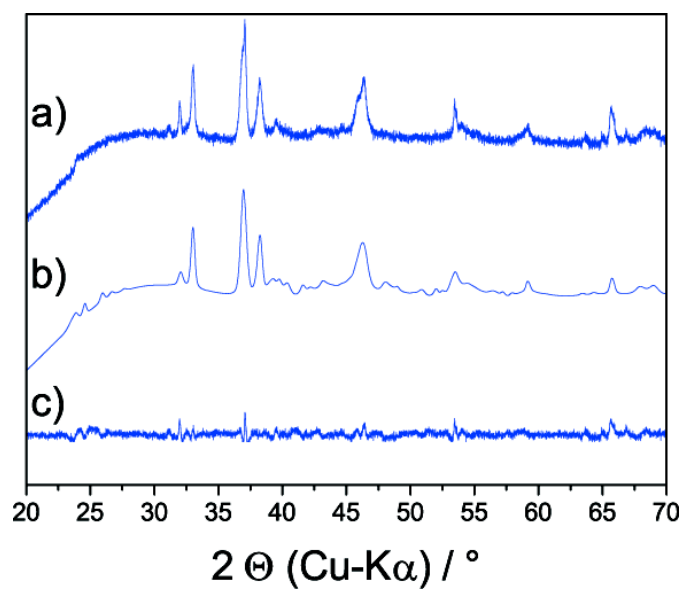
Figure 4: a) X-ray diffraction pattern, b) Rietveld refined structure data and c) difference

curve of a powder sample at 873 K.

Figure 5: a) X-ray diffraction pattern, b) Rietveld refined structure data and c) difference

curve of a powder sample at 1023 K.

Figure 6: a) X-ray diffraction pattern, b) Rietveld refined structure data and c) difference curve of a powder sample at 1173 K.

Figure 7: a) X-ray diffraction pattern, b) Rietveld refined structure data and c) difference curve of a powder sample at 303 K.
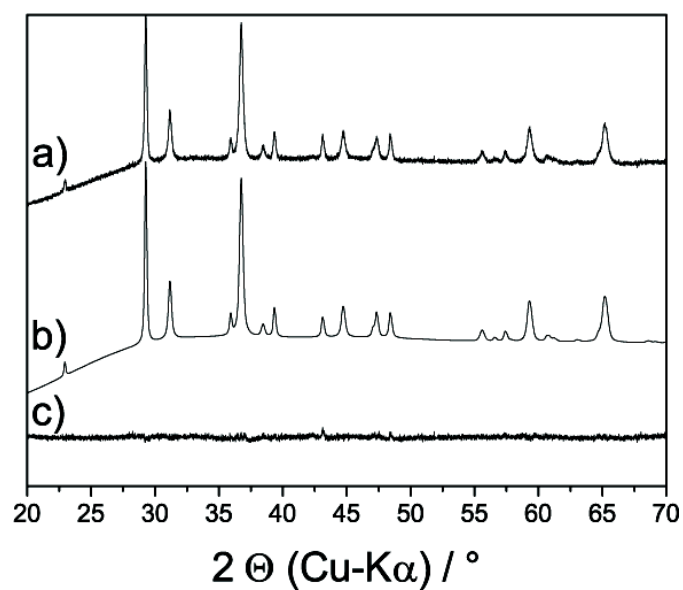
Figure 8: a) X-ray diffraction pattern, b) Rietveld refined structure data and c) difference curve of a ceramic sample at 293 K.

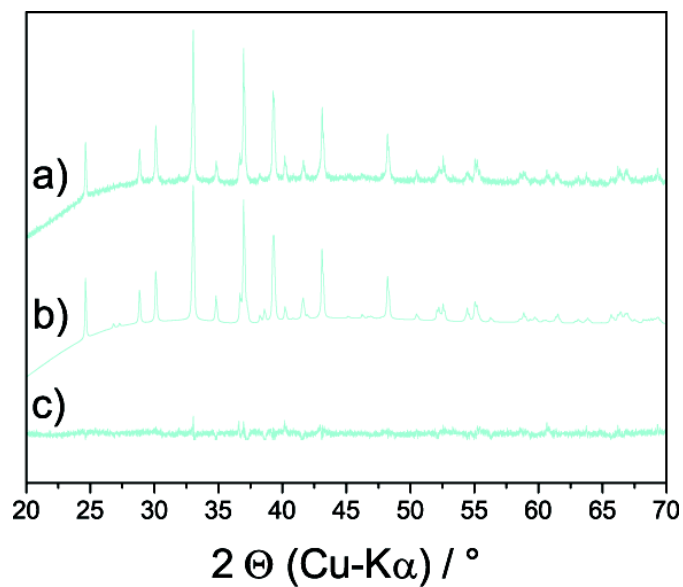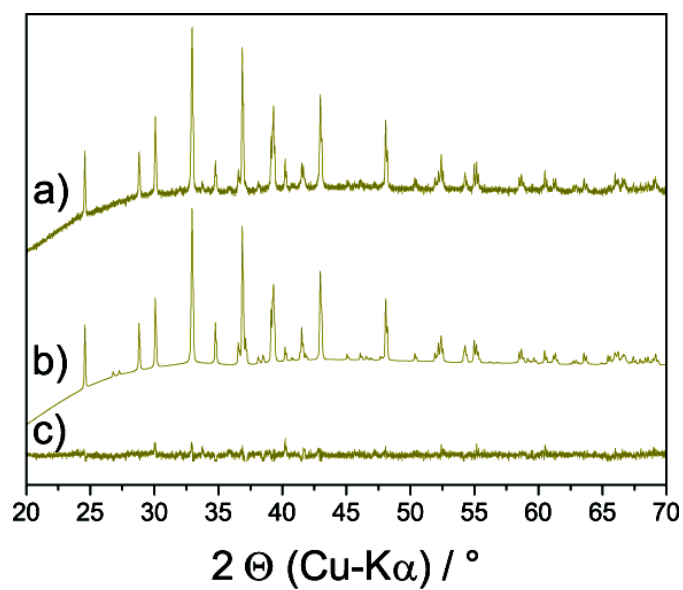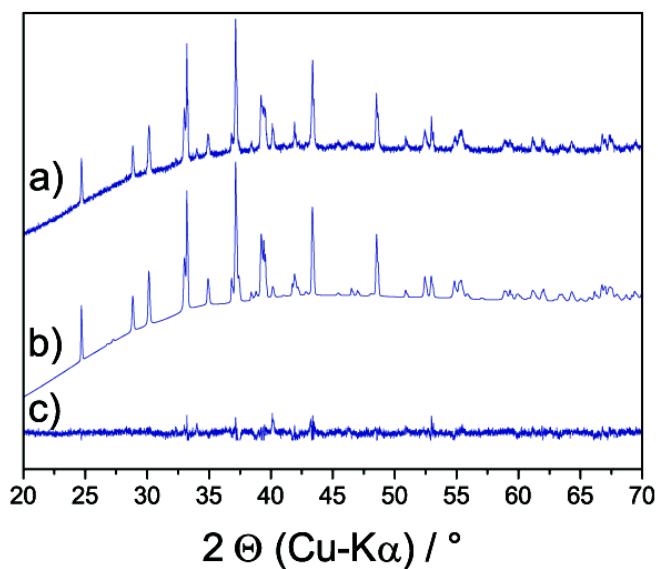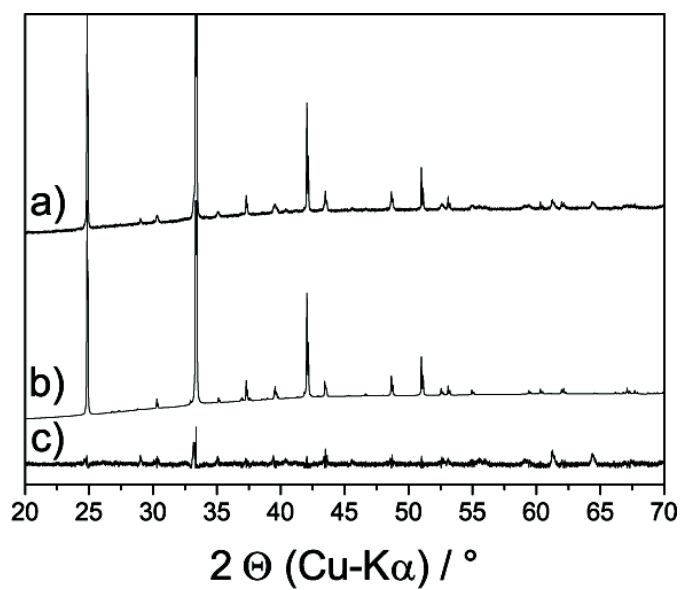## 2.3 Triple-phase ceramic 2D nanocomposite with enhanced thermoelectric properties

Michael Bittner, Nikola Kanas, Richard Hinterding,

Frank Steinbach, Dennis Groeneveld, Piotr Wemhoff, Kjell Wiik,

Mari-Ann Einarsrud, Armin Feldhoff

Triple-phase ceramic 2D nanocomposite with enhanced thermoelectric properties[†]

Michael Bittner[1,*], Nikola Kanas[2], Richard Hinterding[1], Frank Steinbach[1], Dennis Groeneveld[1], Piotr Wemhoff[1], Kjell Wiik[2], Mari-Ann Einarsrud[2], Armin Feldhoff[1,*]

[1]*Institute of Physical Chemistry and Electrochemistry, Leibniz University Hannover, DE-30167, Hannover, Germany, Fax: +49(511)762-4009;*
Tel: +49(511)762-3555; E-mail: michael.bittner@pci.uni-hannover.de ; armin.feldhoff@pci.uni-hannover.de
[2]*Department of Materials Science and Engineering, NTNU Norwegian University of Science and Technology, Sem Saelands vei 12, N-7491 Trondheim, Norway*

Abstract

A thermoelectric triple-phase p-type $Ca_3Co_4O_9$-Na_xCoO_2-$Bi_2Ca_2Co_2O_9$ (CCO-NCO-BCCO) 2D nanocomposite was obtained from pressureless sintering in air. The anisotropic thermoelectric properties of the nanocomposite exhibit a high electrical conductivity of $116 \ S \cdot cm^{-1}$ and a power factor of $6.5 \ \mu W \cdot cm^{-1} \cdot K^{-2}$ perpendicular to the pressing direction at 1073 K in air. A corresponding zT value of 0.35 was obtained. Three co-doped, thermoelectrically active misfit-layered materials were stacked to form a triple-phase nanocomposite, which combines the advantages of all three materials. The resulting nanocomposite enables simultaneous increases of the isothermal electrical conductivity σ and the Seebeck coefficient α by charge carrier concentration engineering and synergistic effects. The $Bi_2Ca_2Co_2O_9$ and Na_xCoO_2 phases were stabilized in a $Ca_3Co_4O_9$ matrix at high temperatures. To evaluate the application of the nanocomposite in high-temperature thermoelectric generators, the representation of the electrical conductivity and power factor in a Ioffe plot was more appropriate than the zT value.

[†] Electronic Supplementary Information (ESI) available.

Keywords: Thermoelectricity; All-scale hierarchical architecture; 2D nanostructures; Nanocomposite; $Ca_3Co_4O_9$

1. Introduction

1.1. Thermoelectric power conversion

Interest in thermoelectric materials (TE) for energy harvesting arises from their ability to convert thermal power directly into electrical power without moving parts. This is mediated by the coupling of currents of entropy I_S and electrical charge I_q in the solid, which can cause a thermally-induced electrical current (Seebeck effect). Under steady state conditions and the assumption of weak temperature dependence of the electron chemical potential as well as of the Seebeck coefficient α, the basic transport equation [1, 2] can be expressed by the difference in temperature ΔT and the electrical voltage U over the thermoelectric material of cross-sectional area A and length L as follows:

$$\begin{pmatrix} I_q \\ I_S \end{pmatrix} = \frac{A}{L} \cdot \begin{pmatrix} \sigma & \sigma \cdot \alpha \\ \sigma \cdot \alpha & \sigma \cdot \alpha^2 + \Lambda \end{pmatrix} \cdot \begin{pmatrix} U \\ \Delta T \end{pmatrix} \quad (1)$$

The thermoelectric material tensor in Equation 1 is composed of three quantities, which are the isothermal electrical conductivity σ, the Seebeck coefficient α and the entropy conductivity at electrical open circuit Λ (i.e., at vanishing electrical current). Note that each quantity σ, α and Λ itself is a tensor. The entropy conductivity Λ is related to the traditional heat conductivity λ by the absolute temperature T, as given in Equation 2.

$$\lambda = T \cdot \Lambda \quad (2)$$

The maximum of the second-law power conversion efficiency $\eta_{II,max}$ is determined solely by the thermoelectric figure-of-merit zT, as given by Equation 3, which results from tensor element 22 in the thermoelectric material tensor in Equation 1 [1].

$$zT = \frac{\sigma \cdot \alpha^2}{\Lambda} = \frac{\sigma \cdot \alpha^2}{\lambda} \cdot T \quad (3)$$

Maximum electrical power output of a thermoelectric material $P_{el,max,mat}$, as shown in Equation 4, is deter-

mined by the geometry (A, L), the power factor $\sigma \cdot \alpha^2$ and the temperature difference to the square $(\Delta T)^2$.

$$P_{el,max,mat} = \frac{1}{4} \cdot \frac{A}{L} \cdot \sigma \alpha^2 \cdot (\Delta T)^2 \qquad (4)$$

The laws of classical physics restrict the scope for enhancing the power factor $\sigma \cdot \alpha^2$ and figure-of-merit zT due to the interrelation of the parameters σ, α and λ. These values depend on the carrier concentration n and the mobility of the carriers μ, which correlate with each other [3].

To overcome these limits, several approaches have been postulated and tested during recent years. Previously, the thermoelectric community was focused on reducing λ and thereby optimizing zT. This was performed by tuning the micro- and nanostructure to scatter phonons on all length scales [7, 8]. The best material would possess an all-scale hierarchical architecture that scatters phonons on the mesoscale by it's microstructure, on the nanoscale by nanoprecipitates or nanostructures and on the atomic scale by point defects (co-doping, cross substitution) [9, 10]. The structures should be coherent (endotaxy) and possess electronic band energies matching those of the host material to avoid electron scattering, which would result in reduced electron mobility [11, 12, 13].

Recently, more attention has been paid to enhancing the power factor $\sigma \cdot \alpha^2$ [14, 15, 16, 17]. Carrier concentration engineering and co-doping can be used to increase the electrical conductivity σ [10]. The approaches of compositionally alloyed nanostructures and band-structure engineering are able to increase the Seebeck coefficient α [11, 13]. The most promising approach to enhance the power factor in an almost temperature-independent manner is band-structure engineering with resonant levels or resonant impurities and the introduction of additional electronic bands [14, 18]. The goals of this effort are the distortion and increase of the electronic density of states (DOS) in the vicinity of the Fermi level as much as possible. Hicks and Dresselhaus forecasted nanostructures such as 2-dimensional (2D) quantum wells and 1D quantum wires to be suitable for tuning the DOS in the vicinity of the Fermi level by the aforementioned techniques [19].

1.2. Oxides

State-of-the-art commercially available bulk thermoelectric materials include alloys, tellurides and half-Heusler or Zintl phases, such as Bi_2Te_3 [20], PbTe-PbS [16], SiGe [21], SnSe [22], FeNbSb [17] and $Yb_{14}MnSb_{11}$ [23]. These materials exhibit inferior stability at high temperature and in oxidizing atmospheres, are toxic, or include expensive and rare elements. However, thermoelectric oxides are expected to be viable materials for addressing these problems due to their benefits, such as non-toxicity, mechanical, thermal and chemical stability at high temperatures in air [24, 25, 26].

Recently, a new thermoelectric oxide material was discovered: BiCuSeO oxyselenides possess excellent thermoelectric properties in the moderate-temperature range (up to 650 °C), being comparable to alloys, Half-Heusler and Zintl phase materials [27, 28, 29]. However, BiCuSeO oxyselenides are not stable at high temperatures under oxidizing conditions [30]. In terms of the figure-of-merit zT, oxides which are stable in air can not compete with other material classes. For this reason, the development of oxides should focus on high power factors and electrical conductivity, to enhance the electrical power output of thermoelectric generators at high temperatures. Narducci postulated that if an infinite heat source is available for thermoelectric energy conversion, a high power factor and a moderate heat conductivity are beneficial for high electrical power outputs [31].

The layer-structured cobalt oxide $Ca_3Co_4O_9$ (CCO), based on CaO, has already been investigated and sustains high temperatures up to 1198 K [32, 33, 34]. CCO possesses a monoclinic crystal structure formed by a misfit-layered structure of a CdI_2-type CoO_2 subsystem with a triangular lattice and a layered rock-salt subsystem of three Ca_2CoO_3 units, which alternate along the c-axis. The two subsystems of the monoclinic system have different b-axis parameters and form an incommensurate structure, as shown in Figure 1a [4]. The synthesis of doped CCO via the well known sol-gel technique, reveals several advantages such as homogeneity, grain size and stoichiometric control [33]. The layered crystal structure affects also grain shape and has significant impact on anisotropy, degree of compacting and thereby on thermoelectric properties, especially on isothermal electrical conductivity and heat conductivity. In this work, sol-gel synthesis is used as a "bottom-up" technique to co-dope Na, Bi and Tb to the Ca-site of the Ca_2CoO_3 subsystem, which is visualized in Figure 1a. Table S 1[†] in the supplementary information shows the ionic radii of the substituted elements and dopants. According to the similarity of the ionic radii, doping should be possible. Co-doping can adjust carrier concentrations and introduce resonant impurities to enhance the thermoelectric properties σ and α. According to Equation 4, this directly improves the electrical power outputs of the obtained materials. Thus, σ can
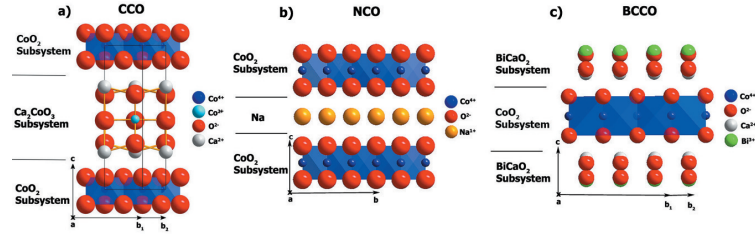
Figure 1: Crystal structures of a) $Ca_3Co_4O_9$ (**CCO**), b) Na_xCoO_2 (**NCO**) and c) $Bi_2Ca_2Co_2O_9$ (**BCCO**) along the a-axis. The ions involved are indicated by spheres of different size and colour: cobalt (small) in blue and turquoise, oxygen (large) in red, calcium (medium) in grey, bismuth (large) in green and sodium (large) in orange. Note b_1 and b_2 in a), b) form an irrational ratio, and the aperiodic crystal structure is described by superspace groups. Crystal structure data were taken from [4, 5, 6].

be enhanced by Na and Bi doping [10, 35, 36], while α can be improved by rare-earth doping (Tb) due to the hybridization of electronic bands with sp character [13, 26, 37, 38].

Increasing the doping level of Na and Bi leads to the formation of a triple-phase nanocomposite of co-doped CCO, Na_xCoO_2 (NCO) and $Bi_2Ca_2Co_2O_9$ (BCCO). NCO and BCCO also have monoclinic misfit-layered crystal structures, revealed in Figure 1b,c, which are comparable to that of CCO [4, 6, 39, 40]. The three structures simply differ in stacking and composition of the rock salt layer. Compared to CCO, BCCO possesses a higher α but a lower σ and NCO vice versa [6, 41, 42]. Overall, a nanocomposite (CCO-NCO-BCCO) of a co-doped CCO phase and "compositionally alloyed nanostructures" [10] of NCO and BCCO with partially coherent layered structures promise enhanced thermoelectric properties compared to those of the single materials. The formation of a high power triple-phase nanocomposite stabilizes the NCO and BCCO phases at elevated temperatures and hence enables application in thermoelectric generators for energy conversion.

2. Materials and Methods

2.1. Synthesis

Na, Bi and Tb co-doped CCO powders were synthesized via a sol-gel route, which provides fine-grained particles of homogenous composition as described by [43] for perovskites and by [33] for pure CCO. Calcium(II) nitrate tetrahydrate 99.98 %, cobalt(II) nitrate hexahydrate ACS 98-102.00 %, bismuth(III) nitrate hydrate 99.999 %, terbium(III) nitrate hydrate 99.9 % and sodium nitrate ≥ 99.5 % from Alfa Aesar were used as sources. The calcined powder samples were

uniaxially cold pressed at 200 MPa and pressurelessly sintered in air for 20 h at 1173 K. Reference samples of CCO, BCCO and NCO phases were cold pressed at 200 MPa and sintered for 10 h at 1173, 1123 and 1073 K, respectively. Table 1 shows the stoichiometry and abbreviation of synthesized samples. All steps, synthesis, calcination and sintering, were conducted under ambient air conditions.

Table 1: Stoichiometry and abbreviation of synthesized nanocomposites (CCO-30-35-6, CCO-30-35-8, CCO-30-35-10) and reference samples (CCO, BCCO, NCO).

stoichiometry	abbreviation
$Ca_3Co_4O_9$	**CCO**
Na_xCoO_2	**NCO**
$Bi_2Ca_2Co_2O_9$	**BCCO**
$Ca_{2.29}Na_{0.3}Bi_{0.35}Tb_{0.06}Co_4O_9$	**CCO-30-35-6**
$Ca_{2.27}Na_{0.3}Bi_{0.35}Tb_{0.08}Co_4O_9$	**CCO-30-35-8**
$Ca_{2.25}Na_{0.3}Bi_{0.35}Tb_{0.1}Co_4O_9$	**CCO-30-35-10**

2.2. Microstructure analysis

The phase compositions of the synthesized powders and sintered ceramics were characterized via X-ray diffraction (XRD) using a Bruker D8 Advance with Cu-K_α radiation. Microstructural characterization and elemental analysis of polished ceramic samples were performed using a JEOL JSM-6700F field-emission scanning electron microscope (FE-SEM) equipped with an Oxford Instruments INCA 300 (energy-dispersive X-ray spectroscopy, EDXS). Transmission electron microscopy (TEM) was performed at 200 kV using a JEOL JEM-2100F-UHR equipped with an Oxford Instruments INCA 300 (EDXS) for elemental analysis. Elemental distribution information of analyzed materials were

3

obtained from Na-K_α, Ca-K_α, Bi-L_α, Co-K_α, Tb-L_α and O-K_α transitions. Density and porosity were measured by Archimedes method (ISO 5018:1983) using isopropanol. Density values were averaged from 3 measurements with less than 2 % deviation. The heat capacity C_P, was estimated by differential scanning calorimetry (DSC) with a Netzsch STA 409 PC/PG in a synthetic air atmosphere with a flow of 30 mL $\cdot$ min^{-1} and a heating rate of 5 K $\cdot$ min^{-1} within the range of 313 K to 1173 K.

2.3. Measurement of thermoelectric properties

To investigate the thermoelectric properties of the manufactured oxide materials, σ, α and λ were measured as functions of temperature and pressing direction. To obtain a large ceramic sample (CCO-30-35-6, 30-35-8 and 30-35-10), the green body was pressed at 200 MPa using a 16 mm die and reground and pressed again, followed by a sintering process of 20 h at 1173 K. Samples were cut from large ceramic pellets (cylindrical, 16 mm $\cdot$ 16 mm) in bar shape (10 mm $\cdot$ 1.2 mm $\cdot$ 1.2 mm and 10 mm $\cdot$ 2.5 mm $\cdot$ 2.5 mm) parallel and perpendicular to the pressing direction. The σ values were estimated by a pseudo 4-point measurement at equilibrium conditions, utilizing a horizontal three-heating-zone tube furnace from Carbolite Gero EVZ 12/450B and a home-made measurement cell. The α values were measured using a ProboStat A setup from NorECs at equilibrium conditions in a furnace from Elite Thermal Systems Ltd. The values were logged using KEITH-LEY 2100 $6\frac{1}{2}$ Digital Multimeters. Data were acquired and converted using Lab VIEW software. The measurements of σ and α (heated to 1073 K and measured down with equilibrium at every temperature) were repeated from samples cut perpendicular and parallel to the pressing direction with less than 5 % deviation. The uncertainties of 5 and 2 % for α and of 10 and 4 % for the power factor (the latter obtained from samples cut parallel to the pressing direction), were averaged from 5 values. The values of λ were estimated using $\lambda = D \cdot C_P \cdot \rho$ and a LFA 457 MicroFlash laser flash setup from Netzsch under synthetic air atmosphere. Measurements of the thermal diffusivity D, averaged from 3 values, showed less than 5 % deviation. Accordingly, the uncertainties for the zT value were calculated to be 10 and 5 % (the latter obtained from samples cut parallel to the pressing direction). More details are given in the supporting information†.

3. Results and Discussion

3.1. Composition of triple-phase nanocomposites

The XRD patterns of all three phases (CCO, NCO, BCCO) within the triple-phase nanocomposite are shown as individual references in Figure 2a-c. With increasing doping level above the solubility limit of the CCO matrix, the formation of a composite material consisting of CCO, NCO and BCCO phases during sintering at 1173 K was enabled, as shown in Figure 2d-g.
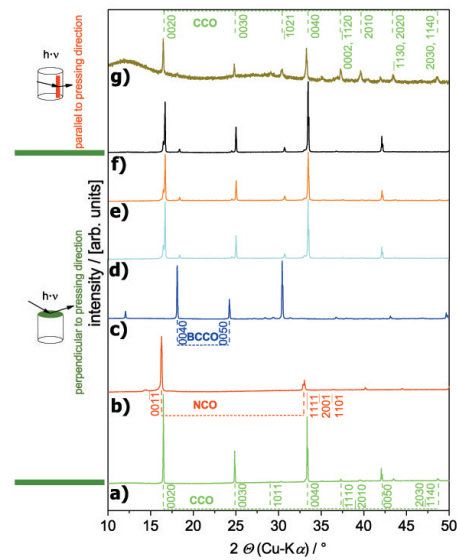
Figure 2: X-ray diffraction patterns of ceramic samples: a) **CCO** (taken from [33]), b) **NCO**, c) **BCCO**, d) **CCO-30-35-6**, e) **CCO-30-35-8**, f) **CCO-30-35-10** (perpendicular to pressing direction), g) **CCO-30-35-10** (parallel to pressing direction). CCO (green) and BCCO (blue) reflections were indexed in superspace group Cm (0 1 - p 0, equivalent to Bm (0 0 γ), no. 8.3 [44, 40]). NCO (red) reflections were indexed in superspace group C2/m [6]. The main NCO reflections (001-1 and 22-1-1, 200-1, 110-1) overlap with CCO (green) reflections. Difference in texture was obtained from samples, which were cut perpendicular (d-f) and parallel to the pressing direction (g). Additional XRD patterns of NCO and BCCO are given in S1†.

As the Tb content was increased, the ceramics became slightly more textured and oriented compared with the CCO reference in Figure 2a (weaker 0020,

Table 2: Density and porosity of reference ceramics (CCO, NCO, BCCO) and nanocomposite ceramics. References were sintered for 10 h at 1173, 1123, 1073 K and nanocomposites for 20 h at 1173 K. Values of the density were measured using ISO (International Organization for Standardization) 5018:1983. Reference values for CCO are taken from [33]. True density of composite ceramics is unknown.

material abbreviation	bulk density / $g \cdot cm^{-3}$	true density / $g \cdot cm^{-3}$	open porosity / %	true porosity / %	closed porosity / %	theoretical density / %
CCO	3.2 ± 0.1	4.68	33.3 ± 0.7	33.5 ± 1.1	0.2 ± 0.7	67.7 ± 1.5
NCO	3.2 ± 0.0	4.65	15.7 ± 2.6	30.6 ± 0.2	14.9 ± 2.8	69.4 ± 0.0
BCCO	5.5 ± 0.0	6.82	1.6 ± 0.9	19.8 ± 0.6	18.1 ± 0.4	80.2 ± 0.0
CCO-30-35-6	3.9 ± 0.0		21.5 ± 0.3			
CCO-30-35-8	3.9 ± 0.0		22.1 ± 0.9			
CCO-30-35-10	3.9 ± 0.0		19.2 ± 0.7			

2010 and stronger 0040, 0050 CCO reflections). Furthermore, the reflections were less shifted to lower angles with increasing Tb-content. Hence, Tb was assumed to facilitate the formation of the CCO-NCO-BCCO nanocomposite, and smaller amounts of Bi were integrated into the CCO structure. Structural similarity of the three phases, as shown in Figure 2a-c, and large overlap of the involved reflections did not allow observation of NCO in the nanocomposites. Depending on the direction of cold pressing and cutting of the ceramic green body, different texture was obtained, as displayed in Figure 2d-f (perpendicular) and Figure 2g (parallel). Parallel to the direction of cold pressing of the green body, the ceramic showed a more variegated mixture of reflections from different planes, although the reflections 00l0 (0020, 0030, 0040, etc.) remained the most intense.

Supplementing the XRD patterns, microstructural characterization by SEM revealed the NCO phase and confirmed the CCO and BCCO phases within the composite material. The microstructure of NCO and BCCO phases are displayed in Figure S 2[†], while SEM micrographs and elemental distributions of polished cross-sections of CCO-NCO-BCCO nanocomposites are shown in Figure 3. Values of the density of NCO and BCCO are given in Table 2. Co-doping with Na, Bi and Tb resulted in a nanocomposite material of CCO, BCCO and NCO grains with pores in between. Increasing the doping level of Tb led to the formation of a denser nanocomposite, as shown in Figure 3a-f, and subsequently decreased porosity, given in Table 2. This porosity has a strong impact on thermal and electrical conductivity, because both values are decreasing with increased thermal and electrical contact resistances [33, 34]. The values of both, thermal and electrical conductivity, are also influenced by the degree of grain orientation, since the grains have anisotropic transport characteristics. Moreover, the higher the grain orientation, the lower is the porosity.

The CCO-30-35-10 nanocomposite was further ex-
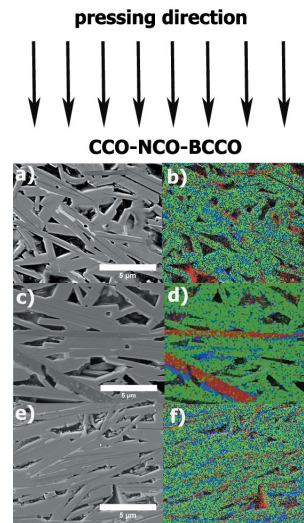
Figure 3: Cross-sectional SEM micrographs and EDXS elemental distributions of CCO-NCO-BCCO nanocomposite ceramics: a, b) **CCO-30-35-6**; c, d) **CCO-30-35-8**; e, f) **CCO-30-35-10**. The CCO phase is dominated by Ca (green), the NCO phase by Na (red) and the BCCO phase by Bi (blue). The direction of uniaxial cold pressing is indicated by black arrows. Additional SEM sites of NCO and BCCO are shown in Figures S 2[†].

amined by TEM. Figure 4a-f identifies semi-coherently aligned 2D nanostructures. The material was pervaded by NCO, BCCO and CCO 2D layers, revealed in Figure 4a,b. These layers were homogeneously distributed throughout the material, alternating in thickness and sequence. As shown in Figure 4b,c, the different layers were co-doped with Na, Bi and Tb in the CCO phase, Ca, Bi and Tb in the NCO phase, and Na and Tb in the BCCO phase, respectively. The Tb content was en-
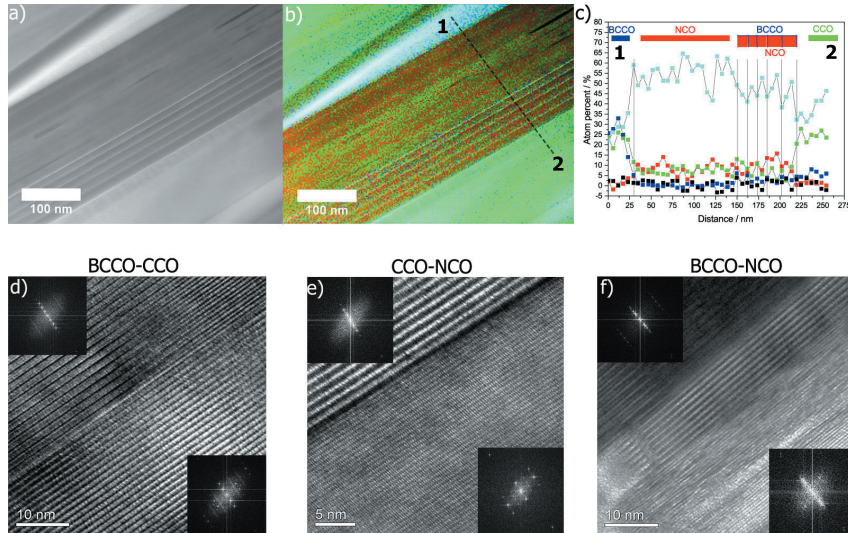
Figure 4: TEM analysis of a **CCO-30-35-10** nanocomposite ceramic: a, b) Scanning transmission electron microscopy (STEM) dark-field micrograph and EDXS elemental distribution (more detail in Figure S 3[†]). The CCO phase is dominated by Ca, the NCO phase by Na and the BCCO phase by Bi. c) Linescan of 5.7 nm point-to-point distance of the elemental distribution of Na (red), Ca (green), Bi (blue), Tb (black) and Co (turquoise) in the area shown in b) and along the indicated dotted line. d-f) High-resolution transmission electron microscopy (HRTEM) micrographs of the heteromaterial interfaces BCCO-CCO, CCO-NCO and BCCO-NCO. Insets show the reduced fast Fourier transformation (rFFT), which are shown in more detail in Figure S 4[†]. Additional TEM sites are shown in Figures S 5-7[†].

riched in the CCO, while decreased in the NCO and BCCO phases.

Table 3: Lattice parameters (in Å) of the CCO, NCO and BCCO phases at the interfaces BCCO-CCO, BCCO-NCO and CCO-NCO within a CCO-30-35-10 nanocomposite, as analyzed by HRTEM (Figure 4). Values were measured from reduced fast Fourier transformations (rFFT). Semi-coherent lattice parameters are in bold.

|	Interfaces		
	1) BCCO-CCO	3) BCCO-NCO	2) CCO-NCO
BCCO	c=15.02	b_1=3.13, c=14.81	
CCO	**a=5.11**, b_2=4.55		c=10.67
	c=10.96		
NCO		**a=5.26**, c=5.47	**a=5.07**, b_1=2.82
			c=5.74

These co-doped layers of NCO and BCCO seemed to be stabilized at high temperatures by the interdiffusion of the doped elements and surrounding phases, represented in the linescan of Figure 4c. The NCO phase, not implemented in the nanocomposite, exhibited the lowest chemical and thermal stability at high temperatures. As illustrated in Figure 5a, the NCO reference phase

began decomposing in air at approximately 963 K. Although, the interdiffusion of Ca, Bi and Tb, as shown in Figure 4c, could stabilize this phase (Bi and Tb may occupy Na positions). The effect of the interdiffusion of Ca into the NCO phase also seemed to depend on the its thickness and surroundings. Figure 4d-f reveals the three feasible heterophase interfaces, BCCO-CCO, CCO-NCO and BCCO-NCO within the nanocomposite. The different phases grew semi-coherently on each other, facilitated by their similar, layered structure. The lattice parameters, given in Table 3, show similar values for the a-axis, while the c-parameter within the different phases was slightly lower than a multiple of the c-parameter in NCO. The NCO phase also exhibited areas of amorphous-like character with many defects, as displayed in Figure 4f. This phase was naturally less stable, but the amorphous-like phase formation could be either attributed to very thin layers, a cation-deficient metastable phase or damage from Ar-ion polishing during specimen preparation. Analyzes from SEM and TEM, as shown in Figures 3 and 4, revealed structures

on the micro- and nanoscale. Figure 4c confirmed point defects on the atomic scale, which were introduced by interdiffusion and co-doping. Overall, structural investigations verified an all-scale hierarchical structure of the nanocomposites. Hence, phonons could be scattered on the microscale, nanoscale and atomic scale, while at the same time, semi-coherently aligned, misfit-layered materials were present as shown.

3.2. Thermoelectric properties

The thermoelectric properties of reference NCO and BCCO materials are shown in Figure 5. The NCO material shows a high electrical conductivity of 142 S · cm^{-1} at 963 K, but low Seebeck coefficient of 175 μV · K^{-1} at 873 K. The NCO material decomposes at about 963 K in air, leading to a decreased conductivity. In contrast to this, the BCCO material has a high Seebeck coefficient of 274 μV · K^{-1} at 973 K, but a low electrical conductivity of 18 S · cm^{-1} at 1023 K. The BCCO material is stable up to 1023 K in air.

The thermoelectric properties of CCO and nanocomposites are based on an anisotropic character, as shown in Figure 6. This anisotropy is caused by the crystal structures of the three basic materials CCO, NCO and BCCO, as illustrated in Figure 1a-c, and by compression and sintering, which led to grain orientation, as shown in Figures 2, 3 and 4. The thermoelectric properties σ, α and power factor of CCO and the nanocomposite ceramics, are illustrated in Figure 6a,b as a function of temperature and depend on the pressing direction. The trend for σ for all samples, displayed in Figure 6b, was almost constant throughout the temperature range and reached 116 S · cm^{-1} at 1073 K for CCO-30-35-10 perpendicular to the pressing direction. The σ values of CCO and of CCO-30-35-10 were also measured parallel to the pressing direction and reached 48 S · cm^{-1} and 51 S · cm^{-1}, respectively, at 1073 K. These materials showed similar behavior because of the enhanced orientation and nanocomposite composition in CCO-30-35-10. As shown in Figure 3, the nanocomposite ceramics contained not only a Na, Bi and Tb co-doped CCO phase, but also NCO phase [6, 45], which is electrically highly conductive, as indicated in Figure 5a. It is concluded, that the incorporated and stabilized, co-doped NCO phase further increased the σ value of the nanocomposite material. Both, the formation of a BCCO phase, which has a high α value [41, 42], as illustrated in Figure 5b, and the integration of Bi and Tb [38] at Ca-site positions, increased the α value of the nanocomposite. The NCO and BCCO materials show inferior stability at temperatures above 963 and 1023 K in air, respectively, as shown in Figure 5. However, the
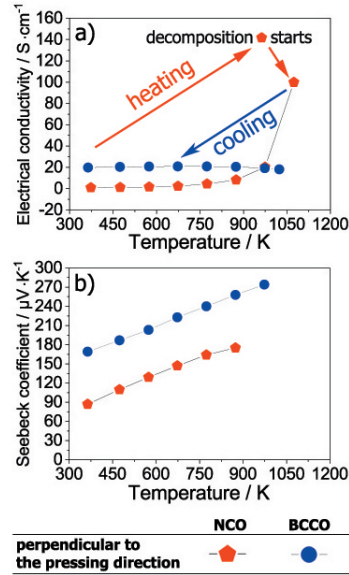
Figure 5: Thermoelectric parameters of **NCO** (pentagon, red) and **BCCO** (circle, blue) as a function of temperature in air: a) Isothermal electrical conductivity σ, direction of heating, cooling, start of NCO decomposition and highest value of NCO before decomposition are indicated. b) Seebeck coefficient α. Samples were cut and measured perpendicular to the pressing direction.

incorporation of NCO and BCCO into a stable matrix like CCO stabilized these materials at high temperatures (above 963 K, 1023 K) in air. The behavior of α for all nanocomposites, shown in Figure 6a, was likewise similar, starting from different values and increased with temperature, reaching 236 and 250 μV · K^{-1} at 1073 K for a CCO-30-35-10 nanocomposite ceramic perpendicular and parallel to the pressing direction, respectively. The absolute values of σ for the different materials increased with doping content of Tb. The simultaneous increases in σ and α indicate an increased charge carrier density n and carrier mobility μ in the nanocomposite ceramics. The impact of Bi on the thermoelectric properties of c-axis-oriented CCO thin films was reported by Sun et al. [46], and Saini et al. [38] showed that Tb-doping increased the value of μ.
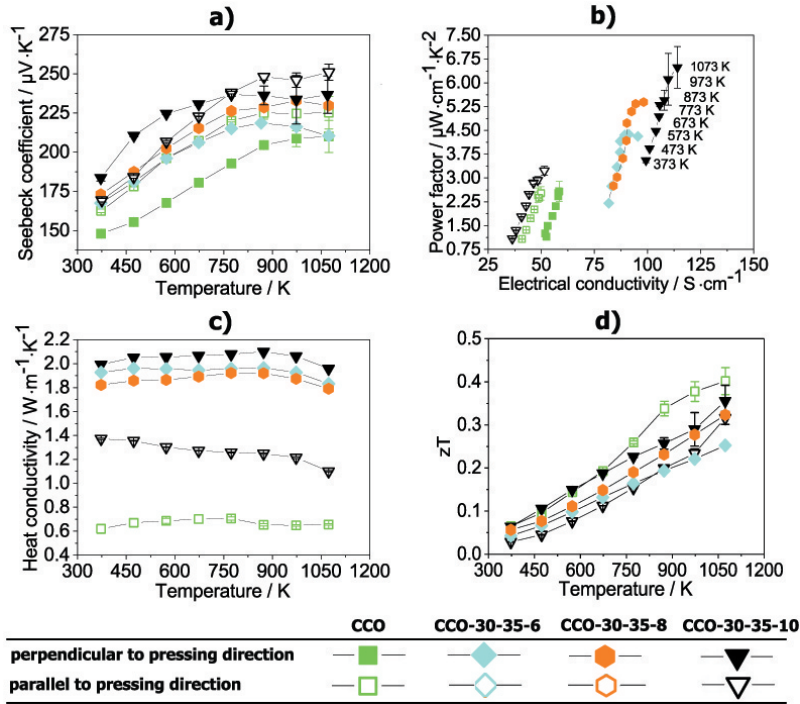
Figure 6: Thermoelectric parameters of **CCO** (square, green, taken from [33]), **CCO-30-35-6** (diamond, turquoise), **CCO-30-35-8** (hexagon, orange) and **CCO-30-35-10** (reverse rectangle, black) as a function of temperature: a) Seebeck coefficient α, b) Ioffe plot, power factor $\sigma \cdot \alpha^2$ as a function of σ [47], c) heat conductivity λ and d) figure-of-merit zT. Closed and open symbols represent values measured from samples perpendicular and parallel to the pressing direction, respectively. Uncertainties are indicated by error bars.

3.3. Challenges in manufacturing

The manufacturing of a large, crack-free and homogeneous ceramic sample from uniaxially pressing and pressureless sintering in air, in order to measure the transport properties parallel to the pressing direction, is challenging. For this reason, thermoelectric properties parallel to the pressing direction were solely reported for the CCO-30-35-10 sample, which showed best values perpendicular to the pressing direction. In previous reports about the anisotropic properties of CCO, large and dense materials were obtained from cold isostatically pressing (CIP) [48], spark plasma sintering (SPS) [49] and hot-pressing (HP) [50, 51].

3.4. Figure-of-merit zT vs. Ioffe plot

The zT values of CCO and CCO-30-35-10 nanocomposite, shown in Figure 6d, were determined according

to Equation 3, from the calculated power factor and the corresponding values of the heat conductivity λ perpendicular and parallel to the pressing direction, respectively. The λ values of the CCO-30-35-10 nanocomposite, as shown in Figure 6c, reached 1.96 and 1.1 W $\cdot$ m^{-1} $\cdot$ K^{-1}, respectively, at 1073 K perpendicular and parallel to the pressing direction. The anisotropy in the thermal transport properties is illustrated by the difference of the heat conductivity perpendicular and parallel to the pressing direction. Figure S 8[†] illustrates the measured values of the heat capacity C_P as a function of temperature in the range from 313 K to 1173 K. The heat capacity C_P reached approximately 0.83 J $\cdot$ K^{-1} $\cdot$ g^{-1} at 1073 K for a CCO-30-35-10 nanocomposite. The trend and values of C_P as a function of temperature were similar to the values for pure CCO reported by Jankovsky et al. [52] and were consistent with phononic Debye-

Einstein behavior. Values of the figure-of-merit zT at 1073 K, as shown in Figure 6d, were as follows: 0.4 (parallel to the pressing direction, CCO), 0.35 (perpendicular, CCO-30-35-10) and 0.31 (parallel, CCO-30-35-10). A very low heat conductivity λ, which is given in Figure 6c, led to a high zT value of CCO in the direction parallel to the pressing direction. However, CCO shows low values in the Ioffe plot of Figure 6b of both thermoelectric power factor $\sigma \cdot \alpha^2$ and electrical conductivity σ [33], which is detrimental for power generation.

The thermoelectric power factor of nanocomposites, calculated from σ and α perpendicular and parallel to the pressing direction, is shown in a Ioffe plot in Figure 6b as a function of the electrical conductivity. The Ioffe plot is suitable to estimate the capability of a thermoelectric material in power generation applications, due to the combined presentation of electrical conductivity σ and the power factor $\sigma \cdot \alpha^2$ [47]. A large improvement was observed due to the simultaneous enhancement of σ and α by Na, Bi and Tb co-doping and the formation of a nanocomposite material, which is, according to Equation 4, beneficial for power generation. The thermoelectric power factor of the CCO-30-35-10 nanocomposite, represented in Figure 6b, reached 6.5 and 3.2 μW $\cdot$ cm^{-1} $\cdot$ K^{-2} at 1073 K, perpendicular and parallel to the pressing direction, respectively. The consideration of all parameters within the figure-of-merit zT, according to Equation 3, conceals the specific properties of the materials, a thermal isolator with low electrical conductivity can provide a high zT value. However, a thermal isolator, which has a high figure-of-merit zT, but poor electrical properties, is not useful for high electrical power generation. The Ioffe plot, illustrated in Figure 6b, which considers the thermoelectric power factor and the electrical conductivity, is more appropriate according to Equation 4, to evaluate the applicability of a material for high-temperature power generation.

3.5. Comparison and evaluation

Nanocomposites from pressureless sintering in air exhibited similar trends of the heat conductivity λ, but absolute values of 1.83, 1.79 and 1.96 W $\cdot$ m^{-1} $\cdot$ K^{-1} at 1073 K differed, as shown in Figure 6c. In contrast to this, dense CCO materials from SPS [49] and HP [50] showed λ values of 3.0 and 2.8 W $\cdot$ m^{-1} $\cdot$ K^{-1} perpendicular to the pressing direction. As shown in Figure 6c, the nanocomposite revealed a λ value of 1.1 W $\cdot$ m^{-1} $\cdot$ K^{-1} at 1073 K parallel to the pressing direction. Previous reports about anisotropic transport properties in highly oriented CCO revealed a heat conductivity of 1.5 and 1.2 W $\cdot$ m^{-1} $\cdot$ K^{-1} parallel to the pressing direction [49, 50]. Concerning the electrical

conductivity σ and the Seebeck coefficient α, Nong et al. were able to enhance σ to about 130 S $\cdot$ cm^{-1} and α to approximately 235 μV $\cdot$ K^{-1} at 1073 K perpendicular to the pressing direction by co-doping with Ag, Lu and spark plasma sintering of a dense material [26]. Saini et al. showed a significant increase in α by Tb-doping up to 325 μV $\cdot$ K^{-1} at 800 K for a Ca$_{3-x}$Tb$_x$Co$_4$O$_9$, x= 0.5 ceramic, perpendicular to the pressing direction [38]. By comparing the thermoelectric properties of the stacked 2D nanocomposite with the aforementioned reports, further improvements could be achieved with enhanced density, for example by utilization of alternative processing techniques. However, the comparison of the anisotropic thermoelectric properties of manufactured nanocomposites with CCO-based materials from literature is difficult. According to the used synthesis route and processing technique, the obtained properties like density, microstructure and degree of orientation of the materials are different. As a consequence, the obtained thermoelectric properties of these materials can not be easily compared to each other.

The pure phases of CCO [49], NCO [53] and BCCO [41] show a thermoelectric power factor of about 5, 3 and 1 μW $\cdot$ cm^{-1} $\cdot$ K^{-2} at 1073 K, 900 K and 1000 K, respectively. These lower values of the thermoelectric power factors, compared to the triple-phase CCO-NCO-BCCO nanocomposite, were obtained from much higher polycrystalline bulk densities of 96-99 %. Strong anisotropy was also observed for σ and α, however, the values perpendicular and parallel to the pressing direction were enhanced due to co-doping and composite formation. The highest power factor and zT value were obtained perpendicular to the pressing direction for the CCO-30-35-10 nanocomposite. The high thermoelectric power factor $\sigma \cdot \alpha^2$, electrical conductivity σ, shown in the Ioffe plot in Figure 6b, and the moderate heat conductivity λ are beneficial for power generation at high temperatures from infinite heat sources [31]. Thermoelectric materials should be designed and utilized in consideration of their application area, for example high energy conversion efficiency or high power generation. In this work, a high power material of semi-coherent 2D nanostructures was developed. This triple-phase nanocomposite has simultaneously enhanced thermoelectric properties and is applicable in the high-temperature range in air for thermoelectric power generation.

4. Conclusions

A material design of semi-coherently layered 2D nanostructures appears promising. Co-doping with suit-

able dopants can enhance the thermoelectric properties, but a triple-phase nanocomposite of co-doped phases provides synergistic effects and increases the thermoelectric properties. The formation of semi-coherent 2D nanostructures enabled the simultaneous enhancement of the thermoelectric properties σ and α. The BCCO and NCO phases are stabilized at elevated temperatures within a co-doped CCO-NCO-BCCO nanocomposite and beneficial properties were extended to the high-temperature range. The integration of materials that are unstable at high temperatures into a stable matrix could utilize synergistic effects and presents new alternatives in material development. The high electrical conductivity and power factor, revealed by the Ioffe plot, offer the application in a thermoelectric generator for waste heat recovery at high temperatures in air. The evaluation of thermoelectric materials for power generation at high temperatures should be discussed critically, since the figure-of-merit zT is misleading to determine the applicability. The Ioffe plot, which shows the thermoelectric power factor as a function of the electrical conductivity, is more suitable to evaluate the ability for high-temperature power generation.

5. Acknowledgment

6. References

[1] H. U. Fuchs, A direct entropic approach to uniform and spatially continuous dynamical models of thermoelectric devices, EHS 1(3-4) (2014) 253–265.

[2] A. Feldhoff, Thermoelectric material tensor derived from the Onsager - de Groot - Callen model, EHS 2 (1) (2015) 5–13.

[3] A. F. Ioffe, Physics of Semiconductors, 1st Edition, Infosearch Ltd. London, 1960.

[4] Y. Miyazaki, M. Onoda, T. Oku, M. Kikuchi, Y. Ishii, Y. Ono, Y. Morii, T. Kajitani, Modulated structure of thermoelectric compound [Ca$_2$CoO$_3$] CoO$_2$, J. Phys. Soc. Jpn. 71 (2002) 491–497.

[5] H. Muguerra, D. Grebille, E. Guilmeau, R. Cloots, Modulated misfit structure of the thermoelectric [Bi$_{0.84}$CoO$_2$][CoO$_2$]$_{1.69}$ cobalt oxide, Inorg. Chem. 47 (2008) 2464–2471.

[6] L. Viciu, J. W. G. Bos, H. W. Zandbergen, Q. Huang, M. L. Foo, S. Ishiwata, A. P. Ramirez, M. Lee, N. P. Ong, R. J. Cava, Crystal structure and elementary properties of Na$_x$CoO$_2$ (x = 0.32, 0.51, 0.6, 0.75, and 0.92) in the three-layer NaCoO$_2$ family, Phys. Rev. B 73 (2006) 174104–1–174104–10.

[7] M. G. Kanatzidis, Nanostructured thermoelectrics: The new paradigm?, Chem. Mater. 22 (2010) 648–659.

[8] M. Martín-González, O. Caballero-Calero, P. Díaz-Chao, Nano-engineering thermoelectrics for 21st century: Energy harvesting and other trends in the field, Renew. Sust. Energ. Rev. 24 (2013) 288–305.

[9] J. Yang, H.-L. Yip, A. K.-Y. Jen, Rational design of advanced thermoelectric materials, Adv. Energy Mater. 3 (2013) 549.

[10] G. Tan, L.-D. Zhao, M. Kanatzidis, Rationally designing high-performance bulk thermoelectric materials, Chem. Rev. 116 (2016) 12123–12149.

[11] M. S. Dresselhaus, G. Chen, M. Y. Tang, R. Yang, H. Lee, D. Wang, Z. Ren, J. P. Fleurial, P. Gogna, New directions for low-dimensional thermoelectric materials, Adv. Mater. 19 (2007) 1043–1053.

[12] D. L. Medlin, G. J. Snyder, Interfaces in bulk thermoelectric materials a review for current opinion in colloid and interface science, Curr. Opin. Colloid In. 14 (2009) 226–235.

[13] J. P. Heremans, B. Wiendlocha, A. M. Chamoire, Resonant levels in bulk thermoelectric semiconductors, Energ. Environ. Sci. 5 (2012) 5510–5530.

[14] Y. Pei, X. Shi, A. Lalonde, H. Wang, L. Chen, G. J. Snyder, Convergence of electronic bands for high performance bulk thermoelectrics, Nature 473 (2011) 66–69.

[15] R. J. Korkosz, T. C. Chasapis, S.-H. Lo, J. W. Doak, Y. J. Kim, C.-I. Wu, E. Hatzikraniotis, T. P. Hogan, D. N. Seidman, D. Wolverton, V. P. Dravid, M. G. Kanatzidis, High ZT in p-type (PbTe)$_{1-2x}$(PbSe)$_x$(PbS)$_x$ thermoelectric materials, J. Am. Chem. Soc. 136 (2014) 3225–3237.

[16] D. Wu, L.-D. Zhao, X. Tong, W. Li, L. Wu, Q. Tan, Y. Pei, L. Huang, J.-F. Li, Y. Zhu, M. G. Kanatzidis, J. He, Superior thermoelectric performance in PbTe-PbS pseudo-binary: extremely low thermal conductivity and modulated carrier concentration, Energ. Environ. Sci. 8 (2015) 2056–2068.

[17] C. Fu, T. Zhu, Y. Liu, H. Xie, X. Zhao, Band engineering of high performance p-type FeNbSb based half-Heusler thermoelectric materials for figure of merit zT > 1, Energ. Environ. Sci. 8 (2015) 216–220.

[18] J. P. Heremans, V. Jovovic, E. S. Toberer, A. Saramat, K. Kurosaki, A. Charoenphakdee, S. Yamanaka, G. J. Snyder, Enhancement of thermoelectric efficiency in PbTe by distortion of the electronic density of states, Science 321 (2008) 554–557.

[19] L. D. Hicks, M. S. Dresselhaus, Thermoelectric figure of merit of a one-dimensional conductor, Phys. Rev. B 47 (1993) 16631–16634.

[20] G. J. Snyder, E. S. Toberer, Complex thermoelectric materials, Nat. Mater. 7 (2008) 105–114.

[21] G. Joshi, H. Lee, Y. Lan, X. Wang, G. Zhu, D. Wang, R. Gould, D. C. Cuff, M. Y. Tang, M. S. Dresselhaus, G. Chen, Z. Ren, Enhanced thermoelectric figure-of-merit in nanostructured p-type silicon germanium bulk alloys, Nano. Lett. 8 (2008) 4670–4674.

[22] L.-D. Zhao, S.-H. Lo, Y. Zhang, H. Sun, G. Tan, C. Uher, C. Wolverton, V. P. Dravid, M. G. Kanatzidis, Ultralow thermal conductivity and high thermoelectric figure of merit in SnSe crystals, Nature 508 (2014) 373–377.

[23] S. R. Brown, S. M. Kauzlarich, F. Gascoin, G. J. Snyder, Yb$_{14}$MnSb$_{11}$: New high efficiency thermoelectric material for power generation, Chem. Mater. 18 (2006) 1873–1877.

[24] D. M. Rowe, CRC Handbook of Thermoelectrics, 89th Edition, CRC Press, Boca Raton, FL, 1995.

[25] M. Ohtaki, K. Araki, K. Yamamoto, High thermoelectric performance of dually doped ZnO ceramics, J. Electron. Mater. 38 (2009) 1234–1238.

[26] N. V. Nong, N. Pryds, S. Linderoth, M. Ohtaki, Enhancement of the thermoelectric performance of p-type layered oxide $Ca_3Co_4O_{9+\delta}$ through heavy doping and metallic nanoinclusions, Adv. Mater. 23 (2011) 2484–2490.

[27] J. Sui, J. Li, J. He, Y.-L. Pei, D. Berardan, H. Wu, N. Dragoe, W. Cai, L.-D. Zhao, Texturation boosts the thermoelectric performance of BiCuSeO oxyselenides, Energ. Environ. Sci. 6 (2013) 2916–2920.

[28] Y. Liu, L.-D. Zhao, Y. Zhu, Y. Liu, F. Li, M. Yu, D.-B. Liu, W. Xu, Y.-H. Lin, C.-W. Nan, Synergistically optimizing electrical and thermal transport properties of BiCuSeO via a dual-doping approach, Adv. Energy Mater. 6 (2016) 1502423.

[29] G.-K. Ren, S.-Y. Wang, Y.-C. Zhu, K. J. Ventura, X. Tan, W. Xu, Y.-H. Lin, J. Yang, C.-W. Nan, Enhancing thermoelectric performance in hierarchically structured BiCuSeO by increasing bond covalency and weakening carrier-phonon coupling, Adv. Energy Mater. 10 (2017) 1590–1599.

[30] C. Barreteau, D. Berardan, N. Dragoe, Studies on the thermal stability of BiCuSeO, J. Solid State Chem. 222 (2015) 53–59.

[31] D. Narducci, Wo we really need high thermoelectric figure of merit? A critical appraisal to the power conversion efficiency of thermoelectric materials, Appl. Phys. Lett. 99 (2011) 102104–1–102104–3.

[32] Y. Miyazaki, Crystal structure and thermoelectric properties of the misfit-layered cobalt oxides, Solid State Ionics 172 (2004) 463–467.

[33] M. Bittner, L. Helmich, F. Nietschke, B. Geppert, O. Oeckler, A. Feldhoff, Porous $Ca_3Co_4O_9$ with enhanced thermoelectric properties derived from sol-gel synthesis, J. Eur. Ceram. Soc. 37 (2017) 3909–3915.

[34] N. Kanas, S. P. Singh, M. Rotan, M. Saleemi, M. Bittner, A. Feldhoff, T. Norby, K. Wiik, T. Grande, M.-A. Einarsrud, Influence of processing on stability, microstructure and thermoelectric properties of $Ca_3Co_{4-x}O_{9+\delta}$, J. Eur. Ceram. Soc. 38 (2018) 1592–1599.

[35] G. Xu, R. Funahashi, M. Shikano, I. Matsubara, Y. Zhou, Thermoelectric properties of the Bi- substituted $Ca_3Co_4O_9$ system, Appl. Phys. Lett. 80 (2002) 3760–3762.

[36] Y. Masuda, D. Nagahama, H. Itahara, T. Tani, W. S. Seo, K. Koumoto, Thermoelectric performance of Bi- and Na-substituted $Ca_3Co_4O_9$ improved through ceramic texturing, J. Mater. Chem. 13 (2003) 1094–1099.

[37] A. I. Klyndyuk, I. V. Matsukevich, Synthesis and properties of $Ca_{2.8}Ln_{0.2}Co_4O_{9+\delta}$ (Ln = La, Nd, Sm, Tb-Er) solid solutions, Inorg. Mater+. 48 (2012) 1052–1057.

[38] S. Saini, H. S. Yaddanapudi, K. Tian, Y. Yin, D. Magginetti, A. Tiwari, Terbium ion doping in $Ca_3Co_4O_9$: A step towards high-performance thermoelectric materials, Sci. Rep-UK. 7 (2017) 44621.

[39] H. Leligny, D. Grebille, O. Pérez, A. C. Masset, M. Hervieu, B. Raveau, A five-dimensional structural investigation of the misfit layer compound $[Bi_{0.87}SrO_2]_2[CoO_2]_{1.82}$, Acta Cryst. B B56 (2000) 173–182.

[40] E. Guilmeau, M. Pollet, D. Grebille, M. Hervieu, M. Muguerra, R. Cloots, M. Mikami, R. Funahashi, Nanoblock coupling effect in iodine intercalated $[Bi_{0.82}CaO_2]_2[CoO_2]_{1.69}$ layered cobaltite, Inorg. Chem. 46 (2007) 2124–2131.

[41] A. Sotelo, E. Guilmeau, S. Rasekh, M. A. Madre, S. Marinel, J. C. Diez, Enhancement of the thermoelectric properties of directionally grown Bi-Ca-Co-O through Pb for Bi substitution, J. Eur. Ceram. Soc. 30 (2010) 1815–1820.

[42] I. V. Matsukevich, A. I. Klyndyuk, E. A. Tugova, A. N. Ko-

valenko, A. A. Marova, N. S. Krasutskaya, Thermoelectric properties of $Ca_{3-x}Bi_xCo_4O_{9+delta}$ ($0.0 \leq x \leq 1.5$) ceramics, Inorg. Mater+. 52 (2016) 644–650.

[43] A. Feldhoff, M. Arnold, J. Martynczuk, T. M. Gesing, H. Wang, The sol-gel synthesis of perovskites by EDTA/citrite complexing method involves nanoscale solid state reactions, Solid State Sci. 10 (2008) 689–701.

[44] T. Janssen, A. Janner, A. Looijenga-Vos, P. M. De Wolff, International Tables for Crystallography: 9.8 Incommensurate and commensurate modulated structures, Volume C Edition, Kluwer Academic Publishers, Dordrecht/Boston/London, 2004.

[45] M. Lee, L. Viciu, Y. Wang, M. L. Foo, S. Watauchi, R. A. Pascal JR, R. J. Cava, N. P. Ong, Large enhancement of the thermopower in Na_xCoO_2 at high Na doping, Nat. Mater. 5 (2006) 537–540.

[46] T. Sun, H. H. Hng, Q. Y. Yan, J. Ma, Enhanced high temperature thermoelectric properties of Bi-doped c-axis oriented $Ca_3Co_4O_9$ thin films by pulsed laser deposition, J. Appl. Phys. 108(8) (2010) 3709.

[47] Q. Zhu, E. M. Hopper, B. J. Ingram, T. O. Mason, Combined Jonker and Ioffe analysis of oxide conductors and semiconductors, J. Am. Ceram. Soc. 94 (2011) 187–193.

[48] J.-W. Moon, D. Nagahama, Y. Masuda, W.-S. Seo, K. Koumoto, Anisotropic thermoelectric properties of crystal-axis oriented ceramics of layer-structured oxide in the Ca-Co-O system, J. Ceram. Soc. Jpn. 109 (2001) 647–650.

[49] C.-H. Lim, H.-H. Park, S.-M. Choi, K.-H. Lee, K. Park, Anisotropy of the thermoelectric figure of merit (ZT) in textured $Ca_3Co_4O_9$ ceramics prepared by using a spark plasma sintering process, J. Korean. Phys. Soc. 66 (2015) 794–799.

[50] D. Kenfaui, B. Lenoir, D. Chateigner, B. Ouladdiaf, M. Gomina, J. G. Noudem, Development of multilayer textured $Ca_3Co_4O_9$ materials for thermoelectric generators: Influence of the anisotropy on the transport properties, J. Eur. Ceram. Soc. 32 (2012) 2405–2414.

[51] D. Kenfaui, D. Chateigner, M. Gomina, J. G. Noudem, B. Ouladdiaf, A. Dauschner, B. Lenoir, Volume texture and anisotropic thermoelectric properties in $Ca_3Co_4O_9$ bulk materials, Mater. Today. 2 (2015) 637–646.

[52] O. Jankovsky, D. Sedmidubsky, Z. Sofer, J. Hejtmanek, Thermodynamic behavior of $Ca_3Co_4O_{9+\delta}$ ceramics, Ceram-Silikaty 56(2) (2012) 139–144.

[53] J.-Y. Tak, K. H. Lee, J.-Y. Kim, C.-H. Lim, W.-S. Seo, Y. S. Lim, H. K. Cho, S.-M. Choi, Optimization of synthesis conditions of $Na_{0.75}CoO_2$ for high thermoelectric performance, J. Electron. Mater. 44 (2014) 1408–1412.

Supplementary information for
"Triple-phase ceramic 2D nanocomposite with enhanced thermoelectric properties"

Michael Bittner[1], Nikola Kanas[2], Richard Hinterding[1], Frank Steinbach[1],
Dennis Groeneveld[1], Piotr Wemhoff[1], Kjell Wiik[2], Mari-Ann Einarsrud[2],
Armin Feldhoff[1]

[1]Institute of Physical Chemistry and Electrochemistry,
Leibniz University Hannover, Germany

[2]Department of Materials Science and Engineering,
Norwegian University of Science and Technology, Norway

1

1   Supplementary

Schemes, diagrams both SEM and TEM micrographs were created using Orig-
inPro 9.1G, ImageJ, Diamond and Digital Micrograph. Figures were arranged,
merged and saved using PowerPoint 2010 and Photoshop CS5. Table S 1 shows
the ionic radii of the substituted elements and inserted dopants. According to the
similarity of the ionic radii of the elements used, doping should be possible. The
XRD patterns of the Na_xCoO_2 (NCO) and $Bi_2Ca_2Co_2O_9$ (BCCO) phases, shown
in Figure S 1 refer to Figure 2 in the main text. A step size of 0.003942, a time
per step of 1.1 seconds, a voltage of 40 kV and a current of 40 mA were used in
the XRD experiments. Pure NCO and nearly pure BCCO phases were subjected
to SEM and elemental distribution analyses of polished cross-sections, as shown
in Figure S 2a-d. Vibration-polished cross-section specimens were prepared by a
multistep (30 μm, 15 μm, 6 μm, 3 μm and 1 μm diamond lapping films) polish-
ing program using a Techprep from Allied - High Tech Products, Inc., followed
by vibration polishing using a Buehler Vibromet-2 and a 50 nm colloidal alumina
suspension. TEM specimens were prepared similar to SEM specimens and put
on a TEM grid. The specimens were pinched out using a precision ion polishing
system (Ar-ion) Model 691 from Gatan. The BCCO phase decomposes at approx-
imately 1023 K, and Ca-containing phases are formed; see Figure S 1[1]. Figure
S 3 gives detailed elemental distribution information referring to Figure 4a-c in
the main document. The interdiffusion of Ca into the NCO phase is clearer, and
the very thin layers of NCO and BCCO are clearly visible in the Na, Ca and Bi
signals shown in Figure S 3d-f. The insets of Figure 4d-f in the main document are
enlarged for a better readability in Figure S 4a-f. Additional TEM micrographs
of other sites of the CCO-30-35-10 nanocomposite ceramic are shown in Figures
S 5, 6 and 7. These other sites clarify the composition and thickness of differ-
ent layers within the material. These sequences continue throughout the ceramic.
Comparing Figure S 5 and Figure S 6 shows that the amount of interdiffusion of
Ca into the NCO phase is not constant, suggesting that the degree of interdiffusion
might also depends on thickness and surroundings (e.g., being embedded between
BCCO phases). Figure S 8 illustrates the measured heat capacities C_P of CCO and
nanocomposite ceramics as a function of temperature in the range from 313 K to
1173 K. The C_P values reached approximately 0.83 J $\cdot$ g^{-1} $\cdot$ K^{-1} at 1073 K for
a CCO-30-35-10 nanocomposite ceramic. The nanocomposite ceramics showed
only small differences in C_P from those of undoped CCO. The system was cali-
brated and the sapphire method was used. The sensitivity S and heat capacity C_P
were calculated as described by Jankovsky et al.[2]. Samples of bar geometry were

2

cut from a ceramic pellet using an O'Well model 3242 precision vertical diamond wire saw.

1.1 Figures
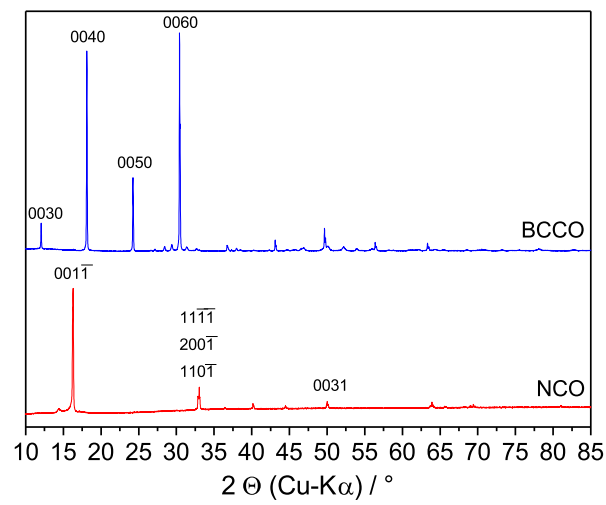
Figure S 1: XRD patterns of **NCO** and **BCCO** with indexed reflections according to superspace group C2/m^{3} and P2/m[4]. NCO and BCCO were obtained after sintering at 1073 and 1123 K for 10 hours, respectively.

3
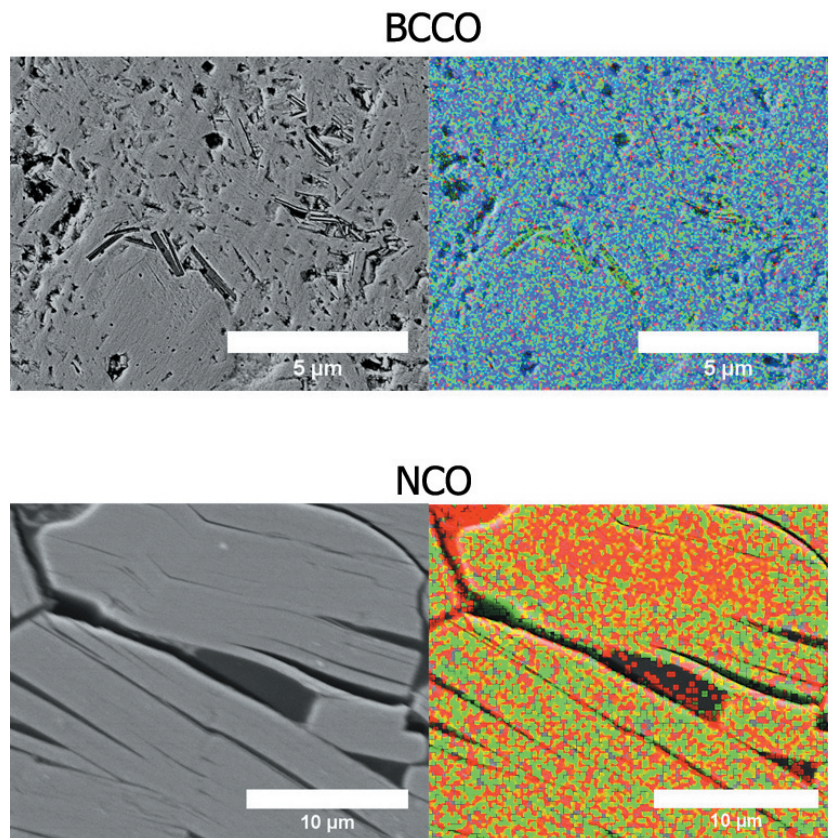
Figure S 2: SEM cross-sectional micrographs and EDXS elemental distributions of a, b) **BCCO** ceramic (Ca-green, Bi-blue and Co-red) and c, d) **NCO** ceramic (Na-green and Co-red).

4
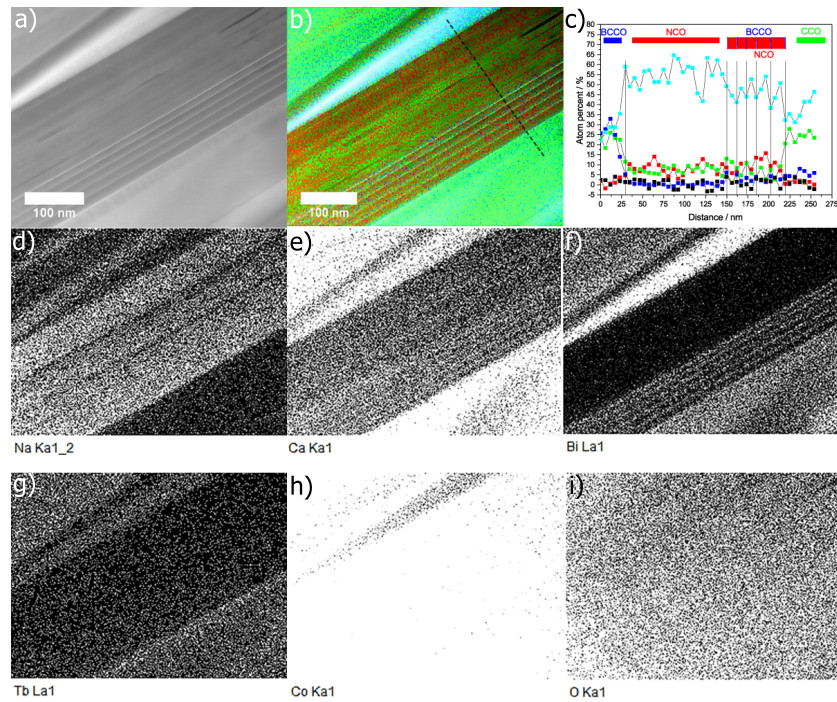
Figure S 3: TEM analysis of a **CCO-30-35-10** nanocomposite ceramic, supplementing Figure 4a-c) of the main document. a, b) STEM dark-field micrograph and EDXS elemental distribution of the region shown. c) Linescan of the elemental distribution of Na (red), Ca (green), Bi (blue), Tb (black) and Co (turquoise) shown in b). Along the indicated direction (dotted line), different phases and their compositions along the linescan are indicated. d-i) Detailed elemental distribution information for Na, Ca, Bi, Co, Tb and O.

5
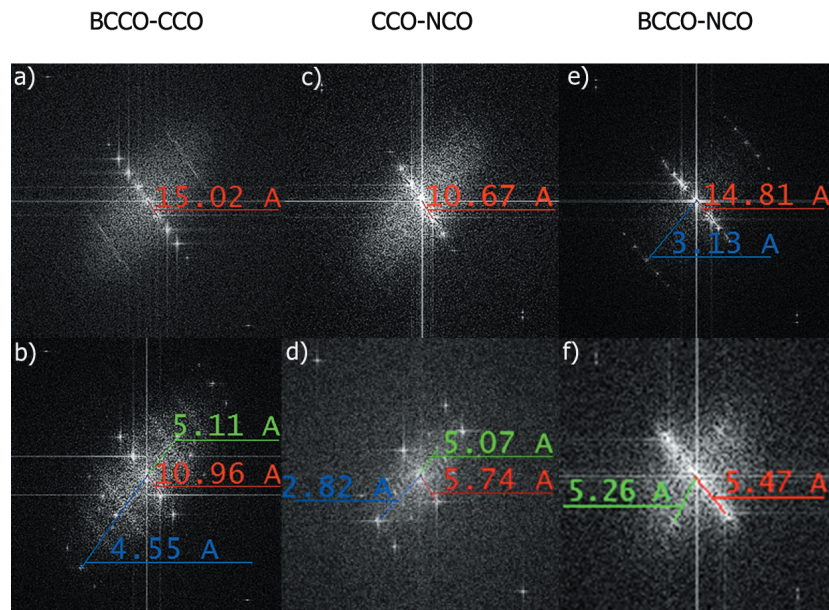
Figure S 4: Enlarged presentation of reduced fast Fourier transformations in insets of Figure 4d-f) showing the TEM analysis of a **CCO-30-35-10** nanocomposite ceramic: a, b) BCCO-CCO-interface; c, d) CCO-NCO-interface; and e, f) BCCO-NCO-interface with indicated lattice parameters of a (green), b (blue) and c (red).
BCCO-CCO: BCCO - c= 15.02 Å, CCO - a= 5.11 Å, b_2= 4.55 Å, c= 10.96 Å
CCO-NCO: CCO - c= 10.67 Å, NCO - a= 5.07 Å, b_1= 2.82 Å, c= 5.74 Å
BCCO-NCO: BCCO - b_1= 3.13 Å, c= 14.81 Å, NCO - a= 5.26 Å, c= 5.47 Å

6
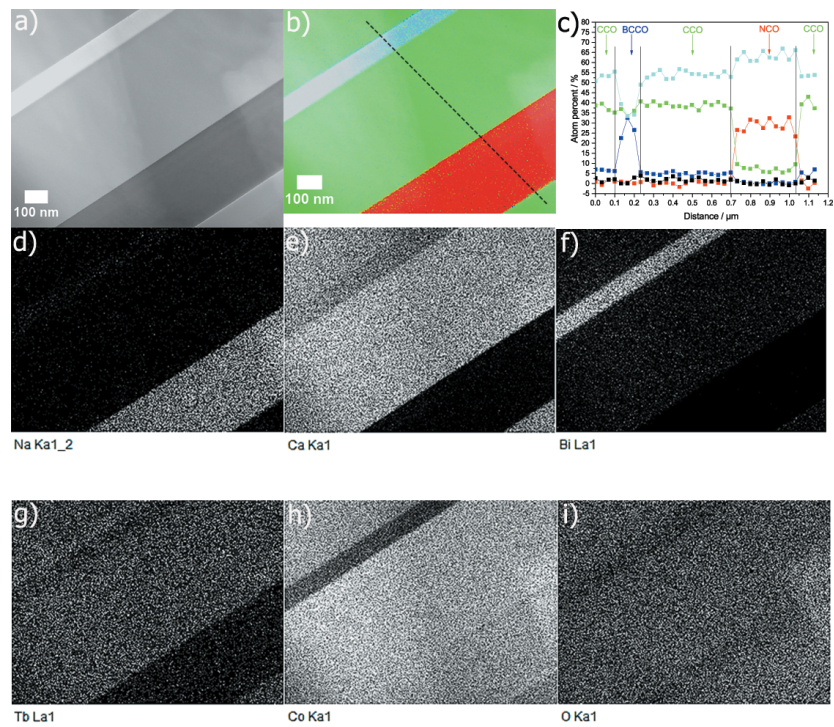
Figure S 5: TEM analysis of a second site of a **CCO-30-35-10** nanocomposite ceramic, a, b) STEM dark-field micrograph and EDXS elemental distribution of the area shown. c) Linescan of the elemental distribution of Na (red), Ca (green), Bi (blue), Tb (black) and Co (turquoise) shown in b). Along the indicated direction (dotted line), different phases and their compositions along the linescan are indicated. d-i) Detailed elemental distribution information for Na, Ca, Bi, Co, Tb and O.

7
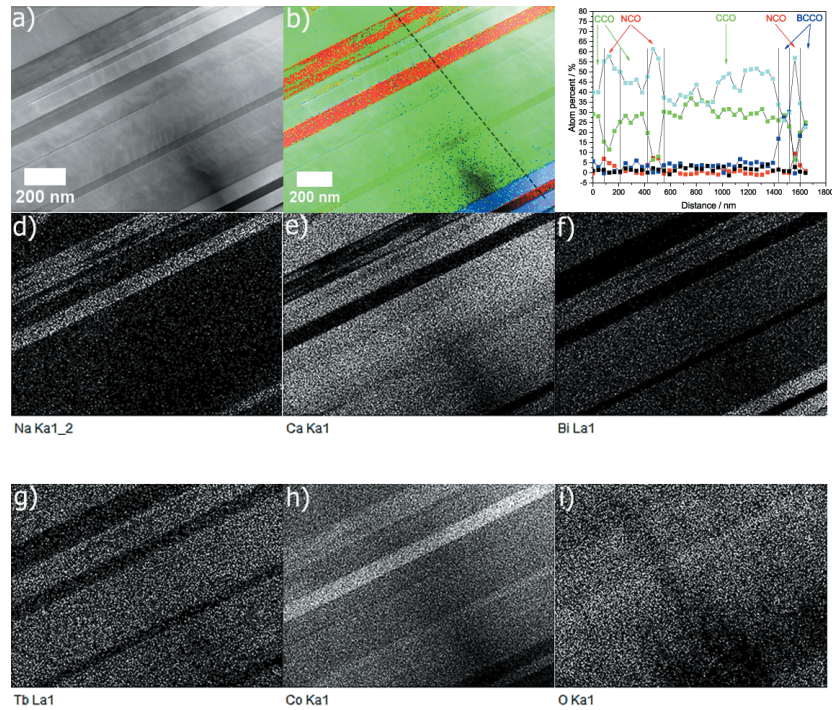
Figure S 6: TEM analysis of a third site of a **CCO-30-35-10** nanocomposite ceramic, a, b) STEM dark-field micrograph and EDXS elemental distribution of the area shown. c) Linescan of the elemental distribution of Na (red), Ca (green), Bi (blue), Tb (black) and Co (turquoise) shown in b). Along the indicated direction (dotted line), different phases and their compositions along the linescan are indicated. d-i) Detailed elemental distribution information for Na, Ca, Bi, Co, Tb and O.

8
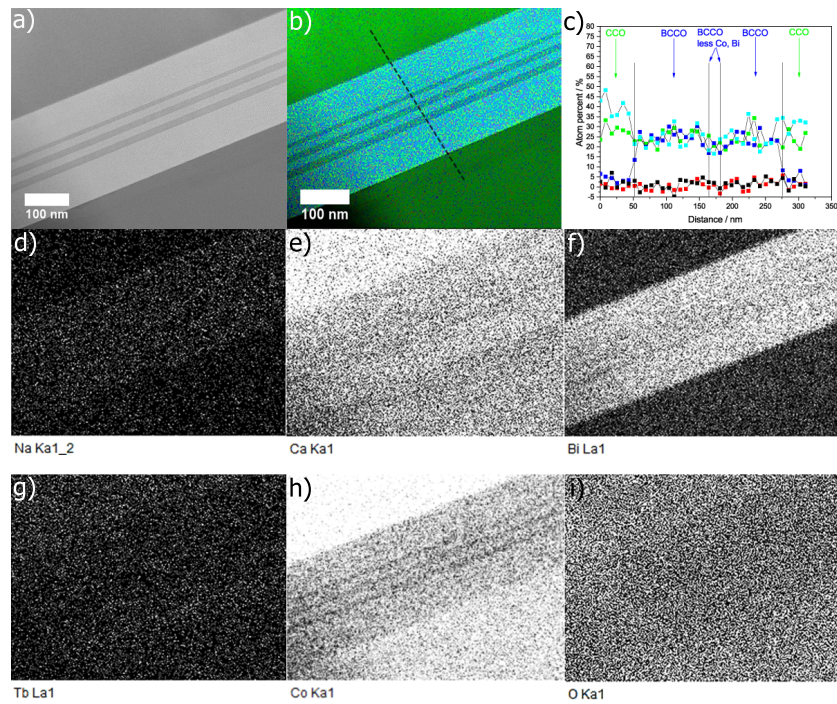
Figure S 7: TEM analysis of a fourth site of a **CCO-30-35-10** nanocomposite ceramic, a, b) STEM dark-field micrograph and EDXS elemental distribution of the area shown. c) Linescan of the elemental distribution of Na (red), Ca (green), Bi (blue), Tb (black) and Co (turquoise) shown in b). Along the indicated direction (dotted line), different phases and their compositions along the linescan are indicated. d-i) Detailed elemental distribution information for Na, Ca, Bi, Co, Tb and O.

9
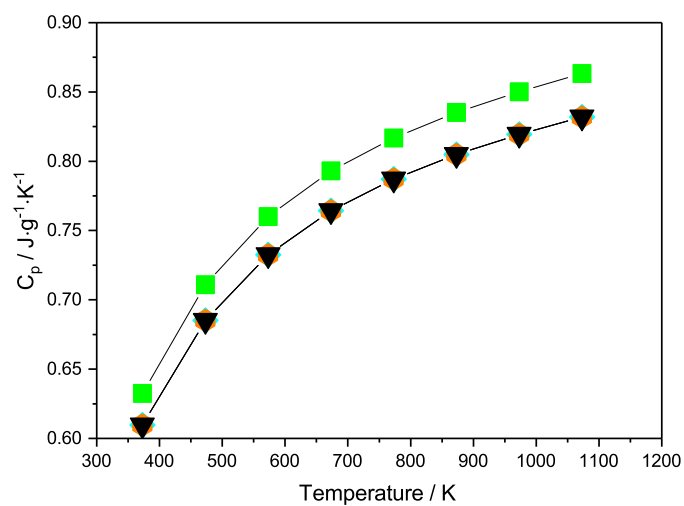
Figure S 8: Heat capacity C_P as a function of temperature of **CCO** (squares, green, taken from [5]), **CCO-30-35-6** (diamonds, turquoise), **CCO-30-35-8** (hexagons, orange) and **CCO-30-35-10** (inverted triangles, black) ceramics.

10

1.2 Tables

Table S 1: Ionic radii of cations and dopants in $Ca_{3-x-y-z}Na_xBi_yTb_zCo_4O_9$ [6].

Element	Ca	Na	Bi	Tb	Co		
coordination number	6	6	6	6	8		
ionic charge	+2	+1	+3	+3	+4	+3	+4
ionic radii / Å	1.12	1.18	1.17	1.04	0.88	0.61	0.53

References

[1] A. Sotelo, E. Guilmeau, S. Rasekh, M. A. Madre, S. Marinel, J. C. Diez, Enhancement of the thermoelectric properties of directionally grown Bi-Ca-Co-O through Pb for Bi substitution, J. Eur. Ceram. Soc. 30 (2010) 1815–1820.

[2] O. Jankovsky, D. Sedmidubsky, Z. Sofer, J. Hejtmanek, Thermodynamic behavior of $Ca_3Co_4O_{9+\delta}$ ceramics, Ceram-Silikaty 56(2) (2012) 139–144.

[3] L. Viciu, J. W. G. Bos, H. W. Zandbergen, Q. Huang, M. L. Foo, S. Ishiwata, A. P. Ramirez, M. Lee, N. P. Ong, R. J. Cava, Crystal structure and elementary properties of Na_xCoO_2 (x = 0.32, 0.51, 0.6, 0.75, and 0.92) in the three-layer $NaCoO_2$ family, Phys. Rev. B 73 (2006) 174104–1–174104–10.

[4] E. Guilmeau, M. Pollet, D. Grebille, M. Hervieu, M. Muguerra, R. Cloots, M. Mikami, R. Funahashi, Nanoblock coupling effect in iodine intercalated $[Bi_{0.82}CaO_2]_2[CoO_2]_{1.69}$ layered cobaltite, Inorg. Chem. 46 (2007) 2124–2131.

[5] M. Bittner, L. Helmich, F. Nietschke, B. Geppert, O. Oeckler, A. Feldhoff, Porous $Ca_3Co_4O_9$ with enhanced thermoelectric properties derived from sol-gel synthesis, J. Eur. Ceram. Soc. 37 (2017) 3909–3915.

[6] R. D. Shannon, Revised effective ionic radii and systematic studies of interatomic distances in halides and chalcogenides, Acta Cryst. A32 (1976) 751–767.

3 Thermoelectric generators

3.1 Summary

Thermoelectric (TE) generators (TEGs) were constructed by a series connection of p- and n-type materials in the conventional chess-board and the all-oxide design. These different possibilities to assemble a TEG offer variable advantages and disadvantages, depending on the desired application.

In section 3.2, an oxide-based TEG for high-temperature application in air is presented, which was made in conventional chess-board design using p-type $Ca_3Co_4O_9$ (CCO) and n-type $In_{1.95}Sn_{0.05}O_3$ legs. The use of an electrically highly conducting indium oxide phase improved both the electrical power output and power density, compared to TEGs with other n-type materials like ZnO or $CaMnO_3$ (CMO).

In section 3.3, a finite element simulation tool was applied to a TEG prototype with conventional chess-board design. The simulation tool was used to predict and estimate power characteristics of a TEG. Input parameters were TE properties of p- and n-type materials and their contact resistances. The importance of minimizing the contact resistance between the p-, n-type materials and the metallic connectors, to enhance the electrical power output and electrical power density, is discussed.

In section 3.4, a novel all-oxide TEG based on p-type CCO and n-type CMO was manufactured via spark plasma sintering and was characterized in terms of its power characteristics. The single materials were chosen based on their thermal expansion coefficients and TE properties, which were investigated and represented in detail. The complex p-p-n junction, which was formed at high-temperatures showed beneficial impact on the electrical power output of the TEG by decreasing its contact resistance and boosting electrical voltage by a transversal thermoelectric effect. Due to its oxide-based p-p-n-junction, the all-oxide generator design is usable at higher temperatures compared to a conventional generator with metallic connectors.

In section 3.5, a comprehensive study on the influence of the TE properties on the electrical power output and power density of conventional TEGs is presented. The electrical conductivity and TE power factor (Ioffe plot) of the p-type $Ca_3Co_4O_9$-Na_xCoO_2-$Bi_2Ca_2Co_2O_9$ (CCO-NCO-BCCO) nanocomposite was improved by different applied processing techniques. New n-type indium oxides with high TE power factor or zT value were developed by co-doping. These specifically developed p- and n-type materials were used in three TEG prototypes to evaluate the impact of high-power or high-zT materials on the TE power generation at high temperatures from infinite heat sources in air. The highest electrical power density of oxide-based TEGs was obtained from high-power materials.

3.2 Oxide-based thermoelectric generator for high-temperature application using p-type $Ca_3Co_4O_9$ and n-type $In_{1.95}Sn_{0.05}O_3$ legs

Michael Bittner, Benjamin Geppert, Nikola Kanas,

Sathya Prakash Singh, Kjell Wiik and Armin Feldhoff

Michael Bittner*, Benjamin Geppert, Nikola Kanas, Sathya Prakash Singh, Kjell Wiik
and Armin Feldhoff

Oxide-Based Thermoelectric Generator for High-Temperature Application Using p-Type $Ca_3Co_4O_9$ and n-Type $In_{1.95}Sn_{0.05}O_3$ Legs

Abstract: A thermoelectric generator couples an entropy current with an electrical current in a way, that thermal energy is transformed to electrical energy. Hereby the thermoelectric energy conversion can be described in terms of fluxes of entropy and electric charge at locally different temperature and electric potential. Crucial for the function of a thermoelectric generator is the sign and strength of the coupling between the entropy current and the electrical current in the thermoelectric materials. For high-temperature application, tin-doped indium oxide ($In_{1.95}Sn_{0.05}O_3$) and misfit-layered calcium cobalt oxide ($Ca_3Co_4O_9$) ceramics were used as n- and p-type legs. The n-type material reaches a power factor of $6.8\,\mu W \cdot cm^{-1} \cdot K^{-2}$ at 1,073 K and a figure of merit ZT of 0.07. The p-type material reaches $1.23\,\mu W \cdot cm^{-1} \cdot K^{-2}$ and a figure of merit ZT of 0.21 at 1,073 K. A thermoelectric generator consisting of ten legs was characterized for different invested temperatures. It delivers 4.8 mW maximum power output and a electrical power density of $2.13\,mW \times cm^{-2}$ when the hot side is at 1,073 K and a temperature difference of 113 K is applied.

Keywords: Thermoelectric power generation, Module, Oxide materials, $Ca_3Co_4O_9$, $In_{2-x}Sn_xO_3$

Introduction

Thermoelectric (TE) materials got lately more and more attention due to climate change and thereby their ability to utilize waste heat from power plants and combustion engines. A thermoelectric generator, which is made of those materials can convert thermal energy into electrical energy. Research in the field of thermoelectric materials focuses on improving the figure of merit ZT, which was originally derived by Ioffe (1957) and is shown in eq. [1]. Improving the figure of merit ZT is one approach to enhance the efficiency of the energy conversion system.

$$ZT := \frac{\sigma \cdot \alpha^2}{\Lambda} \qquad [1]$$

The involved material parameters are the isothermal electrical conductivity σ, the Seebeck coefficient α and the electric open-circuit entropy conductivity Λ. For clarity the latter is preferred over the thermal energy ("heat") conductivity λ, which is related to it by eq. [2]; see Fuchs (2010) and Feldhoff (2015):

$$\lambda = \Lambda \cdot T \qquad [2]$$

For high-temperature electric power generation in air, n- and p-type semi-conducting thermoelectric oxides are supposed to be promising materials, due to their advantages, such as non-toxicity, thermal and mechanical stability at high temperatures and moreover high chemical stability under oxidizing conditions; see Rowe (1995). Several publications focus on the layer-structured cobalt oxide $Ca_3Co_4O_9$, based on CaO, and Sn-doped indium oxide ($In_{2-x}Sn_xO_3$) due to their high power factor $\sigma \cdot \alpha^2$ and thus the efficiency of TEGs made of it, see Xu et al. (2002), Miyazaki (2004), Bérardan et al. (2008) and Guilmeau et al. (2009).

$Ca_3Co_4O_9$ exhibits a misfit-layered structure, which consists of CdI_2-type CoO_2 triangular lattice and a layered rock-salt part of three Ca_2CoO_3 units which are stacked alternatingly along the c-axis. The electronic structure of $Ca_3Co_4O_9$ is beneficial for thermoelectric applications due to it's density of states (DOS), which consists of two non-bonding, degenerated e'_g levels and thus a broad delocalized e'_g band and a bonding, non-degenerated a_{1g} level and thereby a localized a_{1g} band. The density of states near the Fermi energy E_F is schematically shown in Figure 1(a). The height of the Fermi energy E_F can be

*Corresponding author: Michael Bittner, Institute of Physical Chemistry and Electrochemistry, Leibniz Universität Hannover, Germany; Department of Materials Science and Engineering, NTNU Trondheim, Norway, E-mail: michael.bittner@pci.uni-hannover.de
Benjamin Geppert, Institute of Physical Chemistry and Electrochemistry, Leibniz Universität Hannover, Germany
Nikola Kanas, Sathya Prakash Singh, Kjell Wiik, Department of Materials Science and Engineering, NTNU Trondheim, Norway
Armin Feldhoff, Institute of Physical Chemistry and Electrochemistry, Leibniz Universität Hannover, Germany
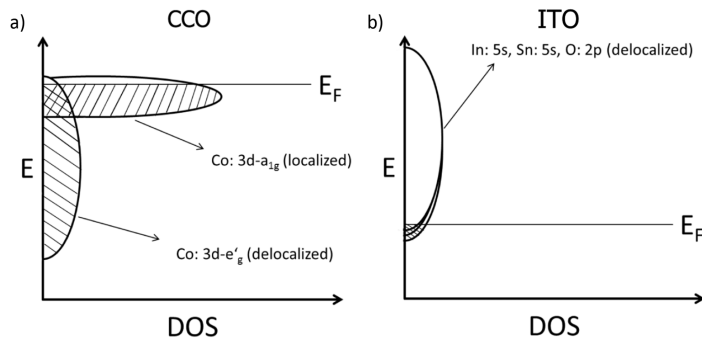
Figure 1: Schematic representation of the density of states (DOS) near the Fermi level E_F, occupied states (hatched) below E_F in: a) Co:3d energy levels of the rhombohedrally distorted CoO_6 octahedron (a_{1g} and e'_g) of $Ca_3Co_4O_9$ after Miyazaki (2004) and b) In:5s, Sn:5s and O:2p energy levels of $In_{1.95}Sn_{0.05}O_3$ after Yan and Wang (2012).

controlled by the valence state of cobalt cations. It can be adjusted with the aid of hole-doping, or with implementing dopants into the structure. When E_F crosses the border where the a_{1g} and e'_g orbitals are hybridized, according to Miyazaki (2004), a high electrical conductivity is expected due to a high density of unoccupied states in the electronic bands above the highest occupied state. The thermoelectric properties like electrical conductivity σ, Seebeck coefficient α and entropy conductivity Λ of $Ca_3Co_4O_9$ can be further enhanced by controlling the micro- and nano-structure. Liu et al. (2005) and Kenfaui et al. (2010) used spark plasma sintering (SPS) and Nagahama et al. (2002) a templated grain growth method to modify the structure of $Ca_3Co_4O_9$.

The Seebeck coefficient α can be expressed after eq. [3] for the degenerate case ($k_B T \ll E_F$) and depends on the ratio of the oxidation states of cobalt ($Co^{3+/4+}$); see Singh (2000) and Miyazaki (2004). Thereby $A(E)$ is proportional to the area of the DOS at the Fermi level E_F.

$$\alpha \sim -\left(\delta lnA(E)/\delta E\right)_{E=E_F} \qquad [3]$$

A prospective n-type oxide is In_2O_3, which is an indirect semiconductor with a band gap of 1.16 eV. The top of the valence band of In_2O_3 shows a small dispersion (localized states), made of hybridized O:2p and In:5d states. The bottom of the conduction band possesses a large dispersion (delocalized states; see Figure 1(b)), which mainly comes from the hybridized O:2p and In:5s orbitals. For heavily doped In_2O_3 or by use of Sn as dopant, the E_F is situated inside the conduction band; see Figure 1(b). The electrical conductivity is strongly affected by the electronic configuration near the Fermi level E_F. When Sn is used as a dopant for In_2O_3, a strong hybridization of the

Sn:5s, In:5s and O:2p orbitals forms antibonding states and thereby affects the states near the bottom of the conduction band, shown in Figure 1(b), which leads to a small band gap after Yan and Wang (2012).

The properties of tin-doped In_2O_3 (ITO) depend on the amount of Sn within the structure; see Guilmeau et al. (2009). For a low Sn fraction, $In_{2-x}Sn_xO_3$ possesses a medium effective mass $m^\star$ and a low carrier concentration n, which are both beneficial to the Seebeck coefficient α. For a highly degenerated semiconductor, the Seebeck coefficient α is defined after eq. [4], γ depends on the dominating scattering process (-0.5 for acoustic phonons, 0 for neutral impurities and 1.5 for ionized impurities); see Seeger (1991) and Guilmeau et al. (2009):

$$\alpha = \frac{2}{3}\left(\frac{\pi}{3}\right)^{\frac{2}{3}}\left(\gamma + \frac{2}{3}\right)\frac{k_B^2 m^\star}{e\hbar^2 n^{\frac{2}{3}}} \qquad [4]$$

Guilmeau et al. (2009) already carried out investigations about tin-doped In_2O_3, and it is assumed to be a promising thermoelectric n-type material. To our knowledge, no thermoelectric generator (TEG) has been constructed and characterized made of $Ca_3Co_4O_9$ as p-type and $In_{1.95}Sn_{0.05}O_3$ as n-type semiconductor.

Experimental

The thermoelectric materials, n-type $In_{1.95}Sn_{0.05}O_3$ (ITO) and p-type $Ca_3Co_4O_9$ (CCO), were synthesized via a sol-gel route, which allows obtaining fine-grained powders of homogenous composition as described by Feldhoff et al. (2008). The nitrates of accordant metal cations were stoichiometrically solved and added to an aqueous ammonia

solution of pH = 9 which also contained citric acid and ethylenediaminetetraacetic acid (EDTA) for complexing the soluted metal ions in the solution. Indium(III) nitrate hydrate from Alfa Aesar, 99.9 % trace metal basis was used as indium source and tin(II) acetate 95.0 % from Alfa Aesar as tin source. For $Ca_3Co_4O_9$, calcium(II) nitrate tetrahydrate ≥ 99.0% from Sigma Aldrich and cobalt(II) nitrate hexahydrate ACS 98–102.00 % from Alfa Aesar were used as sources. The obtained powders were calcined for 10 h at 973 K, in case of $In_{1.95}Sn_{0.05}O_3$ and for 5 h at 1,073 K in case of $Ca_3Co_4O_9$ with a heating and cooling rate of 3 min · K^{-1}, respectively. The calcined powders were cold pressed and sintered. The n-type material $In_{1.95}Sn_{0.05}O_3$ was sintered for 15 h at 1,873 K with a heating and cooling rate of 3 min · K^{-1}. The p-type material $Ca_3Co_4O_9$ was sintered for 10 h at 1,173 K with the same heating and cooling parameters. All steps, synthesis, calcination and sintering, were performed under ambient air conditions.

The phase compositions of synthesized powders and sintered ceramics for both materials were characterized by X-ray diffraction (XRD) using a Bruker D8 Advance with $Cu – K_\alpha$ radiation. A time per step of 0.3 s, a step size of 0.0105 °, a voltage of 40 kV and a current of 40 mA were applied for XRD measurement. Microstructural characterization was carried out by field-emission scanning electron microscope (FE-SEM) of the type JEOL JSM-6700F, which was equipped with an energy-dispersive X-ray spectrometer (EDXS) of the type Oxford Instruments INCA 300 for elemental analysis. N-type specimen were vibration-polished on a Buehler Vibromet-2 using 50 nm colloidal alumina suspension. P-type specimen were polished with a Struers Tegramin-20 using a multistep polishing program with colloidal diamond suspensions with grain sizes from 9 to 1 µm. Density measurements were performed by an Archimedes setup using ISO 5018:1983 (the International Organization for Standardization) in which the dry mass, mass in solvent and wet mass of the sample, was measured. The coefficient of thermal expansion (CTE) was estimated in synthetic air using a dilatometer DIL 402 C from Netzsch.

To determine the thermoelectric properties of the chosen materials, electrical conductivity σ, Seebeck coefficient α and entropy conductivity measurements Λ were measured as a function of temperature. Thereby the power factor $\sigma \cdot \alpha^2$ and the figure of merit ZT of $Ca_3Co_4O_9$ as well as for $In_{1.95}Sn_{0.05}O_3$ were estimated. Thermoelectric properties were measured with a home-made measurement cell after Indris (2001). The used furnace is an ELITE thermal system. The electronic parameters were measured with KEITHLEY 2100 $6\frac{1}{2}$ Digit Multimeters. Data were acquired and converted using LAB VIEW software. The measurements of

the heat conductivity λ and entropy conductivity Λ, respectively were carried out by a laser flash setup LFA 457 MicroFlash from Netzsch.

Characterization of the thermoelectric generator and estimation of ZT of the module were realized with a load-resistance dependent measurement under steady-state conditions, as shown schematically in Figure 2.
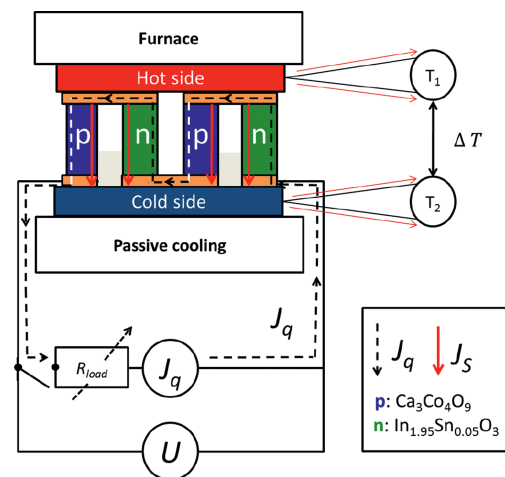
Figure 2: Sketch of the measurement setup to characterize the oxide-based thermoelectric generator in ambient air. Remind the alternating directions of coupling an entropy current J_S with an electrical current J_q in p- ($\alpha > 0$) and n-type ($\alpha < 0$) semiconducting legs. If a closed electrical circuit is present (closed switch), a circular electrical current (drawn in dotted lines) is driven by the entropy currents (red arrows), which expresses the power conversion. When the switch is open, the open circuit voltage is measured. Electrical current J_q and voltage U are measured with multimeters as a function of the load resistance R_{load}, which are adjusted by a variable resistor. The temperatures T_1 and T_2 and thereby the temperature difference ΔT between hot and cold side are measured with Pt-Rh thermocouples, which are operated in electrical open-circuit conditions. Here, entropy fluxes are present but small as compared to the ones running the generator.

Materials Properties

To verify the crystal structure and phase purity of n- and p-type powders and ceramics, XRD analyses were carried out. The $Ca_3Co_4O_9$ powder obtained after calcination at 1,073 K for 5 h is phase pure. After cold pressing and sintering at 1,173 K for 10 h a pure $Ca_3Co_4O_9$ ceramic was obtained. Comparing the powder pattern with the pattern of the $Ca_3Co_4O_9$ ceramic, a texture is visible (reflection 2010 (overbar on 2)); see Figure 3(a). Based on the results of
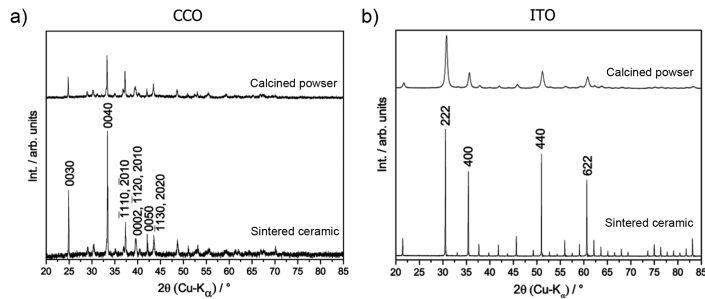
Figure 3: X-ray diffraction patterns of: a) CCO calcined powder and sintered ceramic, indexed reflections of superspace group Cm (0 1-p 0), equivalent to Bm (0 0 γ), no. 8.3; see Prince (2004) and b) ITO calcined powder and sintered ceramic, indexed reflections of space group Ia-3 (no. 206), taken from PDF-2 database (01-089-4596).

Miyazaki et al. (2002), a Rietveld refinement, utilizing Topas 4.2 software, was performed to analyze the $Ca_3Co_4O_9$ ceramic. The best results were accomplished for superspace group Cm (0 1-p0), equivalent to Bm (0 0 γ), no. 8.3; see Prince (2004), the crystal system was monoclinic base-centered with $a = 4.84\,Å$, $c = 10.84\,Å$, $\beta = 96.11°$ and $\alpha = \gamma = 90°$. The b-axis was refined to be $b_1 = 2.82\,Å$ for the CoO_2 subsystem and $b_2 = 4.55\,Å$ for the Ca_2CoO_3 subsystem; see Miyazaki et al. (2002). For the n-type material $In_{1.95}Sn_{0.05}O_3$, a pure nanopowder is obtained after calcination at 973 K for 10 h. The powder got pressed and sintered at 1,873 K for 15 h and a pure $In_{1.95}Sn_{0.05}O_3$ ceramic was

obtained; see Figure 3(b). It crystallized in space group Ia-3 (no. 206) in a cubic body-centered unit cell with $a = 10.12\,Å$, taken from PDF-2 database (01-089-4596).

For microstructural characterization of the thermoelectric materials by SEM, the sintered ceramics were prepared by polishing steps. The n-type ceramic was treated with a multistep polishing program followed by vibration polishing. The p-type material was also prepared with a multistep polishing program finished with a fine polishing step with a diamond grains solution. Figure 4 reveals the results of microstructural investigation of the n-type $In_{1.95}Sn_{0.05}O_3$ and p-type $Ca_3Co_4O_9$ materials.
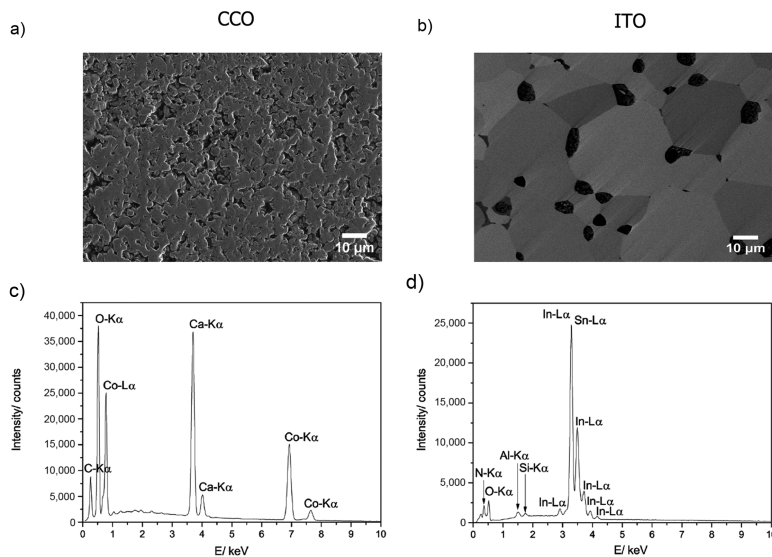
Figure 4: a,b) Sintered ceramics prepared by a single polishing program for $Ca_3Co_4O_9$ sample, and polishing and vibration-polishing program for $In_{1.95}Sn_{0.05}O_3$ sample, analyzed cross-section in SEM, c,d) EDX spectra of $Ca_3Co_4O_9$ and $In_{1.95}Sn_{0.05}O_3$ ceramic.

The SEM investigations of the $Ca_3Co_4O_9$ polished sample shown in Figure 4(a) exhibits no visible grain distribution of the p-type material. The sintered $Ca_3Co_4O_9$ ceramic shows a high porosity with a connected pore network. Figure 4(c) shows the EDX spectra of the $Ca_3Co_4O_9$ sample, a C peak due to the polishing steps is obtained in the spectrum but no other impurities. The SEM investigations in Figure 4(b, d), of the vibration-polished $In_{1.95}Sn_{0.05}O_3$ sample, show grain sizes which are varying from 10 to 40 μm. The sample possesses a closed porosity. The pores are isolated and do not form a network. An Al peak was detected in the EDX spectrum, shown in Figure 4(d). This can be explained by the insertion of Al_2O_3 nanoparticles into the pores during the vibration-polishing step. In the elemental distribution analysis made by EDX no impurities are visible except those of the polishing steps, i. e. Al and Si.

Density measurements of the n-type $In_{1.95}Sn_{0.05}O_3$ and p-type $Ca_3Co_4O_9$ materials were performed with an Archimedes setup. For the n-type material, 92.12% of the theoretical density could be achieved. The sintered $Ca_3Co_4O_9$ sample achieved a theoretical density of 54.0% only. Table 1 shows the measured values for the

density of the bulk ceramic as well as calculated values for open porosity, true porosity and closed porosity for both materials.

These measurements confirm the SEM investigations. $In_{1.95}Sn_{0.05}O_3$ possesses a low open porosity and a slightly higher closed porosity. $Ca_3Co_4O_9$ exhibits a high open porosity and almost no closed porosity. This indicates that there is a connected network present between the pores. The coefficient of thermal expansion was measured with a dilatometer from Netzsch 402C as a function of temperature for $In_{1.95}Sn_{0.05}O_3$ and $Ca_3Co_4O_9$ ceramics. Starting from powder samples, two dilatometer measurements were performed. First cycles represent the sintering curves for $In_{1.95}Sn_{0.05}O_3$ and $Ca_3Co_4O_9$ samples, respectively. The second cycles depict the dilatometer measurements, shown in Figure 5(a, b). Figure 5(a, b) shows the quotient of the variation in length and initial length dL/L_0 in percent as a function of temperature, the value of the CTE during heating and cooling was estimated from the measured values (dashed lines). The CTE between 400 °C and 900 °C during heating and cooling exhibits almost the same value of $14.7 \cdot 10^{-6} K^{-1}$ for $In_{1.95}Sn_{0.05}O_3$. The CTE of $Ca_3Co_4O_9$ between 673 K and 1073 K represents $15.0 \cdot 10^{-6} K^{-1}$ during heating and $18.1 \cdot 10^{-6} K^{-1}$ during cooling, respectively.

Figure 6(a, b) shows the measured values for σ and α of $In_{1.95}Sn_{0.05}O_3$ and $Ca_3Co_4O_9$ as a function of temperature. The electrical conductivity σ of $Ca_3Co_4O_9$ is almost constant over the whole temperature range and reaches $32.5 S \cdot cm^{-1}$ at 1,073 K. The electrical conductivity of $In_{1.95}Sn_{0.05}O_3$ increases exponentially at about 900 K and achieves $608 S \cdot cm$ at 1,073 K. The Seebeck coefficient α of $Ca_3Co_4O_9$ is almost constant from 500 to 1,100 K and decreases to lower temperatures. The α value of $In_{1.95}Sn_{0.05}O_3$ increases slightly with temperature. The

Table 1: Measured values of density and porosity of $In_{1.95}Sn_{0.05}O_3$ (15 h at 1,873 K) and $Ca_3Co_4O_9$ (10 h at 1,173 K) ceramic, using ISO 5018:1983 (the International Organization for Standardization).

Material	Bulk density/ g·cm^{-3}	True density/ g·cm^{-3}	Open porosity/%	Closed porosity/%	True porosity/%
$In_{1.95}Sn_{0.05}O_3$	6.55	7.11	3.48	4.46	7.94
$Ca_3Co_4O_9$	2.53	4.68	45.2	0.64	45.8
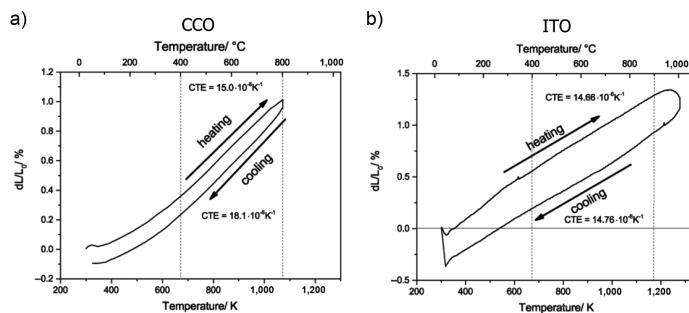
Figure 5: Coefficient of thermal expansion (CTE): thermal expansion and shrinkage during heating and cooling as a function of temperature of a) $Ca_3Co_4O_9$ and b) $In_{1.95}Sn_{0.05}O_3$ ceramic. Dashed lines indicate the temperature ranges for which the CTE was estimated, respectively.
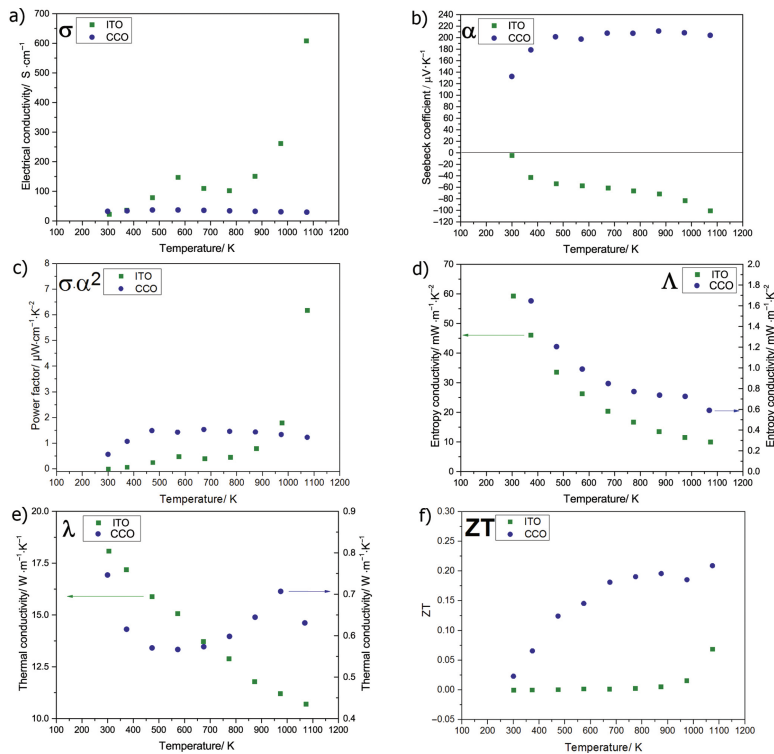
Figure 6: Thermoelectric properties as a function of temperature of n-type $In_{1.95}Sn_{0.05}O_3$ (squares, ITO) and p-type $Ca_3Co_4O_9$ (circles, CCO). a) Electrical conductivity σ and b) Seebeck coefficient α. c) power factor $\sigma \cdot \alpha^2$, d) entropy conductivity Λ, e) heat conductivity λ (eq. [2]) and f) figure of merit ZT, estimated according to eq. [1].

Seebeck values for both materials reach $203.8\,\mu V \cdot K^{-1}$ and $-100.8\,\mu V \cdot K^{-1}$ at 1,073 K, respectively. The values for tin-doped indium oxide are in the same order as those reported by Guilmeau et al. (2009). The electrical conductivity σ of $Ca_3Co_4O_9$ differs in absolute values, and the course of the Seebeck coefficient α turns slightly different, due to a lower density of the ceramic, compared to other studies, see Rasekh et al. (2013) and Xu et al. (2002). The values for the power factor in Figure 6(c) of $Ca_3Co_4O_9$ and $In_{1.95}Sn_{0.05}O_3$, calculated from σ and α differ between 300 and 900 K. The power factor of $In_{1.95}Sn_{0.05}O_3$ exceeds that of $Ca_3Co_4O_9$ after 1,000 K due to an exponential increase in the electrical conductivity. The figure of merit ZT of $In_{1.95}Sn_{0.05}O_3$ and $Ca_3Co_4O_9$ were estimated from the ciphered power factors $\sigma \cdot \alpha^2$, of $6.8\,\mu W \cdot cm^{-1} \cdot K^{-2}$ (ITO), and $1.23\,\mu W \cdot cm^{-1} \cdot K^{-2}$ (CCO) and the entropy conductivity Λ respectively, which was measured via a laser flash setup.

Figure 6(d) shows the entropy conductivity Λ of $In_{1.95}Sn_{0.05}O_3$ and $Ca_3Co_4O_9$ as a function of the temperature. And Figure 6(f) shows the calculated figure of merit of $In_{1.95}Sn_{0:05}O_3$ and $Ca_3Co_4O_9$ after eq. [1] as a function of temperature. The entropy conductivity Λ reaches $10\,mW \cdot m^{-1} \cdot K^{-2}$ at 1,073 K for $In_{1.95}Sn_{0.05}O_3$ and $0.59\,mW \cdot m^{-1} \cdot K^{-2}$ for $Ca_3Co_4O_9$. The estimated figure of merit for $In_{1.95}Sn_{0.05}O_3$ and $Ca_3Co_4O_9$ as a function of temperature achieve 0.07 and 0.21 at 1,073 K, respectively. The measured values for the heat conductivity λ of $10.6\,W \cdot m^{-1} \cdot K^{-1}$ at 1,073 K for a $In_{1.95}Sn_{0.05}O_3$ sample vary slightly, compared to $8.5\,W \cdot m^{-1} \cdot K^{-1}$ at 1,000 K for an indium oxide sample, which is doped with the same tin fraction, reported by Guilmeau et al. (2009). Because of a slightly lower heat conductivity λ reported in literature, the ZT value in this study also differs a little from literature, maybe because of a different density of the measured samples. The trend for the heat conductivity λ

and the measured values of $0.63\,\mathrm{W\cdot m^{-1}\cdot K^{-1}}$ at 1,073 K for $Ca_3Co_4O_9$ also differ compared to the trend and value of $1.7\,\mathrm{W\cdot m^{-1}\cdot K^{-1}}$ at 1,073 K, reported by Nong, Liu, and Ohtaki (2010). According to this trend, the value of $0.63\,\mathrm{W\cdot m^{-1}\cdot K^{-1}}$ at 1,073 K seems to be undersized. This can be attributed to a lower density and high open porosity of the measured $Ca_3Co_4O_9$ sample, allowing gas to permeate and thus contributing to the heat conductivity. The figure of merit ZT matches with the reported values in literature.

Thermoelectric Generator

To assemble a thermoelectric generator, legs of n- and p-type semiconductor materials were cut out of disk-shaped ceramics, utilizing a wire saw. The n-type $In_{1.95}Sn_{0.05}O_3$ legs have an area of $1.1\,\mathrm{mm^2}$ and a length of 2 mm. The p-type $Ca_3Co_4O_9$ legs possess an area of $1.5\,\mathrm{mm^2}$ and a length of 2 mm. The constructed oxide-based thermoelectric generator consists of 5 n-type $In_{1.95}Sn_{0.05}O_3$ and 5 p-type $Ca_3Co_4O_9$ legs. The legs were connected to each other on the top and bottom plate via a gold connector. The gold connector was placed on the electrical insulating Al_2O_3 plates via coating of an Au-paste from HERAEUS. The legs were placed on a Al_2O_3 plate in electrical serial connection. The Al_2O_3 plates are rectangles with 15 mm lateral lengths. Platinum wires were attached for electrical contacting to an external electrical circuit. The manufactured module

was baked at 1,173 K for 2 hours to obtain a mechanically stable device with metallic gold contacts.

Figure 7 shows a sketch of the thermoelectric generator and a side view of the constructed TEG with n- and p-type legs, contacts, Al_2O_3-plates and Pt-wires. The oxide-based thermoelectric generator was characterized at high-temperature conditions in air. Figure 2 shows the utilized measurement setup schematically. The upper side of the generator was heated by a furnace up to $T_{hot} = 1,073\,\mathrm{K}$ while the bottom side was cooled by a passive cooler (T_{cold}) to establish a temperature gradient over the device obtaining a temperature drop of $\Delta T = 113\mathrm{K}$. Two Pt/Rh thermocouples measure the temperature at the hot and cold side, respectively and thereby ΔT. The generator is connected with a voltmeter and an amperemeter in parallel connection. The electrical power output of the generator can be measured if a variable resistor is prior to the amperemeter. The electrical power output is maximum if the resistivity of the module is equal to the load resistivity. The thermoelectric generator couples an entropy current J_S and an electric current J_q in a way that energy is transferred from thermal to electric process; see Figure 2. An oxide-based generator possesses a good thermal, chemical stability in oxidizing atmosphere and a conventional TEG setup provides also good mechanical stability. Oxides own still inferior thermoelectric properties, so improvement is needed for Seebeck coefficient α and entropy conductivity Λ of $In_{1.95}Sn_{0.05}O_3$ and electrical conductivity σ and entropy conductivity Λ of $Ca_3Co_4O_9$. After a period of time of 1 hour, the device was in equilibrium and the variable
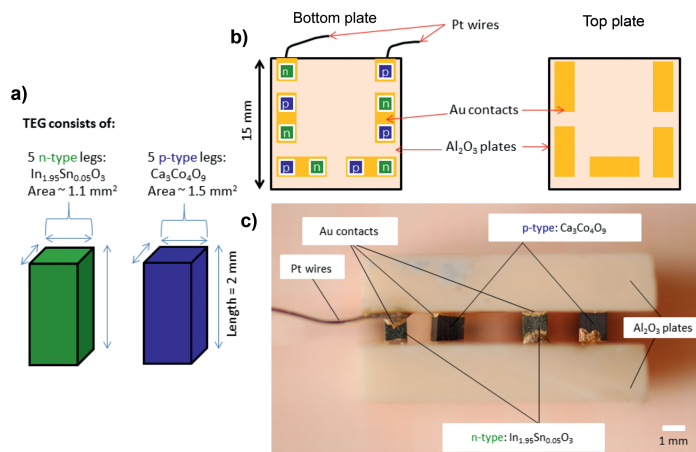
Figure 7: a) Dimensions of n- and p-type legs, b) sketch of TEG setup, c) side-view photograph of the TEG.

resistor in the external circuit was switched and thereby different load resistances R_{load} were applied. The electrical parameters electrical current J_q and voltage U were measured in dependence of R_{load} and different T_{hot}. Every measuring step last 5 min. The first measurement was always under quasi closed-circuited conditions, this means without any load resistance R_{load} other than the internal resistance by cables etc. The electrical power output P_{el} of the device is related to the current and the voltage, while the area-specific electrical power density ω_{el} depends on the quotient of the power output P_{el} and the area of the device. The electrical power output P_{el} was estimated by multiplying the measured values of U and J_q. The area-specific electrical power density was calculated by dividing P_{el} with the area of 2.25 cm^2. Figure 8 shows the measured data points and continuously fitted plots of U and P_{el} as a function of J_q. The maximum electrical power output $P_{el,max}$, the associated electrical current $J_q(P_{max})$ and voltage $U(P_{max})$ can be estimated and read from the fitted data plots. The short-circuit current $J_{q,SC}$ and open-circuit voltage U_{OC} can also be

determined from the fitted plots in Figure 8. The calculated values of the electrical power density of $\omega_{el} = 2.13$ mW $\cdot$ cm^{-2} at $T_{hot} = 1,073$ K, $\omega_{el} = 1.6$ mW $\cdot$ cm^{-2} at $T_{hot} = 1,023$ K and $\omega_{el} = 1.36$ mW $\cdot$ cm^{-2} at $T_{hot} = 973$ K are also plotted in Figure 8. The TEG possesses a fill factor of 5.78 % when an area of the p,n couples of 0.13 cm^2 and an area of the top and bottom plates of 2.25 cm^2 are assumed. The measured thermoelectric parameters of the device at different applied steady-state temperature conditions are listed in Table 2. The electrical power output P_{el} depends on the load-resistance R_{load} in the external circuit, which can be expressed by eq. [5].

The maximum electrical power output is a load-resistance dependent parameter. It becomes becomes maximal if the load resistance R_{load} is equal to R_{module} after eq. [6]; see Möschwitzer and Lunze (1998).

$$P_{el} = \frac{U_{OC}^2}{4 \cdot R_{load} \cdot \frac{U_{OC} - U_{load}}{U_{load}}} \qquad [5]$$

$$R_{load} = R_{module} = \left(\sum R_n + \sum R_p \right) \qquad [6]$$
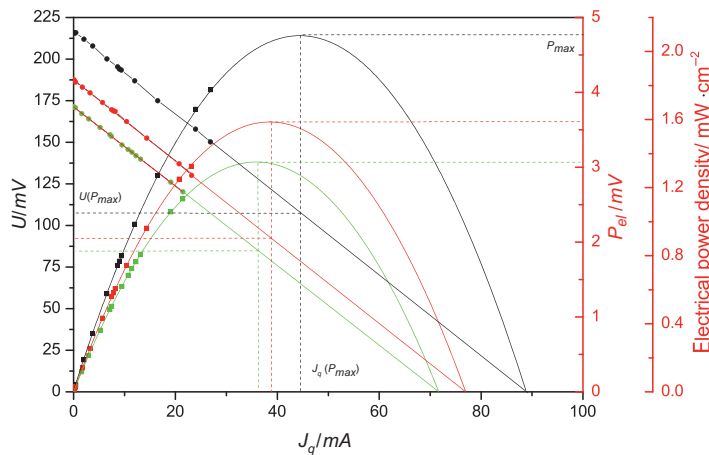
Figure 8: Fitted electrical power output P_{el} (rectangular dots) and voltage (spherical dots) as a function of the electrical current J_q at different applied T_{hot} temperatures (1,073 K in black, 1,023 K in red and 973 K in green). $U(P_{max})$ and $J_q(P_{max})$ of the respective $P_{el,max}$ at different temperature conditions are indicated (dashed lines).

Table 2: Measured and calculated values of the thermoelectric generator at different applied temperature conditions.

T_{hot}/K	$\Delta T/K$	R_{module}/Ω	U_{OC}/mV	$J_{q,SC}/mA$	$U(P_{max})/mV$	$J_q(P_{max})/mA$	P_{max}/mW
1,073	113	2.44	216.51	88.65	108.25	44.32	4.8
1,023	113	2.43	187.83	77.18	93.91	38.59	3.62
973	113	2.39	171.46	71.67	85.73	35.83	3.06

At the maximum power output, when R_{load} is equal to R_{module} (eq. [6]) and $U_{load} = \frac{1}{2}U_{OC}$, eq. [5] becomes eq. [7].

$$P_{max} = \frac{U_{OC}^2}{4 \cdot R_{module}} \qquad [7]$$

The measured and calculated parameters of the TEG are listed in Table 2. The maximum electrical power output $P_{el,\,max}$ of the thermoelectric generator for three different applied temperatures, when a temperature difference of 113 K is established, can be read from the extrapolated curves. At a hot-side temperature of $T_{hot} = 1073\,K$, the TEG provides and electrical power output of $P_{el} = 4.8\,mW$, at $T_{hot} = 1,023\,K$, $P_{el} = 3.62\,mW$ and at $T_{hot} = 973\,K$, $P_{el} = 3.06\,mW$. The $U(P_{max})$ and $J_q(P_{max})$ of the respective $P_{el,max}$ at different temperatures can be read from the linearly extrapolated $U - J_q$ plot. The values for U_{OC} were measured and $J_{q,SC}$ values were extrapolated from the measured $U - J_q$ curves.

The figure of merit ZT of the generator can be calculated from these measured values by eq. [8] after Min and Rowe (2001). At a hot-side temperature of $T_{hot} = 1,073\,K$ and an applied temperature drop of $\Delta T = 113\,K$, a figure of merit of 0.02 can be reached. This value for the whole generator is similar to the value for the material $In_{1.95}Sn_{0.05}O_3$, see Figure 6f, which is the efficiency-limiting part of the generator.

$$ZT = \frac{U_{OC}}{J_{q,SC} \cdot R_{module}} - 1 \qquad [8]$$

An oxide-based TEG made of $In_{1.95}Sn_{0.05}O_3$ and $Ca_3Co_4O_9$ provides a better balance of voltage U and current $J_q(U(P_{max}) = 108.25\,mV,\ J_q(P_{max}) = 44.32\,mA)$ and thus a high electrical power output, compared with a generator made of ZnO and $Ca_3Co_4O_9$ see Feldhoff and Geppert (2014), which offers not more than 0.55 mW at an almost doubled temperature difference. Nevertheless it is difficult to compare thermoelectric generators with each other due to the different dimensions of the n- and p-type legs, different applied temperatures and temperature differences, see Choi et al. (2011) and Matsubara et al. (2001). But if we consider that the electrical power output depends on the product of U and J_q, the combination of $In_{1.95}Sn_{0.05}O_3$ and $Ca_3Co_4O_9$ possess beneficial properties for power generation at high-temperature conditions in ambient atmosphere.

Conclusions

An oxide-based thermoelectric generator consisting of n-type $In_{1.95}Sn_{0.05}O_3$ and p-type $Ca_3Co_4O_9$ semiconductor legs was successfully constructed and characterized. The maximum electric power output depends and increases with increasing hot-side temperature. A high voltage and electric current is advantageous and could be accomplished by the use of a highly electrically conductive $In_{1.95}Sn_{0.05}O_3$ n-type material. The efficiency of the whole system is limited by the figure of merit ZT of the $In_{1.95}Sn_{0.05}O_3$ n-type legs. A ZT value of 0.02 for the device was achieved and a maximum electric power output of 4.8 mW was obtained at 1,073 K hot-side temperature and a temperature difference of $\Delta T = 113\,K$. To improve the power output of the thermoelectric generator, the cross sections of the electric conductors can be adapted to each other in terms of the specific resistance.

References

Bérardan, D., E. Guilmeau, A. Maignan, and B. Raveau. 2008. "Enhancement of the Thermoelectric Performances of In_2O_3 by the Coupled Substitution of M^{2+}/Sn^{4+} for In^{3+}." *Journal of Applied Physics* 104:064918–1–064918–5.

Choi, S. M., K. H. Lee, C. H. Lim, and W. S. Seo. 2011. "Oxide-Based Thermoelectric Power Generation Module Using p-Type $Ca_3Co_4O_9$ and n-Type $(ZnO)_7In_2O_3$ Legs." *Energy Conversion and Management* 52:335–9.

Feldhoff, A. 2015. "Thermoelectric Material Tensor Derived From the Onsager - De Groot - Callen Model." *Energy Harvesting and Systems* 2 (1):5–13.

Feldhoff, A., M. Arnold, J. Martynczuk, T. Gesing, and H. Wang. 2008. "The Sol-Gel Synthesis of Perovskites by EDTA/Citrite Complexing Method Involves Nanoscale Solid State Reactions." *Solid State Sciences* 10:689–701.

Feldhoff, A., and B. Geppert. 2014. "A High-Temperature Thermoelectric Generator Based on Oxides." *Energy Harvesting and Systems* 1 (1–2):69–78.

Fuchs, H. 2010. *The Dynamics of Heat – a Unified Approach to Thermodynamics and Heat Transfer*, Graduate Texts in Physics, 2nd ed. New York: Springer.

Guilmeau, E., D. Bérardan, C. Simon, A. Maignan, B. Raveau, D. Ovono Ovono, and F. Delorme. 2009. "Tuning the Transport and Thermoelectric Properties of In_2O_3 Build Ceramics Through Doping at In-Site." *Journal of Applied Physics* 106:053715–1–053715–7.

Indris, S. 2001. *Perkolation Von Grenzflächen in Nanokristallinen Keramischen Kompositen - Li-Ionenleitfähigkeit Und 7li-NMR-Relaxation*. Göttingen: Cuvillier.

Ioffe, A. 1957. *Semiconductor Thermoelements and Thermoelectric Cooling*, 1st ed. London: Infosearch Ltd.

Kenfaui, D., G. Bonnefont, D. Chateigner, G. Fantozzi, M. Gomina, and J. G. Noudem. 2010. "$Ca_3Co_4O_9$ Ceramics Consolidated by SPS Process: Optimisation of Mechanical and Thermoelectric Properties." *Material Research Bulletin* 45:1240–9.

Liu, Y., Y. Lin, Z. Shi, and C. Nan. 2005. "Preparation of $Ca_3Co_4O_9$ and Improvement of Its Thermoelectric Properties by Spark Plasma Sintering." *Journal of the American Ceramic Society* 88:1337–40.

Matsubara, I., R. Funahashi, T. Takeuchi, and S. Sodeoka. 2001. "Fabrication of an All-Oxide Thermoelectric Power Generator." *Applied Physics Letters* 78:3627–9.

Min, G., and D. Rowe. 2001. "A Novel Principle Allowing Rapid and Accurate Measurement of a Dimensionless Thermoelectric Figure of Merit." *Measurement Science and Technology* 12:1261–2.

Miyazaki, Y. 2004. "Crystal Structure and Thermoelectric Properties of the Misfit-Layered Cobalt Oxides." *Solid State Ionics* 172:463–7.

Miyazaki, Y., M. Onoda, T. Oku, M. Kikuchi, Y. Ishii, Y. Ono, Y. Morii, and T. Kajitani. 2002. "Modulated Structure of Thermoelectric Compound [Ca_2CoO_3]CoO_2." *Journal of the Physical Society of Japan* 71:491–7.

Möschwitzer, A., and K. Lunze. 1998. *Lehrbuch Halbleiterelektronik*, 8th ed. Heidelberg: Dr. Alfred Hüthig Verlag.

Nagahama, D., T. Tani, Y. Masuda, H. Itahara, T. Yonezawa, and K. Koumoto. 2002. "Thermoelectric Properties of $Ca_3Co_{4-x}Ga_xO_9$-Based Ceramics Textured by Templated Grain Growth Method." *21st International Conference on Thermoelectrics* 21:211–14.

Nong, N. V., C. -J. Liu, and M. Ohtaki. 2010. "Improvement on the High Temperature Thermoelectric Performance of Ga- Doped Misfit-Layered $Ca_3Co_{4-x}Ga_xO_{9+\delta}$ (x = 0, 0.05, 0.1, and 0.2)." *Journal of Alloys and Compounds* 491:53–6.

Prince, E. 2004. *International Tables for Crystallography*, volume C ed. Dordrecht/Boston/London: Kluwer Academic Publishers.

Rasekh, S., M. A. Torres, G. Constantinescu, M. A. Madre, J. C. Diez, and A. Sotelo. 2013. "Effect of Cu by Co Substitution on $Ca_3Co_4O_9$ Thermoelectric Ceramics." *Journal of Materials Science: Materials in Electronics* 24:2309–14.

Rowe, D. 1995. *CRC Handbook of Thermoelectrics*, 89th ed. Boca Raton, FL: CRC Press.

Seeger, K. 1991. *Semiconductor Physics*. Berlin: Springer.

Singh, D. J. 2000. "Electronic Structure of $NaCo_2O_4$." *Physical Review B* 61:13397–402.

Xu, G., R. Funahashi, M. Shikano, I. Matsubara, and Y. Zhou. 2002. "Thermoelectric Properties of the Bi- Na- Substituted $Ca_3Co_4O_9$ System." *Applied Physics Letters* 80:3760–2.

Yan, Y. L., and Y. X. Wang. 2012. "Electronic Structure and Low Temperature Thermoelectric Properties of $In_{24}M_8O_{48}$(M = Ge^{4+}, Sn^{4+}, Ti^{4+}, and Zr^{4+})." *Journal of Computational Chemistry* 33:88–92.

3.3 Experimental characterisation and finite-element simulations of a thermoelectric generator with ceramic p-type Ca$_3$Co$_4$O$_9$ and metallic n-type Cu$_{0.57}$Ni$_{0.42}$Mn$_{0.01}$ legs

91

3.3 Experimental characterisation and finite-element simulations of a thermoelectric generator with ceramic p-type Ca$_3$Co$_4$O$_9$ and metallic n-type Cu$_{0.57}$Ni$_{0.42}$Mn$_{0.01}$ legs

B. Geppert, D. Groeneveld, M. Bittner and Armin Feldhoff

B. Geppert*, D. Groeneveld, M. Bittner and A. Feldhoff

Experimental Characterisation and Finite-element Simulations of a Thermoelectric Generator with Ceramic p-type $Ca_3Co_4O_9$ and Metallic n-type $Cu_{0.57}Ni_{0.42}Mn_{0.01}$ Legs

Abstract: This study presents the characterisation of a prototype thermoelectric generator including ceramic $Ca_3Co_4O_9$ p-type and metallic $Cu_{0.57}Ni_{0.42}Mn_{0.01}$ n-type legs. The generator was constructed applying the conventional rigid chessboard design, which provides an electrical series connection of the thermoelectrically active materials in between of two electrical isolating cover plates made of alumina. Ag-epoxy resin was used for electric connectors which were directly bond to the thermoelectrically active materials. The generator was rebuild in the framework of a finite-element model to simulate the generator's transport characteristics using the physical data of the single materials as input parameters for the simulation tool. The simulation results give a view to the distributions of temperature and electric potential as well as vector plots showing the generated current density of charge inside the regarded materials. The finite-element simulation tool was used to consider the electrical contact resistivities between the thermoelectric legs and the connector material. The input parameter for the specific isothermal electric resistivity of the Ag-epoxy connectors were varied by including the electrical contact resistances to match the simulated to the measured data in order to receive the correct electric current densities in the modeled device.

Keywords: thermoelectric generator, finite-element simulation, electrical power

Introduction

The development and application of thermoelectric materials, for example, for harvesting electrical power from waste heat sources, is a current field of study that requires interdisciplinary investigations. The implementation of newly developed thermoelectric materials into thermoelectric generators (TEGs) benefits from modeling the thermoelectric properties of the generators with respect to the individual properties of the employed materials. A TEG is a device that transfers energy from thermal (entropy) current to electric current; see Fuchs (2010, 2014) and Feldhoff (2015). The concept of energy carriers as outlined by Falk, Herrmann, and Schmid (1983) enables an elegant description of a thermoelectric device, which relies on considering the flux densities of the aforementioned fluid-like quantities entropy S and electric charge q and their linkage to the conjugated potentials, which are the absolute temperature T and the electric potential φ, respectively. The currents of thermal energy (heat) and electric energy are then obtained as shown by Fuchs (2014), Feldhoff and Geppert (2014a, 2014b) and Feldhoff (2015). Taking the cross-sectional areas A_{leg} and the length L_{leg} of the thermoelectric material samples into account, the currents of entropy I_S and electric charge I_q in a thermoelectric material, that is subjected to differences of thermal potential ΔT and electric potential $\Delta \varphi$, can be easily obtained if a thermoelectric material tensor is considered; see Feldhoff (2015):

$$\begin{pmatrix} I_S \\ I_q \end{pmatrix} = -\frac{A_{leg}}{L_{leg}} \cdot \begin{pmatrix} \sigma \cdot \alpha^2 + \Lambda & \sigma \cdot \alpha \\ \sigma \cdot \alpha & \sigma \end{pmatrix} \cdot \begin{pmatrix} \Delta T \\ \Delta \varphi \end{pmatrix} \qquad (1)$$

The thermoelectric tensor consists of three tensorial quantities, the specific electrical conductivity σ under isothermal conditions (i. e., $\nabla T = 0$), the specific entropy conductivity Λ under electric open-circuited conditions (i. e., $I_q = 0$) and the Seebeck coefficient α. Special cases that can be received under certain conditions of eq. (1) were elucidated by Fuchs (2014), Feldhoff and Geppert (2014a, 2014b) and Feldhoff (2015).

The basic unit of a thermoelectric generator can be constructed by connecting two materials with different algebraic signs for the Seebeck coefficient α thermally in parallel and electrically in series. For $\alpha < 0$, the motions of thermal and electrical fluxes are directed in the same

*Corresponding author: B. Geppert, Institute of Physical Chemistry and Electrochemistry, Leibniz Universität Hannover, Hannover, Germany, E-mail: benjamin.geppert@pci.uni-hannover.de
D. Groeneveld, M. Bittner, A. Feldhoff, Institute of Physical Chemistry and Electrochemistry, Leibniz Universität Hannover, Hannover, Germany

way. In contrast, for $\alpha > 0$, the thermal and electrical fluxes are directed in opposite directions; see Feldhoff and Geppert (2014b). By additively connecting several of these basic units thermally in parallel and electrically in series, the electric potential φ can be increased over the device; see Feldhoff (2015) for illustration. The choice of the thermoelectric materials that comprise the TEG depends on the conditions under which the energy conversion is to be performed.

Among the various thermoelectric materials, semiconductors exhibit the best thermoelectric conversion efficiency because of their moderate charge carrier concentration, and they provide a good balance between specific electric conductivity σ, the Seebeck coefficient α and the thermal conductivity; see Ioffe (1957). Alloys provide high values of the so-called power factor $\sigma \cdot \alpha^2$, which is the charge-coupled entropy conductivity and occurs as part of the thermoelectric tensor in eq. (1). Consequently, alloys and semiconductors are chosen as thermoelectrically active materials. To obtain a good TEG performance, the combination of n- and p-type materials and a low-resistance electrical connection between them realized by metals or alloys is preferred. In case of the present study, a composite connector material, Ag-epoxy resin, was used.

Additionally, the geometric properties of the materials that are combined to form the complete device have to be optimized for every system. Finite-element method (FEM) simulations are useful for calculating the thermoelectric performance in terms of the used materials and their geometric properties without constructing a real TEG. The thermoelectric properties can be measured for each individual material. Afterwards, the materials can be combined in a simulated TEG system with a specific geometry. The absolute currents I are correlated to the current densities j considering the cross-sectional areas of the thermoelectric material legs A_{leg}, as shown in eqs (2) and (3).

$$I_S = A_{leg} \cdot j_S \qquad (2)$$

$$I_q = A_{leg} \cdot j_q \qquad (3)$$

Under electric open-circuit conditions, eq. (1) yields the entropy current I_S through the thermoelectric material by Fourier's law:

$$I_S = -\frac{A_{leg}}{L_{leg}} \cdot \Lambda \cdot \Delta T \qquad (4)$$

The specific entropy conductivity Λ is related to the specific heat conductivity λ by the absolute working temperature T, see Fuchs (2010, 2014) and Feldhoff (2015).

$$\lambda = T \cdot \Lambda \qquad (5)$$

Under isothermal conditions, eq. (1) yields the electric current I_q through the thermoelectric material by Ohm's law:

$$I_q = -\frac{A_{leg}}{L_{leg}} \cdot \sigma \cdot \Delta \varphi \qquad (6)$$

Experimental

Thermoelectric Measurement Setup

To characterize the thermoelectric properties of the materials, the temperature-dependent isothermal specific electric resistivity and the Seebeck coefficient, as estimated from the thermovoltage, were measured. A precision vertical diamond wire-saw model 3242 from O'WELL was used for sample preparation. Thermoelectric properties were measured using a measurement cell constructed in-house. The sample was clamped between two platinum electrodes to close the electric circuit in a pseudo-four-point measurement. The applied furnace was an ELITE thermal system. The Seebeck coefficient was measured using a NORECS Probostat measurement system. The electronic parameters were measured with KEITHLEY 2100 $6\frac{1}{2}$ digit multimeters. The measured data were converted using LAB VIEW software.

To estimate the thermoelectric characteristics of the constructed TEG, it was placed between a heat source (ceramic hot-plate) and a heat sink (passive cooler). A photomicrograph of the measurement setup is shown in Figure 1.

The temperature data were collected using thermocouples. The voltage $\Delta \varphi$ was measured as the drop of the electric potential on the external load R_{load}. The electric output power P_{el} was estimated according to:

$$P_{el} = I_q \cdot \Delta \varphi \qquad (7)$$

The resistivity of the thermoelectric generator was estimated by analysing the electric current-voltage characteristics using Ohm's law for the entire device (see eq. (6) for the corresponding relation for single materials).

$$\Delta \varphi = -R_{TEG} \cdot I_q \qquad (8)$$

The geometric parameters of applied materials, that are input parameters for the FEM tool, are listed in Table 1.

Microstructure Analysis

The phase composition of the metallic n-type and ceramic p-type materials was analyzed by X-ray diffraction (XRD)
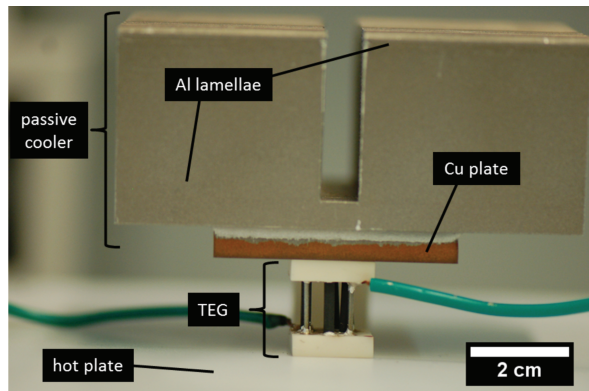
Figure 1: Photomicrograph of the measurement setup for determination of the thermoelectric characteristics of the constructed TEG. Note that the p-type ceramic material is integrated as rectangular bars while the n-type wire material exhibits the form of a cylinder.

Table 1: Measured geometric properties of the TEG's components: length L and cross-sectional area A of applied material. The fill-factor of the TEG exhibits a value of 7.5 %.

Component	Material	L/mm	A/mm²	Description
p-type leg	$Ca_3Co_4O_9$	10.0	3.23	House-made ceramic
n-type leg	$Cu_{0.57}Ni_{0.42}Mn_{0.01}$	10.0	0.79	Commercial alloy
el. connector	Ag-epoxy resin	0.44	5.32	Commercial composite
Cover plates	Al_2O_3	3.8	225	Commercial ceramic

using a Bruker D8 Advance with Cu-K$_\alpha$ radiation. The thermoelectric bulk materials were polished using diamond-lapping films (Allied High Tech Multiprep) for field-emission scanning electron microscopy (FE-SEM) investigations using a JEOL JSM-6700F, which was equipped with an Oxford Instruments INCA 300 energy-dispersive X-ray spectrometer (EDXS) for elemental analysis.

Materials Choice

The p-type leg material was realized by applying ceramic $Ca_3Co_4O_9$. This layered cobaltite phase exhibits an incommensurate structure and provides attractive thermoelectric properties, see Lambert, Leligny, and Gebrille (2001). Measured thermoelectric parameters for polycrystalline samples from various laboratories were assembled by Fergus (2011). Single crystals of $Ca_3Co_4O_9$ exhibit a figure

of merit $ZT = 0.83$ at 973 K, see Shikano and Funahashi (2003). The high charge carrier density around room temperature makes the $Ca_3Co_4O_9$ ceramic also usable as thermoelectric material for low- and intermediate-temperature devices. As n-type material a Cu-Ni based alloy was used. For energy conversion in the intermediate temperature range such metallic compounds show useful properties. The electric resistance is very low and the value for the Seebeck coefficent is acceptable. That makes such alloys the material class reaching highest values of the power factor. We already used this material combination for the construction of flexible thermoelectric generators, see Geppert and Feldhoff (2015). Measured thermoelectric properties were summarized in round-robin measurements and reported by Lu et al. (2009) and Lowhorn et al. (2009).

The series connection of n- and p-type legs of the generator was realized using Ag-epoxy resin as electrical conductive glue. The bulk resistivity was reported with a value of 0.9 mΩcm^{-1}.

For the cover plates, commonly used Al_2O_3 was applied.

Finite-element Simulations

In this work, a prototype thermoelectric generator was constructed and rebuild in the FEM tool using ANSYS Mechanical APDL version 15.0 academic. The specific resistivity of the Ag-epoxy resin was adapted in the simulation to match the measured transport properties and to obtain the correct electric currents in the modeled device. The model consists of 14,268 elements. Each thermoelectric p-type leg is build up by 48 elements (total number of p-type material elements for the thermoelectric legs is

192) while the total number of elements for the electrical Ag-epoxy connectors is 2964. Each alumina cover plate consists of 1482 elements. The simulation procedure was performed using the 3-D steady-state thermoelectric analyser. The residual method was done using the thermal power P_{th} and electric current I_q as convergence parameters. The convergence values were set to $1 \cdot 10^{-3}$ for both parameters. The entire fit function is presented in eq. (9).

$$P_{th} = \alpha_{TEG} \cdot T_h \cdot I_q - \frac{1}{2} \cdot I_q^2 \cdot R_{TEG} + \lambda \cdot \Delta T \qquad (9)$$

The non-linear solution converged after 5 equilibrium iterations. The constructed and modeled device is presented in Figure 2.

Results and Discussion

Microstructure of Materials

The crystallographic phases of the sintered p-type $Ca_3Co_4O_9$ ceramic and the n-type $Cu_{0.57}Ni_{0.42}Mn_{0.01}$ were confirmed by Rietveld refinement of measured X-ray diffractograms. The diffractograms (blue curves) of the thermoelectric materials are presented in Figure 3 together with the Rietveld fits (red curves). $Ca_3Co_4O_9$ crystallizes in the monoclinic system and exhibits the Cm symmetry for both subsystems (b_1, b_2). $Cu_{0.57}Ni_{0.42}Mn_{0.01}$ crystallizes in the cubic system exhibiting the spacegroup $Fm\bar{3}m$.

The p-type $Ca_3Co_4O_9$ ceramic was vibration-polished to estimate the arrangement of plate-like grains inside the bulk material. In Figure 4, a secondary electron micrograph of the ceramic material is presented. The black areas are internal pores.

Thermoelectric Investigations

Table 2 lists measured or reported values for the transport properties of each material that was applied in the generator. The electronic and thermal quantities for the Al_2O_3 plates and for the Ag-epoxy resin were taken from manufacturers data.

To estimate the thermoelectric properties of the TEG, the device was characterized in the setup shown in Figure 1. The temperature-dependent resistivity of the entire device R_{TEG} was estimated by applying Ohm's law (eq. (8)) to the TEG's measurement data. In Table 3, the
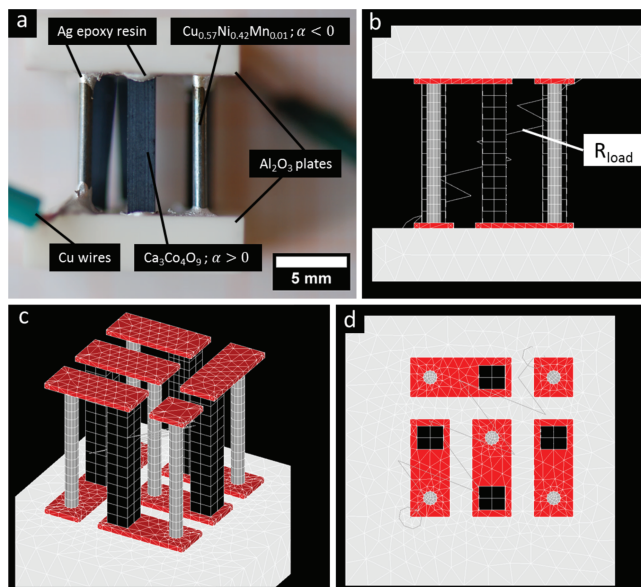
Figure 2: View on the constructed and modeled thermoelectric device. (a) Side-view of constructed TEG, (b) Side-view of modeled device, (c) Perspective view of modeled device, (d) Top-view on modeled device.
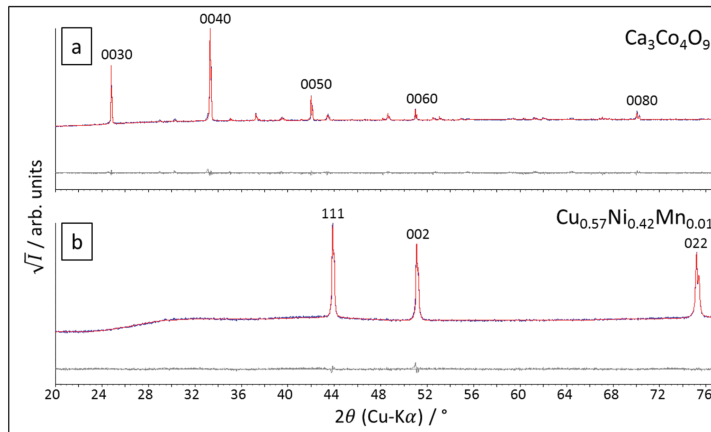
Figure 3: Measured X-ray diffractograms (blue curves) with Rietveld fits (red curves) and differential curve (grey curves). (a) p-type $Ca_3Co_4O_9$ ceramic, (b) n-type $Cu_{0.57}Ni_{0.42}Mn_{0.01}$ alloy. The counts are presented as square-root values.
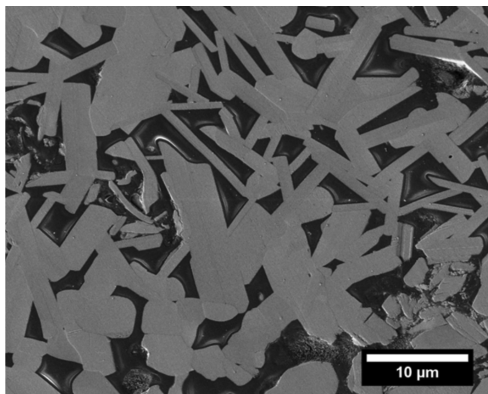
Figure 4: Secondary electron micrograph of the vibration-polished p-type $Ca_3Co_4O_9$ ceramic material.

values for the determined contact resistances are listed together with the maximum electric current $I_{q,SC}$ under electric short-circuit conditions (i. e. $\Delta\varphi = 0$), the open-circuit voltage $\Delta\varphi_{OC}$ (i. e. $I_q = 0$) and the maximum electric output power $P_{el,max}$. All quantities are related to the established temperature drops ΔT and the median temperature of the device T_{median}.

The FEM simulation resulted in accurate values for the open-circuit voltage $\Delta\varphi_{OC}$ (device Seebeck-voltage) but in too high values for the short-circuit electric current $I_{q,SC}$. This makes the calculated values for the resistivity of the generator too low and the electric output power too high. The reason for the FEM solutions to be inaccurate is seen in contact resistivities between the Ag-epoxy resin and the thermoelectrically active materials. In order to match the characteristics of the real constructed TEG to the modeled device in the FEM tool, the specific electric resistivity of the Ag-epoxy resin was refined by the implementation of the magnitude of the contact resistances into the values of the specific resistivity of the connector material. The values of the resistivity of the electric connector material was varied until the Ohm-lines of the FEM simulation fitted the measurement data points. In the framework of thermoelectric generator fabrication the formation of contact resistances is a major concern and affects the thermoelectric properties of a certain device on a large scale. The modification of interfaces in thermoelectric generators is an extensive field of study. LeBlanc (2014) compared material and generator efficiency and he showed that the efficiency can decrease up to 59% comparing the single thermoelectric materials and the entire assembled systems. The $Ca_3Co_4O_9$-related oxide-metal interfaces were studied by Holgate et al. (2014).

Figure 5(a) shows $\Delta\varphi - I_q$ curves with bad agreement of the FEM Simulation A, that does not consider the electrical contact resistances (dotted lines), and good agreement of the FEM Simulation B, that does consider the electrical contact resistances (solid lines), with the measurement (data points) for all temperature conditions. Note, that the absolute value of the slope of the lines refers to the internal resistance R_{TEG}, as indicated in

Table 2: Determined or reported thermoelectrical parameters of applied materials. Simulation A assumes vanishing contact resistances and Simulation B accounts for non-vanishing contact resistances by considering them by varying the effective resistance ρ of the connector material.

Material	T/K	$\rho/m\Omega \cdot cm$	$\alpha/\mu V \cdot K^{-1}$	$\lambda/W \cdot m^{-1} \cdot K^{-1}$	$\Lambda/W \cdot m^{-1} \cdot K^{-2}$
$Ca_3Co_4O_9$	363	59.21	147.39	0.62	$1.7 \cdot 10^{-3}$
	403	49.93	154.95	0.59	$1.5 \cdot 10^{-3}$
	443	36.58	162.53	0.57	$1.3 \cdot 10^{-3}$
	478	32.66	169.12	0.57	$1.2 \cdot 10^{-3}$
$Cu_{0.57}Ni_{0.42}Mn_{0.01}$	300–500	$4.7 \cdot 10^{-2}$	-40	23	$7.7 \cdot 10^{-2}$
Al_2O_3 plates	300	$1 \cdot 10^{17}$	n.a.	30	$1 \cdot 10^{-1}$
Ag-epoxy resin (Simulation A)	300	0.9	n.a.	1	$3.3 \cdot 10^{-3}$
Ag-epoxy resin (Simulation B)	363	$2.55 \cdot 10^3$	n.a.	1	$2.8 \cdot 10^{-3}$
	403	$1.65 \cdot 10^3$	n.a.	1	$2.5 \cdot 10^{-3}$
	443	$5.10 \cdot 10^2$	n.a.	1	$2.3 \cdot 10^{-3}$
	478	$4.30 \cdot 10^2$	n.a.	1	$2.1 \cdot 10^{-3}$

Table 3: Estimated thermoelectric parameters of the constructed TEG for different temperature conditions.

T_{hot}/K	$\Delta T/K$	T_{median}/K	R_{TEG}/Ω	$P_{el, max}/\mu W$	$\Delta\varphi_{OC}/mV$	$I_{q, SC}/mA$	$R_{contact}/\Omega$ per contact
389	60	363	415.24	0.93	39.4	0.09	22.66
441	80	403	250.36	2.90	53.9	0.22	19.12
492	100	443	74.50	16.54	70.2	0.94	3.89
536	120	478	63.93	32.52	91.2	1.43	3.33

Tables 3 and 4. The electric output power P_{el} was estimated in terms of different load resistivities R_{load}. The electrical contact resistances limit the magnitude of the electric current inside the device and therefore the electric power output. Deviations of simualtion B and the measurement data are probably caused by the applied approximations. The electrical contact resistances were assumed to be identical at each junction. Due to the usage of different material classes such an approach is very rude and causes slightly inaccurate values for the internal load R_{TEG}. The power characteristics of measured data and FEM results are displayed in Figure 5(b). The results of simulation A are highly overestimated. For simulation B and the measurement data, the characteristic power-plots show a comparable curvature. For decreasing temperature, the measured electric current deviates more and more from the values of simulation B. This simulation concerns the electric contact resistances but thermal contact resistances were neglected. Therefore, the thermal current densities inside the simulated materials are not absolutely correct. Such a lack of accuracy for the values of the thermal power P_{th} can cause deviations in the solutions for the electric power

output P_{el} because these quantities depend on each other at constant thermoelectric conversion efficieny η_{TE}. The relation is given in eq. (10).

$$P_{el} = \eta_{TE} \cdot P_{th} \tag{10}$$

For absolutely correct solutions of FEM simulations in the framework of thermoelecric generator performance, both, the electric and the thermal contact resistances have to be considered, see Högblom and Andersson (2014). Implementation of contact resistances (electrical and thermal) into FEM simulations is not straight forward (see Annapragada et al. (2012)).

The simulation results are presented as contour-plots for the potential distributions and as vectorial plots that refer to the density of electric current j_q in simulation A and simulation B. The colors of the vectors refer to the local value of the flux density of the transported quantity, which is indicated in the legend. Figure 6(a) shows the distribution of the entropy potential T, obtained from the FEM simulation and a perspective view of the TEG at maximum electric power output for a potential drop of $\Delta T = 120K$. The situation of temperature distribution is equal for
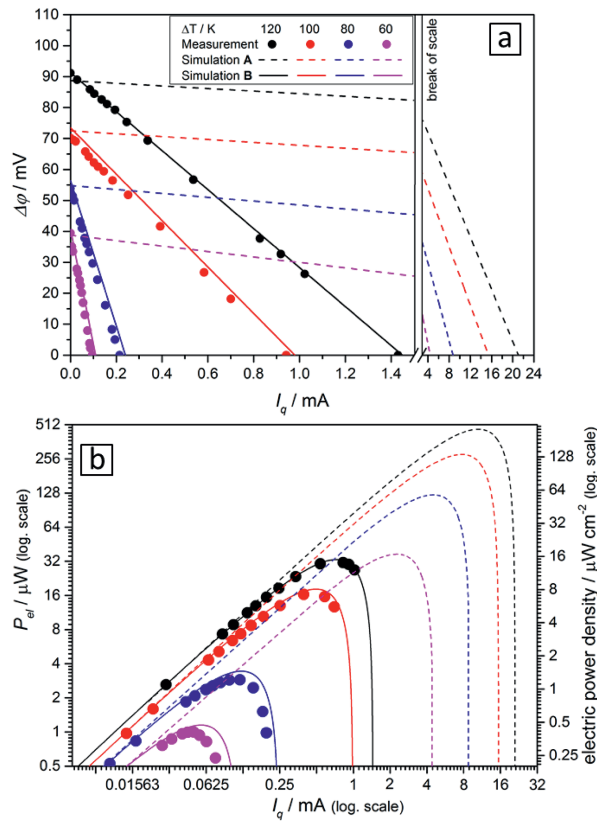
Figure 5: Measured (dots) and simulated (lines) results for the thermoelectric characteristics of the constructed TEG. (a) Electric voltage-current $\Delta\varphi$-I_q characteristics of the measured data and the FEM simulation A (dashed lines) and simulation B (solid lines), (b) Electric power-current P_{el}-I_q characteristics for measured data and the FEM simulation A and B. For better comparison, the values are plotted logarithmically.

Table 4: Thermoelectric parameters of the modeled TEG for Simulation A and Simulation B.

			Simulation A				Simulation B			
T_{hot}/K	ΔT/K	T_{median}/K	R_{TEG}/Ω	$P_{el, max}$/μW	$\Delta\varphi_{OC}$/mV	$I_{q, SC}$/mA	R_{TEG}/Ω	$P_{el, max}$/μW	$\Delta\varphi_{OC}$/mV	$I_{q, SC}$/mA
389	60	363	7.33	37.01	40.4	5.32	355.85	1.15	40.5	0.11
441	80	403	6.11	123.31	53.9	8.82	231.66	3.43	56.4	0.24
492	100	443	4.53	280.01	73.3	15.3	74.31	18.17	73.5	0.98
536	120	478	4.04	467.13	91.0	21.1	62.89	33.12	91.3	1.45

simulations A and B. Figure 6(b) shows the respective distribution of the electric potential $\Delta\varphi$ along the electrical serial connection of the assembled thermoelectric legs and electric connectors (Ag-epoxy resin) inside the thermoelectric generator. The displayed simulation results of the TEG are related to the conditions of electric power maximum (from Figure 5(b)) for a temperature drop of 120 K.
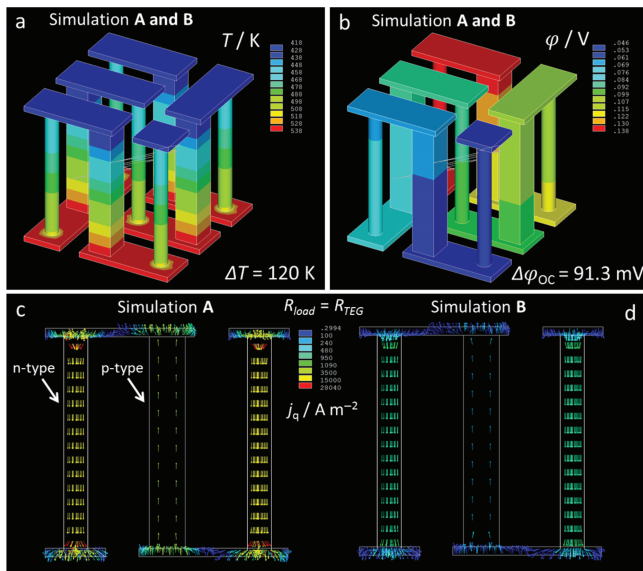
Figure 6: Simulated results for the thermoelectric characteristics of the constructed TEG. (a) Temperature distribution for $\Delta T = 120K$ for simulation A and B, (b) distribution of electric potential along the electric series connection of TE legs for electric open-circuit conditions (nearly equal values for simulation A and B), (c) electric current density j_q for simulation A, (d) electric current density j_q for simulation B. Note that the current densities for simulation A and simulation B are correlated to the same color-related legend and refer to electric maximum power condition. For comparison of temperature related quantities see Table 4.

The flux density of electric charge j_q depends on the material of the TEG's components and on the local potential gradients according to the potential distributions shown in Figure 6(a) and (b). The modeling of TEGs using the FEM method has the advantage of providing deep insight into the distribution of all relevant quantities throughout the entire device. From Figure 6(c) and (d), it is obvious that the electric current density j_q inside the entire arrangement of materials is much smaller than predicted by simulation A. Therefore, the electric power output predicted by simulation A is more than 10 times higher compared to the electric power received by simulation B and the experiment. In the metallic $Cu_{0.57}Ni_{0.42}Mn_{0.01}$ legs the electric current density is more than 3 times lower in simulation B compared to the results of simulation A. Varying the specific electric resistivity of the electric connector Ag-epoxy resin, by taking the contact resistances into account, results in almost correct densities of electric current inside each material. The contact region of the Ag-epoxy resin and the thermoelectric materials limits the electric current density inside the entire generator because electric contact resistances between the connector material and the thermoelectric legs are formed. The

results from the finite-element simulation illustrate the relation between the entropy potential T and electric potential φ, which is given algebraically in eq. (1) by the respective distribution of potentials, and the obtained electric current I_q.

Summary and Conclusions

The model thermoelectric system created from the finite-element simulation provides results with acceptable accuracy in terms of the values for the open-circuit voltages. The simulation for the current densities and therefore for the electric power output of the generator was predicted with too high values. The overestimation of the electric current density is based on the formation of contact resistivities that were formed at the material boundaries of the Ag-epoxy resin as electric connector and the thermoelectrically active materials. Those contacts in TEG devices can be realized by different materials. The Ag-epoxy resin exhibits good properties in terms of processability and mechanical fixation. The adhesive is more heat proved than Sn-Pb based solders. However, the

contact resistances in thermoelectric generators are an important concern. Using the finite-element simulation tool, the quantitative electrical contact resistances could be determined.

After including the contact resistances into the electric resistivities of the connector material a good match of measured and simulated data were obtained. The Ag-epoxy resin was used as an alternative to soldering that can also exhibit high contact resistivities when ceramic materials are applied. The used thermoelectric materials are p-type $Ca_3Co_4O_9$ ceramic and n-type $Cu_{0.57}Ni_{0.42}Mn_{0.01}$ alloy. The FEM simulation was used to estimate the limiting factor in terms of electric power output. The theoretical maximum power was calculated to almost 500 μW with a temperature difference of $\Delta T = 120$ K, while the measured maximum electric power output for the same temperature conditions was only 32.5 μW. The FEM results show that a minimization of the contact resistances in TEG devices can dramatically increase the electric output power. At lower temperatures the $Ca_3Co_4O_9$ ceramic provides a charge carrier density that is usable also in devices for low-temperature applications. Deep insights into the local variations of the relevant thermoelectric parameters can be obtained from this type of FEM modeling. Overall, the developed model system can predict the thermoelectric properties of a certain TEG quite well if the proper parameters for feeding the simulation tool are selected. Work on thermoelectric materials and systems benefits from the use of FEM simulations to compare the properties of the modeled and the measured device to gain knowledge on the factors that limit the electric power output of a certain thermoelectric generator.

References

Annapragada, S., T. Salamon, P. Kolodner, M. Hodes, and S. Garimella. 2012. "Determination of Electrical Contact Resistivity in Thermoelectric Modules (TEMs) from Module-Level Measurements." *Transactions on Components, Packaging and Manufactering Technology* 2 (4):668–676.

Falk, G., F. Herrmann, and G. Schmid. 1983. "Energy Forms or Energy Carriers?." *American Journal Physical* 51:1074–1077.

Feldhoff, A. 2015. "Thermoelectric Material Tensor Derived from the Onsager – De Groot – Callen Model." *Energy Harvesting and Systems* 2 (1–2):5–13.

Feldhoff, A., and B. Geppert. 2014a. "Erratum to EHS 1 (1-2), 69-78 (2014): A High-Temperature Thermoelectric Generator Based on Oxides." *Energy Harvesting and Systems* 1 (3–4):251.

Feldhoff, A., and B. Geppert. 2014b. "A High-Temperature Thermoelectric Generator Based on Oxides." *Energy Harvesting and Systems* 1 (1–2):69–78.

Fergus, J. 2011. "Oxide Materials for High Temperature Thermoelectric Energy Conversion." *Journal of the European Ceramic Society* 32:525–540.

Fuchs, H. 2010. *The Dynamics of Heat – A Unified Aproach to Thermodynamics and Heat Transfer*, Graduate Texts in Physics, 2nd ed. New York: Springer.

Fuchs, H. 2014. "A Direct Entropic Approach to Uniform and Spatially Continuous Dynamical Models of Thermoelectric Devices." *Energy Harvesting and Systems* 1 (3–4):253–265.

Geppert, B., and A. Feldhoff. 2015. "An Approach to a Flexible Thermoelectric Generator Fabricated Using Bulk Materials." *Energy Harvesting and Systems* 2:1–11.

Högblom, O., and R. Andersson. 2014. "Analysis of Thermoelectric Generator Performance by Use of Simulations and Experiments." *Journal of Electronic Materials* 46 (6):2247–2254.

Holgate, T., L. Han, N. Wu, E. Bojesen, M. Christensen, B. Iversen, N. Nong, and N. Pryds. 2014. "Characterisation of the Interface between an Fe-Cr Alloy and the P-Type Thermoelectric Oxide $Ca_3Co_4O_9$." *Journal of Alloys and Compounds* 585:827–833.

Ioffe, A. 1957. *Semiconductor Thermoelements and Thermoelectric Cooling*, 1st ed. London: Infosearch Ltd.

Lambert, S., H. Leligny, and D. Gebrille. 2001. "Three Forms of the Misfit Layered Cobaltite $[Ca_2CoO_3]$ $[CoO_2]_{1.62}$ · A 4D Structural Investigation." *Journal of Solid State Chemistry* 160:322–331.

LeBlanc, S. 2014. "Thermoelectric Generators: Linking Material Properties and Systems Engineering for Waste Heat Recovery Applications." *Sustainable Materials and Technologies* 1–2:26–35.

Lowhorn, N.D., W. Wong-Ng, W. Zhang, Z.Q. Lu, M. Otani, E. Thomas, M.G.T.N. Tran, N. Dilly, S. Ghamaty, N. Elsner, T. Hogan, A.D. Downey, Q. Jie, Q. Li, H. Obara, J. Sharp, C. Caylor, R. Venkatasubramanian, R. Willigan, J. Yang, J. Martin, G. Nolas, B. Edwards, and T. Tritt. 2009. "Round-Robin Measurements of Two Candidate Materials for a Seebeck Coefficient Standard Reference Material." *Applied Physics A* 94:231–234.

Lu, Z.Q.J., N.D. Lowhorn, W. Wong-Ng, W. Zhang, Z.Q. Lu, M. Otani, E. Thomas, M.G.T.N. Tran, N. Dilly, S. Ghamaty, N. Elsner, T. Hogan, A.D. Downey, Q. Jie, Q. Li, H. Obara, J. Sharp, C. Caylor, R. Venkatasubramanian, R. Willigan, J. Yang, J. Martin, G. Nolas, B. Edwards, and T. Tritt. 2009. "Statistical Analysis of a Round-Robin Measurement Survey of Two Candidate Materials for a Seebeck Coefficient Standard Reference Material." *Journal of Research of the National Institute of Standards and Technology* 114:37–55.

Shikano, M., and R. Funahashi. 2003. "Electrical and Thermal Properties of Single-Crystalline $(Ca_2CoO_3)_{0.7}CoO_2$ with a $Ca_3Co_4O_9$ Structure." *Applied Physics Letter* 82 (12):1851–1851.

3.4 All-oxide thermoelectric generator with in-situ formed
non-rectifying complex p-p-n junction and transverse thermoelectric 101
effect

3.4 All-oxide thermoelectric generator with in-situ formed non-rectifying complex p-p-n junction and transverse thermoelectric effect

Nikola Kanas, Michael Bittner, Temesgen Debelo Desissa,

Sathya Prakash Singh, Truls Norby, Armin Feldhoff, Tor Grande,

Kjell Wiik and Mari-Ann Einarsrud

All-oxide thermoelectric module with *in-situ* formed non-rectifying complex p-p-n junction and transverse thermoelectric effect

Nikola Kanas[1, 2], Michael Bittner[2], Temesgen Debelo Desissa[3], Sathya Prakash Singh[1], Truls Norby[3], Armin Feldhoff[2], Tor Grande[1], Kjell Wiik[1] and Mari-Ann Einarsrud[1*]

[1]*Department of Material Science and Engineering, NTNU Norwegian University of Science and*

Technology, Trondheim, Norway

[2]*Institute of Physical Chemistry and Electrochemistry, Leibniz University, Hannover, Germany*

[3]*Department of Chemistry, Centre for Materials Science and Nanotechnology, University of Oslo,*

Norway

KEYWORDS: *oxide processing, thermoelectric module, p-p-n junction, transverse thermoelectric effect*

ABSTRACT: All-oxide thermoelectric modules for energy harvesting are attractive due to high temperature stability, low cost, and the potential to use non-scarce and non-toxic elements. Thermoelectric modules are mostly fabricated in the conventional π-design, associated with the challenge of unstable metallic interconnects at high temperature. Here, we report on a novel approach to fabrication of a thermoelectric module with an *in-situ* formed p-p-n junction made of state-of-the-art oxides $Ca_3Co_{4-x}O_{9+\delta}$ (p-type) and $CaMnO_3$-$CaMn_2O_4$ composite (n-type). The module was fabricated by spark plasma co-sintering of p- and n-type powders partly separated by insulating $LaAlO_3$. Where the n- and p-type materials originally were in contact, a layer of p-type Ca_3CoMnO_6 was formed *in-situ*. The hence formed p-p-n junction exhibited ohmic behavior and a transverse thermoelectric effect, boosting the open circuit voltage of the module. The performance of the module was characterized at 700 - 900 °C, with the highest power output of 5.7 mW (around 23 mW/cm²) at 900 °C and a temperature difference of 160 K. The thermoelectric properties of the p- and n-type materials were measured in the temperature range 100 - 900 °C, where the highest zT of 0.39 and 0.05 were obtained at 700 and 800 °C, respectively, for $Ca_3Co_{4-x}O_{9+\delta}$ and the $CaMnO_3$-$CaMn_2O_4$ composite.

1. Introduction

Energy harvesting from waste heat from e.g. combustion engines or metallurgical processes or other industry has great potential for energy savings and emission reductions. Thermoelectric (TE) generators present a promising technology for such energy recovery [1]. A thermoelectric generator (TEG) is based on two dissimilar materials (p- and n-type) connected together and when exposed to a temperature gradient, converts thermal energy into electrical energy [1]. Power density ($P_{density}$) and the figure of merit (zT) are used to evaluate TE modules and their consisting p- and n-type materials, respectively. Figure of merit for any p- or n-type material can be calculate using

$$zT = \frac{S^2 \sigma T}{\kappa} \qquad (1)$$

where *S*, *σ,* and *κ* represent Seebeck coefficient, electrical conductivity, and thermal conductivity, respectively [2]. In a conventional module (π-design), p- and n-type materials are connected electrically in series and thermally in parallel, with conductive metallic interconnects between legs (mostly Ag or Au) [3-4]. Conventional modules normally suffer from limited temperature, which obstructs the high-temperature advantage of oxides. Furthermore, conventional modules demonstrate short lifetimes due to the instability of the metallic interconnects, and even at low temperature resulting in a decrease in power output as a function of time [5]. All-oxide TE modules with direct oxide-oxide p-n junction would therefore be beneficial. However, such direct p-n junction will normally have high resistance due to charge carrier depletion in the space charge regions [6].

Shin *et al.* demonstrated for the first time the prototype of a direct p-n oxide module using Li-doped NiO and (Ba, Sr)PbO₃, and 14 mW at Δ*T* = 552 K was achieved [7]. Later,

Hayashi *et al.* reported a stacked module with direct p-n oxide junctions based on p-type $(La_{1.97}Sr_{0.03})CuO_4$ and n-type $(Nd_{1.97}Ce_{0.03})CuO_4$, where the maximum power density obtained from 25 pairs was 40 mW/cm² at 400 °C and ΔT = 360 K [8]. Moreover, Funahashi *et al.* demonstrated a module using a non-oxide p-type $Ni_{0.9}Mo_{0.1}$ and n-type $La_{0.035}Sr_{0.965}TiO_3$ [9] where the maximum obtained power density from 50 pairs was 450 mW/cm² at ΔT = 360 K. Furthermore, Chavez *et al.* showed another concept of using large area p-n junctions (containing no insulator) as a TE module where 1.3 mW was generated from one pair at ΔT = 300 K [10]. The chemical compatibility, long-term stability, and electrical performance of the p-n junctions/modules were not considered in these studies.

$Ca_3Co_{4-x}O_{9+\delta}$ (CCO) has a misfit-layered complex crystal structure containing triangular CoO_2 and rock-salt Ca_2CoO_3 layers [11]. CCO shows p-type conductivity and exhibits excellent thermoelectric power at elevated temperatures in ambient air [12]. $CaMnO_{3-\delta}$ (CMO) has a perovskite structure and exhibits n-type conductivity resulting from an intrinsic oxygen deficiency. By introducing a secondary $CaMn_2O_4$ spinel phase, the TE properties of the $CaMnO_{3-\delta}$-$CaMn_2O_4$ composite are improved compared to single phase $CaMnO_{3-\delta}$, as shown by Singh *et al.* [13]. TE properties of these oxides can further be improved by doping or co-doping [14]. So far, only a few reports on conventional modules based on the CCO-CMO based system are available [15-22].

Here we report on high-temperature thermoelectric performance for an all-oxide TE module based on the system p-type $Ca_3Co_{4-x}O_{9+\delta}$ (CCO) and n-type $CaMnO_3$-$CaMn_2O_4$ (CMO-composite). $LaAlO_3$ (LAO) was selected as the electrical insulating component, due to its ferroelastic properties [23] and high thermal expansion coefficient (TEC) compared to other potential insulating oxide candidates. Undoped CCO and a CMO-composite were selected as model materials in this work focusing on developing processing methods of the layered module and thereby analyzing the effect of a direct oxide-oxide p-n junction at high-temperature on TE performance of the module. The performance of the module critically depends on the properties of an *in-situ* formed complex p-p-n-junction, which was studied with respect to stability, interdiffusion, compatibility and electrical conductivity. Finally, we report on an environment friendly processing method for all oxide TE-devices based on aqueous tape casting and co-sintering of the three materials using spark plasma sintering.

2. Experimental

2.1 Materials and ceramic processing

The ceramic powders used in this work were prepared by spray pyrolysis (CerPoTech AS, Norway). Slurry for aqueous tape casting of the LAO insulator was prepared according to the schematics shown in Fig. S1 (Supplementary data). The slurry was casted on polyester (Mylar) film

using a height of the doctor blade of 30 μm. After drying at ambient temperature, lamination of 8 layers was conducted by hot-pressing at 150 MPa and 80 °C for 3 min. The laminated tape was cut into 12 mm discs with one segment cut off (around 3 mm) in order to make the direct p-n junction. Binder burnout was done at 440 °C for 4 h in air, placing the tape between two alumina plates to avoid bending. The TE module was fabricated by spark plasma sintering (SPS, Dr Sinter 825) in a 12 mm graphite die at 880 °C and 75 MPa for 5 min using heating and cooling rates of 120 °C/min. Initially, the graphite die was filled with the CMO-composite powder (1.5 g), then the cut LAO tape was placed on CMO-composite powder, followed by filling of CCO powder (0.5 g) onto the LAO tape.

In addition, CMO-composite and CCO materials were separately sintered by SPS using the same conditions as used for the TE module. These pellets were cut into bar-shape (20×5×2.5 mm) for electrical conductivity and Seebeck coefficient measurements and discs (12.7 mm diameter) for thermal conductivity measurements. Densities of pellets and bars were determined by Archimedes measurement in isopropanol. In order to do a separate analysis of the direct CCO – CMO-composite junction, two samples were prepared by SPS co-sintering at 820 °C and 50 MPa for 10 min. One of these samples was further annealed at 900 °C for 100 h in air.

2.2 Characterization

Phase composition and particle size/morphology were characterized by powder X-ray diffraction (Bruker D8 DaVinci) and scanning electron microscope (SEM, Hitachi S-3400N), respectively. Sinterability and TEC were determined by dilatometer (Netzsch DIL 402) in ambient air. TEC was measured both parallel and perpendicular to the pressing direction for CCO made by SPS. Thermoelectric performance of CCO and CMO materials were analyzed by measuring Seebeck coefficient (ProboStat™, NORECS AS), electrical conductivity (home-made setup) and thermal conductivity (Netzsch LFA 457 MicroFlash) at 100 - 900 °C in ambient air as described elsewhere [24-25].

For the power-current-voltage characterization, the layered disc-shaped TE module was placed horizontally on an alumina plate with the direct p-n junction at the top (hot temperature side).

To ensure better physical stability of the free-standing module, a small area of about 0.25 cm² was removed on the cold side. Both semiconductors were contacted by Pt-wires at the lower, colder end, using gold paste (Heraeus). The alumina plate with the TE module connected to Pt-wires was heated at 700 °C for 4 h in ambient air, in order to establish good electrical contact between the metal electrodes and semiconducting oxides.

The power output test in ambient air was performed via load-resistance dependent measurement, in a vertical

furnace at 700, 800 and 900 °C, and ΔT = 160 K. The temperature gradient was established by heating the hot side of the module in the furnace, while the cold side was cooled by an active cooler. The temperature difference ΔT was measured by two Pt-Pt10Rh (type S) thermocouples. During the power output measurement, the voltmeter was connected in parallel to the amperemeter, variable resistor (in series to each other) and to the TE module. When thermal equilibria were established at each temperature, electrical current and voltage were measured with increasing load resistance. More details could be found in reference number 4.

Finally, annealed and as-sintered p-n junctions were characterized by current-voltage measurements at 300, 500 and 700 °C in a vertical furnace, using a ProboStat™ cell (NORECS, Norway). A two-electrode set-up was used, where a DC voltage was applied to the junction followed by measuring current output using Multimeter-Agilent E3642A. After the measurements, the samples were embedded in "EpoFix" resin, polished by diamond paste (DiaPro NapB1) to 1 μm and coated with carbon (Cressington Carbon Coater 208) for microstructural characterization. Interface reaction and inter-diffusion at the p-n junction were investigated using SEM and energy dispersive spectrometry (EDS) (Hitachi S-3400N).

1. Results

3.1 Powder characteristics

X-ray diffraction patterns of CCO, CMO-composite and LAO powders are presented in Fig. 1a, confirming the phase purity of CCO and LAO as well as the composite nature of the CMO-composite ($CaMnO_3$ with minor amount of $CaMn_2O_4$ secondary phase). Included in Fig. 1a are also XRD patterns of polycrystalline CCO prepared by SPS, both parallel and perpendicular to the pressing direction. A high degree of texture is observed (c oriented parallel to the pressing direction) as well as small amounts of $Ca_3Co_2O_6$ and Co_3O_4 secondary phases.

Fine-grained powders of the three starting oxides are confirmed from the SEM images in Fig. 1b. Sintering curves for the CCO, CMO-composite and LAO powders shown in Fig. 1c demonstrate the onset of sintering at around 650, 900 and 1000 °C for CCO, CMO-composite and LAO, respectively.

TECs of CCO (perpendicular and parallel to pressing direction during SPS), CMO-composite and LAO are summarized in Table 1. CCO and CMO-composite show similar TECs while LAO has a significantly lower value.
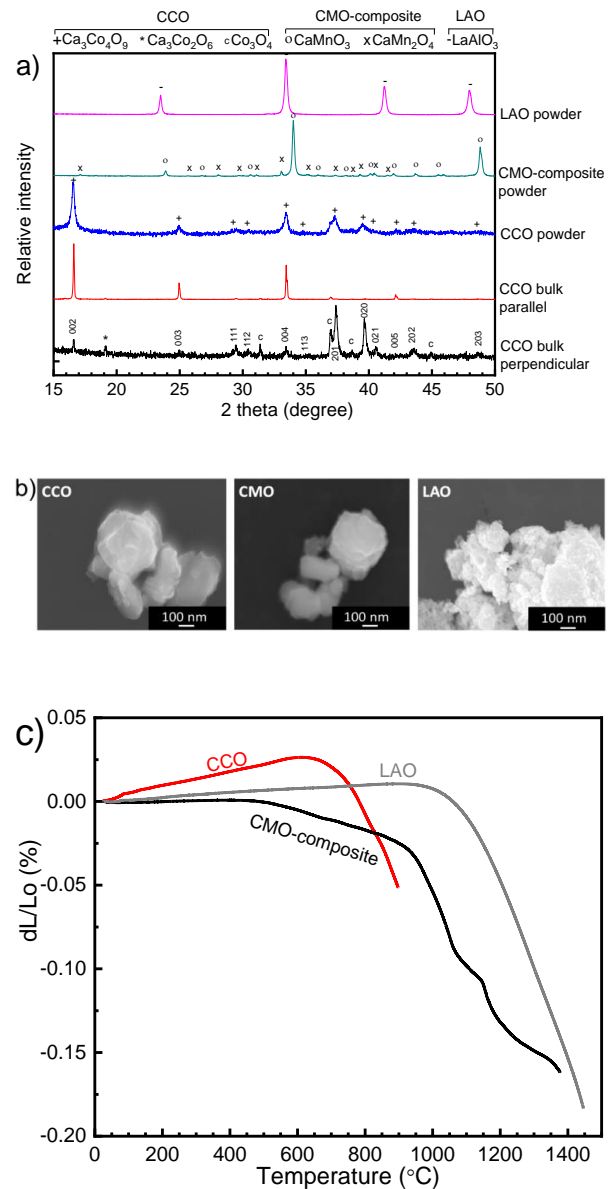

Fig. 1. a) XRD patterns of CCO, CMO-composite and LAO powders as well as a sample of CCO made by SPS in the directions parallel and perpendicular to the pressing direction, b) SEM micrographs and c) sintering curves of CCO, CMO-composite and LAO powders produced by spray pyrolysis. Diffraction lines from articles CCO [26], LAO [23] and CMO [13] are indicated in a).

Table 1. Thermal expansion coefficients (TEC) of CCO (perpendicular and parallel to the pressing direction during SPS), CMO and LAO.

	CCO parallel to the press-ing direction	CCO perpendicular to the press. direction	LAO	CMO-composite
400-800 °C (heating)	17.0	14.4	9.7	18.0
700-400 °C (cooling)	17.8	14.5	9.7	18.2

3.2 TE performance of the materials

 Electrical conductivity, thermal conductivity, Seebeck coefficient, power factor and *zT* as a function of tempera-ture, for the p- and n-type oxides are presented in Fig. 2. CCO shows a maximum electrical conductivity in the range of 500 - 600 °C, reaching approximately 100 S/cm (Fig. 2a). On the other hand, the electrical conductivity of the CMO-composite has a constant value of 7 S/cm up to 600 °C from where it increases to 28 S/cm at 900 °C. The thermal conductivity of both materials decreases with temperature, reaching minima of 0.85 $Wm^{-1}K^{-1}$ at 700 °C for CCO and 1.42 $Wm^{-1}K^{-1}$ at 800 °C for the CMO-composite (Fig. 2b). A maximum Seebeck coefficient of 186 μVK^{-1} at 500 °C for CCO and -325 μVK^{-1} at 400 °C for the CMO-composite (Fig. 2c) was achieved. A maximum power factor for CCO (3.6 $\mu Wcm^{-1}K^{-2}$) was obtained at ~ 500 °C. The figure-of-merit, *zT,* presented in Fig. 2d in-creased with temperature, reaching 0.39 at 700 °C for CCO and 0.05 at 800 °C for the CMO-composite. The electrical conductivity and Seebeck coefficients were measured in the direction perpendicular to the pressing direction, while the thermal conductivity was recorded parallel to the pressing direction of the sample. The measurements in the two different orientations resulted in a higher *zT* than the real one since the reported ther-mal conductivity of CCO is strongly anisotropic [27].

3.3 TE module

Schematic of the cross-section of the TE module design is shown in Fig. 3a. The thickness of the CMO-composite after co-sintering is approximately four times larger than the thickness of the CCO layer. Resistance, *R*, of both conductors was calculated by the formula $R = \rho \cdot l/A$ where ρ is electrical resistivity (cm·S^{-1}), *l* height/length (cm) and *A* is area (cm^2). The electrical resistance of CMO-composite at e.g. 800 °C is about 1.6 more than one of CCO, and therefore the CMO-composite represents more electrically resistive part in spite of larger thickness com-pared to CCO and limits the charge carrier flow. Due to significant increase in electrical conductivity of CMO-composite above 800 °C, and slight decrease of CCO, the electrical resistance of CMO-composite at 900 °C is about 0.7 times less than one of CCO, hence the CCO represents more electrically resistive part.

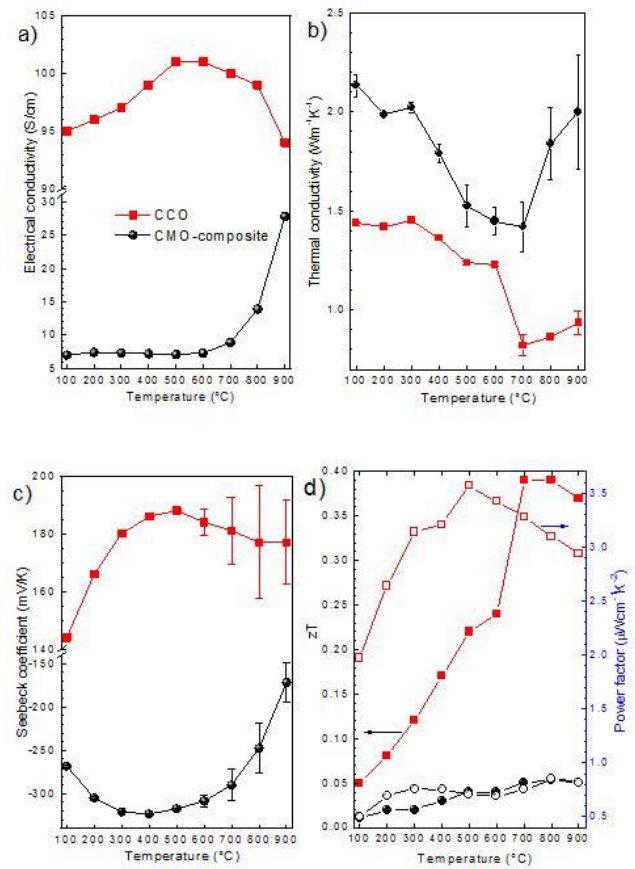

Fig. 2. a) Electrical conductivity, b) thermal conductivity, c) Seebeck coefficient, and d) *zT* (full symbols) and power factor (open symbols) as a function of temperature for CCO and CMO-composite ceramics. Error bars represent standard deviation based on five (Seebeck coefficient) and three (thermal conductivity) measured values. The uncer-tainty in electrical conductivity is within ± 1 %.

Table 2. Open-circuit voltage U_{OC}, short-circuit current $J_{q,sc}$, electrical resistance R, electrical power output P_{max} and power density of CCO-CMO TE module at 700, 800 and 900 °C at 160 K temperature difference between the hot and cold side.

T_h (°C)	U_{oc} (mV)	$J_{q,sc}$ (mA)	R_{couple} (Ω)	P_{max} (mW)	P_{max} (mW/cm²)
700	181	82	2.2	4.0	16
800	208	101	2.1	5.2	21
900	213	108	2.0	5.7	23

Voltage (polynomial fitting) and power output of the TE module as a function of measured current output are shown in Fig. 3b. Dashed lines represent current and voltage at maximum power at 700, 800 and 900 °C at the hot side of the module. Power output increases with temperature, reaching a maximum of about 5.7 mW at 900 °C. The effective power density of about 23 mW/cm² at this temperature was calculated from the effective area of TE module (approximately 0.25 cm²). Open-circuit voltage U_{OC} and short-circuit current $J_{q,SC}$ were determined by extrapolation from the measured J_q–U line and reached 213 mV and 108 mA at 900 °C, respectively. Data from the characterization of the TE module performance is summarized in Table 2.

Since the power output is dependent on load-resistance, the maximum power output could be measured when the set-up-load from an external circuit of 5.7 Ω became equal to the TE module's resistance of about 2.1 Ω (at 800 °C) [28]. The calculated ZT of the module is 0.01, using

$$ZT = \frac{U_{OC}}{J_{q,SC}R_{module}} - 1 \qquad (2)$$

where U_{OC}, $J_{q,SC}$ and R_{module} represents open-circuit voltage, short-circuit current and resistance of the module, respectively [29].

3.4 p-p-n junction

The microstructure of the CCO-CCMO-CMO p-p-n junction before and after annealing at 900 °C for 100 h are shown in Fig. 4a. Elongated grain growth parallel to the interface is evident in CCO. A thin Ca_3CoMnO_6 (CCMO) layer, confirmed by EDS, is formed *in-situ* between CCO and CMO during the co-sintering. The CCMO layer has grown to approximately 5 µm after annealing at 900 °C for 100 h. In addition, a layer of approximately 35 µm thickness close to the interface displayed a higher density than the rest of the CCO. From the EDS profiles of the CCO-CMO interface presented in Fig. 4b the Ca content in this dense layer is lower than in CCO showing a Co-rich and a Ca-deficient region at the interface. The Ca:Co ratio equals the initial Ca:Co ratio corresponding to pure CCO approximately 40 µm from the interface. A Co-oxide phase seen as grains with higher Co-content in Fig. 4a is present both in the dense interface layer as well as in the CCO far from the interface.

Current-voltage curves across the CCO-CCMO-CMO complex junction before and after annealing at 900 °C for 100 h, measured at 300, 500 and 700 °C are presented in Fig. 5a. Ohmic behavior is observed in the whole temperature range for both the as-sintered and annealed junctions, and the resistance decreases with increasing temperature. The difference in the resistance for the as-sintered and annealed samples is less pronounced as the temperature increases, and at 700 °C almost no difference is observed.
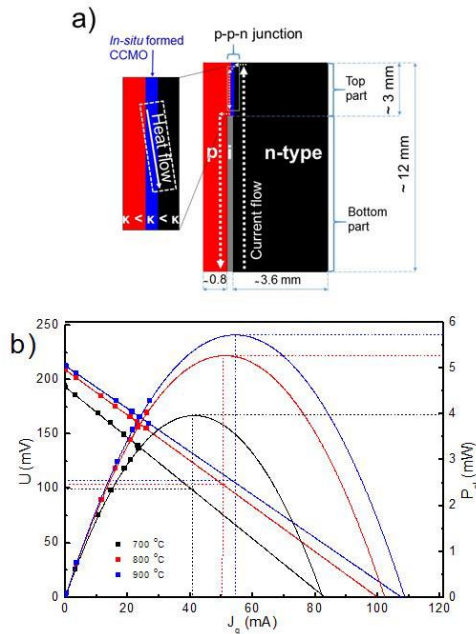

Fig. 3. a) Schematic of the cross-section of the TE module with illustrated top part and bottom part as well as flow direction of heat at top part b) polynomial fitting of electrical power output (P_{el}) and linear fitting of voltage (U) as a function of the electrical current (J_q) at different T_{hot} temperatures (700, 800 and 900 °C) and constant ΔT = 160 K. Voltage and current at maximum power $U(P_{max})$ and $J_q(P_{max})$ at different temperatures are also indicated by dotted lines.
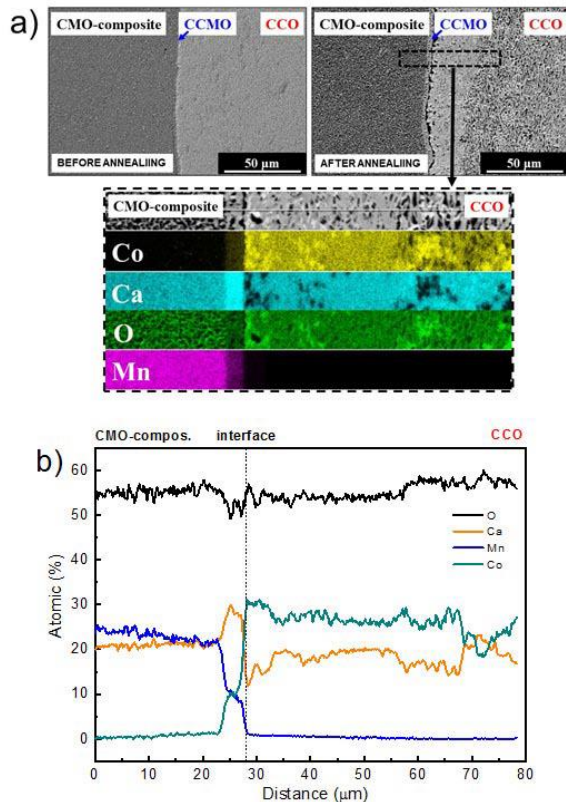
Fig. 4. a) SEM micrographs of CCO-CCMO-CMO junction before and after annealing at 900 °C for 100 h and EDS maps of the magnified section of the annealed junction given by the dashed lines and b) EDS line profiles across the CCO-CCMO-CMO junction after annealing.

The resistance of the as-sintered and the annealed samples is presented in Fig. 5b. The inset presents the activation energy for conduction of the as-sintered and annealed samples according to the Arrhenius equation, where the annealed sample demonstrates twice the activation energy of the as-sintered.

4. Discussion

4.1 Ceramic processing

A new co-sintering route to an all-oxide TE module was developed. The maximum sintering temperature was limited by the decomposition temperature of CCO. Moreover, CMO possesses a phase transition at 896-913 °C [30] from orthorhombic to tetragonal phase associated with a volume change, which also could introduce stresses in the device. Therefore, 880 °C was selected as the maximum co-sintering temperature. Since this temperature is low for efficient densification of CMO-composite and LAO (Fig. 1c), a maximum pressure of 75 MPa was applied in the SPS with optimal 5 min hold, which resulted in 70 and 46 % relative density for CMO-composite and LAO, re-

spectively. CCO was completely densified after 2 min at 880 °C, but due to grain growth and micro-delamination the final density after 5 min was 91 % of theoretical. The CMO-composite possesses the highest TEC of the three materials (Table 1) and tensional stress is induced during cooling, hence the CMO-composite represents the most sensitive part of the module during processing being prone to crack formation. The crack formation could be controlled by designing a thin CCO (~0.8 mm) and thick CMO (~3.6 mm) layer reducing the tensile stresses in the CMO-composite. The calculated tensile stresses in the CMO-composite (Supplementary data, Fig. S2) developed during the cooling from 880 °C decreases both with increasing CMO-composite thickness and decreasing CCO thickness [31].
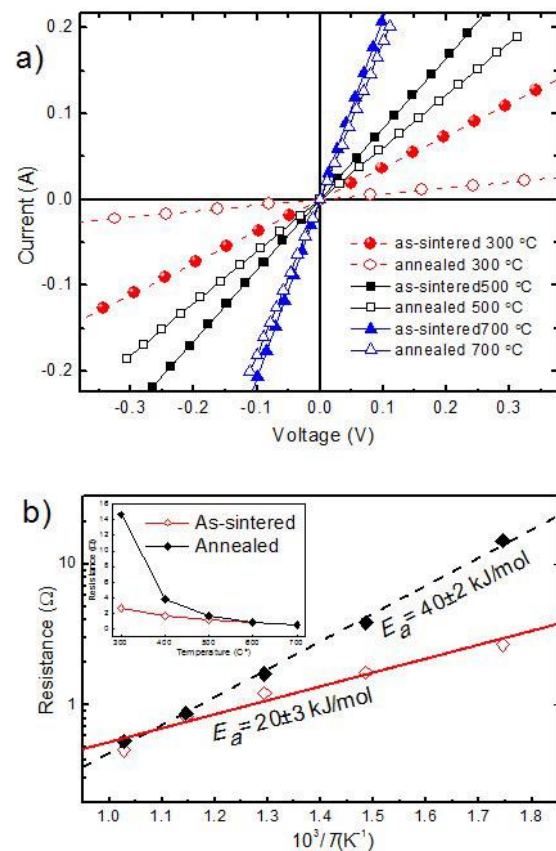
Fig. 5. a) Current-voltage curves of CCO-CMO-CMO p-p-n junctions before and after annealing at 900 °C for 100 h and b). The activation energies for electrical conduction for the as-sintered and annealed sample. The inset shows resistance of p-p-n junctions before and after annealing as a function of temperature.

4.2 Origins of high power output and open circuit voltage

As evident from Table 3, there are large differences in the output power of conventionally designed CCO-CMO TE modules dependent on whether CCO and CMO are doped

Table 3. Thermoelectric performance of conventional modules based on p-type CCO and n-type CMO reported in the literature.

System	N-pairs	T_{hot} (K°)	ΔT (K°)	P_{max} (mW)	$P_{density}$ (mW/cm²)	P/one pair (mW)	Reference
$Ca_3Co_4O_9$ $CaMnO_3$	12	473	200	1.98	3.3*	0.165*	Seetawan *et al.* [15]
$Ca_3Co_4O_9$ $CaMno_3$	31		200	$1.47 \cdot 10^{-3}$	$23.7 \cdot 10^{-3}$*	$4.74 \cdot 10^{-5}$*	Phaga *et al.* [16]
$Ca_{2.7}Bi_{0.3}Co_4O_9$ $CaMn_{0.98}Mo_{0.02}O_3$	8	897	565	170	42.5	21.2*	Urata *et al.* [17]
$Ca_{2.75}Gd_{0.25}Co_4O_9$ $Ca_{0.92}La_{0.08}MnO_3$	8	773	390	63.5	44.1	7.9*	Matsubara *et al.* [18]
$Ca_3Co_4O_9$ $Ca_{0.95}Sm_{0.05}MnO_3$	2	1000	925	31.5	49.2*	15.7*	Reddy *et al.* [19]
$Ca_3Co_4O_9$ $Ca_{0.9}Nd_{0.1}MnO_3$	1	1175	727	95	93.2	95	Lim *et al.* [20]
$Ca_{0.76}Cu_{0.24}Co_4O_9$ $Ca_{0.8}Dy_{0.2}MnO_3$	4		346	8.42		2.1*	Park *et al.* [21]
$Ca_3Co_4O_9$ $Ca_{0.95}Sm_{0.05}MnO_3$	2	990	630	31.5	49.2	15.7*	Noudem *et al.* [22]

The values marked with * are calculated, based on the data available in the given references

or (like in our case) undoped, as well as on the applied temperatures and gradients.

Urata *et al.* [17] reported as much as 42.5 mW/cm² for a doped system with a T_{hot} of about 900 °C and a gradient as high as 565 K, while undoped CCO-CMO systems at lower temperature and gradients of 200 K yielded merely 3.3 mW/cm² (Phaga *et al.* [16]) and $23.7 \cdot 10^{-3}$ mW/cm² (Seetawan *et al.* [16]).

Our prototype TE module with undoped CCO/CMO and a complex p-p-n junction could not be exposed to a larger ΔT than 160 K due to limitations of the set-up. Yet, a maximum power density of about 23 mW/cm² was generated at 900 °C. This we attribute to the remarkably high open circuit voltage and low interface resistance of the complex p-p-n-junction, as will be discussed next.

According to Kanas *et al.*, electrical conductivity of the CCMO phase formed at the interface increases sharply with increasing temperature from 800 to 900 °C and reaches around 0.1 S/cm at 900 °C, where the positive Seebeck coefficient furthermore reaches as high as 668 μV/K [32]. The three-layered CCO-CCMO-CMO junction

exhibits ohmic behavior with relatively modest interfacial resistance above 700 °C as evidenced in Fig. 5a. We tentatively interpret this as an effect of the electron energy levels of CCMO as laying intermediate of those of CCO and CMO, hence decreasing the depletion of charge carriers at the CCO-CCMO and CCMO-CMO interfaces as compared to a hypothetical pristine CCO-CMO p-n interface. This facilitates an electrical current flow through the p-p-n interface as illustrated in Fig. 3a.

The CCMO reaction layer is thicker in the annealed sample compared to the as-sintered one (Fig. 4 a), and in the temperature range 300 to 500 °C resistivity is higher for the annealed sample (Fig. 5). At 700 °C, the resistivity of both samples are almost equal (Fig. 5), showing that the same concentration of charges will be excited to conduction level due to thermal activation, demonstrating no effect of CCMO thickness on the current density above 700 °C. The CCMO layer is therefore contributing equally to the electrical conduction process at this high temperature.

When two materials A and B dissimilar in thermal conductivity and Seebeck coefficient are contacted over an area exposed to a parallel thermal gradient, a voltage is generated in the transversal direction, and an effective transversal Seebeck coefficient of the couple can be expressed according to Goldsmid [33];

$$S_{yo} = (S_A/K_A + S_B/K_B)/(1/K_A + 1/K_B) \qquad (3)$$

where S_A, S_B, K_A and K_B represent the Seebeck coefficients and thermal resistances of the two materials. In our case, the thermal conductivity of CCO at 900 °C is 0.94 $Wm^{-1}K^{-1}$ while that for CCMO is 1.3 $Wm^{-1}K^{-1}$ [32] and the CMO-composite is 2.0 $Wm^{-1}K^{-1}$. This will give rise to different heat flows down the n- and p-type materials, resulting in an increasing transversal temperature gradient down the CCMO interface layer corresponding to the transversal heat flow illustrated in Fig. 3a.

For the following discussion, the module may be divided into a top hot part above the LAO insulator and a bottom conventional part. The top part contains three material layers and two sub-junctions which contribute to a transversal thermoelectric voltage according to Equation (5), while the bottom part contribute to standard longitudinal thermoelectric voltages. Based on the dimensions of the module we may estimate a temperature difference of 40 K over the top part and the remaining 120 K cover the bottom part. Since the Seebeck coefficient of CMO is strongly influenced by temperature (Fig. 2 c), average values are used for summing up all possible contributions from materials and interfaces in the transversal and longitudinal parts. We arrive at an estimated open circuit potential of 125 mV, as compared with the estimate of 64 mV from a regular CCO and CMO couple with a total gradient of 160 K, based on their Seebeck coefficients of +177 µV/K and -171 µV/K (at 900 °C), and about +179 µV/K and -270 µV/K (at approximately 740 °C), respectively. Average absolute values of the Seebeck coefficient and thermal conductivity of CCO and CMO for the top and bottom

parts of the module used for the calculations are: 178 μVK^{-1} (CCO_{bottom}), 177 µV/K (CCO_{top}), 0.89 $Wm^{-1}K^{-1}$ (CCO_{top}), 229 μVK^{-1} (CMO_{bottom}), 189 μVK^{-1} (CMO_{top}) and 1.88 $Wm^{-1}K^{-1}$ (CMO_{top}). A transversal thermoelectric effect occurs when anisotropy in the electrical and thermal transport occurs [34], as in our top part of the module. This phenomenon is beneficially used for enhancing the voltage in transversal thermoelectric modules and related applications [34-38]. For instance, the transversal thermoelectric voltage in Ca_xCoO_2 textured thin films can be significantly higher than the ones generated by regular thermoelectric effect [34-36]. The transversal voltage significantly affected the open-circuit voltage U_{OC} and the maximum electrical power output P_{el}. The presence of a transverse thermoelectric effect can also be observed by comparison of U_{OC} of the TE module (Fig. 3b) and Seebeck coefficient together with the power factor of individual materials from 700 to 900 °C. The Seebeck coefficients (Fig. 2c) of the two individual materials decrease as temperature increases, as well as power factor of CCO (Fig. 2d), while U_{OC} of TE module increases with temperature (Fig. 3b). The experimentally measured U_{OC} of 213 mV is hence remarkably larger than both theoretical estimates. Further experimental and theoretical studies (e.g. FEM simulations) will be necessary to fully understand the effect of thin layers of materials with high Seebeck coefficients in the interface of p-n thermoelectric junctions. However, the *in-situ* formed complex p-p-n junctions evidently improved the performance of the all-oxide TE module, hence representing a significant step forward towards the possible application of oxide TE-modules in high-temperature energy recovery.

5. Conclusions

A novel all-oxide TE module was successfully developed and fabricated by careful processing of materials in the CCO-CMO system using LAO as an electrical insulator. Fabrication of this all-oxide TE module is simpler and faster than assembling conventional modules. The CCO-CMO module demonstrated a power of about 5.7 mW corresponding to a power density of 23 mW/cm^2 at T_{hot} = 900 °C and ΔT = 160 K, a TE performance comparable and better than some conventional CCO-CMO modules. The all-oxide layered TE module produces a large open circuit voltage, which was attributed to the presence of a thin CCMO reaction layer and transversal thermoelectric effect across the top p-p-n part of the TE module. The effect of the CCMO reaction layer is due to the large Seebeck coefficient, working transversally and reducing the charge carrier depletion and resistance at the high temperature p-n junction. The present investigation demonstrates an example of novel engineering of oxide thermoelectric modules without metallic interconnects.

REFERENCES

[1] S. Walia; S. Balendhranet; H. Nili; S. Zhuiykov; G. Rosengarten; Q.H. Wang; M. Bhaskaran; S. Sriram; M.S. Strano; K. Kalantar-Zadehal, Transition metal oxides – Thermoelectric properties. *Prog. Mater. Sci.* **2013**, 58, 1443-1489.

[2] A.F. Ioffe, *Semiconductor thermoelements and thermoelectric cooling*, 1st ed.; Info-search Ltd.: London, 1957.

[3] M. Bittner; B. Geppert; N. Kanas; S.P. Singh; K. Wiik; A. Feldhoff, Oxide-based thermoelectric generator for high-temperature application using p-type $Ca_3Co_4O_9$ and n-type $In_{1.95}Sn_{0.05}O_3$ legs. *EHS*, **2016**, 3, 213-222.

[4] P. Tomeš; R. Robert; M. Trottmann; L. Bocher; M.N. Aguirre; A. Bitschi; J. Hejtmanek; A. Weidenkaff, Synthesis and characterization of new ceramic thermoelectrics implemented in a thermoelectric oxide module. *J. Electron. Mater.* **2010**, 39, 1696-1703.

[5] M.T. Barako; W. Park; A.M. Marconnet; M. Asheghi; K.E. Goodson, Thermal cycling, mechanical degradation, and the effective figure of merit of a thermoelectric module. *J. Electron. Mater.* **2013**, 42, 372-381.

[6] B.G. Streetman; S.K. Banerjee, *Solid state electronic devices, 6th edition*, PHI Learning Private Limited, New Delhi, 2009.

[7] W. Shin; N. Murayama; K. Ikeda; S. Sago, Thermoelectric power generation using Li-doped NiO and (Ba, Sr)PbO$_3$ module. *J. Power Sources.* **2001**, 103, 80-85.

[8] S.F. Hayashi; T. Nakamura; K. Kageyama; H. Takagi, Monolithic thermoelectric devices prepared with multilayer cofired ceramics technology. *Jpn. J. Appl. Phys.* **2010**, 49, 096505-1-4.

[9] S. Funahashi; T. Nakamura; K. Kageyama; H. Ieki, Monolithic oxide–metal composite thermoelectric generators for energy harvesting. *J. Appl. Phys.* **2011**, 109, 124509-1-4.

[10] R. Chavez; S. Angst; J. Hall; J. Stoetzel; V. Kessler; L. Bitzer; F. Maculewicz; N. Benson; H. Wiggers; D. Wolf; G. Schierning; R. Schmechel, High temperature thermoelectric device concept using large area p-n junctions, *J. Electron. Mater.* **2014**, 43, 2376-2383.

[11] A.C. Masset; C. Michel; A. Maignan; M. Hervieu; O. Toulemonde; F. Studer; B. Raveau, Misfit-layered cobaltite with an anisotropic giant magnetoresistance: $Ca_3Co_4O_9$. *Phys. Rev. B.* **2000**, 62, 166-175.

[12] T. Takeuchi; T. Kondo; K. Sonda; U. Mizutani; R. Funahashi; M. Shicano; S. Tsuda; T. Yokoya; S. Shin; T. Muro, Electronic structure and large thermoelectric power in $Ca_3Co_4O_9$. *J. Electron. Spectrosc.* **2004**, 137-140, 595-599.

[13] S.P. Singh; N. Kanas; M.-A. Einarsrud; T. Norby; K. Wiik, Thermoelectric properties of $Ca_xMnO_{3-\delta}$ composites ($0.934 \leq x \leq 1.028$) in air at temperatures between 100 and 900 °C. *To be submitted.*

[14] J.W. Ferguson, Oxide materials for high temperature thermoelectric energy conversion. *J. Eur. Ceram. Soc.* **2012**, 32, 525–540.

[15] T. Seetawan; K. Singsoog; S. Srichai; C. Thanachayanont; V. Amornkitbamrung; P. Chindaprasirt, Thermoelctric energy conversion of p-$Ca_3Co_4O_9$/n-CaMnO$_3$ module. *Energy. Proceed.* **2014**, 61, 1067-1070.

[16] P. Phaga; A. Vora-Ud; T. Seetawan, Invention of low cost thermoelectric generators. *Procedia Engineer.* **2012**, 32, 1050-1053.

[17] S. Urata; R. Funahashi; T. Mihara, *Proc. Int. Conf. on Thermoelectrics 2006*, Vienna, Austria (6-10 Aug 2006), p 501.

[18] I. Matsubara; R. Funahashi; T. Takeuchi; S. Sodeoka, Fabrication of all-oxide thermoelectric power generator. *Appl. Phys. Lett.* **2001**, 78, 3627-3629.

[19] E.S. Reddy; J.G. Noudem; S. Hebert; C. Goupil, Fabrication and properties of four-leg oxide thermoelectric modules. *J Phys D: Appl. Phys.* **2005**, 38, 3751-3755.

[20] C.-H. Lim; S.-M. Choi; W.-S. Seo; H.-H. Park, A power-generation test for oxide-based thermoelectric modules using p-type $Ca_3Co_4O_9$ and n-type $Ca_{0.9}Nd_{0.1}MnO_3$ legs. *J. Electron. Mater.* **2012**, 41, 1247-1255.

[21] K. Park; G.W. Lee, Fabrication and thermoelectric power of π-shaped $Ca_3Co_4O_9$/CaMnO$_3$ modules for renewable energy conversion. *Energ. Syst.* **2013**, 60, 87-93.

[22] J.G. Naudem; S. Lemonnier; M. Prevel; E.S. Reddy; E. Guilmeau; C. Goupil, Thermoelectric ceramic for generators. *J. Eur. Ceram. Soc.* **2008**, 28, 41-48.

[23] M.N. Islam; W. Arakib; Y. Araib, Mechanical behavior of ferroelastic LaAlO$_3$. *J. Eur. Ceram. Soc.* **2017**, 37, 1665-1671.

[24] V. Øygarden; T. Grande, Crystal structure, electrical conductivity and thermal expansion of Ni and Nb co-doped LaCoO$_3$. *Dalton Trans.* **2013**, 42, 2704-2715.

[25] I. Wærnhus; P.E. Wullum; R. Holmestad; T. Grande; K. Wiik, Electronic properties of polycrystalline LaFeO$_3$. Part 1: Experimental results and the quantitative role of Schottky defects. *Solid State Ionics.* **2005**, 176, 2783-2790.

[26] M.-G. Kang; K.-H. Cho; J.-S. Kim; S. Nahm; S.-J. Yoon; C.-Y. Kang, Post-calcination, a novel method to synthesize cobalt oxide-based thermoelectric materials. *Acta Mater.* **2014**, 73, 251-258.

[27] M. Bittner; L. Helmich; F. Nietschke; B. Geppert; O. Oeckler; A. Feldhoff, Porous $Ca_3Co_4O_9$ with enhanced thermoelectric properties derived from sol–gel synthesis. *J. Eur. Ceram. Soc.* **2017**, 37, 3909 - 3915.

[28] S. Priya; D.J. Inman, *Energy harvesting technologies*. Springer, New York, 2009.

[29] J.G. Snyder, *Thermoelectrics handbook: macro to nano*. ed. D.M. Rowe, Boca Raton, CRC Taylor and Francis, p. 9, 2006.

[30] H. Taguchi; M. Nagao; T. Sato; M. Shimada, High-temperature phase transition of $CaMnO_3$. *J. Solid State Chem.* **1989**, 78, 312–315.

[31] S. Faaland, Heterogeneous ceramic interfaces in solid oxide fuel cells and dense oxygen permeable membranes. PhD thesis, *Norwegian University of Science and Technology NTNU*, Trondheim, Norway, 2000.

[32] N. Kanas; S.P. Singh; T.D. Desissa; T. Norby; K. Wiik; T. Grande; M.-A. Einarsrud, Thermoelectric properties of $Ca_3Co_{2-x}Mn_xO_6$, x = 0.05, 0.2, 0.5, 0.75 and 1. *To be submitted*.

[33] H.J. Goldsmid, Application of the transverse thermoelectric effects. *J. Electron. Mater.* **2011**, 40, 1254-125.

[34] S. Teichert; A. Bochmann; T. Reimann; T. Schulz; C. Dreßler; J. Töpfer, An oxide-based thermoelectric generator: Transversal thermoelectric strip-device. *AIP Adv.* **2015**, 5, 077105-1-6.

[35] T. Kanno; K. Takahashi; A. Sakai; H. Tamaki; H. Kusada; Y. Yamada, Detection of thermal radiation, sensing of heat flux and recovery of waste heat by the transverse thermoelectric effect. *J. Electron. Mater.* **2014**, 43, 2072-2079

[36] K. Takahashi; T. Kanno; A. Sakai; H. Tamaki; H. Kusada; Y. Yamada, Bifunctional thermoelectric tube made of tilted multi-layer material as an alternative to standard heat exchangers. *Nature Sci. Rep.* **2013**, 3, 1501-1-5.

[37] K. Takahashi; T. Kanno; A. Sakai; H. Adachi; Y. Yamada, Light-induced off-diagonal thermoelectric effect via indirect optical heating of incline-oriented Ca_xCoO_2 thin films. *Appl. Phys. Lett.* **2012**, 100, 181907-1-4.

[38] G. Yan; S. Wang; S. Chen; F. Liu; Z. Bai; J. Wang; W. Yu; G. Fu, The effect of microstructure on the on the laser-induced transverse voltage in Pb-doped $Bi_2Sr_2Co_2O_y$ thin films on tilted substrates. *Appl. Phys. A*. **2013**, 111, 1203-1206.

Insert Table of Contents artwork here
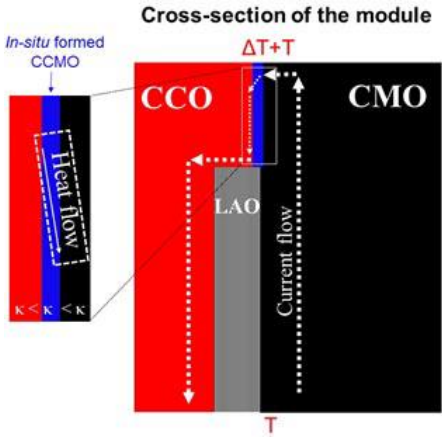
Cross-section of the module

All-oxide thermoelectric module with *in-situ* formed non-rectifying complex p-p-n junction and transverse thermoelectric effect

Nikola Kanas[1, 2], Michael Bittner[2], Temesgen Debelo Desissa[3], Sathya Prakash Singh[1], Truls Norby[3], Armin Feldhoff[2], Tor Grande[1], Kjell Wiik[1] and Mari-Ann Einarsrud[1#]

1 Department of Material Science and Engineering, NTNU Norwegian University of Science and

Technology, Trondheim, Norway

2 Institute of Physical Chemistry and Electrochemistry, Leibniz University, Hannover, Germany

3 Department of Chemistry, SMN, University of Oslo, Oslo, Norway

Slurry for the aqueous tape casting of the $LaAlO_3$ insulator was prepared by mixing dispersant (Darvan) with water and thereafter mixing this solution with the ceramic powder. After mixing for 6 h on a ball mill with zirconia balls, binder (43 g, 15 weight % solution of poly vinyl alcohol), plasticizer (1.5 g, poly ethylene glycol) and defoamer (0.7 g, poly propylene glycol) were added before further mixing for 24 h. Additional defoamer was added after 20 h of mixing.
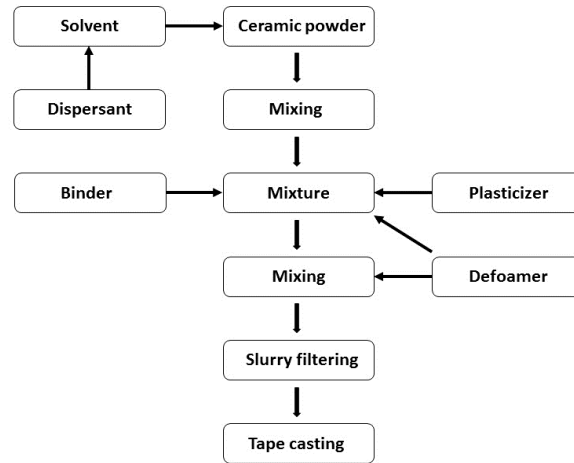
Fig. S1. Schematic illustration of tape casting of LaAlO$_3$ tapes.

The cross-sectional profile of the module is given in Fig. 3a. Based on the thickness of CCO and CMO composite, tensile stress developed in the CMO composite will vary. Developed stress can be calculated using equations for σ$_1$, σ$_2$ and σ$_3$, where α present coefficient of thermal expansion, E = Young's modulus, ν = Poison ratio, t = thickness of each layer at a constant temperature difference (ΔT) [33].

$$\sigma_1 = -\frac{\Delta T\left((\alpha_1 - \alpha_2)\frac{E_2 t_2}{(1-\nu_2)} + (\alpha_1 - \alpha_3)\frac{E_3 t_3}{(1-\nu_3)}\right)}{t_1 + \frac{(1-\nu_1)}{(1-\nu_2)}\frac{E_2 t_2}{E_1} + \frac{(1-\nu_1)}{(1-\nu_3)}\frac{E_3 t_3}{E_1}}$$

$$\sigma_2 = -\frac{\Delta T\left((\alpha_2 - \alpha_1)\frac{E_1 t_1}{(1-\nu_1)} + (\alpha_2 - \alpha_3)\frac{E_3 t_3}{(1-\nu_3)}\right)}{t_2 + \frac{(1-\nu_2)}{(1-\nu_1)}\frac{E_1 t_1}{E_2} + \frac{(1-\nu_2)}{(1-\nu_3)}\frac{E_3 t_3}{E_2}}$$

$$\sigma_3 = -\frac{\Delta T\left((\alpha_3 - \alpha_2)\frac{E_2 t_2}{(1-\nu_2)} + (\alpha_3 - \alpha_1)\frac{E_1 t_1}{(1-\nu_1)}\right)}{t_3 + \frac{(1-\nu_3)}{(1-\nu_1)}\frac{E_1 t_1}{E_3} + \frac{(1-\nu_3)}{(1-\nu_2)}\frac{E_2 t_2}{E_3}}$$

Fig. S2. Developed tensile stress (during cooling after SPS co-sintering) in CMO-composite as a function of CMO-composite and CCO thicknesses in the staking system.

3.5 A comprehensive study on improved power materials for high-temperature thermoelectric generators

Michael Bittner, Nikola Kanas, Richard Hinterding,

Frank Steinbach, Jan Räthel, Matthias Schrade,

Kjell Wiik, Mari-Ann Einarsrud, Armin Feldhoff

A comprehensive study on improved power materials for high-temperature thermoelectric generators[†]

Michael Bittner[1,*], Nikola Kanas[2], Richard Hinterding[1], Frank Steinbach[1], Jan Räthel[3], Matthias Schrade[4], Kjell Wiik[2], Mari-Ann Einarsrud[2], Armin Feldhoff[1]

[1]*Institute of Physical Chemistry and Electrochemistry, Leibniz University Hannover, DE-30167, Hannover, Germany, Fax: +49(511)762-4009; Tel: +49(511)762-3555; E-mail: michael.bittner@pci.uni-hannover.de*
[2]*Department of Materials Science and Engineering, NTNU Norwegian University of Science and Technology, N-7491 Trondheim, Norway*
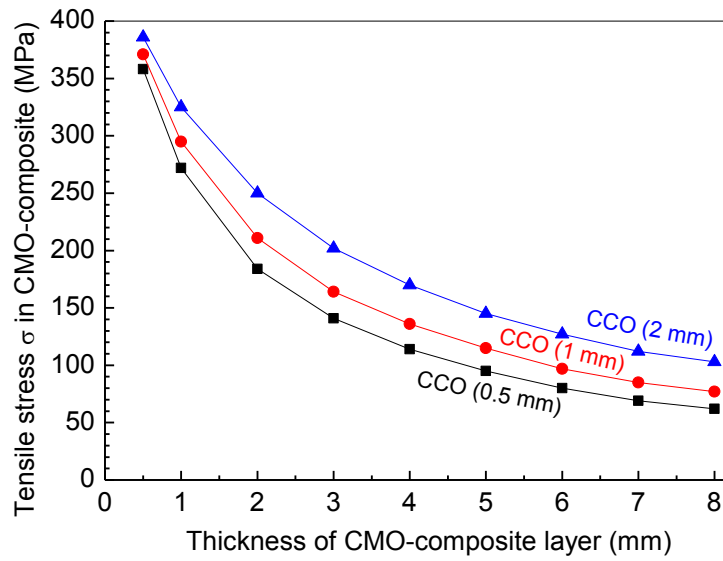[3]*Fraunhofer-Institute for Ceramic Technologies and Systems IKTS, DE-01109 Dresden, Germany*
[4]*Department of Physics, Centre for Materials Science and Nanotechnology, University of Oslo, N-0371 Oslo, Norway*

Abstract

Dense $Ca_3Co_4O_9$-Na_xCoO_2-$Bi_2Ca_2Co_2O_9$ (CCO-NCO-BCCO) nanocomposites were produced from sol-gel derived $Ca_{2.25}Na_{0.3}Bi_{0.35}Tb_{0.1}Co_4O_9$ powder by four methods: Hot-pressing (HP), spark plasma sintering (SPS) and pressureless sintering in air or O_2 atmosphere. Nanocomposites from HP and SPS revealed nanosized grains and showed a thermoelectric power factor of 4.8 and 6.6 μW $\cdot$ cm^{-1} $\cdot$ K^{-2}, respectively, at 1073 K in air. A dense 2D nanocomposite with structures on multiple length scales and enhanced thermoelectric properties was obtained from pressureless sintering in O_2 atmosphere. The resulting 2D nanocomposite enabled the simultaneous increase in isothermal electrical conductivity σ and Seebeck coefficient α, and showed a thermoelectric power factor of 8.2 μW $\cdot$ cm^{-1} $\cdot$ K^{-2} at 1073 K in air. The impact of materials with enhanced electrical conductivity and power factor on the electrical power output of thermoelectric generators was verified in prototypes. A high electrical power output and power density of 22.7 mW and 113.5 mW$\cdot$cm^{-2}, respectively, were obtained, when a hot-side temperature of 1073 K and a temperature difference of 251 K were applied. Different p- and n-type materials were used to verify the effect of the thermoelectric figure-of-merit zT and power factor on the performance of thermoelectric generators.

[†] Electronic Supplementary Information (ESI) available.

Keywords: Thermoelectricity; Power factor; Power generation; Thermoelectric generator; $Ca_3Co_4O_9$

1. Introduction

1.1. Energy conversion - limited or infinite heat source

Thermoelectric materials and their ability to directly convert heat into electrical energy can play a key role to solve challenges with respect to energy. Thermoelectric oxides are applicable at high temperatures and under oxidizing conditions, allowing recovery of waste heat from power plants and industrial processes [1]. Thermoelectricity relies on the coupling of currents of entropy I_S and electrical charge I_q in a material with each other, as shown in Equation 1 for steady-state conditions and the assumption of weak temperature dependence of both, the electrochemical potential of the electrons and the Seebeck coefficient α [2, 3].

$$\begin{pmatrix} I_q \\ I_S \end{pmatrix} = \frac{A}{L} \cdot \begin{pmatrix} \sigma & \sigma \cdot \alpha \\ \sigma \cdot \alpha & \sigma \cdot \alpha^2 + \Lambda \end{pmatrix} \cdot \begin{pmatrix} U \\ \Delta T \end{pmatrix} \quad (1)$$

Across the thermoelectric material of cross-sectional area A and length L, a temperature difference ΔT and an electrical voltage U exist. In Equation 1, the thermoelectric material appears as a tensor, which consists of the Seebeck coefficient α, isothermal electrical conductivity σ and the entropy conductivity at electrical open-circuit Λ. The entropy conductivity is related to the traditionally considered heat conductivity λ by the absolute temperature T, as given by Equation 2 [2, 3].

$$\lambda = T \cdot \Lambda \quad (2)$$

The maximum electrical power output $P_{el,max,mat}$ of p- and n-type materials is primarily determined by the power factor $\sigma \cdot \alpha^2$ (PF) and the temperature difference to the square $(\Delta T)^2$ according to Equation 3 [4].

$$P_{el,max,mat} = \frac{1}{4} \cdot \frac{A}{L} \cdot \sigma \alpha^2 \cdot (\Delta T)^2 \quad (3)$$

The maximum electrical power output $P_{el,max,TEG}$ of a combination of p- ($\alpha > 0$) and n-type ($\alpha < 0$) materials in a thermoelectric generator (TEG) [5], can be described as the sum of contributions of the p- and n-type legs or by the open-circuit voltage U_{OC} to the square and the generator resistance R_{TEG}, given in Equation 4 [4].

$$P_{el,max,TEG} = \frac{1}{4} \cdot \frac{A}{L} \cdot \frac{(\Sigma\,\alpha_{p-leg} - \Sigma\,\alpha_{n-leg})^2}{(\Sigma\,\frac{1}{\sigma_{p-leg}} + \Sigma\,\frac{1}{\sigma_{n-leg}})} \cdot (\Delta T)^2 \quad (4)$$
$$= \frac{U_{OC}^2}{4 \cdot R_{TEG}}$$

Narducci [6] postulated that, in case of infinite heat soruces, the electrical power output of a thermoelectric generator can be maximized by enhancing the power factor $\sigma \cdot \alpha^2$ of the materials and keeping a moderate heat conductivity λ, which is present for configuration A in Figure 1.
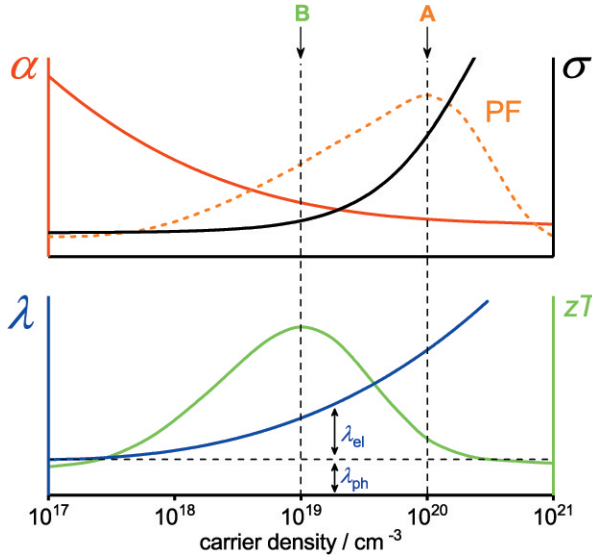

Figure 1: Thermoelectric parameters: Seebeck coefficient α, isothermal electrical conductivity σ, phononic and electrical part of the heat conductivity λ_{ph}, λ_{el}, power factor $\sigma \cdot \alpha^2$ (PF) and figure-of-merit zT as a function of the charge carrier density n. Modified from [7]. **A** and **B** indicate materials charge carrier concentrations, which should be used for high power generation (infinite heat sources), or high energy conversion efficiency (limited heat sources), respectively.

Thermoelectric materials should be designed in terms of their application areas, for example power generation from infinite or limited heat sources. To improve the electrical power output of thermoelectric materials and generators, according to Equations 3-5, it is important to enhance the electrical conductivity σ and the Seebeck coefficient α. If a limited heat source is present, thermoelectric generators made of high zT materials like

tellurides with configuration B in Figure 1, should be used.

$$zT = \frac{\sigma \cdot \alpha^2}{\Lambda} = \frac{\sigma \cdot \alpha^2}{\lambda} \cdot T \quad (5)$$

The figure-of-merit zT consists of the isothermal electrical conductivity σ, the Seebeck coefficient α and the open-circuited entropy conductivity Λ. A material, which shows a high charge carrier density n and subsequently high electrical conductivity and thermoelectric power factor, as shown in Figure 1 (A), is superior for maximum electrical power generation, compared to a material with high figure-of-merit zT (B). Accordingly, thermoelectric materials should be either optimized for maximum conversion efficiency (B in Figure 1) or maximum electrical power generation (A in Figure 1). Otherwise, working conditions for one or the other task will be suboptimal.

1.2. Concepts to improve the thermoelectric properties

The improvement of all three thermoelectric parameters σ, α and λ is the general challenge in thermoelectrics, since these quantities are interrelated to each other by the charge carrier concentration n, as shown in Figure 1. The band structures of the materials define the charge carrier concentration n and the charge carrier mobility μ, and changes in one of them also influence the other and thereby also σ and α [8, 9]. Nanostructuring has been used to decrease the heat conductivity λ, because a material with an all-scale hierarchical architecture (mesoscale, nanoscale and atomic scale) would scatter phonons on each length scale [8, 9, 10, 11]. Approaches like coherent structures with energy-matched electronic bands, carrier concentration engineering, compositionally alloyed nanostructures or band-structure engineering seem promising to increase the thermoelectric power factor by optimizing σ and α simultaneously [12, 13, 14, 15, 16, 17]. Possible processing techniques to obtain a nanostructured material are hot-pressing (HP) or spark plasma sintering (SPS) [18, 19, 20, 21]. These techniques provide dense materials, but reducing conditions might reduce the materials [16, 22, 23].

1.3. Oxides

The BiCuSeO oxyselenide shows competitive properties in the moderate-temperature range compared to alloys, Half-Heusler or Zintl phase materials. However, BiCuSeO is not stable at high temperatures and under oxidizing conditions [24, 25]. $Ca_3Co_4O_9$ (CCO) is a viable candidate for energy conversion at high temperatures and under oxidizing conditions from infinite heat

sources, in agreement with configuration A of Figure 1. Regarding the figure-of-merit zT, CCO can not compete with other materials, but it is non-toxic, mechanically, thermally (stable up to about 1173 K) and chemically stable in the high-temperature range in air [11, 26, 27, 28, 29]. CCO is a cobalt oxide and belongs to the monoclinic crystal class forming an incommensurate, misfit-layered structure [30, 31, 32]. CCO has a CdI_2-type CoO_2 subsystem 1 with triangular lattice and a layered rock-salt part of three Ca_2CoO_3 units in the subsystem 2, which are stacked alternatingly along the c-axis. The b-axis parameters of the two subsystems are diverse, forming an incommensurate structure [33]. The synthesis, processing and characterization of pure CCO and triple-phase $Ca_3Co_4O_9$-Na_xCoO_2-$Bi_2Ca_2Co_2O_9$ (CCO-NCO-BCCO) 2D nanocomposites, derived by the sol-gel technique, reveal several advantages, such as small grain size, homogeneity and stoichiometry [4, 32]. The CCO-NCO-BCCO nanocomposite shows improved thermoelectric properties of σ and α [4].

In this work, several processing techniques like HP, SPS and pressureless O_2-sintering were used to obtain dense triple-phase nanocomposite ceramics. Both, the thermoelectric power factor and subsequently power generation from O_2-sintering in comparison to air-sintered materials were improved [34, 23, 29, 35, 36]. The influence of these different processing techniques on the thermoelectric properties were compared. These dense nanocomposite ceramics were combined with recently developed, co-doped n-type indium oxides [37, 38, 39] in thermoelectric generators. The impact of materials with a high electrical conductivity and thermoelectric power factor on the electrical power output at high temperatures in air from infinite heat sources, as postulated by Narducci [6], was verified. The application of developed high power materials in thermoelectric generators improved the power generation performance significantly.

2. Materials and Methods

2.1. Synthesis

The p-type Na, Bi, Tb co-doped CCO and n-type In_2O_3-based powders were synthesized via a sol-gel route, as described elsewhere [4, 32, 40]. Indium(III) nitrate 99.999 %, tin(II) acetate 95 %, aluminium(III) nitrate 99.0-102 %, germanium(IV) ethoxide 99.995 %, manganese(II) nitrat 99.98 % and zinc nitrate 99.998 % were used as precursors. The stoichiometry, applied sintering techniques and abbreviations of synthesized samples are shown in Table 1.

Table 1: Stoichiometry, applied sintering techniques, pressureless sintering (p.l.) in air and O_2, hot-pressing (HP), spark plasma sintering (SPS) and abbreviations of synthesized nanocomposites (**CCO-30-35-10-air**, **CCO-30-35-10-SPS**, **CCO-30-35-10-HP**, **CCO-30-35-10-O₂**), reference (**CCO-air**) and co-doped indium oxide (**Sn,Al:In₂O₃**, **Ge,Mn,Zn:In₂O₃**) samples.

stoichiometry	sintering	abbreviation
$Ca_3Co_4O_9$	p.l. air	**CCO-air**
$Ca_{2.25}Na_{0.3}Bi_{0.35}Tb_{0.1}Co_4O_9$	p.l. air	**CCO-30-35-10-air**
$Ca_{2.25}Na_{0.3}Bi_{0.35}Tb_{0.1}Co_4O_9$	HP	**CCO-30-35-10-HP**
$Ca_{2.25}Na_{0.3}Bi_{0.35}Tb_{0.1}Co_4O_9$	SPS	**CCO-30-35-10-SPS**
$Ca_{2.25}Na_{0.3}Bi_{0.35}Tb_{0.1}Co_4O_9$	p.l. O_2	**CCO-30-35-10-O₂**
$In_{1.9}Sn_{0.05}Al_{0.05}O_3$	p.l. air	**Sn,Al:In₂O₃**
$In_{1.95}Ge_{0.01}Mn_{0.01}Zn_{0.03}O_3$	p.l. air	**Ge,Mn,Zn:In₂O₃**

2.2. p-type ceramics

The calcined p-type CCO-30-35-10 powder (10 h, 1023 K) was precompressed at 200 MPa for 60 s, subsequently ground and sieved with a 100 μm sieve before hot-pressing. The compacted powder was hot-pressed in vacuum in a graphite die between two Al_2O_3 plates at 1148 K for 1 h, using a pressure of 50 MPa (applied from 1023 to 1148 K) with applied heating and cooling rates of 5 K $\cdot$ min^{-1}. The CCO-30-35-10 powder was processed by spark plasma sintering at 1023 K for 4 min with an applied pressure of 75 MPa. Spark plasma sintering was done using a graphite die (20 mm) in vacuum (Dr Sinter 825). The CCO-30-35-10 powder was pressed into a green body at 200 MPa using a 16 mm die and subsequently sintered in air (conventional furnace, as described in [4]) or O_2 (6.0 purity from Linde) atmosphere in a tube furnace (STF 15/180 220-240V 1PH from Carbolite Gero) for 20 h at 1248 K with a flow rate of 40 mL $\cdot$ min^{-1} with heating and cooling rates of 3 K $\cdot$ min^{-1}.

2.3. n-type ceramics

The n-type, co-doped Sn,Al:In_2O_3 and Ge,Mn,Zn:In_2O_3 powders were pressed into a green body at 200 MPa using a 16 mm die, followed by conventional pressureless sintering at 1873 K and 1573 K for 15 h in air, respectively. The green body was placed on a twisted platinum wire (Sn,Al:In_2O_3) [37, 39] and Sn-solder (Ge,Mn,Zn:In_2O_3).

2.4. Analysis of composition and properties

Phase compositions of sintered and annealed ceramics were characterized by X-ray diffraction (XRD) using a Bruker D8 Advance with Cu-K$_\alpha$ radiation. Microstructural characterization and elemental analysis of ceramic samples were done by a field-emission scanning electron microscope (FE-SEM) of the type

3

JEOL JSM-6700F, which was equipped with an energy-dispersive X-ray spectrometer (energy-dispersive X-ray spectroscopy, EDXS) of the type Oxford Instruments INCA 300 and a backscattered electron detector. Nanostructures were investigated by transmission electron microscopy (TEM) and high-resolution TEM (HRTEM) using a JEOL JEM-2100F-UHR, which was equipped with an EDXS of the type Oxford Instruments INCA 300 for elemental analysis. Elemental distribution information of analyzed materials were obtained from $Na-K_\alpha$, $Ca-K_\alpha$, $Bi-L_\alpha$, $Co-K_\alpha$, $Tb-L_\alpha$ and $O-K_\alpha$ transitions.

Density and porosity were measured by Archimedes method (ISO 5018:1983) using isopropanol. The density and porosity were averaged over 3 measurements with less than 5 % deviation. Thermogravimetric measurements were done in O_2 and subsequently in synthetic air atmosphere with a gas flow of 30 mL · min^{-1} and a heating rate of 5 K · min^{-1}, within the range of 313 K to 1248 K for O_2 and 313 K to 1173 K for air, using a Netzsch STA 409 PC/PG. Ceramic samples were prepared for Hall effect measurements by painting four Au electrodes on the surfaces using a Metalor M-0034 ink, followed by an annealing step at 1123 K in air to ensure ohmic contacts. The electric properties were measured on a single sample from different treatments (HP, SPS, air, O_2). The charge carrier mobility μ and charge carrier concentration n were evaluated as described in [41].

The thermoelectric properties, such as isothermal electrical conductivity σ and Seebeck coefficient α of the ceramic samples were carried out as a function of temperature (heated to 1073 K and measured down with equilibrium at every temperature). Samples were cut into bar shape from discs (10 mm · 1.0 mm · 1.0 mm and 10 mm · 2.5 mm · 1.5 mm). The isothermal electrical conductivity σ was measured by a pseudo 4-point measurement, utilizing a horizontal tube furnace from Carbolite Gero EVZ 12/450B with three heating zones and a home-made measurement cell. The Seebeck coefficient α was estimated with a ProboStat A setup from NorECs, using an ELITE thermal system. The values were logged by KEITHLEY 2100 $6\frac{1}{2}$ Digit Multimeters. Electrical measurements (p-type) of σ and α were repeated with less than 5 % deviation. Calculated uncertainties of 0.1 for σ, 10 % for α and 20 % for the power factor, were averaged from 5 values at the maximum examined temperature of 1073 K. Lower temperatures led to significantly diminishing uncertainties. Calculated uncertainties of σ, α, power factor and zT of n-type materials were as follows: 0.1, 2.6, 5.1, 5.1 % for $Sn,Al:In_2O_3$ and 0.1, 5.1, 10, 10 % for

$Ge,Mn,Zn:In_2O_3$, averaged from 5 values at 1073 K.

2.5. Assembling of thermoelectric generators

Thermoelectric generators were assembled using 10 couples of p and n-type legs (3 mm x 1 mm x 1 mm) in a conventional generator design, shown in Figure S 10†. An Au-paste from Heraeus was used as a metallic connector. To obtain ohmic contacts, the generators CCO-30-35-10-air/$Sn,Al:In_2O_3$ and CCO-30-35-10-air/$Ge,Mn,Zn:In_2O_3$ were annealed twice at 1073 K for 4 h, whereas the generators CCO-30-35-10-SPS/$Sn,Al:In_2O_3$ and CCO-30-35-10-O_2/$Sn,Al:In_2O_3$ twice at 1023 K for 4 h in air. The thermoelectric generators were characterized using a load resistance dependent measurement under steady-state conditions at different hot-side temperatures [40].

3. Results and Discussion

3.1. Influence of sintering on p-type materials

The triple-phase CCO-NCO-BCCO nanocomposite ceramics were obtained by processing a co-doped CCO powder [4], via HP (CCO-30-35-10-HP), SPS (CCO-30-35-10-SPS) and pressureless sintering in air and (CCO-30-35-10-air) O_2-atmosphere (CCO-30-35-10-O_2). The microstructure of the materials prepared by HP and SPS are shown in Figure 2a-d.
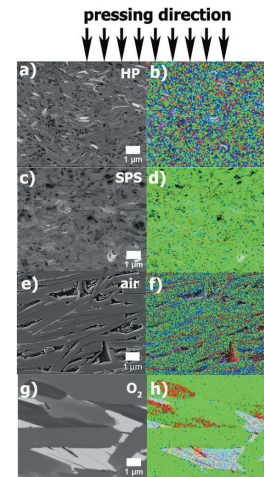
Figure 2: SEM micrographs of backscattered electrons and EDXS elemental distributions of cross sections: a, b) **CCO-30-35-10-HP**, c, d) **CCO-30-35-10-SPS**, e, f) **CCO-30-35-10-air** (taken from [4]), g, h) **CCO-30-35-10-O_2**. The direction of pressing is indicated by black arrows. Phase compositions are shown in Figures S 1, 2†. SEM micrographs and elemental distributions of O_2-sintered nanocomposites are shown in Figure S 3†. CCO phase is dominated by Ca (green), NCO phase by Na (red) and BCCO phase by Bi (blue).

Table 2: Density and porosity of CCO and nanocomposite ceramics, processed with different techniques: pressureless sintering in air (10 h: 1173 K **CCO-air**, 20 h: 1173 K **CCO-30-35-10-air**), O_2-sintering (20 h: 1248 K **CCO-30-35-10-O_2**),HP (50 MPa, 1 h: 1148 K **CCO-30-35-10-HP**), SPS (50 MPa, 4 min: 1048 K **CCO-30-35-10-SPS**), and of n-type **Sn,Al:In$_2$O$_3$, Ge,Mn,Zn:In$_2$O$_3$** (15 h: 1873 K and 15 h: 1573 K) using ISO 5018:1983 (the International Organization for Standardization). Values for CCO-air and CCO-30-35-10-air taken from [32, 4]. Additional values of O_2-sintered nanocomposites are shown in Table S 1[†]. True density of composite ceramics is unknown.

type	material abbreviation	bulk density / g $\cdot cm^{-3}$	true density / g $\cdot cm^{-3}$	open porosity / %	true porosity / %	closed porosity / %	theoretical density / %
p	**CCO-air**	3.2 ± 0.1	4.68	33.3 ± 0.4	33.5 ± 1.1	0.2 ± 0.7	67.7 ± 1.5
p	**CCO-30-35-10-air**	3.9 ± 0.0		19.2 ± 0.7			
p	**CCO-30-35-10-HP**	4.9 ± 0.0		0.8 ± 0.2			
p	**CCO-30-35-10-SPS**	4.9 ± 0.0		0.8 ± 0.4			
p	**CCO-30-35-10-O_2**	4.9 ± 0.0		3.6 ± 2.6			
n	**Sn,Al:In$_2$O$_3$**	6.6 ± 0.0	7.116	3.2 ± 2.8	7.8 ± 0.6	4.6 ± 2.2	92.2 ± 0.6
n	**Ge,Mn,Zn:In$_2$O$_3$**	5.5 ± 0.2	7.116	19.4 ± 7.8	22.3 ± 2.9	2.9 ± 6.5	77.7 ± 2.9

Nanocomposites from SPS and HP showed a very narrow grain size distribution, in the range of 500 nm to 900 nm of all three phases CCO, NCO and BCCO (Figure 2a-d). The materials prepared by pressureless sintering in air [4] and O_2 atmosphere showed an multiscale structure (Figure 2e-h) of μm-sized grains of all three phases. The phase composition of powders and ceramics processed via HP, SPS, and pressureless sintering in air, O_2 atmosphere are shown in Figure S 1[†]. The CCO-30-35-10-HP and CCO-30-35-10-SPS materials show less pronounced texture compared to the CCO-30-35-10-O_2 material. Both, texture and composition can be controlled by the applied temperature during O_2-sintering, as displayed in Figure S 2[†]. The phase composition, revealed in Figure 2, and porosity of triple-phase ceramics, given in Table 2, differ due to composite formation during sintering.

Table 3: Lattice parameters (Å) of the CCO and BCCO phases of the HRTEM sites of **CCO-30-35-10-O_2** and **CCO-30-35-10-SPS** nanocomposites, shown in Figure 3. Values were measured from reduced fast Fourier transformations (rFFT). Semi-coherent lattice parameters are highlighted.

	HRTEM sites	
	CCO-30-35-10-O_2	CCO-30-35-10-SPS
CCO	**a=5.35, b$_1$=2.47**, b$_2$=3.93	c=10.98 (c=10.95)
BCCO	**a=4.96, b$_1$=2.48**, c=13.27	c=16.39

The density of CCO-30-35-10-HP, CCO-30-35-10-SPS and CCO-30-35-10-O_2 are comparable, but their micro- and nanostructure are different, shown in Figures 2a-h and 3a-f. CCO-30-35-10-HP and CCO-30-35-10-SPS show no μm-sized grains (Figures 2a-d and 3d-f), according to the fast processing techniques. The CCO-30-35-10-O_2 ceramic forms an aligned multiscale structure of μm-sized grains (Figure 2g,h) and nanostructures (Figure 3a-c). Table 3 shows the lattice parameters of CCO and BCCO, calculated from reduced fast Fourier transformations of Figure 3c,f. The processing

via O_2-sintering facilitates a dense ceramic with highly aligned and semi-coherent CCO, NCO and BCCO 2D nanostructures. Detailed information on elemental distribution mappings of the HRTEM micrographs are shown in Figures S 5-8[†].
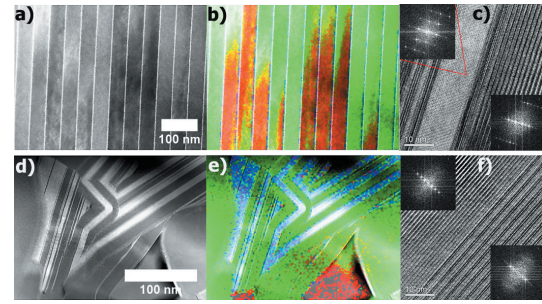
Figure 3: TEM analysis of **CCO-30-35-10-O_2** in a-c) and of **CCO-30-35-10-SPS** in d-f): a, d) STEM dark-field micrograph. b, e) EDXS elemental distribution of the shown scopes, more detailed elemental distribution information is given in S 4, 6[†]. c, f) HRTEM micrographs, more detailed information is given in S 5, 7[†]. Insets show the reduced fast Fourier transformation (rFFT). CCO phase is dominated by Ca (green), NCO phase by Na (red) and BCCO phase by Bi (blue).

3.2. Composition and microstructure of n-type materials

The phase composition, shown in Figure S 1h,i[†], and microstructure, represented in Figure S 4a-d[†], of manufactured n-type materials Sn,Al:In$_2$O$_3$ and Ge,Mn,Zn:In$_2$O$_3$ reveal homogeneously doped indium phases. The n-type Sn,Al:In$_2$O$_3$ is dense, as shown in Table 2. The Ge,Mn,Zn:In$_2$O$_3$ n-type has a certain porosity, given in Table 2. This porosity was generated while sintering on Sn-solder, which evaporated at high temperatures, causing porosity within the ceramic body.

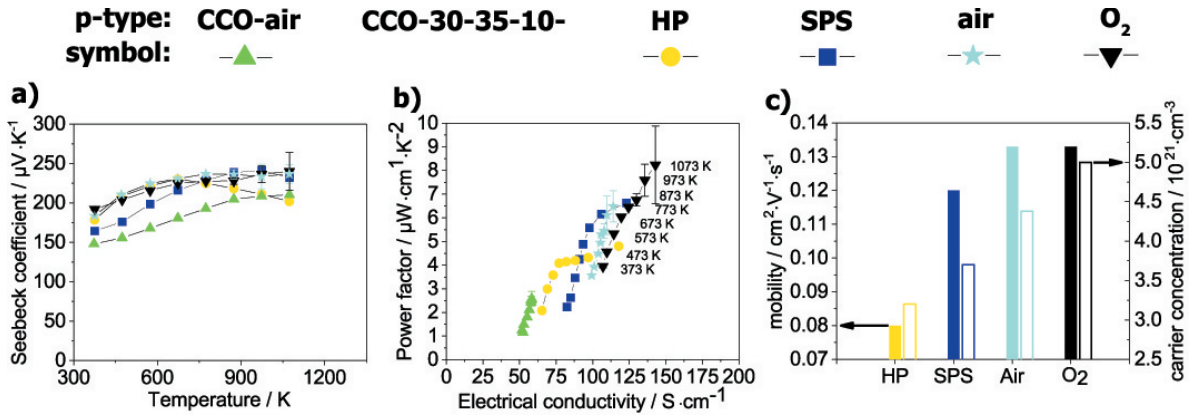Figure 4: Thermoelectric properties of **CCO-air** (rectangle, green, taken from [32]), **CCO-30-35-10-air** (stars, turquoise, taken from [4]), **CCO-30-35-10-HP** (circle, yellow), **CCO-30-35-10-SPS** (square, dark blue) and **CCO-30-35-10-O₂** (reverse rectangle, black) as a function of temperature: a) Seebeck coefficient α, b) Ioffe plot: power factor $\sigma \cdot \alpha^2$ as a function of the isothermal electrical conductivity σ. c) Hall effect measurements: charge carrier mobility μ (closed bars) and charge carrier concentration n (open bars) at room temperature. Uncertainties are indicated with error bars. Note, all samples were cut and measured perpendicular to the pressing direction.

3.3. Thermoelectric properties

3.3.1. p-type ceramics

The thermoelectric transport properties of p-type materials are presented in Figure 4. The Seebeck coefficient α of CCO-30-35-10-air and CCO-30-35-10-O₂ nanocomposites, shown in Figure 4a, reaches 236 and 240 μV $\cdot$ K^{-1} at 1073 K. The α values of CCO-30-35-10-SPS and CCO-30-35-10-HP nanocomposites, represented in Figure 4a, differ in trend and absolute values. Reference values of samples, which were O₂-sintered at different temperatures, are given in Figure S 9a[†].

3.3.2. n-type ceramics

The Seebeck coefficient α of the n-type materials Sn,Al:In₂O₃ and Ge,Mn,Zn:In₂O₃ is revealed in Figure 5a. It differs in absolute values and reaches 82 and 174 μV $\cdot$ K^{-1} at 1073 K, respectively. The Seebeck coefficient α of the Ge,Mn,Zn:In₂O₃ material could be increased by Mn and Zn co-doping. This influence was previously reported for single element doping by Kosir et al., Kumar et al. and Ohtaki et al. [42, 43, 44].

3.3.3. Ioffe plot

Figures 4b and 5b show the thermoelectric power factor $\sigma \cdot \alpha^2$ of p- and n-type materials in Ioffe plots as a function of the electrical conductivity σ [45]. The Ioffe plot can be used to estimate the applicability of thermoelectric materials for power generation. The p-type materials CCO-30-35-10-air and CCO-30-35-10-O₂ have the best combination of a high electrical conductivity σ of 116, 143 S $\cdot$ cm^{-1} and a high thermoelectric power

factor $\sigma \cdot \alpha^2$ of 6.5, 8.2 μW $\cdot$ cm^{-1} $\cdot$ K^{-2} at 1073 K in air. The best properties of a fast processed material, shown in Figure 4b, are obtained from the CCO-30-35-10-SPS sample of 123 S $\cdot$ cm^{-1} and 6.6 μW $\cdot$ cm^{-1} $\cdot$ K^{-2} at 1073 K in air. Hall effect measurements of CCO-30-35-10-HP, CCO-30-35-10-SPS, CCO-30-35-10-air and CCO-30-35-10-O₂, shown in Figure 4c, reveal simultaneously enhanced carrier mobility μ of 0.133 cm^{-2} $\cdot$ V^{-1} $\cdot$ s^{-1} and carrier concentrations n of 5 and 4.38 10^{21} $\cdot$ cm^{-3} for the CCO-30-35-10-air, CCO-30-35-10-O₂ materials. These measurements could explain the simultaneous increase of the electrical conductivity σ and the Seebeck coefficient α in CCO-NCO-BCCO nanocomposites. Thermoelectric power factors of O₂-sintered reference samples are given in Figure S 9b[†]. The behavior of the n-type materials is different, which is shown in the Ioffe plot of Figure 5b [37, 46]. Ge,Mn,Zn:In₂O₃ and Sn,Al:In₂O₃ show an electrical conductivity of 98, 867 S $\cdot$ cm^{-1} and a thermoelectric power factor of 2.9 and 5.9 μW $\cdot$ cm^{-1} $\cdot$ K^{-2} at 1073 K in air, respectively. Sn,Al:In₂O₃ shows a high thermoelectric power factor and similar behavior to p-type materials, shown in Figures 5b and 4b [37, 46], while Ge,Mn,Zn:In₂O₃ reveals a lower thermoelectric power factor and intrinsic semiconducting behavior.

3.3.4. Figure-of-merit zT of n-type materials

The heat conductivity λ, represented in Figure 5c, of 2.9 W $\cdot$ m^{-1} $\cdot$ K^{-1} for Ge,Mn,Zn:In₂O₃ is significantly reduced compared to the highly electrically conductive Sn,Al:In₂O₃ of 11.3 W $\cdot$ m^{-1} $\cdot$ K^{-1} at 1073 K. The zT value of 0.1 in comparison to 0.056 at 1073 K, shown
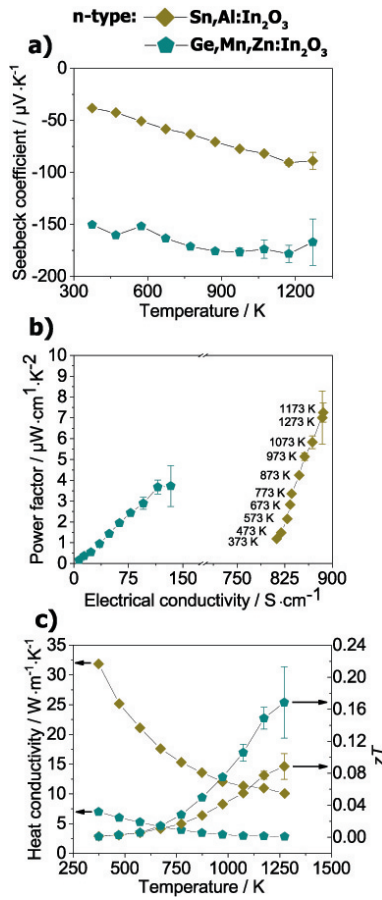
Figure 5: Thermoelectric properties of **Sn,Al:In$_2$O$_3$** (diamond, dark yellow) and **Ge,Mn,Zn:In$_2$O$_3$**) (pentagon, dark green) as a function of temperature: a) Seebeck coefficient α, b) Ioffe-plot: power factor $\sigma \cdot \alpha^2$ as a function of the isothermal electrical conductivity σ and c) heat conductivity λ and figure-of-merit zT. Uncertainties are indicated with error bars.

in Figure 5c, of the Ge,Mn,Zn:In$_2$O$_3$ and Sn,Al:In$_2$O$_3$, respectively, is subsequently enhanced. However, the course of the thermoelectric power factor, shown in Figure 5b, of Sn,Al:In$_2$O$_3$ as a function of the electrical conductivity in the Ioffe plot is more similar to the p-type materials. The behavior, as displayed in Figure 5b, of the Ge,Mn,Zn:In$_2$O$_3$ material differs to Sn,Al:In$_2$O$_3$ substantially. For this reason, the influence on the performance of thermoelectric generators was estimated for both n-type materials.

3.4. Cycle and high-temperature stability

The material CCO-30-35-10-O$_2$, having the highest electrical conductivity and thermoelectric power factor,

was sintered under oxidizing conditions. For this reason, the stability was investigated by cycle testing, thermogravimetry and XRD, shown in Figure 6, to evaluate their applicability in a thermoelectric generator in air. Figure 6a shows a good cycle stability of the material from 373 to 1073 K in air. However, Figure 6b,c shows that a thermal treatment for 20 h at 1173 K in air leads to a change of the phase composition of the CCO-30-35-10-O$_2$ material. The mass change of a CCO-30-35-10-O$_2$ sample is shown in Figure 6b. The sample was annealed in O$_2$ up to 1248 K and subsequently cooled down to room temperature and annealed again in air up to 1173 K, showing a small mass change of 0.8 %. This can be explained either by a change of the phase composition or by differences in the oxygen content [49, 50]. The initial high mass change of 13 % of the calcined CCO-30-35-10 powder (10 h, 1023 K) in Figure 6b (solid green line), is attributed to reactions during sintering. Possible reactions are decompositions of residual precursors or a change in the oxygen content. In addition, the phase compositions of the CCO-30-35-10-O$_2$ material before and after exposure at 1173 K in air, were analyzed with XRD. The change of phase composition of the CCO-30-35-10-O$_2$ material is indicated by vertical red lines, as shown in Figure 6c, indicating an increased NCO phase content. Changes in texture of the CCO-30-35-10-O$_2$ material are highlighted by green stars, as displayed in Figure 6c. As a result of a changed phase composition, the Seebeck coefficient is decreased while the electrical conductivity increased. The thermoelectric power factor of the CCO-30-35-10-O$_2$ material at 1073 K, after exposure for 20 h at 1173 K in air, was decreased by a factor of about 1.75 and is revealed in the Ioffe plot of Figure 6a.

3.5. Thermoelectric generators - power characteristics

The p-type CCO-30-35-10-air, CCO-30-35-10-O$_2$ and the n-type materials Sn,Al:In$_2$O$_3$ and Ge,Mn,Zn:In$_2$O$_3$ were used to build three prototypes of thermoelectric generators. The results from CCO-30-35-10-air/Sn,Al:In$_2$O$_3$ and CCO-30-35-10-air/Ge,Mn,Zn:In$_2$O$_3$ generators showed increased electrical power outputs when the high power Sn,Al:In$_2$O$_3$ material was used. For this reason, the p-type material CCO-30-35-10-O$_2$ was combined with the n-type material Sn,Al:In$_2$O$_3$ to further improve power generation in thermoelectric generators. The impact of high thermoelectric power factor and zT materials on the electrical power output from infinite heat sources was estimated. A conventional design, shown in Figure S 10[†], for thermoelectric generators of 10 p/n couples was used [51, 52, 53, 54]. Figure 7a-c
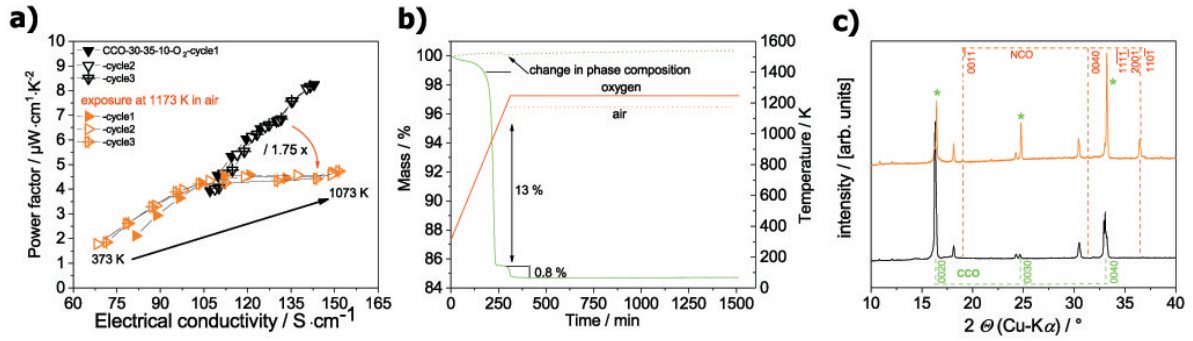
Figure 6: a) Cycle stability testing in air of the power factor $\sigma \cdot \alpha^2$ as a function of the isothermal electrical conductivity σ of **CCO-30-35-10-O$_2$**. Closed, open and crossed symbols represent different cycles (closed - first, open - second, crossed - third cycle) before (black, reverse rectangle) and after (orange, rotated rectangle) annealing for 20 h at 1173 K in air. b) Thermogravimetry measurements of a CCO-30-35-10 powder sample, 20 h in O$_2$ (solid lines), followed by 20 h in air (dotted lines). c) X-ray diffraction patterns of CCO-30-35-10-O$_2$ before and after annealing for 20 h at 1173 K in air. Reflections of CCO (green stars) [47] and NCO (red vertical lines) [48] indicate changes in relative intensity and phase composition, respectively.

shows the U-I_q and P-I_q curves of the three generators at different hot-side temperatures T_{hot}. Measured parameters of the TEGs are listed in Table 4.

3.5.1. Influence of high power materials

The highest electrical power output and electrical power density, shown in Figure 7c and Table 4, of 22.7 mW and 113.5 mW·cm^{-2}, respectively, were obtained from CCO-30-35-10-O$_2$/Sn,Al:In$_2$O$_3$ TEG, when a hot-side temperature of 1073 K and a temperature difference of 251 K was applied. Due to the change of phase composition at higher temperature, shown in Figure 6b,c, and a subsequently reduced thermoelectric power factor, shown Figure 6a, the generator CCO-30-35-10-O$_2$/Sn,Al:In$_2$O$_3$ was only measured until 1073 K hot-side temperature. The generators CCO-30-35-10-air/Sn,Al:In$_2$O$_3$ and CCO-30-35-10-air/Ge,Mn,Zn:In$_2$O$_3$ were measured up to 1173 K hot-side temperature and delivered a maximum electrical power output and electrical power density of 25 mW, 125 mW·cm^{-2} and 22.8 mW, 114.5 mW·cm^{-2}, from 250 and 280 K temperature difference, given in Table 4, respectively. The enhancement of the power generation performance of the CCO-30-35-10-O$_2$/Sn,Al:In$_2$O$_3$ TEG, shown in Figure 7c, in comparison to the CCO-30-35-10-air/Sn,Al:In$_2$O$_3$ TEG, shown in Figure 7a, can be attributed to the improved electrical conductivity and slightly enhanced Seebeck coefficient of the O$_2$-sintered nanocomposite in Figure 4a,b. This improvement can be directly connected to the course of the p- and n-type materials in the Ioffe plots of Figures 4b and 5b. The influence of the improved nanocomposite from O$_2$-sintering is also proven by the reduced resistances and open-

circuit voltages of the CCO-30-35-10-O$_2$/Sn,Al:In$_2$O$_3$ TEG, shown in Table 4. Furthermore, the performance of the CCO-30-35-10-air/Ge,Mn,Zn:In$_2$O$_3$ TEG can be directly derived from its values in the Ioffe plot of Figure 5b. As shown in Table 4, the TEG resistances are rapidly decreasing with temperature and accordingly the slope of the U-I_q curve is reduced. This course can be referred to the intrinsic semiconducting behavior of the Ge,Mn,Zn:In$_2$O$_3$, illustrated in the Ioffe plot of Figure 5b. The zT value of the Ge,Mn,Zn:In$_2$O$_3$ is doubled, as shown in Figure 5c, compared to the Sn,Al:In$_2$O$_3$ material. However, the TEG, shown in Figure 7b, shows inferior power generation performance. Hence, combinations of CCO-30-35-10-air and CCO-30-35-10-O$_2$ with the high power Sn,Al:In$_2$O$_3$ material have much higher values of electrical power output and electrical power density and seem to be more appropriate for thermoelectric energy conversion at high temperatures in air from infinite heat sources.

3.6. Comparison and evaluation

In this work, the values of the electrical power density of 97 and 113.5 (1073 K hot-side) are higher than previously reported results of 2.1 (1100 K hot-side), 85 (1273 K hot-side) and 45.3 mW·cm^{-2} (906 K hot-side) [54, 55, 56], which applied even higher temperature differences. This improvement is attributed to the enhanced electrical conductivity and thermoelectric power factor of CCO-NCO-BCCO nanocomposites, which were sintered in air and O$_2$-atmosphere, revealed in the Ioffe plot of Figure 4b. Thereby, the combination of high power materials delivered the highest values of electrical power output and electrical power density.
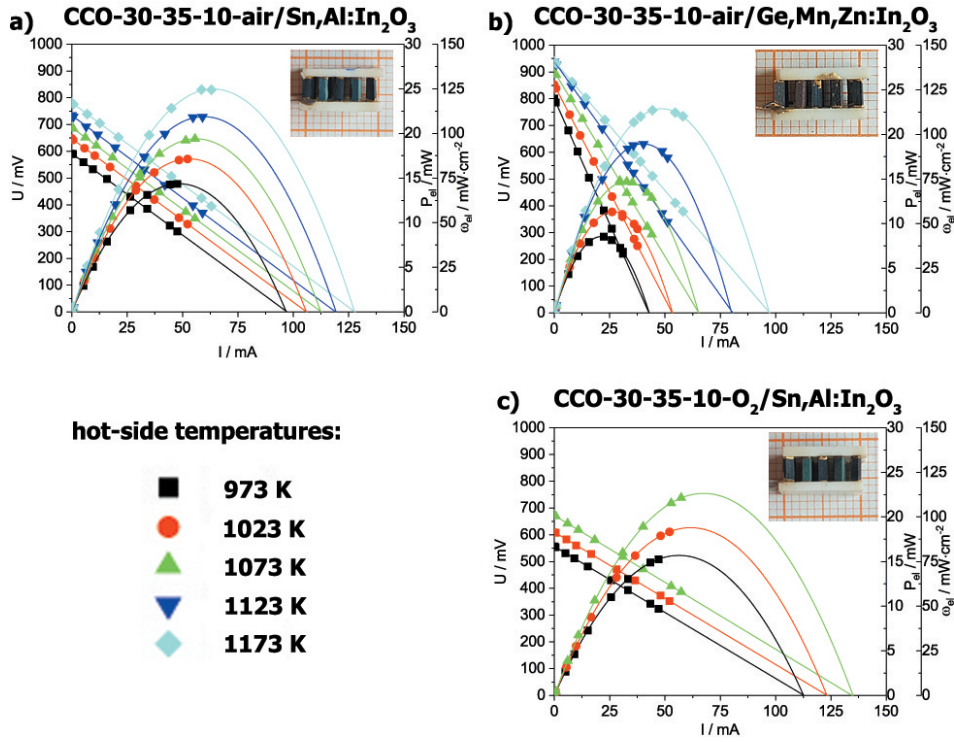
Figure 7: Characteristics of TEGs as a function of the electrical current I_q. Electrical voltage U (linear curves) and electrical power output P_{el} (parabolic curves) at different hot-side temperatures T_{hot} and as a function of the electrical current I_q of: a) **CCO-30-35-10-air/Sn,Al:In$_2$O$_3$**, b) **CCO-30-35-10-air/Ge,Mn,Zn:In$_2$O$_3$**, c) **CCO-30-35-10-O$_2$/Sn,Al:In$_2$O$_3$**. Electrical power densities ω_{el} were calculated from the active area of 10 p/n couples. Generator in c was measured until 1073 K due to limited thermal stability, shown in Figure 6.

Table 4: Measured parameters of the three thermoelectric generators (10 p/n couples) **CCO-30-35-10-air/Sn,Al:In$_2$O$_3$**, **CCO-30-35-10-air/Ge,Mn,Zn:In$_2$O$_3$** and **CCO-30-35-10-O$_2$/Sn,Al:In$_2$O$_3$**: hot-side temperature T_{hot}, temperature difference ΔT, TEG resistance R_{TEG}, open-circuit voltage U_{OC}, electrical short-circuit current $I_{q,SC}$, voltage at maximum power output U ($P_{el,TEG,max}$), electrical current at maximum power output I_q ($P_{el,TEG,max}$), maximum electrical power output $P_{el,TEG,max}$, electrical power density ω_{el} and temperature difference dependent electrical power density $\omega_{el}/(\Delta T)^2$, both calculated from the active area of 0.2 cm^{2†}.

generator p/n	T_{hot} /K	ΔT /K	R_{TEG} /Ω	U_{OC} /mV	$I_{q,SC}$ /mA	U ($P_{el,max}$) /mV	I_q ($P_{el,max}$) /mA	$P_{el,max}$ /mW	ω_{el} /mW·cm^{-2}	$\omega_{el}/(\Delta T)^2$ /μW·cm^{-2}·K^{-2}
	1173	250	6.13	782	127.5	387.7	54.2	25.0	125.0	2.00
	1123	255	6.17	735	119.0	364.0	60.0	21.8	109.0	1.68
p-CCO-30-35-10-air/	1073	254	6.12	688	112.5	341.6	57.1	19.4	97.0	1.50
n-Sn,Al:In$_2$O$_3$	1023	249	6.14	648	105.6	317.4	53.8	17.1	85.5	1.38
	973	243	6.12	591	96.5	280.5	51.0	14.4	72.0	1.22
	1173	280	9.69	940	97.0	468.2	48.8	22.9	114.5	1.46
	1123	278	11.7	938	80.2	467.1	40.6	18.9	94.5	1.22
p-CCO-30-35-10-air/	1073	277	13.8	902	65.3	450.6	32.9	14.7	73.5	0.96
n-Ge,Mn,Zn:In$_2$O$_3$	1023	271	16.03	853	53.2	420.9	27.2	11.4	57.0	0.78
	973	269	18.76	801	42.7	397.4	21.5	8.6	43.0	0.59
	1073	258	4.97	672	135.2	331.9	68.1	22.7	113.5	1.70
p-CCO-30-35-10-O$_2$/	1023	257	4.94	610	123.4	304.0	61.8	18.8	94.0	1.42
n-Sn,Al:In$_2$O$_3$	973	252	4.94	557	112.7	277.1	56.8	15.7	78.5	1.19

The main area of application of thermoelectric oxides is energy conversion at high temperatures in air from infinite heat sources. For this application scenario, a maximized thermoelectric power factor of p- and n-type materials is much more important than tuning the zT value [6]. A comparison with other generators published in literature is difficult because of different applied hot-side temperatures, temperature differences ΔT and di-

9

mensions of p- and n-type legs. However, the calculated electrical power density ω_{el} of different generators can be compared. If the electrical power density is further standardized by dividing it with the applied temperature difference to the square $(\Delta T)^2$, a generator specific value of $\omega_{el}/(\Delta T)^2$ of 1.7 (this work), as shown in Table 4, can be obtained. This value can be used to compare different generators by considering all variables and results in 0.005 [54], 0.09 [55] and 0.18 [56] $\mu W \cdot cm^{-2} \cdot K^{-2}$ for the aforementioned previous reports.

4. Conclusions

Processing via O_2-sintering appears more promising for densifying a p-type composite material than using fast, expensive and partially reducing techniques like HP or SPS. The thermoelectric power factor of the CCO-NCO-BCCO nanocomposite was significantly enhanced by pressureless sintering in O_2 atmosphere. The benefits of oxides are thermal and chemical stability at high temperatures. For this reason, long-term annealing is advantageous for the stability of oxides in air. Furthermore, the power factor as a function of the electrical conductivity in the Ioffe plot is more suitable than the zT value, to estimate the applicability of thermoelectric materials for energy conversion at high temperatures from infinite heat sources. The power generation of oxide-based thermoelectric generators at high-temperatures from infinite heat sources was greatly enhanced by use of high power materials. The power generation could be probably further improved, if contact resistances would be decreased, for example by use of more appropriate solders.

5. Acknowledgment

6. References

[1] L. E. Bell, Cooling, heating, generating power, and recovering waste heat with thermoelectric systems, Science 321 (2008) 1457–1461.

[2] H. U. Fuchs, A direct entropic approach to uniform and spatially continuous dynamical models of thermoelectric devices, EHS 1(3-4) (2014) 253–265.

[3] A. Feldhoff, Thermoelectric material tensor derived from the Onsager - de Groot - Callen model, EHS 2 (1) (2015) 5–13.

[4] M. Bittner, N. Kanas, R. Hinterding, F. Steinbach, D. Groeneveld, P. Wemhoff, K. Wiik, M.-A. Einarsrud, A. Feldhoff, Triple-phase ceramic 2D nanocomposite with enhanced thermoelectric properties, submitted to J. Eur. Ceram. Soc.

[5] A. Feldhoff, B. Geppert, A high-temperature thermoelectric generator based on oxides, EHS 1(1-2) (2014) 69–78.

[6] D. Narducci, Wo we really need high thermoelectric figure of merit? A critical appraisal to the power conversion efficiency of thermoelectric materials, Appl. Phys. Lett. 99 (2011) 102104–1–102104–3.

[7] A. F. Ioffe, Semiconductor Thermoelements and Thermoelectric cooling, 1st Edition, Infosearch Ltd. London, 1957.

[8] M. G. Kanatzidis, Nanstructured thermoelectrics: The new paradigm?, Chem. Mater. 22 (2010) 648–659.

[9] M. Martín-González, O. Caballero-Calero, P. Díaz-Chao, Nano-engineering thermoelectrics for 21st century: Energy harvesting and other trends in the field, Renew. Sust. Energ. Rev. 24 (2013) 288–305.

[10] J. Yang, H.-L. Yip, A. K.-Y. Jen, Rational design of advanced thermoelectric materials, Adv. Energy Mater. 3 (2013) 549.

[11] G. Tan, L.-D. Zhao, M. Kanatzidis, Rationally designing high-performance bulk thermoelectric materials, Chem. Rev. 116 (2016) 12123–12149.

[12] M. S. Dresselhaus, G. Chen, M. Y. Tang, R. Yang, H. Lee, D. Wang, Z. Ren, J. P. Fleurial, P. Gogna, New directions for low-dimensional thermoelectric materials, Adv. Mater. 19 (2007) 1043–1053.

[13] J. P. Heremans, B. Wiendlocha, A. M. Chamoire, Resonant levels in bulk thermoelectric semiconductors, Energ. Environ. Sci. 5 (2012) 5510–5530.

[14] Y. Pei, X. Shi, A. Lalonde, H. Wang, L. Chen, G. J. Snyder, Convergence of electronic bands for high performance bulk thermoelectrics, Nature 473 (2011) 66–69.

[15] R. J. Korkosz, T. C. Chasapis, S.-H. Lo, J. W. Doak, Y. J. Kim, C.-I. Wu, E. Hatzikraniotis, T. P. Hogan, D. N. Seidman, D. Wolverton, V. P. Dravid, M. G. Kanatzidis, High ZT in p-type $(PbTe)_{1-2x}(PbSe)_x(PbS)_x$ thermoelectric materials, J. Am. Chem. Soc. 136 (2014) 3225–3237.

[16] D. Wu, L.-D. Zhao, X. Tong, W. Li, L. Wu, Q. Tan, Y. Pei, L. Huang, J.-F. Li, Y. Zhu, M. G. Kanatzidis, J. He, Superior thermoelectric performance in PbTe-PbS pseudo-binary: extremely low thermal conductivity and modulated carrier concentration, Energ. Environ. Sci. 8 (2015) 2056–2068.

[17] C. Fu, T. Zhu, Y. Liu, H. Xie, X. Zhao, Band engineering of high performance p-type FeNbSb based half-Heusler thermoelectric materials for figure of merit zT > 1, Energ. Environ. Sci. 8 (2015) 216–220.

[18] J. Li, J. Sui, Y. Pei, C. Barreteau, D. Berardan, N. Dragoe, W. Cai, J. He, L.-D. Zhao, A high thermoelectric figure of merit ZT > 1 in Ba heavily doped BiCuSeO oxyselenides, Energ. Environ. Sci. 5 (2012) 8543–8547.

[19] F. Li, T.-R. Wei, F. Kang, J.-F. Li, Enhanced thermoelectric performance of Ca-doped BiCuSeO in a wide temperature range, J. Mater. Chem. A 1 (2013) 11942–11949.

[20] J.-L. Lan, Y.-C. Liu, B. Zhan, Y.-H. Lin, B. Zhang, X. Yuan, W. Zhang, W. Xu, C.-W. Nan, Enhanced thermoelectric properties of Pb-doped BiCuSeO ceramics, Adv. Mater. 25 (2013) 5086–5090.

[21] Z. Li, C. Xiao, S. Fan, Y. Deng, W. Zhang, B. Ye, Y. Xie, Dual vacancies: An effective strategy realizing synergistic optimization of thermoelectric property in BiCuSeO, J. Am. Chem. Soc. 137 (2015) 6587–6593.

[22] C. Barreteau, D. Berardan, L. Zhao, N. Dragoe, Influence of Te

substitution on the structural and electronic properties of thermoelectric BiCuSeO, J. Mater. Chem. A 1 (2013) 2921–2926.

[23] J. G. Noudem, D. Kenfaui, D. Chateigner, M. Gomina, Toward the enhancement of thermoelectric properties of lamellar $Ca_3Co_4O_9$ by edge-free spark plasma texturing, Scripta Mater. 66 (2012) 258–260.

[24] Y. Liu, L.-D. Zhao, Y. Zhu, Y. Liu, F. Li, M. Yu, D.-B. Liu, W. Xu, Y.-H. Lin, C.-W. Nan, Synergistically optimizing electrical and thermal transport properties of BiCuSeO via a dual-doping approach, Adv. Energy Mater. 6 (2016) 1502423.

[25] C. Barreteau, D. Berardan, N. Dragoe, Studies on the thermal stability of BiCuSeO, J. Solid State Chem. 222 (2015) 53–59.

[26] Y.-L. Pei, H. Wu, D. Wu, F. Zheng, J. He, High thermoelectric performance realized in a BiCuSeO system by improving carrier mobility through 3D modulation doping, J. Am. Chem. Soc. 136 (2014) 13902–13908.

[27] D. M. Rowe, CRC Handbook of Thermoelectrics, 89th Edition, CRC Press, Boca Raton, FL, 1995.

[28] M. Ohtaki, K. Araki, K. Yamamoto, High thermoelectric performance of dually doped ZnO ceramics, J. Electron. Mater. 38 (2009) 1234–1238.

[29] N. V. Nong, N. Pryds, S. Linderoth, M. Ohtaki, Enhancement of the thermoelectric performance of p-type layered oxide $Ca_3Co_4O_{9+\delta}$ through heavy doping and metallic nanoinclusions, Adv. Mater. 23 (2011) 2484–2490.

[30] G. Xu, R. Funahashi, M. Shikano, I. Matsubara, Y. Zhou, Thermoelectric properties of the Bi- Na-substituted $Ca_3Co_4O_9$ system, Appl. Phys. Lett. 80 (2002) 3760–3762.

[31] Y. Miyazaki, Crystal structure and thermoelectric properties of the misfit-layered cobalt oxides, Solid State Ionics 172 (2004) 463–467.

[32] M. Bittner, L. Helmich, F. Nietschke, B. Geppert, O. Oeckler, A. Feldhoff, Porous $Ca_3Co_4O_9$ with enhanced thermoelectric properties derived from sol-gel synthesis, J. Eur. Ceram. Soc. 37 (2017) 3909–3915.

[33] Y. Miyazaki, M. Onoda, T. Oku, M. Kikuchi, Y. Ishii, Y. Ono, Y. Morii, T. Kajitani, Modulated structure of thermoelectric compound $[Ca_2CoO_3] CoO_2$, J. Phys. Soc. Jpn. 71 (2002) 491–497.

[34] N. V. Nong, C.-J. Liu, M. Ohtaki, Improvement on the high temperature thermoelectric performance of Ga- doped misfit-layered $Ca_3Co_{4-x}Ga_xO_{9+\delta}$ (x=0, 0.05, 0.1, and 0.2), J. Alloy. Compd. 491 (2010) 53–56.

[35] L. Xu, F. Li, Y. Wang, High-temperature transport and thermoelectric properties of $Ca_3Co_{4-x}Ti_xO_9$, J. Alloy. Compd. 501 (2010) 115–119.

[36] Y. Wang, Y. Sui, P. Ren, L. Wang, X. Wang, W. Su, H. Fan, Strongly correlated properties and enhanced thermoelectric response in $Ca_3Co_{4-x}M_xO_9$ (M = Fe, Mn, and Cu), Chem. Mater. 22 (2010) 1155–1163.

[37] D. Bérardan, E. Guilmeau, A. Maignan, B. Raveau, Enhancement of the thermoelectric performances of In_2O_3 by the coupled substitution of M^{2+}/Sn^{4+} for In^{3+}, J. Appl. Phys. 104 (2008) 064918–1–064918–5.

[38] Y. L. Yan, Y. X. Wang, Electronic structure and low temperature thermoelectric properties of $In_{24}M_8O_{48}$ (M=Ge^{4+}, Sn^{4+},Ti^{4+}, and Zr^{4+}), J. Comput. Chem. 33 (2012) 88–92.

[39] E. Guilmeau, D. Bérardan, C. Simon, A. Maignan, B. Raveau, D. Ovono Ovono, F. Delorme, Tuning the transport and thermoelectric properties of In_2O_3 build ceramics through doping at In-site, J. Appl. Phys. 106 (2009) 053715–1–053715–7.

[40] M. Bittner, B. Geppert, N. Kanas, S. P. Singh, K. Wiik, A. Feldhoff, Oxide-based thermoelectric generator for high-temperature application using p-type $Ca_3Co_4O_9$ and n-type $Ca_{1.95}Sn_{0.05}O_3$ legs, EHS 3(3) (2016) 213–222.

[41] M. Schrade, T. Norby, T. G. Finstad, Hall effect measurements on themoelectric $Ca_3Co_4O_9$: On how to determine the charge carrier concentration in strongly correlated misfit cobaltites, J. Appl. Phys. 117 (2015) 205103–1–205103–6.

[42] M. Košir, M. Podlogar, N. Daneu, A. Rečnik, E. Guilmeau, S. Bernik, Phase formation, microstructure development and thermoelectric properties of $(ZnO)_k In_2O_3$ ceramics, J. Eur. Ceram. Soc. 37 (2017) 2833–2842.

[43] S. K. S. R. Sarath Kumar, Transparent ITO-Mn:ITO thin-film thermocouples, IEEE Sens. J. 9 (2009) 809–813.

[44] M. Ohtaki, D. Ogura, K. Eguchi, H. Arai, High-temperature thermoelectric properties of In_2O_3-based mixed oxides and their applicability to thermoelectric power generation, J. Mater. Chem. 4(5) (1994) 653–656.

[45] Q. Zhu, E. M. Hopper, B. J. Ingram, T. O. Mason, Combined Jonker and Ioffe analysis of oxide conductors and semiconductors, J. Am. Ceram. Soc. 94 (2011) 187–193.

[46] E. Guilmeau, D. Bérardan, C. Simon, A. Maignan, B. Raveau, D. O. Ovono, F. Delorme, Tuning the transport and thermoelectric properties of In_2O_3 bulk ceramics through doping at In-site, J. Appl. Phys. 106 (2009) 053715–1–053715–7.

[47] T. Janssen, A. Janner, A. Looijenga-Vos, P. M. D. Wolff, International Tables for Crystallography: 9.8 Incommensurate and commensurate modulated structures, 3rd Edition, Kluwer Academic Publishers, Dordrecht/Boston/London, 2004.

[48] L. Viciu, J. W. G. Bos, H. W. Zandbergen, Q. Huang, M. L. Foo, S. Ishiwata, A. P. Ramirez, M. Lee, N. P. Ong, R. J. Cava, Crystal structure and elementary properties of Na_xCoO_2 (x = 0.32, 0.51, 0.6, 0.75, and 0.92) in the three-layer $NaCoO_2$ familiy, Phys. Rev. B 73 (2006) 174104–1–174104–10.

[49] M. Schrade, H. Fjeld, T. G. Finstad, T. Norby, Electronic transport properties of $[Ca_2CoO_{3-\delta}]_q[Co_2]$ for high thermoelectric performance, J. Phys. Chem. C 118 (2014) 2908–2918.

[50] M. Schrade, S. Casolo, P. J. Graham, C. Ulrich, S. Li, O.-M. Løvvik, T. G. Finstad, T. Norby, Oxygen nonstoichiometry in $[Ca_2CoO_3]_{0.62}[Co_2]$: A combined experimental and computational study, J. Phys. Chem. C 118 (2014) 18899–18907.

[51] X. Hu, P. Jood, M. Ohta, M. Kunii, K. Nagase, H. Nishiate, M. G. Kanatzidis, A. Yamamoto, Power generation from nanostructured PbTe-based thermoelectrics: comprehensive development from materials to modules, Energ. Environ. Sci. 9 (2016) 517–529.

[52] S. M. Choi, K. H. Lee, C. H. Lim, W. S. Seo, Oxide-based thermoelectric power generation module using p-type $Ca_3Co_4O_9$ and n-type $(ZnO)_7In_2O_3$ legs, Energ. Convers. Manage. 52 (2011) 335–339.

[53] K. Park, G. W. Lee, Fabrication and thermoelectric power of Π-shaped $Ca_3Co_4O_9/CaMnO_3$ modules for renewable energy conversion, Energy 60 (2013) 87–93.

[54] L. Han, Y. Jiang, S. Li, H. Su, X. Lan, K. Qin, T. Han, H. Zhong, L. Chen, D. Yu, High temperature thermoelectric properties and energy transfer devices of $Ca_3Co_{4-x}Ag_xO_9$ and $Ca_{1-y}Sm_yMnO_3$, J. Alloys Compd. 509 (2011) 8970–8977.

[55] S. Urata, R. Funahashi, T. Mihara, A. Kosuga, S. Sodeoka, T. Tanaka, Power generation of a p-type $Ca_3Co_4O_9$/n-type $CaMnO_3$ module, Int. J. Appl. Ceram. Technol. 4 (2007) 535–540.

[56] N. V. Nong, N. Pryds, Nanostructured oxide materials and modules for high-temperature power generation from waste heat, Adv. Nat. Sci. : Nanosci. Nanotechnol. 4 (2013) 023002.

Supplementary information for ”A comprehensive study on improved power materials for high-temperature thermoelectric generators”

Michael Bittner[1,*], Nikola Kanas[2], Richard Hinterding[1], Frank Steinbach[1], Jan Räthel[3], Matthias Schrade[4], Kjell Wiik[2], Mari-Ann Einarsrud[2], Armin Feldhoff[1]

[1]Institute of Physical Chemistry and Electrochemistry, Leibniz University Hannover, Hannover, Germany

[2]Department of Materials Science and Engineering, NTNU Norwegian University of Science and Technology, Trondheim, Norway

[3]Fraunhofer − Institute for Ceramic Technologies and Systems IKTS, Dresden, Germany

[4]Department of Physics, University of Oslo, Oslo, Norway

1

1 Supplementary

Schemes and diagrams were created using OriginPro 9.1G. Both, SEM and TEM micrographs were created using ImageJ and Digital Micrograph. Figures were arranged, merged and saved using PowerPoint 2010 and Photoshop CS5. The XRD patterns of the single-phase references of $Ca_3Co_4O_9$ (CCO-Air), $Bi_2Ca_2Co_2O_9$ (BCCO) and Na_xCoO_2 (NCO) and different triple-phase nanocomposites CCO-30-35-10-powder, CCO-30-35-10-SPS, CCO-30-35-10-HP, CCO-30-35-10-O_2 and n-type materials $In_{1.9}Sn_{0.05}Al_{0.05}O_3$ (Sn,Al:In_2O_3), $In_{1.95}Ge_{0.01}$ $Mn_{0.01}Zn_{0.03}O_3$ (Ge,Mn,Zn:In_2O_3) are shown in Figure S 1a-h. The XRD patterns of O_2-sintered reference samples are shown in Figure S 2f-h. A step size of 0.003942, a time per step of 1.1 seconds, a voltage of 40 kV and a current of 40 mA were used for diffraction experiments.

For SEM investigations, the powder specimen was prepared by spreading the powder on a graphite mount. The ceramic specimen of vibration-polished cross sections were prepared by cutting cross-sections from discs, using a precision vertical diamond wire saw from O'Well model 3242, followed by a multistep (30 μm, 15 μm, 6 μm, 3 μm, 1 μm diamond lapping films) polishing program using Techprep from Allied - High Tech Products, Inc. The primed samples were afterwards polished by a vibration polishing step using a Buehler Vibromet-2 and a 50 nm colloidal alumina suspension. The O_2-sintered reference samples were investigated by SEM and elemental distribution analyzes, as shown in Figure S 3a-d. The n-type materials Sn,Al:In_2O_3 and Ge,Mn,Zn:In_2O_3 were also analyzed by SEM and elemental distribution spectroscopy, shown in Figure S 4a-d.

The density and porosity of O_2-sintered samples were analyzed using the Archimedes measurements shown in Table S 1. The bulk density of O_2-sintered composite phases increased with applied temperatures of 1198 K (CCO-30-35-10-1198-O_2) and 1223 K (CCO-30-35-10-1223-O_2) to 3.58 and 4.23 g $\cdot cm^{-3}$, respectively.

The TEM specimen was prepared as the SEM specimen, downsized in dimensions to fit on a TEM grid. The specimen was pinched out using a precision ion polishing system (Ar-ion) Model 691 from Gatan. Figure S 5 gives detailed elemental distribution information of different elements, referring to Figure 3a,b in the main document. The different 2D nanostructures and their elemental composition are shown in Figure S 5a-h. Detailed information about the HRTEM site of Figure 3c of the main document is shown in Figures S 6a-h. Figure S 7 provides detailed elemental distribution information of different elements, referring to Figure 3d,e in the main document. The SPS technique forces the material in a distinct form, leading to the formation of artificial structures. Detailed information about the

2

HRTEM site of Figure 3f of the main document is given in Figures S 8a-h.
Electrical measurements were recorded and transduced using LAB VIEW software. Figure S 9a-d shows the thermoelectric properties of O_2-sintered reference materials. The measured values of the heat capacity C_P of n-type materials were consistent with phononic Debye-Einstein behavior and reached $0.86 \text{ J} \cdot \text{g}^{-1} \cdot \text{K}^{-1}$ at 1073 K.

Figure S 10 represents the used conventional generator design of 10 p/n couples, each leg in the dimensions of 1 mm x 1 mm x 3 mm to construct the thermoelectric generators. Al_2O_3 plates (1 cm^2 area) were used as templates, the Au metal connectors were painted on the plates, utilizing an Au-paste, and Pt-wires were mounted to contact the generator.

3

1.1 Figures

Figure S 1: X-ray diffraction patterns of ceramic samples: a) **CCO-Air** (taken from [1]), b) **NCO**, c) **BCCO**, d) **CCO-30-35-10-Air** (taken from [2]) powder, e) **CCO-30-35-10-SPS**, f) **CCO-30-35-10-HP**, g) **CCO-30-35-10-O$_2$**. CCO (green) and BCCO (blue) reflections were indexed for superspace group Cm (0 1 - p 0, equivalent to Bm (0 0 γ), no. 8.3; see [3,4]). NCO (red) reflections were indexed in superspace group C2/m [5]. The main NCO and CCO reflections (001-1 and 22-1-1, 200-1, 110-1) are overlapping. Highest texture (0020, 0040, CCO reflections) was obtained after O$_2$-sintering. The patterns of e-g) are shifted to lower angles due to the integration of Bi. h,i) **Sn,Al:In$_2$O$_3$** and **Ge,Mn,Zn:In$_2$O$_3$**, indexed reflections of space group Ia$\bar{3}$ (no. 206, PDF-2 database 01-089-4596).
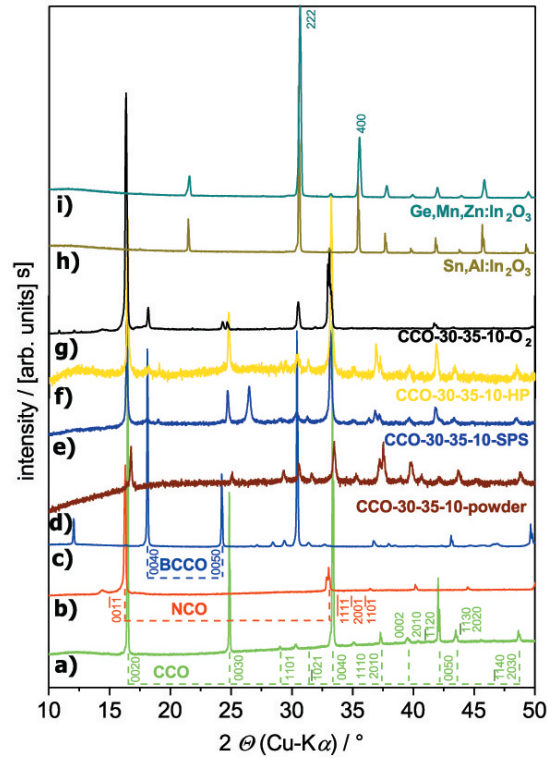
4

Figure S 2: X-ray diffraction patterns of ceramic samples: a) **CCO-Air**, (taken from[1]), b) **NCO**, c) **BCCO**, d) **CCO-30-35-10-Air** powder (taken from[2]), e) **CCO-30-35-10-Air** ceramic (taken from[2]), f) **CCO-30-35-10-1198-O$_2$**, g) **CCO-30-35-10-1223-O$_2$**, h) **CCO-30-35-10-1248-O$_2$**. CCO (green) and BCCO (blue) reflections were indexed for superspace group Cm (0 1 - p 0, equivalent to Bm (0 0 γ), no. 8.3; see[3,4]). NCO (red) reflections were indexed in superspace group C2/m[5]. The main NCO and CCO reflections (001-1 and 22-1-1, 200-1, 110-1) are overlapping. Highest texture (0020, 0040, CCO reflections) was obtained after O$_2$ sintering at 1248 K. The patterns of g-j) are shifted to lower angles due to the integration of Bi.
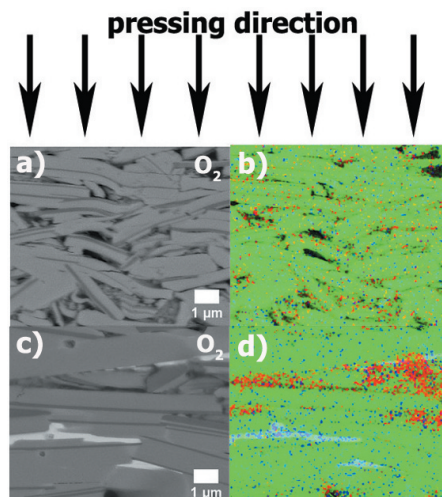
5

Figure S 3: SEM micrographs and EDXS elemental distributions of cross sections: a, b) **CCO-30-35-10-1198-O$_2$**, c, d) **CCO-30-35-10-1223-O$_2$**. The direction of pressing is indicated by black arrows. CCO phase is dominated by Ca (green), NCO phase by Na (red) and BCCO phase by Bi (blue).
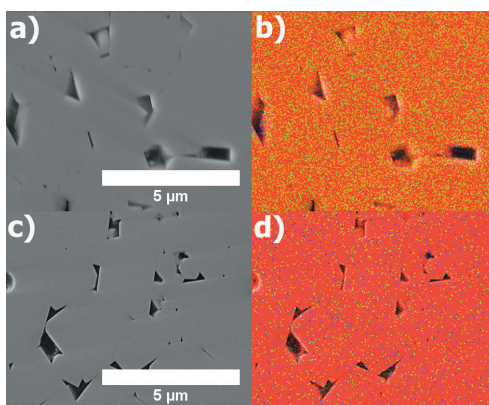

Figure S 4: SEM micrographs and EDXS elemental distributions of cross sections: a, b) Sn,Al:In$_2$O$_3$ and c, d) Ge,Mn,Zn:In$_2$O$_3$.
b) In (red), Sn (green), Al (blue)
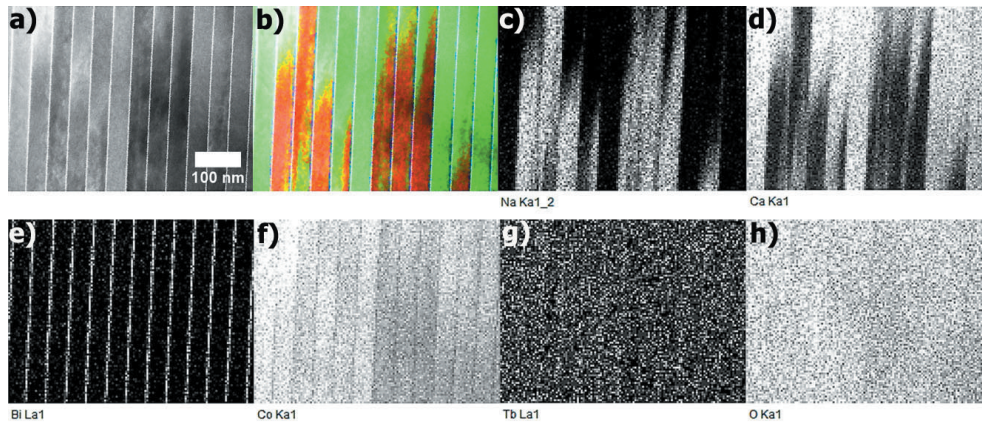d) In (red), Ge (green), Mn (blue)

6

Figure S 5: STEM analysis of a **CCO-30-35-10-1248-O$_2$** nanocomposite ceramic, supplementing Figure 3a, b) of the main document. a, b) STEM dark-field micrograph and EDXS elemental distribution of Na (red), Ca (green) and Bi (blue) of the region shown. c-h) Detailed elemental distribution information for Na, Ca, Bi, Co, Tb and O.
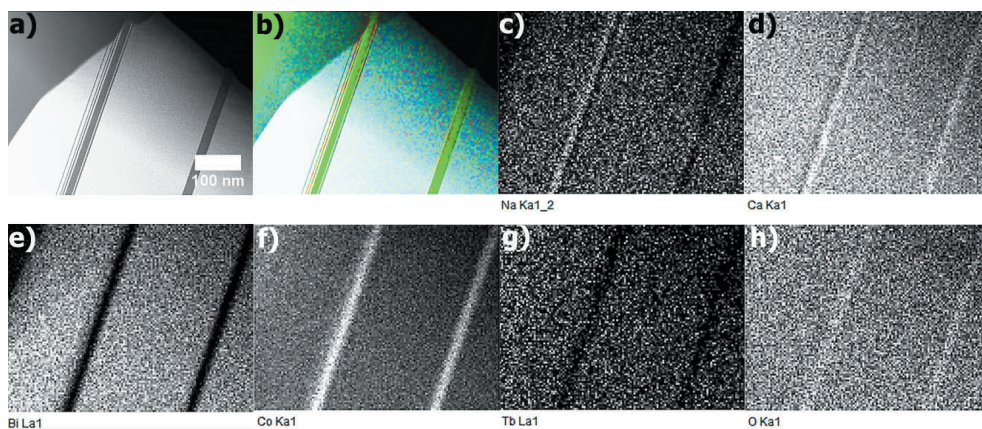
Figure S 6: STEM analysis of a **CCO-30-35-10-1248-O$_2$** nanocomposite ceramic, showing site of HRTEM micrograph in Figure 3c of the main document. a, b) STEM dark-field micrograph and EDXS elemental distribution of Na (red), Ca (green) and Bi (blue) of the region shown. c-h) Detailed elemental distribution information for Na, Ca, Bi, Co, Tb and O.

7
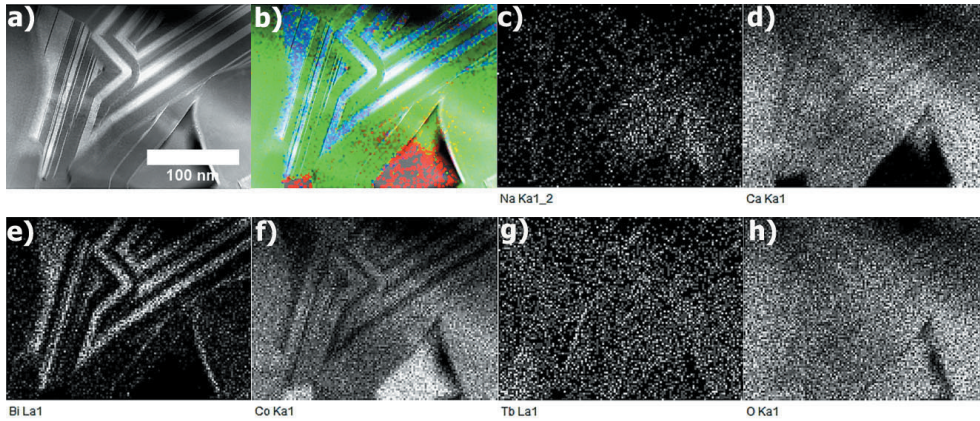
Figure S 7: STEM analysis of a **CCO-30-35-10-SPS** nanocomposite ceramic, supplementing Figure 3d,e of the main document. a, b) STEM dark-field micrograph and EDXS elemental distribution of Na (red), Ca (green) and Bi (blue) of the region shown. c-h) Detailed elemental distribution information for Na, Ca, Bi, Co, Tb and O.
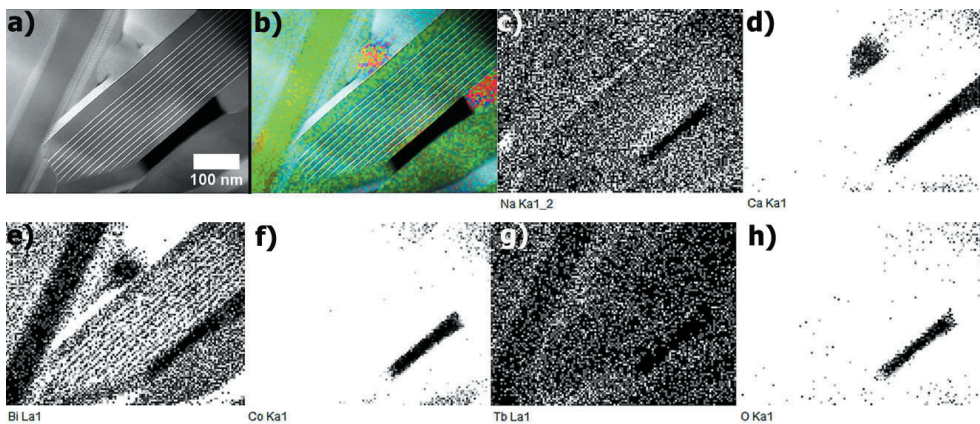
Figure S 8: STEM analysis of a **CCO-30-35-10-SPS** nanocomposite ceramic, showing site of HRTEM micrograph in Figure 3f of the main document. a, b) STEM dark-field micrograph and EDXS elemental distribution of Na (red), Ca (green) and Bi (blue) of the region shown. c-h) Detailed elemental distribution information for Na, Ca, Bi, Co, Tb and O.

8
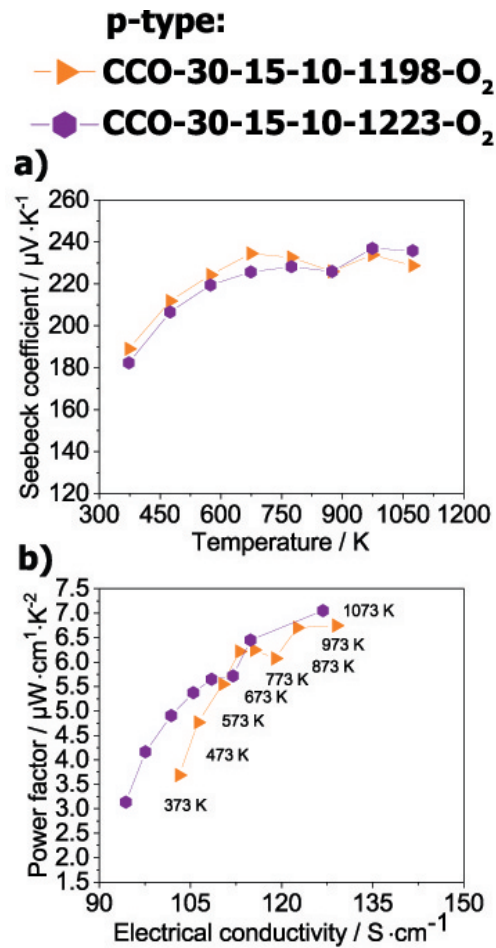
Figure S 9: Thermoelectric parameters of **CCO-30-35-10-1198-O$_2$** (rotated rectangle, orange) and **CCO-30-35-10-1223-O$_2$** (hexagon, purple) ceramics: a) Seebeck coefficient α and b) Ioffe plot: power factor $\sigma \cdot \alpha^2$ as a function of the isothermal electrical conductivity σ.

9

Figure S 10: Schematic representation of conventional thermoelectric generator design.

10

1.2 Tables

Table S 1: Measured values of density and porosity for **CCO-30-35-10-1198-O$_2$** and **CCO-30-35-10-1223-O$_2$** (20 h at 1198 K, 1223 K, O$_2$) using ISO (International Organization for Standardization) 5018:1983.
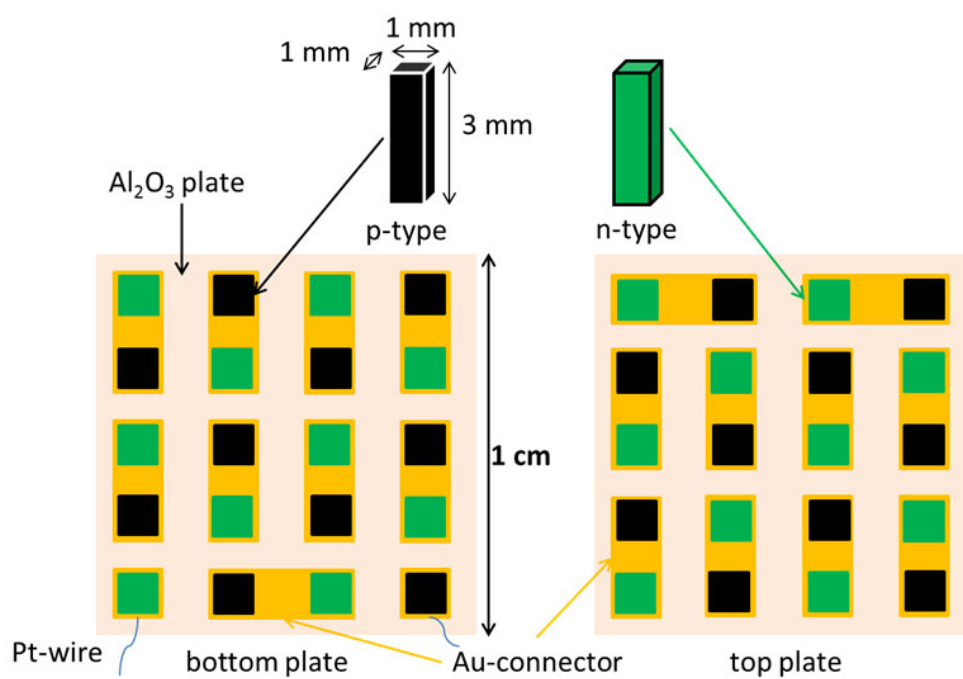
material		bulk dens.	open poros.
abbreviation	stoichiometry	/ g $\cdot cm^{-3}$	/ %
CCO-30-35-10-1198-O$_2$	Ca$_{2.25}$Na$_{0.3}$Bi$_{0.35}$Tb$_{0.1}$Co$_4$O$_9$	3.6 ± 0.0	25.0 ± 3.2
CCO-30-35-10-1223-O$_2$	Ca$_{2.25}$Na$_{0.3}$Bi$_{0.35}$Tb$_{0.1}$Co$_4$O$_9$	4.2 ± 0.0	12.4 ± 2.9

References

[1] M. Bittner, L. Helmich, F. Nietschke, B. Geppert, O. Oeckler, A. Feldhoff, Porous Ca$_3$Co$_4$O$_9$ with enhanced thermoelectric properties derived from sol-gel synthesis, J. Eur. Ceram. Soc. 37 (2017) 3909–3915.

[2] M. Bittner, N. Kanas, R. Hinterding, F. Steinbach, D. Groeneveld, P. Wemhoff, K. Wiik, M.-A. Einarsrud, A. Feldhoff, Triple-phase ceramic 2D nanocomposite with enhanced thermoelectric properties, submitted to J. Eur. Ceram. Soc.

[3] T. Janssen, A. Janner, A. Looijenga-Vos, P. M. D. Wolff, International Tables for Crystallography: 9.8 Incommensurate and commensurate modulated structures, 3rd Edition, Kluwer Academic Publishers, Dordrecht/Boston/London, 2004.

[4] E. Guilmeau, M. Pollet, D. Grebille, M. Hervieu, M. Muguerra, R. Cloots, M. Mikami, R. Funahashi, Nanoblock coupling effect in iodine intercalated [Bi$_{0.82}$CaO$_2$]$_2$[CoO$_2$]$_{1.69}$ layered cobaltite, Inorg. Chem. 46 (2007) 2124–2131.

[5] L. Viciu, J. W. G. Bos, H. W. Zandbergen, Q. Huang, M. L. Foo, S. Ishiwata, A. P. Ramirez, M. Lee, N. P. Ong, R. J. Cava, Crystal structure and elementary properties of Na$_x$CoO$_2$ (x = 0.32, 0.51, 0.6, 0.75, and 0.92) in the three-layer NaCoO$_2$ familiy, Phys. Rev. B 73 (2006) 174104–1–174104–10.

4 Conclusions and outlook

In this work presented studies cover topics from solid state chemistry, solid state physics to process engineering and electrical engineering. The objective was a better understanding of thermoelectric (TE) power conversion at elevated temperatures. The thermoelectric material research in these studies was focused on comprehensive investigations of synthesis, processing and properties of p-type $Ca_3Co_4O_9$ (CCO) and of $Ca_3Co_4O_9$-Na_xCoO_2-$Bi_2Ca_2Co_2O_9$ (CCO-NCO-BCCO) nanocomposites.

A specific control of particle size and phase composition of powders was assured by utilization of a "bottom up" sol-gel technique. This is important to adjust the properties of processed thermoelectric ceramics. The sol-gel synthesis is much faster, simpler and avoids inadvertent contamination compared to the most commonly used solid state reaction route. Furthermore, the sol-gel technique enables an excellent control of the doping content and provides nano-scaled particles. These nano-sized particles can be further processed by different sintering techniques to control properties like micro-, nanostructure as well as porosity. The porosity of a ceramic has significant influence on the thermoelectric properties, particularly on the electrical conductivity and heat conductivity. The influence was shown in highly porous CCO ceramics, which revealed a significantly reduced heat conductivity and a subsequent record figure-of-merit zT value. Degree of compression and porosity are directly related to each other. A porous ceramic shows a low degree of both, compression and orientation of grains. Due to a balanced orientation of CCO grains in a porous CCO ceramic, the anisotropic transport behavior of CCO is less pronounced. In order to tune the zT value of pure CCO, finding an ideal proportion between the thermoelectric power factor and the heat conductivity is a possible approach. However, porous materials show poor electrical properties, these are counteractive to improve the power generation. The application of a $In_{2-x}Sn_xO_3$ (ITO) material, which shows both, a high electrical conductivity and a high-power factor, increased the electrical power output of the first in this work reported thermoelectric generator (TEG). In addition, simulations confirmed these results, materials of high electrical conductivity and power factor are desired for power generation. For this reason, the CCO phase was heavily co-doped by Na, Bi and Tb, resulting in a novel CCO-NCO-BCCO nanocomposite of significantly increased electrical conductivity and power factor at high temperatures in air. The Ioffe plot, which shows the thermoelectric power factor as a function of the electrical conductivity is useful to estimate the applicability of materials for high-temperature power generation. Pressureless sintering of the heavily co-doped CCO powder at high temperatures in air led to the formation of a triple-phase nanocomposite of an all-scale hierarchical structure. Interdiffusion and

incorporation in a CCO matrix stabilized the NCO and BCCO phases at high temperatures in air and enabled utilization of synergistic effects. The incorporation of thermally or chemically instable phases into a stable host matrix in order to stabilize them at high temperatures or under oxidizing conditions, could offer new alternatives in material development. Since porosity influences the thermoelectric properties significantly, several alternative processing techniques were carried out to obtain dense CCO-NCO-BCCO nanocomposites. From literature, the hot-pressing (HP) or spark plasma sintering (SPS) technique were expected to maintain a dense nanocomposite with improved thermoelectric properties. However, a dense nanocomposite with further enhanced electrical conductivity and thermoelectric power factor at high temperatures in air was obtained from pressureless sintering in O_2 atmosphere. The processing by O_2-sintering seems more promising to densify a composite material than using fast, expensive and partially reducing techniques like HP or SPS. The nanocomposite from SPS showed nano-sized grains and a nanostructure, which was forced into a certain shape and possessed a subsequently decreased stability in air. In contrast, the nanocomposite from O_2-sintering exhibit a multiscale structure of highly aligned 2D layers of CCO, NCO and BCCO. The pressureless sintering in air or O_2 atmosphere appears more appropriate to ensure a high stability of materials under oxidizing conditions at elevated temperatures.

The main research activity of the thermoelectric community is focused on enhancing the figure-of-merit zT of thermoelectric materials and subsequently improving the energy conversion efficiency of thermoelectric devices. This approach should be discussed critically and rerated in terms of the desired area of application for different material classes. The most important question and determining fact should be: Is a limited or an infinite heat source available. If a limited heat source is present, for example in space or automotive application, materials with high figure-of-merit zT are needed, which show an accordingly high energy conversion efficiency. However, if an infinite heat source in the high-temperature range is present, materials of high thermoelectric power factor, electrical conductivity and moderate heat conductivity are needed to recover waste heat. Regarding the figure-of-merit zT, oxides can not compete with other material classes. Research on thermoelectric oxides should, therefore, focus on enhancing the thermoelectric power factor of p- and n-type oxides in the high-temperature range in air. For this reason, two n-type materials were developed to assemble them with the aforementioned p-type materials into TEG prototypes. The Sn, Al co-doped $Sn,Al:In_2O_3$ shows a high electrical conductivity and thermoelectric power factor (Ioffe plot), while the Ge, Mn and Zn co-doped $Ge,Mn,Zn:In_2O_3$ material possess a comparable high-zT value. The specifically designed and improved p- and n-type materials were used to estimate the influence of high-power and high-zT materials on the power characteristics of TEGs. The highest ever reported electrical power density of oxide-based TEGs was obtained from these high-power materials. The power characteristics of the generator, which was made of the n-type high-zT material, were significantly decreased compared to these of the high-power TEG. Furthermore, the electrical power output of the TEGs was directly related to the trends of the electrical conductivity and the

thermoelectric power factor in the Ioffe plot. The comparison of TEGs is difficult, due to the multiplicity of changeable paramaters, like dimensions of used p- and n-type legs, hot-side temperatures or applied temperature differences. The electrical power density considers the electrical power output and the geometrical dimensions of the TEG, but a temperature dependent electrical power density mW·cm^{-2}·K^{-2} is a more standardized alternative and would be much more suitable to compare TEGs with each other.

Theoretical postulations were experimentally proved in characterizing prototypes of TEGs made of high-power and high-zT materials. The possibility to improve the electrical power output and electrical power density at high temperatures in air, using specifically designed materials, was presented.

The developed materials could be assembled in a more advanced TEG design in order to further improve power generation at high temperatures. For this reason, a proof of principle all-oxide TEG was manufactured for the first time, processed via SPS of CCO and CaMnO$_3$ powders. The all-oxide TEG can abstain from use of metallic connectors and thereby decrease the contact resistance significantly. Furthermore, interlayers can boost the power generation by synergistic effects like the transversal thermoelectric effect. However, additional research is needed to overcome processing related challenges in up-scaling all-oxide generators.

To further increase power generation and energy conversion at high temperatures, either materials or contact resistance have to be improved. One approach to improve the p-type materials could exist in introducing a fourth layer like BiCuSeO into the CCO-NCO-BCCO nanocomposite. The BiCuSeO oxyselenide shows limited thermal and chemical stability at elevated temperatures under oxidizing atmosphere. Hence, the stabilization and utilization by incorporation in a stable matrix could further boost p-type oxides. The thermoelectric properties of co-doped n-type oxides could be improved by application of different sintering techniques, like HP, SPS and O$_2$-sintering. The importance to decrease the contact resistance of TEGs was shown in this work and could be accomplished by a substitution of metallic connectors or commitment of an all-oxide generator design. Furthermore, TEGs should be used in a temperature range, which is adapted to the properties of applied p- and n-type materials. The temperature range of hot- and cold-side should be chosen, depending on the course of the thermoelectric power factor and electrical conductivity in the Ioffe plot. In order to improve electrical power generation, the best course of the thermoelectric power factor and electrical conductivity in the Ioffe plot, would be an as narrow as possible distribution of high values.

Publications and conferences

Puclications included in this work:

(1) Porous $Ca_3Co_4O_9$ with enhanced thermoelectric properties derived from Sol-Gel synthesis

<u>Michael Bittner</u>, Lailah Helmich, Frederik Nietschke, Benjamin Geppert, Oliver Oeckler, Armin Feldhoff

Journal of the European Ceramic Society, 37 (2017) 3909-3915
http://dx.doi.org/10.1016/j.jeurceramsoc.2017.04.059

(2) Triple-phase ceramic 2D nanocomposite with enhanced thermoelectric properties

<u>Michael Bittner</u>, Nikola Kanas, Richard Hinterding,
Frank Steinbach, Dennis Groeneveld, Piotr Wemhoff, Kjell Wiik,
Mari-Ann Einarsrud, Armin Feldhoff

submitted to *Journal of the European Ceramic Society*

(3) Oxide-based thermoelectric generator for high-temperature application using p-type $Ca_3Co_4O_9$ and n-Type $In_{1.95}Sn_{0.05}O_3$ legs

<u>Michael Bittner</u>, Benjamin Geppert, Nikola Kanas,
Sathya Prakash Singh, Kjell Wiik and Armin Feldhoff

Energy Harvesting and Systems, 3(3) (2016) 213-222
DOI 10.1515/ehs-2016-0002

(4) Experimental characterisation and finite-element simulations of a thermoelectric generator with ceramic p-type $Ca_3Co_4O_9$ and metallic n-type $Cu_{0.57}Ni_{0.42}Mn_{0.01}$ legs

B. Geppert, D. Groeneveld, <u>Michael Bittner</u> and Armin Feldhoff

Energy Harvesting and Systems, 4(2) (2017) 77-85
DOI 10.1515/ehs-2016-0022

(5) All-oxide thermoelectric module with in-situ formed non-rectifying complex p-p-n junction and transverse thermoelectric effect

Nikola Kanas, <u>Michael Bittner</u>, Temesgen Debelo Desissa, Sathya Prakash Singh, Truls Norby, Armin Feldhoff, Tor Grande, Kjell Wiik and Mari-Ann Einarsrud

submitted to *ACS Omega*

(6) A comprehensive study on improved power materials for high-temperature thermoelectric generators

<u>Michael Bittner</u>, Nikola Kanas, Richard Hinterding, Frank Steinbach, Matthias Schrade, Jan Räthel, Kjell Wiik, Mari-Ann Einarsrud, Armin Feldhoff

submitted to *Journal of Power Sources*

Puclications not included in this work:

(7) Novel CO_2-tolerant Al-containing membranes for high-temperature oxygen separation

Kaveh Partovi, <u>Michael Bittner</u>, Jürgen Caro

Journal of Materials Chemistry A, 3, (2015) 2400824015
DOI: 10.1039/c5ta04405g

(8) Enhanced flexible thermoelectric generators based on oxide-metal composite materials

Benjamin Geppert, Artur Brittner, Lailah Helmich, <u>Michael Bittner</u> and Armin Feldhoff

Journal of Electronic Materials, 46, No.4, (2017) 2356-2365
DOI: 10.1007/s11664-017-5281-7

(9) Influence of processing on stability, microstructure and thermoelectric properties of $Ca_3Co_{4-x}O_{9+\delta}$

Nikola Kanas, Sathya Prakash Singh, Magnus Rotan, Moshin Saleemi, <u>Michael Bittner</u>, Truls Norby, Kjell Wiik, Tor Grande, Mari-Ann Einarsrud

Journal of the European Ceramic Society, 38 (2018) 1592-1599
https://doi.org/10.1016/j.jeurceramsoc.2017.11.011

Patent:

(10) Deutsche Patentanmeldung DE 10 2017 2016 990.7 - Thermoelektrische Oxidkeramik und Verfahren zu ihrer Herstellung (Thermoelectric oxide ceramic and process for its preparation)

Michael Bittner, Armin Feldhoff

Deutsches Patent- und Markenamt, (2018), DE 10 2017 216 990.7 (pending)

Contributions to conferences:

(1) Oxide based thermoelectric generator for high-temperature application using p-type $Ca_3Co_4O_9$ and n-type $In_{2-x}Sn_xO_3$ legs

<u>Michael Bittner</u>, Benjamin Geppert, Kjell Wiik, Armin Feldhoff

34th International Conference on Thermoelectrics (ICT) and 13th European Conference on Thermoelectrics (ECT), Dresden (Germany), 28th-2nd June-July (2015) (Talk)

(2) Nanostructured oxide thermoelectrics for high-temperature energy harvesting

Armin Feldhoff, Benjamin Geppert, <u>Michael Bittner</u>

Microscopy Conference - German Society for Electron Microscopy, Göttingen (Germany), 6th-11th September (2015) (Poster)

(3) Flexible thermoelectric generator fabricated using bulk materials

Armin Feldhoff, Artur Brittner, Lailah Helmich, <u>Michael Bittner</u>, Benjamin Geppert

14th European Conference on Thermoelectrics (ECT), Lisbon (Portugal), 20th-23th September (2016) (Poster)

(4) Dynamics of entropy in thermoelectric materials and devices: Fundamentals and impact

Armin Feldhoff, Benjamin Geppert, <u>Michael Bittner</u>

THELMA workshop, Hurtigruten (Norway), 12th-16th September (2016) (Talk)

(5) Application of thermoelectric materials in flexible thermoelectric generator

Armin Feldhoff, Artur Brittner, Lailah Helmich, <u>Michael Bittner</u>, Benjamin Geppert

2nd Workshop Energy Harvesting Systems - FlexTEG, Fraunhofer IWS, Dresden (Germany), 26th-27th September (2016) (Talk and Poster)

(6) Dynamics of entropy, charge and energy in oxide-based thermoelectric materials and generators

Armin Feldhoff, <u>Michael Bittner</u>

University of California in Davis (UC Davis) (2017) (Talk)

(7) Porous $Ca_3Co_4O_9$ (CCO) with enhanced thermoelectric properties

<u>Michael Bittner</u>, Lailah Helmich, Frederik Nietschke, Benjamin Geppert, Oliver Oeckler, Armin Feldhoff

The Second Stuttgart Workshop on Thermoelectrics, Stuttgart (Germany), 8th August (2017) (Talk)

(8) Flexible thermoelectric generator fabricated from bulk materials

Armin Feldhoff, Artur Brittner, Lailah Helmich, <u>Michael Bittner</u>, Benjamin Geppert

12th Annual Energy Harvesting Workshop, Falls Church (USA), 11th-14th September (2017) (Talk)

(9) Porous $Ca_3Co_4O_9$ (CCO) with enhanced thermoelectric properties

<u>Michael Bittner</u>, Lailah Helmich, Frederik Nietschke, Benjamin Geppert, Oliver Oeckler, Armin Feldhoff

15th European Conference on Thermoelectrics (ECT), Padua (Italy), 25th-27th September (2017) (Talk)

(10) Self-assembly of a thermoelectric nanocomposite in a complex oxide system

<u>Michael Bittner</u>, Nikola Kanas, Frank Steinbach, Dennis Groneveld, Richard Hinterding, Piotr Wemhoff, Kjell Wiik, Mari-Ann Einarsrud, Armin Feldhoff

Bunsentagung, Hannover (Germany), 10th-12th May (2018) (Poster)

(11) Self-assembled oxide 2D nanocomposite with enhanced thermoelectric power factor and reduced thermal conductivity

Armin Feldhoff, <u>Michael Bittner</u>, Nikola Kanas, Frank Steinbach, Dennis Groneveld, Richard Hinterding, Piotr Wemhoff, Kjell Wiik, Mari-Ann Einarsrud

37th International Conference on Thermoelectrics (ICT) and 16th European Conference on Thermoelectrics (ECT), Caen (France), 1st-5th July (2018) (Talk)

(12) Self-assembled oxide nanocomposite with enhanced thermoelectric power factor and diminished thermal conductivity

Armin Feldhoff, <u>Michael Bittner</u>, Nikola Kanas, Frank Steinbach, Dennis Groneveld, Richard Hinterding, Piotr Wemhoff, Kjell Wiik, Mari-Ann Einarsrud

16th Electroceramics, Hasselt (Belgium), 9th-12th July (2018) (Talk)

(13) Triple-phase ceramic nanocomposite with enhanced thermoelectric power factor

Armin Feldhoff, <u>Michael Bittner</u>, Nikola Kanas, Frank Steinbach, Dennis Groneveld, Richard Hinterding, Piotr Wemhoff, Kjell Wiik, Mari-Ann Einarsrud

The 2nd Annual Energy Harvesting Society Conference, Philadelphia (USA), 5th-7th September (2018) (Talk)

Curriculum vitae

Michael Bittner

stay abroad – Norway 04.2015 – 08.2015	scientific exchange between **Leibniz University Hannover** and **NTNU**, **Norwegian University of Science and Technology**, financed by the E.ON Stipendienfonds
dissertation since 08.2014	*"Nanostructured Materials and their Application in Thermoelectric Energy Harvesting"*, dissertation at **Leibniz University Hannover**, **Institute of Physical Chemistry and Electrochemistry**
master thesis 11.2013 – 05.2014	*"Development of a lithium-ion-battery cell second generation with nanoscaled high energy materials"*, at **Leibniz University Hannover**, **Institute of Physical Chemistry and Electrochemistry** and **Volkswagen AG, department for research, operating power**
university education-Master 04.2012 – 05.2014	studies of Nanotechnology at **Leibniz University Hannover**
bachelor thesis 01.2011 – 07.2012	*"Transport and exchange of oxygen in doped cerium oxides"*, at **Leibniz University Hannover**, **Institute of Physical Chemistry and Electrochemistry**
internship 04.2011 – 09.2011	**Volkswagen AG, department for research, operating power**
university education-Bachelor 09.2008 – 07.2012	studies of Nanotechnology at **Leibniz University Hannover**
education 09.2000 – 06.2007 09.1998 – 07.2000 09.1994 – 07.1998	 high school **Willmsstraße**, Delmenhorst middle school **Wilhelm von der Heyde**, Delmenhorst elementary school **Bungerhof/Hasbergen**, Delmenhorst